Manganese and Iron-Based Layered Oxide Positive Electrodes for Sodium-Ion Batteries

by

Elahe Talaie-Pashiri

A thesis
presented to the University of Waterloo
in fulfillment of the
thesis requirement for the degree of
Doctor of Philosophy
in
Electrical and Computer Engineering (Nanotechnology)

Waterloo, Ontario, Canada, 2016

AUTHOR'S DECLARATION

I hereby declare that I am the sole author of this thesis. This is a true copy of the thesis, including any required final revisions, as accepted by my examiners.

I understand that my thesis may be made electronically available to the public.

Abstract

Electrical energy generation from clean and renewable energy sources is a topic of growing importance, considering the concerns over the environmental impacts and the resource constraints of fossil fuels, combined with the increasing worldwide energy demand. Development of low-cost energy storage systems is necessary to realize economical harvest of energy from intermittent renewable sources, such as the wind and solar energy. Lithium-ion battery, the state-of-the-art energy storage technology, provides high energy density and long cycle life, leading to its extensive use in portable electronic devices and its rapidly increasing application in electric vehicles. However, the large-scale application of electrical energy storage systems, to integrate renewable energy sources into the grid or to supply energy stored from local solar plants in remote areas, calls for important requirements: low-cost, material sustainability, and environmental safety. Lithium-ion batteries are presumed to fail these requirements as their cost is estimated to increase by the growth of electric vehicle market, due to the resource limitations of lithium.

Owing to the large abundance of sodium, sodium-ion battery technology is emerging as a promising alternative to the lithium-ion battery for large-scale applications, where sustainability and cost-effectiveness are more important criteria than gravimetric energy. Over the past few years, many efforts have been devoted to the development of sodium-ion batteries, including exploring new materials and novel chemistries and understanding the science underlying those systems. Layered oxides are the most studied and promising materials for the positive electrode in sodium-ion batteries; among them, P2-$Na_{0.67}[Mn_{0.5}Fe_{0.5}]O_2$ has attracted much attention from the research community. P2-$Na_{0.67}[Mn_{0.5}Fe_{0.5}]O_2$ is made from earth-abundant elements and delivers high specific energy, higher than 500 $Wh.kg^{-1}$, which is comparable to $LiFePO_4$ positive electrode material in lithium-ion batteries. Despite the advantages that P2-$Na_{0.67}[Mn_{0.5}Fe_{0.5}]O_2$ offers, instability in the ambient atmosphere and capacity fading are important challenges that hinder the commercial application of this material. Understanding

of those aging mechanisms and implementing tailored cation substitutions to mitigate them have been the objective of this thesis.

The instability of layered sodium transition metal oxides in ambient atmosphere is known. The study presented in Chapter 3 shows the important impact of exposure of P2-$Na_{0.67}[Mn_{0.5}Fe_{0.5}]O_2$ to air on its electrochemical performance; this issue was underestimated in the previously reported studies and is probably not limited to this particular material. An air exposed P2-$Na_{0.67}[Mn_{0.5}Fe_{0.5}]O_2$ electrode demonstrates lower capacity and higher voltage polarization compared to an air-protected one. The nature of the reactivity of this material with air is investigated by a combination of thermogravimetric analysis, mass spectrometry, diffraction techniques, electron microscopy, and electrochemical measurements. A mechanism is proposed to describe this reactivity; carbonate anions are formed upon the exposure of the material to CO_2, H_2O, and O_2 in air at room temperature and are inserted into the lattice, balanced by oxidation of Mn^{3+} ions to Mn^{4+}. The Ni-substituted materials, P2-$Na_{0.67}[Mn_{0.5+y}Fe_{0.5-2y}Ni_y]O_2$ (y = 0.1, 0.15) exhibit lower reactivity, as evidenced by the electrochemical performance.

The structural evolutions of P2-$Na_{0.67}[Mn_{0.5}Fe_{0.5}]O_2$ and P2-$Na_{0.67}[Mn_{0.65}Fe_{0.20}Ni_{0.15}]O_2$ induced by electrochemical extraction and insertion of sodium ions upon charge and discharge are investigated by *Operando* X-ray diffraction measurements (Chapter 4). The materials undergo similar phase transitions: one at high voltage and one at low voltage. The phase emerging at high voltage is investigated by pair distribution function analysis and Mössbauer spectroscopy; the migration of transition metals out of MO_2 layers into the interlayer space is proposed to occur at high voltage, induced by the stabilization of Fe^{4+} ions. The phase transitions are shown to have a detrimental impact on the electrochemical performance of the materials. Similar *operando* X-ray diffraction characterization, pair distribution function analysis, and electrochemical measurements are performed on P2-$Na_{0.67}[Mn_{0.66}Fe_{0.20}Cu_{0.14}]O_2$ (Chapter 5). P2-$Na_{0.67}[Mn_{0.65}Fe_{0.20}Ni_{0.15}]O_2$ outperforms the parent

P2-$Na_{0.67}[Mn_{0.5}Fe_{0.5}]O_2$ and the Cu-substituted composition, owing to its increased structural stability upon cycling and higher specific capacity achieved by Ni^{2+}/Ni^{4+} redox couple.

The redox processes involved in the cycling of P2-$Na_{0.67}[Mn_{0.66}Fe_{0.20}Cu_{0.14}]O_2$ and $Na_{0.67}[Mn_{0.65}Fe_{0.20}Ni_{0.15}]O_2$ are investigated by *operando* X-ray absorption spectroscopy. The evolution of the local structure of each transition metal upon charge and discharge is probed by the change in the X-ray absorption near-edge structure spectra collected at the transition metal K-edge. The data suggests the reversible contribution of oxide ions to the redox processes at high voltage.

Acknowledgements

I would like to extend my utmost gratitude and appreciation to my supervisor, Professor Linda F. Nazar, for giving me the opportunity to learn and grow throughout my doctoral studies and for providing me with her continuous support and advice. I would also like to thank my advisory committee members: Professor Hany Aziz, Professor William Wong, Professor Holger Kleinke, Professor Andrei Sazonov, and Professor Bo Cui for their time and guidance. I am very thankful to my external committee member, Professor Obrovac, for his time and suggestions.

I have been extremely fortunate to have the opportunity to work in a collaborative team environment. I would like to thank all the friendly and supportive members, past and present, of Nazar's group. I am very thankful to Dr. Rajesh Tripathi, Dr. Guerman Popov, and Dr. Brian Ellis for their support and assistance at the beginning of my Ph.D. studies. I would like to thank Professor Victor Duffort for providing me with his expertise and experience and for his wonderful contribution to this research. The studies presented in Chapter 3 and Chapter 4 are the results of our collaboration. I am thankful to Dr. Robert Black for operating the Mass Spectrometry experiments. I am very grateful to Se-Young Kim for his assistance in performing the X-ray absorption spectroscopy experiments, and to Quan Pang for his help with the design of the cells. I would also like to thank Dr. Dipan Kundu for his insightful discussions and suggestions.

I would like to extend my gratitude to Professor Brent Fultz and Dr. Hillary Smith (California Institute of Technology) to accomplish the Mössbauer spectroscopy analyses. I am very grateful to Dr. Ning Chen (the Canadian Light Source) for his kind assistance and support in the X-ray absorption spectroscopy study. I would also like to thank Professor Eric Prouzet (University of Waterloo) for his guidance for the analysis of X-ray absorption spectroscopy data.

I appreciate the National Sciences and Engineering Research of Canada, BASF, and the Canadian Light Source (CLS) for their financial support.

I am indebted to all my past and present teachers and advisors for their guidance. I am sincerely grateful to my family for their heartwarming love, encouragement, and support. Parham, Sepehr, and Borna, thinking of you makes me smile. I would like to thank all my friends in Waterloo for their companionship that made these years more joyful. Foremost, I am grateful to my dearest Amin, for his love, care, and support.

Table of Contents

List of Figures

List of Tables

Abbreviations

BSE - backscattered electron

ccp - cubic close packed

CLS - Canadian light source

CO_2 - carbon dioxide

DFT - density functional theory

EDS - energy dispersive X-ray spectroscopy

EES - electrochemical energy storage

EQS - electric quadrupole splitting

EV - electric vehicles

EXAFS - extended X-ray absorption fine structure

FEC - fluorinated ethylene carbonate

HEV - hybrid electric vehicles

HMF - hyperfine magnetic field

ICP-AES - inductively coupled plasma atomic emission spectroscopy

IS - isomer shift

LIB - lithium-ion battery

LMCT - ligand to metal charge transfer

LMO - $LiMn_2O_4$

MAS-NMR - magic angle spinning-nuclear magnetic resonance

MS - mass spectrometry

Na_2CO_3 - sodium carbonate

$Na_2CO_3 \cdot H_2O$ - thermonatrite

Na/S - sodium sulfur

NASICON - natrium super ionic conductor

NCA - $LiNi_{1-x-y}Co_xAl_yO_2$

NIB - sodium ion battery

NMC - $Li_{1+x}Ni_{1-y-z}Mn_yCo_zO_2$

NMP - N-methyl-2-pyrrolidinone

NMR - nuclear magnetic resonance

NPD - neutron powder diffraction

OCV - open circuit voltage

OEMS - online electrochemical mass spectrometery

ORNL - Oak Ridge National Laboratory

PC - propylene carbonate

PDF - pair distribution function

PHEV - plug-in hybrid electric vehicles

PV - photovoltaic

PVDF - polyvinylidene fluoride

RMC - reverse Monte Carlo

SE - secondary electrons

SEI - solid-electrolyte interphase

SEM - scanning electron microscopy

SNS - spallation Neutron Source

SXRD - synchrotron X-ray diffraction

TGA - thermogravimetric analysis

t.o.f - time of flight

XANES - X-ray absorption near-edge structure

XAS - X-ray absorption spectroscopy

XRD - X-ray diffraction

XRPD - X-ray powder diffraction

Chapter 1

Introduction

1.1 Overview

Electrical energy generation worldwide is currently estimated above 20 trillion kilowatt-hours and is predicted to reach 39 trillion kilowatt-hours in 2040.[1] Fossil fuels supply the majority of the electrical energy today and are expected to make a major contribution to electrical energy generation for at least next 25 years (**Figure 1.1**). The growing demand for energy combined with concerns about the environmental consequences of the use of fossil fuels and their resource constraints have incited the importance of the development of alternative sources of energy. Solar and wind energies are the cleanest and the most abundant sources of renewable energies. The capacities of power generation from these sources have expanded significantly over the past decade. Solar photovoltaic (PV) power capacity grew remarkably from 2.6 GW in 2004 to 177 GW in 2014, and the total installed capacity of wind power increased from 48 GW to 370 GW over the same period.[2] Further progress in the share of solar

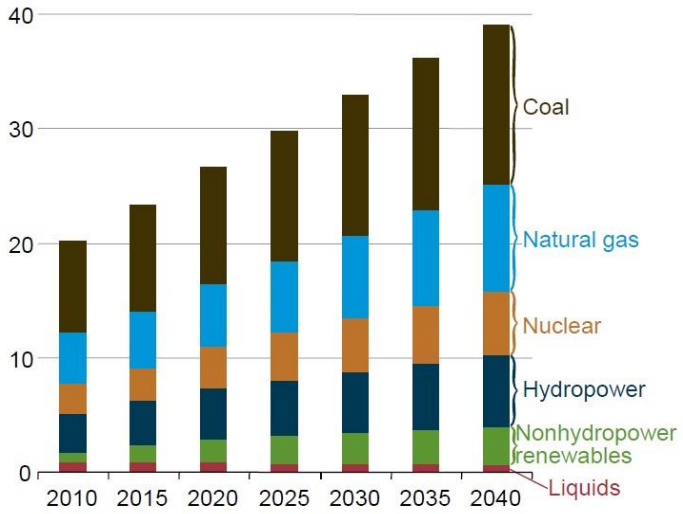

Figure 1.1 World net electricity generation by energy source, 2010-2040 (trillion kilowatt-hours). Adapted from reference 1.

and wind energy sources in the energy supply mix requires the development of large-scale, efficient energy storage systems due to the intermittent nature of renewable sources of energy.

Currently, pumped hydroelectric systems dominate large-scale energy storage.[3] However, electrochemical energy storage (EES) technologies have emerged as promising candidates owing to many breakthroughs in the field. Batteries, in particular, represent a feasible energy storage technology for the integration of renewable resources into the grid and storage and management of the energy, such as load leveling. Off-grid, batteries can be used to store the energy produced by local solar plants to supply energy for remote areas. Lithium-ion (Li-ion), high-temperature sodium sulfur (Na/S), and lead acid (Pb-acid) batteries are dominant among commercially available electrochemical energy storage technologies; Li-ion battery (LIB) is preeminent. Li-ion batteries are the major power supply utilized in portable electronic devices, hybrid electric vehicles (HEVs), plug-in hybrid electric vehicles (PHEVs), and electric vehicles (EVs). The application of LIBs is expected to expand with the forecasted growth of the electric vehicle market. Nonetheless, increased demand for LIBs has raised concerns about the resource availability and cost increase of lithium. The potential for the cost of lithium to increase makes currently expensive lithium ion batteries less affordable for large-scale applications.

Sodium ion battery (NIB) technology has emerged as a promising candidate for LIB for large-scale applications, where cost is a more important criterion than the volumetric and gravimetric energy density, owing to the high abundance and low cost of sodium. The amount of sodium in the earth's crust is over 1000 times higher than that of lithium.[4] Sodium is also found in vast amounts in the ocean. Moreover, aluminum foil can be used as the current collector at the negative electrode since sodium does not alloy with it, whereas copper current collectors are used for LIBs because lithium alloys with aluminum. This feature is advantageous regarding both the cost and energy density. Sodium is the second-lightest alkali element, after lithium. The redox potential of sodium ($E^{o}_{(Na+/Na)}$ = -2.71 V versus the standard hydrogen electrode) is only 0.3 V above that of lithium, resulting in a small drop in energy

compared to the Li^+/Li redox. The lower potential of sodium host positive electrodes is advantageous from a different perspective; opportunities are available to explore materials whose lithium analogues have potentials higher than the stability limits of many conventional electrolytes.

The electrochemical energy storage based on the sodium redox chemistry has a long history. The discovery of the high-temperature solid-state sodium ionic conductor β"-alumina[5] about fifty years ago was a breakthrough in the field of solid-state ionic conductors and sodium electrochemistry. The material was used as a separator/electrolyte in high-temperature Na/S batteries, which were commercialized in 2003 and are used for grid storage.[6] The Na/S cell operates at about 300 ºC at which both sulfur and sodium are molten and the ionic conduction of β"-alumina is enhanced. Safety concerns and the costly high-temperature requirements of the Na/S technology have increased interest in the development of lower temperature operating batteries. Natrium (sodium) super ion conductor (NASICON) types of materials, $Na_xM_2(XO_4)_3$; X = P^{5+}, Si^{4+}, S^{6+}, Mo^{6+}, As^{5+}, have gained much attention for the solid-state electrolyte application in sodium batteries that operate at lower temperatures between 110-130 ºC.[7] Room temperature all solid state sodium batteries based on sulfide glass-ceramics have shown promise for further exploration.[8]

Sodium batteries based on an intercalation material positive electrode, a sodium metal negative electrode, and a non-aqueous electrolyte were explored in the mid-1980s[9,10] along with lithium intercalation batteries. However, the higher energy density of lithium ion batteries (LIBs) and their commercialization in the 1990s shifted the focus of rechargeable batteries research to this technology. The need for a cost-effective and sustainable alternative to the LIB technology, along with the discovery of promising new chemistry of sodium intercalation materials, has boosted research interest in Na-ion batteries. The fundamental principles of the Na-ion battery technology are identical to those of Li-ion batteries. The structures investigated for Li-ion batteries are suitable starting points for exploring electrode materials for their sodium analogues even though novel chemistries have been found.[11-13]

Because of the importance of the knowledge developed on LIBs for NIB research, next section presents a brief introduction to the working mechanism and principles of LIBs. It is followed by an introduction to NIBs focusing on layered oxide positive electrode materials, which are investigated in the study presented in this thesis.

1.2 Li-Ion Batteries (LIBs)

A lithium ion battery cell works based on insertion and extraction of lithium ions between a positive electrode and a negative electrode through an electrolyte (**Figure 1.2**). A battery is composed of electrochemical cells connected in parallel or in series to provide the desired power and voltage. Upon discharge, lithium ions shuttle from the negative electrode to the positive electrode through the electrolyte, whereas electrons spontaneously flow in the same direction through an external circuit. The driving force for this process is the difference in the chemical potential of the electrode materials with respect to Li. Upon charge, the lithium ions are deintercalated from the positive electrode and move to the negative electrode through the electrolyte by applying a voltage higher than the electrochemical potential difference between the negative electrode and positive electrode. The electrolyte is electronically insulating and prevents direct flow of electrons between the electrodes. A thin electronically insulating porous membrane, which is permeable to Li^+, separates the positive and negative electrodes and prevents a short circuit. Current collectors provide electronic conduction to and from the electrodes. An aluminum current collector is typically used for the positive electrode, and a copper current collector is used for the negative electrode due to the reactivity of lithium with aluminum. The positive and negative electrodes are composite materials made from a mixture of the active material, an additive carbon, and a binder. The additive carbon increases the electronic conductivity, and the binder enhances the contact between the particles.

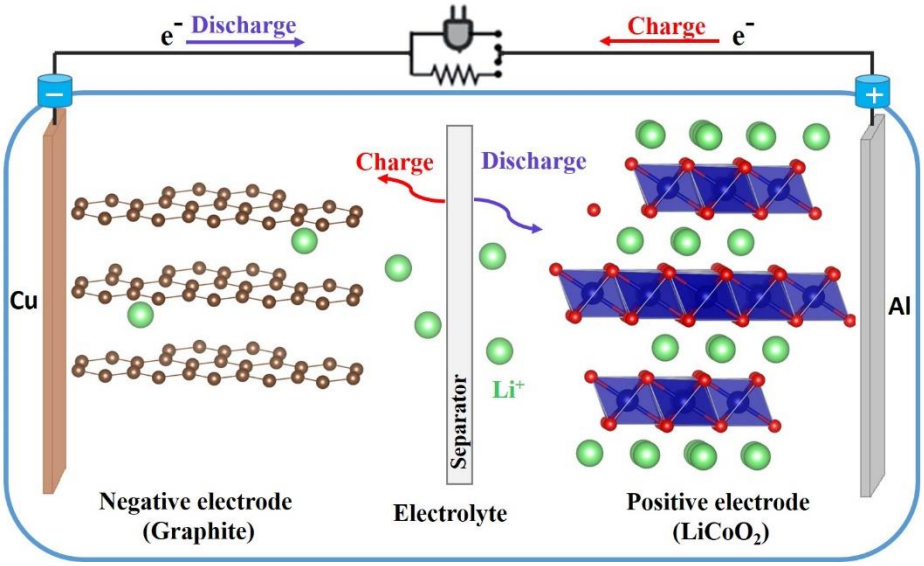

Figure 1.2 Schematic representation of a Li-ion battery cell.

The electrochemical redox reactions in a $LiCoO_2$/graphite cell upon charge can be described as follows:

Positive electrode: $LiCoO_2 \rightarrow Li_{1-x}CoO_2 + xLi^+ + xe^-$ **(1.1)**

Negative electrode: $C6 + xLi^+ + xe^- \rightarrow Li_xC_6$ **(1.2)**

where during discharge, the reactions occur in the opposite direction. The application of $LiCoO_2$ as an intercalation material in an electrochemical cell with the lithium metal negative electrode was first introduced by Goodenough *et al.* in 1980.[14] The application of lithium metal in batteries was eventually rejected due to safety concerns. Lithium tends to form a dendritic structure on the metal surface after repeated lithium plating during charge after several cycles. Lithium dendrites actively reduce the electrolyte and may penetrate into the separator and reach the positive electrode leading to a short circuit, overheating of the cell, and a fire. The introduction of much safer carbonaceous materials as the negative electrode active material provided a great leap forward in the development of Li-ion batteries. A $LiCoO_2$/carbon cell with a nonaqueous electrolyte (1M $LiPF_6$ in a 1:1 (by volume) mixture of propylene carbonate and 1,2-dimethoxyethane) was commercialized first by Sony Corporation in the

1990s.[15] The positive electrode materials used in the majority of current generation of electric vehicles are either from the family of oxides, including layered and spinel structures, or olivine structure: layered $Li_{1+x}Ni_{1-y-z}Mn_yCo_zO_2$ (NMC) in Daimler Smart EV; layered $LiNi_{1-x-y}Co_xAl_yO_2$ (NCA) in Tesla Model S and BMW Active Hybrid 7, a blend of layered NMC with spinel $LiMn_2O_4$ (LMO) in Chevrolet Volt, BMW i3, and Nissan Leaf; olivine $LiFePO_4$ in BMW Active Hybrid 3 and 5 series, Fisker Karma, and Chevrolet Spark.[16] The energy density, power, cycle life, safety, and cost are the critical criteria based on which a battery system is evaluated. A key limiting factor of LIBs is the positive electrode material. The practical specific capacity and the average operating voltage of three important classes of positive electrode materials for LIB are as follows: 170 $mAh.g^{-1}$ and 3.8 V for $Li[Ni_{1/3}Mn_{1/3}Co_{1/3}]O_2$, 190 $mAh.g^{-1}$ and 3.8 V for $Li[Ni_{0.8}Co_{0.15}Al_{0.05}]O_2$, 120 $mAh.g^{-1}$ and 4.7 V for $Li[Mn_{3/2}Ni_{1/2}]O_4$, 160 $mAh.g^{-1}$ and 3.45 for $LiFePO_4$.[17,18] In general, positive electrode materials that contain polyanionic groups, *i.e.*, $(PO_4)^{3-}$, $(SiO_4)^{4-}$, and $(SO_4)^{2-}$, provide superior structural and thermal stability, therefore long cycling life and safety, to the layered oxide host materials. The major drawback with olivine $LiMPO_4$ (M = Fe, Mn) materials is their poor electronic and ionic conductivity, in addition to low volumetric energy density. Particle size reduction, carbon coating, and aliovalent cation doping are strategies that remarkably enhance the ionic and electronic conduction of olivine $LiMPO_4$.[19,20]

In general, aging mechanisms in each particular Li-ion cell is influenced by the nature of the cell components, *e.g.,* active materials, electrode design, electrolyte composition, *etc*., and depend on cycling conditions, and state of the charge. The dominant aging mechanisms of a graphite/layered lithium metal oxide cell with an organic electrolyte can be summarized as follows:[21]

Negative electrode side:

- Reductive decomposition of the electrolyte at the negative electrode/electrolyte interface at the charged state of the electrode results in the formation of a protective layer, which is so-called solid-

electrolyte interphase (SEI). The protective SEI layer decreases further electrolyte decomposition and is permeable to lithium ions, but not electrolyte components and electrons. Irreversible consumption of lithium ions due to SEI formation, however, causes irreversible capacity loss. SEI layer formation is usually accompanied by the release of gaseous electrolyte decomposition products, which raises safety concerns. Electrolyte decomposition and SEI formation occur mainly upon the first few cycles. The SEI layer grows over the following cycles causing an increase in the cell impedance. Elevated temperatures accelerate the growth of the SEI layer upon cycling and storage. Also, the reaction of the electrolyte salt $LiFeP_6$ with trace water forms HF that makes a destructive impact on the SEI layer.

- At low temperatures and high current rates, lithium plating might occur at the negative electrode surface. The growth of lithium dendrites and the reaction of metallic lithium with electrolyte are the consequences.

- Graphite exfoliation and graphite particles crack might occur due to the co-intercalation of solvent molecules and contribute to electrode aging.

- Mechanical or electronic contact loss among different components of the composite electrode, *e.g.,* current collector, active material, binder, is another origin of electrode degradation. Important sources of the contact loss include volume change of the active material, reaction of the negative electrode with fluorine-containing materials in the cell (such as binder) that forms LiF, and corrosion of the current collector.

Positive electrode side:

Important aging mechanisms occurring at the positive electrode side include:

- Phase transitions and structural evolution of the active material

- Chemical decomposition and dissolution reactions

- Oxidation of the electrolyte and formation of surface films

- Degradation of composite electrode components (binder, conductor additive, and current collector)

- Interaction of the degradation products with the negative electrode

Chemical composition modification (cation substitution), surface coating, and the use of electrolyte additives are important strategies to address these challenges.[19]

1.3 Na-Ion Batteries (NIBs)

The operation principle of a Na-ion battery cell is similar to its Li-ion analogue; sodium ions are shuttled between the positive and negative electrodes through an electrolyte, in parallel with the transfer of electrons through an external circuit. A common electrolyte is comprised of a sodium salt, *e.g.*, $NaClO_4$ or $NaPF_6$, in an organic solvent, such as propylene carbonate (PC). Application of electrolyte additives, fluorinated ethylene carbonate (FEC) in particular, was found critical for a satisfactory capacity retention, owing to the enhanced passivation at the negative electrode and the electrolyte interface.[22,23,24] The negative electrode is one of the most troublesome components of the NIBs. Sodium metal cannot be employed as the negative electrode in a full cell because of safety concerns and unstable passivation in most organic electrolytes.[25] Nevertheless, sodium ions do not intercalate significantly into graphite. Hard carbon (disordered carbon) is one of the most studied materials for the negative electrode in NIBs.[23-26] The electrochemical potential of sodium inserted hard carbon is close to that of sodium metal itself. Na ions fill the porosity in the disordered hard carbon structure rather than intercalate between graphitic layers.[27]

The development of sodium ion batteries was sought after in the 1980s, along with lithium-ion batteries. Shortly after the report of the electrochemical intercalation of lithium ions into TiS_2 and its application as the basis of a new battery system by Whittingham in 1976,[28] electrochemical intercalation

of sodium ions in a $NaTiS_2$/Na cell at room temperature was demonstrated in 1980.[29] Several polytypes of layered structure Na_xCoO_2 ($0.5 \leq x \leq 1$) were examined as the positive electrode in the sodium cell in 1981,[30] following the report of the electrochemical performance of $LiCoO_2$ in a lithium cell in 1980.[14] Li-ion batteries dominated the research for electrochemical energy storage in the 1990s owing to their higher potential and lower mass, and therefore, higher specific energy compared to their sodium counterpart. **Figure 1.3** shows a comparison of the charge and discharge profile of Li/$LiCoO_2$ and Na/$NaCoO_2$ cells.[4] $LiCoO_2$ and $NaCoO_2$ adopt similar layered structure made up of edge-sharing CoO_6 layers accommodating lithium or sodium octahedra within the interlayer space. However, the operating voltage of the Na/$NaCoO_2$ cell is much lower (> 1.0 V) than the voltage of the Li/$LiCoO_2$ cell at the end of discharge. Consequently, the available energy density of $NaCoO_2$ as a positive electrode is about 30% lower than that of $LiCoO_2$.[4] Also, there are several flat and sloping regions on the voltage profile of $NaCoO_2$ indicating the structural evolution of the material over charge/discharge. There are no reports of direct synthesis of sodium analogues of spinel $LiMn_2O_4$ and olivine $LiFePO_4$ positive electrode materials, to the best of the author's knowledge. Sodium manganese oxide cannot be prepared in the spinel structure due to the unavailability of tetrahedral sites for sodium ions. $NaFePO_4$ crystallizes

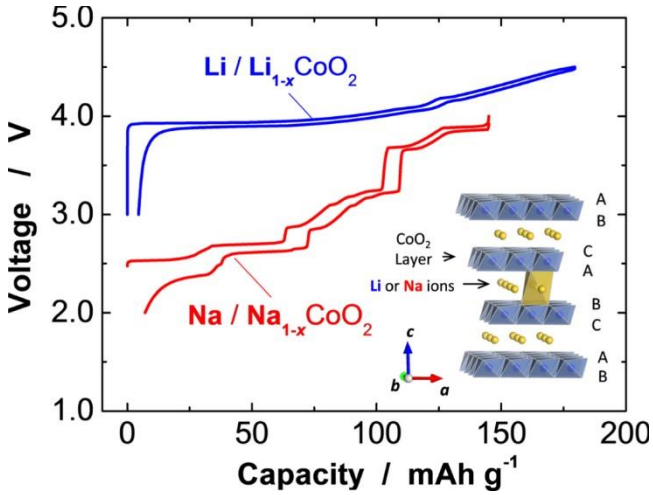

Figure 1.3 Charge/discharge curves of Li/$LiCoO_2$ (blue) and Na/$NaCoO_2$ (red) cells, and a schematic illustration of $LiCoO_2$ and $NaCoO_2$ crystal structure. Adapted from Ref. 4.

in the more thermodynamically stable maricite structure, which has no open channels for the diffusion of Na ions.[31,32] These examples indicate the importance of the discovery of new materials with different chemistry compared to that of the Li system to realize the commercialization of Na-ion batteries.

Substitution of lithium by sodium enables the access to redox couples, such as $NaFeO_2$[11,12] and $NaCrO_2$[13], that are inactive in the corresponding lithium metal oxides. Electrochemically active materials based on Fe^{3+}/Fe^{4+} redox, which is unique to the Na system, are promising candidates to explore for high energy and low-cost positive electrodes in sodium-ion batteries. The size difference between sodium ions and lithium ions provides the opportunity of various material structures. Owing to the large mismatch between the ionic radii of sodium ions and transition metal ions, sodium layered oxides with different stacking schemes are synthesized for many transition metals.[33] Polyanionic compounds with open-framework structures, thermal stability, and tunable potential (by modifying the local environment) open another avenue of opportunity for the electrode materials research.[34,35] Larger ionic radius of Na^+ compared to that of Li^+ provides other advantages for NIBs over LIBs:[35] i) relatively lower energy for the sodium ion desolvation process in polar solvents (which is probably at the origin of higher ion conductivity of Na^+ electrolytes compared to Li^+ electrolytes)[36], and ii) relatively lower activation energy of Na^+ diffusion compared to that of Li^+ calculated for layered structure $ACoO_2$ (A = Li, Na).[37]

In spite of all the opportunities and the promise that room temperature NIBs offer for sustainable and efficient energy storage, several barriers should be overcome to accomplish NIBs commercialization. One important challenge is insufficient cycle life, which requires the design of new materials for the positive and negative electrodes and the electrolyte. Research in NIBs has significantly increased over the last few years. Many efforts have been devoted to addressing the challenges with this technology. This section is followed by a brief review of some important knowledge achieved from the studies

performed over the last few years on manganese and iron-based sodium metal oxide materials, which are the focus of the study presented in this thesis.

1.4 Layered Sodium Transition-Metal Oxides for Positive Electrode Materials in NIBs

1.4.1 Classification of Layered Oxides

Layered Na_xMO_2 and Li_xMO_2 (M: transition metal, $x \leq 1$) are built up of layers of edge-sharing MO_6 octahedra in the *ab*-plane. Various stacking orientations of MO_2 layers along the *c*-axis result in polytypism. Layered sodium transition metal oxides commonly crystallize in two polytypes: P2 and O3 (**Figure 1.4**), according to the Delmas's notation.[38] In this notation, P and O represent the trigonal prismatic and octahedral sites, respectively, at which sodium ions are accommodated between MO_2 layers. The number (2, 3, etc.) following the sodium site coordination (O, P) indicates the number of MO_2 layers in each unit cell, *e.g.*, two MO_2 layers in P2 and three MO_2 layers in O3.

The P2-type phase is empirically known to be synthesized upon sodium deficiency condition (Na_xMO_2, $x < 1$). An ideal P2-type phase (ABBA oxygen stacking) is described with the space group of $P6_3/mmc$. An ideal O3 phase with the space group $\boldsymbol{R\bar{3}m}$ consists of a cubic close packed (ccp) oxygen array (ABCABC stacking) which accommodates alternate layers of M and Na, due to their different ionic radii. A prime symbol (′) in the Delmas's nomenclature represents an in-plane distortion, such as monoclinic distortion in O′3-$NaMnO_2$ (space group *C2/m*)[39] and orthorhombic distortion in P′2-Na_xMnO_2 (*Cmcm* space group)[40]. Electrochemical extraction of sodium ions form O3 and P2-type phases (and also insertion of sodium ions into the P2 phase) results in phase transitions.[41-43] When sodium ions are partially extracted from an O3-type phase, prismatic sites could be energetically favored for sodium ion accommodation. Prismatic sites can be realized by the gliding of MO_2 slabs,

without breaking metal-oxygen bonds, resulting in the formation of a P3-type phase (**Figure 1.4**). The P3-type phase is possible to be directly synthesized by a solid-state reaction method.[44] Electrochemical extraction of sodium ions from a P2-type phase can derive a transition to the O2-type phase, which is achieved by the gliding of MO_2 layers.[43] The oxygen array in O2-type structure can be described as an alternate cubic close packed and hexagonal close packed stacking. The obtained phases of synthesized layered sodium metal oxides rely on the synthesis conditions, such as the precursor compositions and preparation method (grinding and pelletizing), heating temperature, heating atmosphere, and cooling rate, as demonstrated by Ceder *et al.*[42] and Obrovac *et al.*[45]

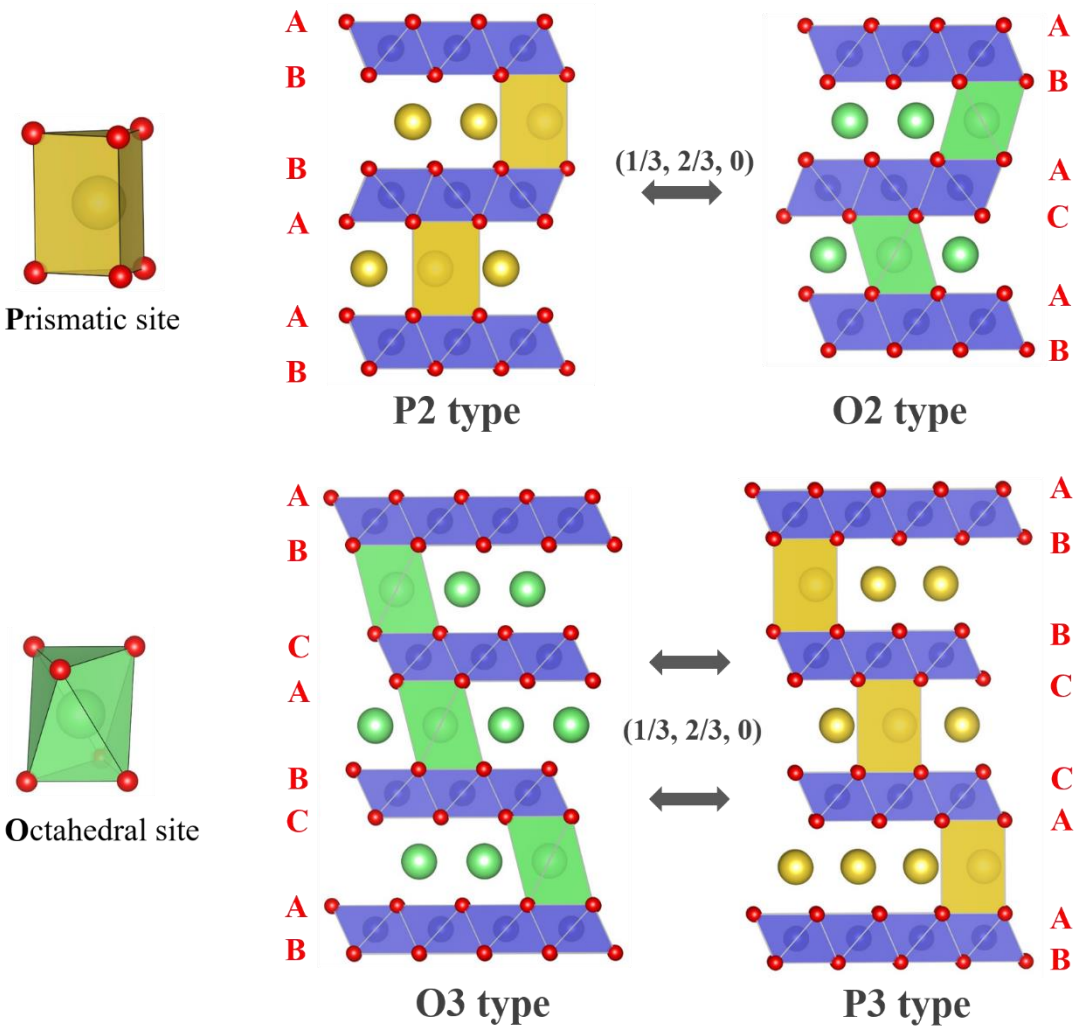

Figure 1.4 The classification of layered sodium transition metal oxides.

In an O3-type structure, sodium ions migrate through the interstitial tetrahedral sites that share faces with the MO_6 octahedra (**Figure 1.5**)[4] because of high activation energy required for a direct ion-hopping from one octahedral site to the neighboring one. Nevertheless, in a P2-type structure, sodium ions migrate from one prismatic site to the adjacent one, leading to a smaller activation barrier due to the smaller repulsive interactions between the sodium ion and the cations in the adjacent MO_2 layers. This difference in sodium ion migration paths is probably the origin of the higher ionic conductivity of P2-type structure materials compared to that of O3-type structure materials at the same sodium/vacancy concentrations.[46] It should be noted that phase transitions (such as O3-P3 or P2-O2) change the ion transport mechanism. The calculated activation energy for sodium ion transport in $Na_x[Ni_{1/3}Mn_{2/3}]O_2$ ($x < 1$) was reported to increase by more than 100 meV upon the P2-O2 phase transition.[47]

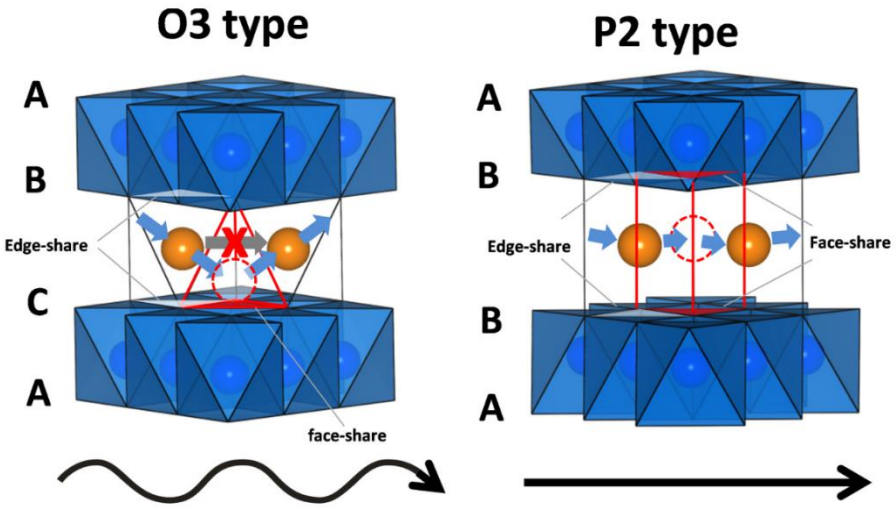

Figure 1.5 Schematic illustration of sodium ion transport path in O3 and P2 type structures. Reproduced from Ref. 4.

1.4.2 Recent Advances in Manganese and Iron-Based Oxides

Solid solutions of layered structure Na_xMnO_2, $NaFeO_2$, $NaNiO_2$, and Na_xCoO_2 ($x \leq 1$) have been extensively investigated to design positive electrode materials with high energy density and long cycle life for NIBs.[33] Low cost and sustainability, which are the major motivations for the development of

NIBs, should be considered for the choice of electrode materials. Therefore, low cobalt content and especially manganese and iron-rich materials have gained much attention from the NIBs research community.

O3-$NaFeO_2$ is electrochemically active,[11] contrary to its lithium analogue where oxygen evolution is believed to be the favorable process at high potentials.[48] However, the reversibility of the reaction ($Fe^{3+/4+}$ redox in O3-$NaFeO_2$) depends on the cutoff voltage because an irreversible phase transition occurs at high voltage. This deleterious structural evolution is characterized by diffraction and spectroscopy methods[4]. Excellent reversibility of the electrode performance is achieved when the cutoff voltage is limited to 3.4 V, at the expense of the specific energy.

Yamada *et al.* [49] investigated the effect of Ni substitution on the electronic and electrochemical properties of O3-$NaFeO_2$. Solid solutions of O3-$NaFeO_2$ and $NaNiO_2$ were formed only for a narrow compositional range, $0.5 \leq y \leq 0.7$ in $Na[Fe_{1-y}Ni_y]O_2$. The electrochemical performance of O3-$Na[Fe_{1-y}Ni_y]O_2$ (y = 0, 0.5, 0.7) showed that substituting iron with nickel ions results in enhanced discharge capacity and improved cyclability (**Figure 1.6**). X-ray diffraction and charge/discharge profile revealed that sodium deintercalation from $Na_x[Fe_{0.3}Ni_{0.7}]O_2$ progresses through a solid-solution process for most of the cycling range in contrast to the two-phase process in Na_xFeO_2. It is proposed that the improved cycling stability in the Ni-substituted electrode materials originates from the large contribution of $Ni^{4+/3+}$ redox couple to the capacity and decreased formation of Jahn-Teller active Fe^{4+} ions.

Layered structure sodium manganese oxide is reported to crystallize in O′3,[39,50] P′2,[51] and P2[39,52] type structures by controlling the synthesis conditions. O′3-$NaMnO_2$ [50] delivers a high specific capacity $\approx$ 185 $mAh.g^{-1}$ when cycled between 2 - 3.8 V at a rate of C/10. Its pronounced stepwise voltage profile

is indicative of structural transitions during charge/discharge. These structural changes limit the cycling life and rate capability of the electrode. Similar behavior is observed for P2-Na_xMnO_2.[4]

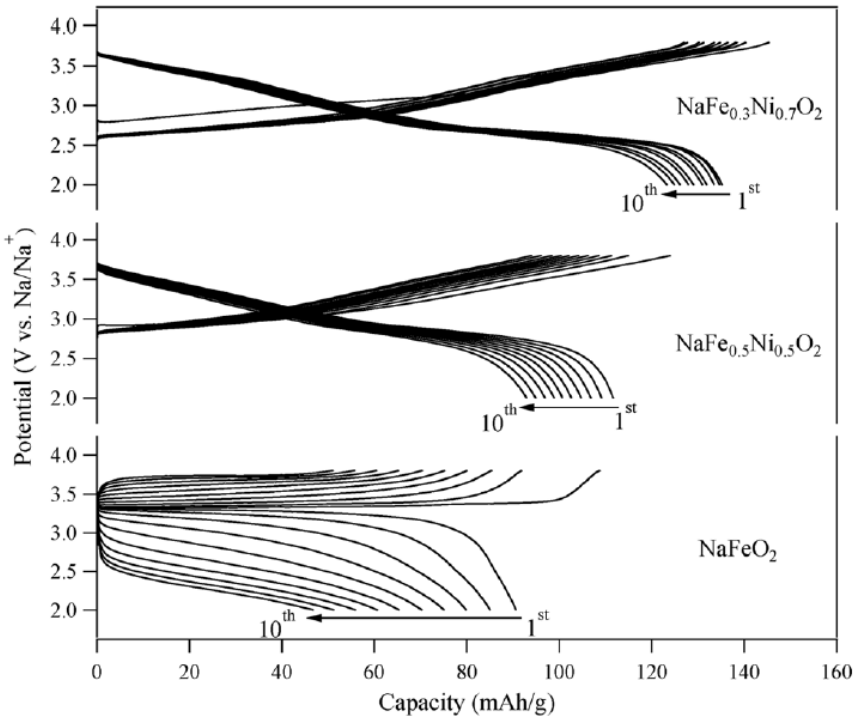

Figure 1.6 Galvanostatic charge/discharge curves of O3-$Na[Fe_{1-y}Ni_y]O_2$ (y = 0, 0.5, 0.7) cycled in the voltage range of 2 - 3.8 V at a rate of 30 $mA.g^{-1}$. Reproduced from Ref. 49.

There is no report of the synthesis of P2-type Na_xFeO_2, to the best of the author's knowledge. However, partially substituted composition, P2-$Na_{2/3}[Mn_{1/2}Fe_{1/2}]O_2$, which is one of the most promising positive electrode materials for Na-ion batteries in terms of both sustainability and the electrochemical performance, was synthesized and studied first by Komaba *et al.*[53] In addition to the low cost of manganese and iron, P2-$Na_{2/3}[Mn_{1/2}Fe_{1/2}]O_2$ delivers a high specific capacity about 190 $mAh.g^{-1}$ and a specific energy over 520 $Wh.kg^{-1}$. This is comparable to $LiFePO_4$, which exhibits a practical positive electrode specific energy of ≈ 530 $Wh.kg^{-1}$. The crystallographic density of P2-$Na_{2/3}[Mn_{1/2}Fe_{1/2}]O_2$ (4.1 $g.cm^{-3}$) is higher than that of olivine $LiFePO_4$ (3.6 $g.cm^{-3}$), and carbon coating and particle size reduction

are not necessary for the electrochemical activity of P2-$Na_{2/3}[Mn_{1/2}Fe_{1/2}]O_2$, contrary to $LiFePO_4$. The P2-$Na_{2/3}[Mn_{1/2}Fe_{1/2}]O_2$/Na cell retains about 70% of its reversible capacity when the discharge rate is increased from C/20 to 1C. The superior rate capability of P2-$Na_{2/3}[Mn_{1/2}Fe_{1/2}]O_2$ compared to that of many other layered transition metal oxides is correlated to its smooth charge/discharge voltage profile, which suggests a facile de/intercalation reaction. Pronounced structural transitions dominate in Na_xMnO_2[50] and Na_xCoO_2[54], for example, and are limiting factors for the high rate performance. The galvanostatic charge/discharge voltage profile of $Na_{0.7}CoO_2$[54] shows potential plateaus, indicative of biphasic regions, and nine potential drops that are related to sodium/vacancy ordering (**Figure 1.7**).

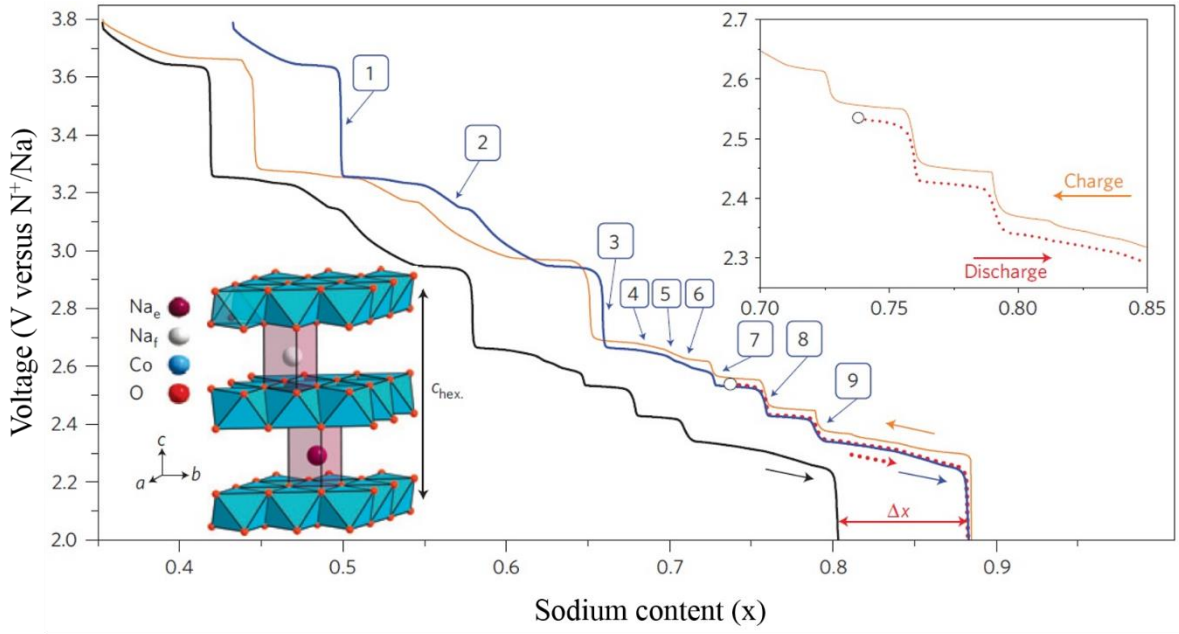

Figure 1.7 Galvanostatic cycling of $Na_{0.7}CoO_2$, 1st discharge (red dot), 1st charge (orange line), 2nd discharge (black line) and shifted 2nd discharge (blue line) in order to compensate the effect of electrolyte decomposition and match the first discharge. The crystal structure of $Na_{0.7}CoO_2$ is schematically illustrated in the inset. Reproduced from Ref. 54.

In spite of much promise that P2-$Na_{2/3}[Mn_{1/2}Fe_{1/2}]O_2$ offers as the positive electrode material for NIBs, there are three important drawbacks associated with this material. First, it is unstable in ambient atmosphere, similar to many other sodium host oxide materials. A study[55] of the reactivity of P2-

$Na_{2/3}[Mn_{1/2}Fe_{1/2}]O_2$ with the atmosphere and the effect of this reactivity on the electrochemical properties of the material are described in Chapter 3. The second challenge with this material is its cyclability. P2-$Na_{2/3}[Mn_{1/2}Fe_{1/2}]O_2$ retains over 75% of its initial capacity after 30 cycles. In the first study of this material,[53] the capacity fading was attributed to a transition from the P2 phase to a low crystalline new phase upon charge. Due to the low crystallinity of the new phase achieved at high voltages, the structure of the phase was not solved. However, an OP4-type structure, consisting of a mixture of O and P-type of stacking, was proposed based on the indexation of the X-ray diffraction pattern. The phase transitions of $Na_{2/3}[Mn_{1/2}Fe_{1/2}]O_2$ upon galvanostatic charge/discharge were studied by *operando* XRD analysis in our research group[56] (presented in Chapter 4) and some other groups[57,58] in parallel. A reversible transition from the hexagonal P2 to the orthorhombic P′2-type structure is induced by the insertion of sodium ions into $Na_x[Mn_{1/2}Fe_{1/2}]O_2$ ($x > 0.8$), originating from the cooperative distortion of Jahn-Teller active Mn^{3+} ions. Another challenge with P2- $Na_{2/3}[Mn_{1/2}Fe_{1/2}]O_2$, or any other P2-type phase in general, is sodium deficiency for application in a full Na-ion cell. Adding some sources of sodium ions, such as Na_2NiO_2[59] (which electrochemically decomposes to sodium and $NaNiO_2$) and NaN_3[60] (which electrochemically decomposes to sodium and N_2 gas), to the positive electrode is reported to be a beneficial approach to overcome the sodium deficiency, in general due to Na^+ loss in the formation of passivating solid-electrolyte-interphase (SEI), and specially for P2-Na_xMO_2 electrode materials ($x < 1$). O3-type $Na[Mn_{1/2}Fe_{1/2}]O_2$ was also synthesized by controlling the ratio of sodium to the transition metals in the precursors.[53] The O3-type material, however, showed a larger voltage polarization and a lower specific capacity compared to the P2-type one.

As demonstrated by X-ray absorption spectroscopy and Mössbauer spectroscopy, the $Fe^{3+/4+}$ redox couple is active in the desodiation process of P2-$Na_{2/3}[Mn_{1/2}Fe_{1/2}]O_2$.[53] The fitting of the Mössbauer spectrum of the sample charged to 4.5 V revealed oxidation of about 32% of iron ions. However, assuming that all the manganese ions are oxidized to tetravalent state in the charged sample (4.2 V, x

= 0.13 in $Na_x[Mn_{1/2}Fe_{1/2}]O_2$), more than 70% of iron ions are expected to be oxidized based on the charge balance ($Na_{0.13}[Mn^{+4}_{0.5}Fe^{+4}_{0.37}Fe^{+3}_{0.13}]O_2$). Much less concentration of oxidized iron ions detected by the Mössbauer spectroscopy raised questions about the nature of charge compensation mechanisms in this system. This question is addressed in the research presented in this thesis (Chapter 4).

Following the initial report of the auspicious properties of P2-$Na_{2/3}[Mn_{1/2}Fe_{1/2}]O_2$,[53] many efforts have been devoted to exploring various compositions of P2 and O3-type $Na_x[Mn_yFe_{1-y}]O_2$[61-65] and their solid solutions with other Na_xMO_2 (M = Ti, Co, Ni, Cu) oxides[41,66-70] to improve their electrochemical performance, in particular stability. Rojo *et al.*[66] reported an excellent capacity retention of 87% over 300 cycles for Mn-rich P2-phase $Na_{2/3}[Mn_{0.8}Fe_{0.1}Ti_{0.1}]O_2$ cycled within the voltage range of 4.0 - 2.0 V at the 1C rate (the average 0.04 % capacity degradation per cycle) (**Figure 1.8**). An average 0.1% capacity degradation on each cycle was observed for the cycling of that material at the same conditions, but at the lower cycling rate of C/10. The improvement of the capacity retention by increasing the cycling rate indicates that the degradation originates from the interaction of the electrode and

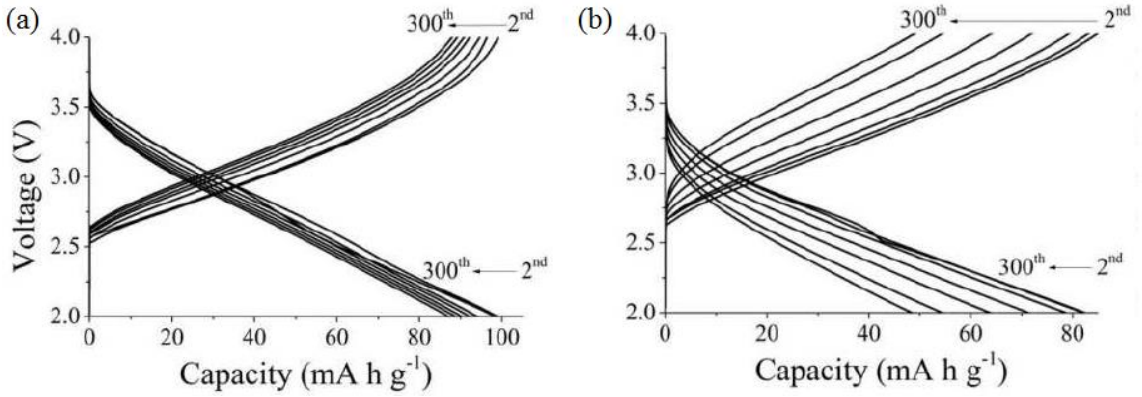

Figure 1.8 Charge/discharge profile of pristine P2-phase $Na_{2/3}[Mn_{0.8}Fe_{0.1}Ti_{0.1}]O_2$ electrode (a) and moisture exposed electrode (b) cycled within the voltage range of 4.0 - 2.0 V at 1C for 300 cycles. Reproduced from Ref. 66.

electrolyte, in addition to the electrode aging. A moisture exposed electrode showed lower capacity and faster degradation under the same conditions and maintained 70% of discharge capacity after 300 cycles at the 1C cycling rate **(Figure 1.8)**. It is proposed that only manganese is electrochemically active in the charge/discharge processes, and electrochemically inactive Ti^{4+} and Fe^{3+} ions enhance the structural stability of the oxide layer and dilute the deleterious effect of Jahn-Teller distortion induced by Mn^{3+} ions.

Ceder *et al.*[67] have reported the highest rate capability for P2-$Na_{2/3}[Mn_{1/2}Fe_{1/4}Co_{1/4}]O_2$ among all the layered oxide electrode materials for NIBs. P2-$Na_{2/3}[Mn_{1/2}Fe_{1/4}Co_{1/4}]O_2$ delivers a high specific capacity of 195 $mAh.g^{-1}$ at the first discharge when cycled between 1.5 and 4.5 V at the C/10 rate. When the cycling rate is increased to 30C, a specific capacity of 130 $mAh.g^{-1}$ is achieved, over a slightly extended voltage window (**Figure 1.9**). The excellent rate capability is attributed to the effect of transition metal mixing in the layered material that perturbs the transition metal ordering and sodium/vacancy ordering. The structural evolution of the material over the charge/discharge at the C/50 rate was investigated by *operando* XRD analysis. A reversible transition from the pristine P2-type structure to a new phase similar to the high voltage $Na_x[Mn_{1/2}Fe_{1/2}]O_2$ phase was observed upon charge.

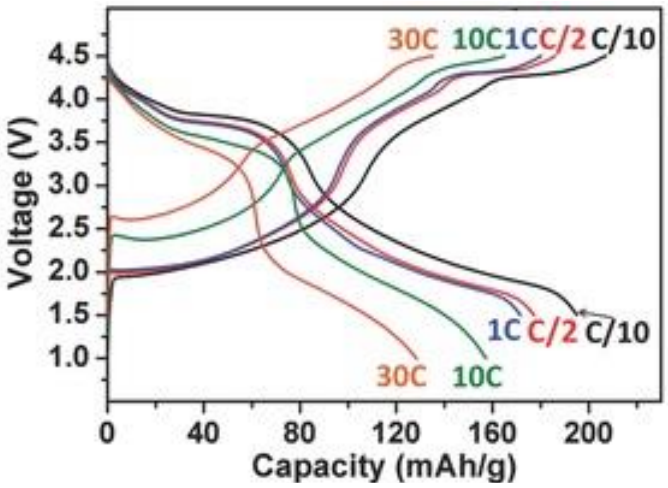

Figure 1.9 First galvanostatic charge/discharge curves of P2-$Na_{2/3}[Mn_{1/2}Fe_{1/4}Co_{1/4}]O_2$ cycled at different current rates. Reproduced from Ref. 67.

The P2-type structure was preserved at voltages as low as 1.5 V, contrary to sodiated $Na_x[Mn_{1/2}Fe_{1/2}]O_2$. This extended range of the P2 single phase domain in the Co-substituted composition is achieved owing to the reduction of Co^{3+} to Co^{2+} instead of Mn^{4+} to the Jahn-Teller active Mn^{3+} ions over the discharge, as shown by electron energy loss spectroscopy. The large Na^+ diffusivity in the wide P2 single phase domain contributes significantly to the high rate performance of P2-$Na_{2/3}[Mn_{1/2}Fe_{1/4}Co_{1/4}]O_2$. Limiting the high cutoff voltage in order to avoid the phase transition was demonstrated to enhance the capacity retention of the cell cycled at a low current rate (C/10). The cyclability of P2-$Na_{2/3}[Mn_{1/2}Fe_{1/4}Co_{1/4}]O_2$ at high current rates was not evaluated in this research.

Ceder *et al.*[41] investigated a quaternary layered material O3-$Na[Mn_{1/4}Fe_{1/4}Co_{1/4}Ni_{1/4}]O_2$ with a high specific energy 578 $Wh.kg^{-1}$ as the positive electrode for NIBs. X-ray absorption spectroscopy (XAS) measurements revealed the valence states of the material's constituent transition metal cations as follows: Mn^{4+}, Fe^{3+}, Co^{3+}, and Ni^{2+}, similar to their valence states in O3-$Na[Ni_{1/2}Mn_{1/2}]O_2$[71] and O3-$Na[Fe_{1/2}Co_{1/2}]O_2$[72]. Three reversible phase transitions (to new hexagonal phases) over the first charge/discharge were detected by an *operando* XRD experiment for $Na_x[Mn_{1/4}Fe_{1/4}Co_{1/4}Ni_{1/4}]O_2$,

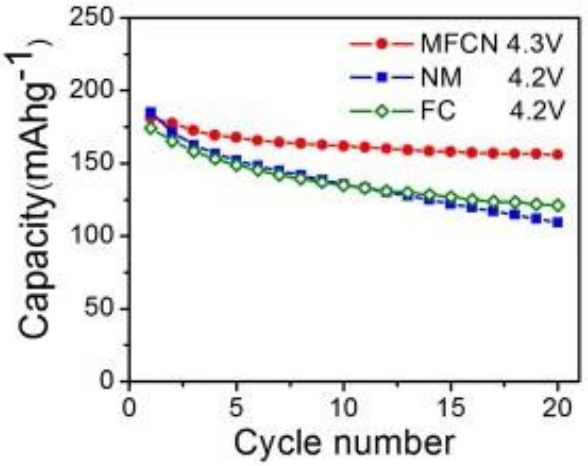

Figure 1.10 The capacity retention of O3-$Na[Mn_{1/4}Fe_{1/4}Co_{1/4}Ni_{1/4}]O_2$ (MFCN) cycled between 1.9 - 4.3 V, O3-$Na[Ni_{1/2}Mn_{1/2}]O_2$ (NM) and O3-$Na[Fe_{1/2}Co_{1/2}]O_2$ (FC) cycled between 1.9 - 4.2V at the C/10 rate. Reproduced from Ref. 41.

explaining its moderate capacity retention. The capacity retention of this material is, however, much superior to those of binary compositions O3-$Na[Ni_{1/2}Mn_{1/2}]O_2$ and O3-$Na[Fe_{1/2}Co_{1/2}]O_2$ at comparable cycling voltage ranges (**Figure 1.10**). An important feature in the structural evolution of $Na_x[Mn_{1/4}Fe_{1/4}Co_{1/4}Ni_{1/4}]O_2$ is that no monoclinic distortion was observed for this composition upon charge/discharge, contrary to $Na_x[Ni_{1/2}Mn_{1/2}]O_2$.[71] It is proposed that the suppression of monoclinic distortion in the quaternary composition indicates the absence of sodium ordering. The sodium disorder originates from transition metals disorder and explains the improved capacity retention of O3-$Na[Mn_{1/4}Fe_{1/4}Co_{1/4}Ni_{1/4}]O_2$ compared to that of O3-$Na[Ni_{1/2}Mn_{1/2}]O_2$.

Pursuing electrode materials with stabilities acceptable for practical Na-ion batteries, Meng *et al*.[73] conducted a comprehensive study on the effect of Li-substitution on the structural and electrochemical properties of a P2 structured binary system, $Na_x[Li_yNi_zMn_{1-y-z}]O_2$ ($0 < x,y,z < 1$). A smooth voltage profile over the entire range of cycling is exhibited by P2-$Na_{0.8}[Li_{0.12}Ni_{0.22}Mn_{0.66}]O_2$, indicating sodium de/intercalation through a solid solution process, in contrast to its structural analogue, $Na_{2/3}[Ni_{1/3}Mn_{2/3}]O_2$,[43] which undergoes a P2-O2 phase transition at high voltages. The cell delivers 115 $mAh.g^{-1}$ capacity between 2.0 - 4.4 V, with excellent retention (91% after 50 cycles) and rate capability. *Operando* synchrotron x-ray diffraction showed no phase transition in the structure upon charge up to 4.4 V (**Figure 1.11**), although the broadening of the peaks deep in charge implies emerging of local stacking faults. Delay in the occurrence of the P2-O2 phase transition in the Li-substituted composition is explained by the presence of more Na^+ ions in the structure (including at the charged state) because of the substitution of low valence Li ions ($Na_{0.8}[Li_yM_{1-y}]O_2$ vs. $Na_{0.67}MO_2$). *Ex-situ* solid state nuclear magnetic resonance (NMR) spectroscopy showed that Li ions are mostly located in the transition metal layers as-synthesized, but tend to migrate to Na layers upon charge to higher voltages since octahedral and tetrahedral positions are available as stacking faults develop. However, the Li migration process is reversible (**Figure 1.11**).

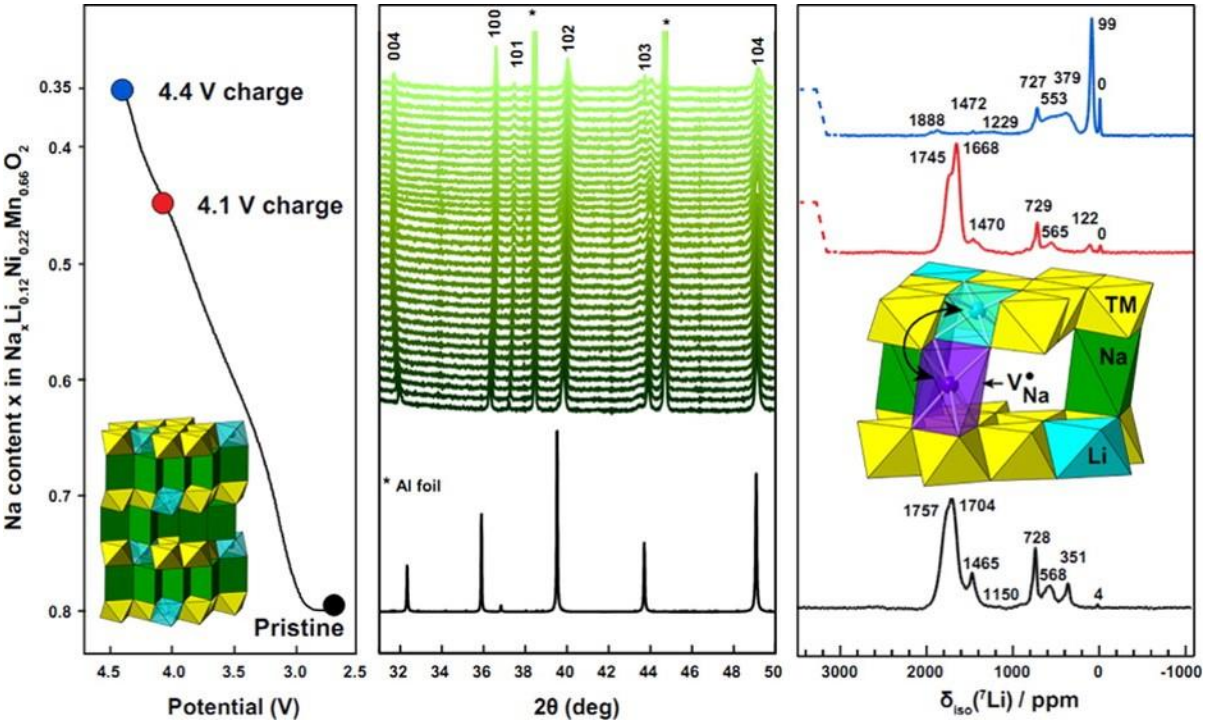

Figure 1.11 (Left and middle): $Na_{0.8-x}[Li_{0.12}Ni_{0.22}Mn_{0.66}]O_2$ preserves its initial-P2 type structure upon charge to 4.4 V, accompanied by progressive increase of O2-like staking faults (Right): *Ex-situ* solid state NMR reveals the reversible migration of Li^+ ions from the transition metal layer to the Na^+ layer upon charge. Adapted from Ref. 73.

Also on the topic of Li-rich layered sodium metal oxides, Komaba *et al.* [74] reported a high reversible capacity of 200 $mAh.g^{-1}$ for P2-$Na_{5/6}[Li_{1/4}Mn_{3/4}]O_2$ cycled at 1.5 - 4.4 V, which is higher than its theoretical capacity based on $Mn^{3+/4+}$ redox. A long voltage plateau at 4.1 V at the first charge characterizes this system similar to layered lithium-rich oxides.[75,76] No transition to O2 or OP4 phases at the fully charged state occurs, similar to the P2-$Na_{0.8}[Li_{0.12}Ni_{0.22}Mn_{0.66}]O_2$ phase discussed above. Interestingly, superlattice peaks associated with Li/Mn ordering disappear when the cell is charged to the high voltage, indicating an in-plane cation rearrangement. Because of the similarities with lithium-rich Li_2MnO_3-based electrodes, (high capacities associated with high voltage plateaus and disappearing superstructure by in-plane cation rearrangement), it is proposed that charge compensation in this material is fulfilled by partial removal of oxygen from the structure. This material shows high promise

for Na-ion battery applications because of its high specific capacity, moderate capacity retention, and also a relatively high sodium content which is advantageous for use in a full Na-ion cell. The long cycle life of the cell, however, was not evaluated in this research[74].

Bruce *et al.*[77] investigated P2-$Na_{0.67}[Mn_{1-y}Mg_y]O_2$ (y = 0, 0.05, 0.1, 0.2) made of earth-abundant elements. Electrochemical studies demonstrated that substitution of Mn by Mg (up to 20%) enhances the capacity retention, decreases the polarization, and suppresses the phase transitions that pure P2-$Na_{0.67}MnO_2$ undergoes during charge/discharge process. The effect of the cooling rate during synthesis on the crystal structure and electrochemical performance of the compounds were also examined. Both Mg-substitution and slow cooling suppress the orthorhombic distortion by increasing the average oxidation state of Mn - or in other words, decreasing the concentration of Jahn-Teller active Mn^{3+} ions, which leads to improved cyclability at the expense of slight loss of capacity. P2-$Na_{0.67}[Mn_{0.8}Mg_{0.2}]O_2$ delivers an initial discharge capacity of 150 $mAh.g^{-1}$ between 1.5 - 4 V with an excellent capacity retention of 96% over 25 cycles. On the other hand, Komaba *et al.*[78] reported a surprisingly high discharge capacity for a similar composition, $Na_{0.67}[Mg_{0.28}Mn_{0.72}]O_2$, when charged to higher voltages. This material delivers a discharge capacity of 220 $mAh.g^{-1}$ between 1.5 - 4.5 V, beyond the capacity

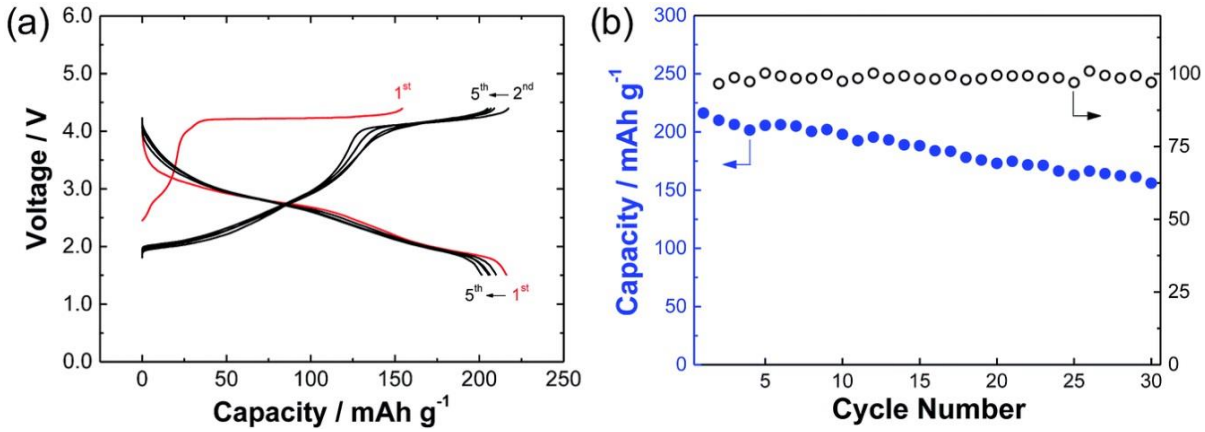

Figure 1.12 Charge/discharge curves of a $Na_{0.67}[Mg_{0.28}Mn_{0.72}]O_2$/Na cell cycled at a rate of 10 $mA.g^{-1}$ in the voltage range of 1.5 - 4.4 V (a), Specific capacity and coulombic efficiency of the cell over 30 cycles (b). Reproduced from Ref. 78.

based on the $Mn^{3+/4+}$ redox reaction, although fading occurs on cycling (**Figure 1.12**). A large fraction of this reversible capacity is associated with a well-defined voltage plateau at 4.2 V. This anomalous reversible capacity is proposed to originate from the activation of the oxide ion redox reaction by Mg ions, similar to the effect of lithium in Li-rich manganese oxides and P2-$Na_{5/6}[Li_{1/4}Mn_{3/4}]O_2$. This is the first report of the activation of oxide ions by Mg ions. While the problem of voltage fading in the Li and Mn-rich analogues of these materials used in Li-ion batteries has proven to be insurmountable to date,[79] it remains an open question as to whether the different structural features of the sodium-based "high voltage" layered oxides will be sufficient to overcome this issue. The concept shows promise for future explorations.

Johnson *et al.* [80] have investigated the performance of a layered sodium metal oxide electrode in a full cell based on O3-$Na[Ni_{1/3}Fe_{1/3}Mn_{1/3}]O_2$/hard carbon. The capacity of the cell is limited due to irreversible processes associated with the carbon negative electrode emerging from the formation of a solid electrolyte interphase (SEI) in the first cycle. Nevertheless, the cell demonstrates excellent stability and a smooth charge/discharge profile coupled with an impressive rate capability. The cell delivered a specific capacity of 100 $mAh.g^{-1}$ for 150 cycles in the voltage range of 1.5 – 4.0 V at a rate of 0.5 C. *Ex-situ* x-ray diffraction analysis showed that the initial structure of the positive electrode material was preserved after 123 cycles.

Johnson *et al.*[81] reported the synthesis of P2/O3 intergrowth layered structure $Na_{1-x}Li_xNi_{0.5}Mn_{0.5}O_{2+d}$ positive electrode materials. Both the end member compositions of the series, $Na[Ni_{0.5}Mn_{0.5}]O_2$ and $Li[Ni_{0.5}Mn_{0.5}]O_2$, adapt an O3-type structure. However, a slight substitution of sodium ions in O3-$Na[Ni_{0.5}Mn_{0.5}]O_2$ (referred to as Na-O3 phase) by lithium ions derives formation and growth of a P2 phase (referred to as Na-P2 phase) at the expense of the O3 phase, as confirmed by the XRD analysis (**Figure 1.13a**). By the increase of the lithium ions concentration, a new O3 phase (Li-O3 phase) with different lattice parameters emerges. **Figure 1.13 b,c** shows high-resolution TEM

images of $Na_{0.7}Li_{0.3}Ni_{0.5}Mn_{0.5}O_{2+d}$, directly illustrating P2 and O3 domains. High-resolution synchrotron X-ray diffraction (SXRD) analysis of $Na_{0.7}Li_{0.3}Ni_{0.5}Mn_{0.5}O_{2+d}$ detected sodium-based O′3 (monoclinic) and P3 (hexagonal) phases, in addition to Na-O3, Na-P2, and Li-O3 phases. The P3 and monoclinic O′3 phases are usually found in sodium deficient compositions. These two phases are speculated to form due to the chemical reaction of the initial O3 phase with atmospheric moisture and carbon dioxide resulting in the extraction of sodium from the layered structure and formation of surface

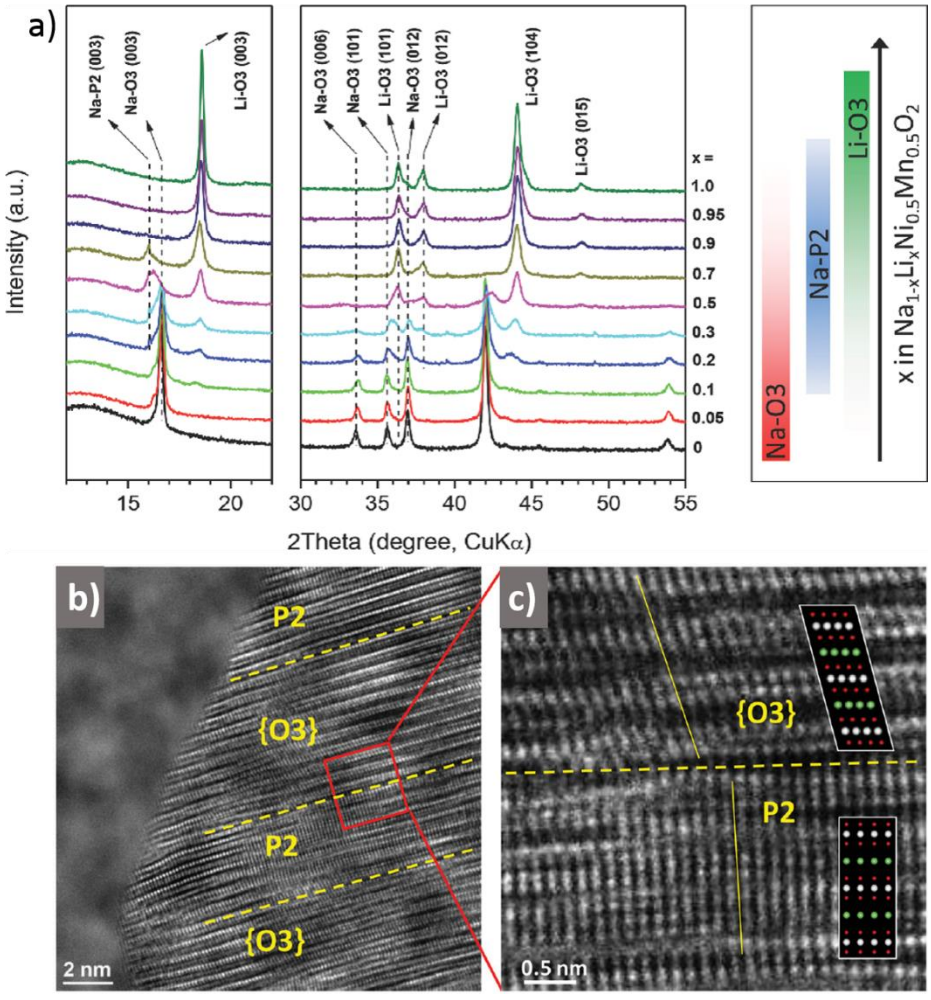

Figure 1.13 X-ray diffraction patterns of $Na_{1-x}[Li_xNi_{0.5}Mn_{0.5}]O_{2+d}$ with different Li content, x ($0 \leq x \leq 1$) (a). High resolution TEM images of $Na_{0.7}[Li_{0.3}Ni_{0.5}Mn_{0.5}]O_{2+d}$ directly showing P2 and O3 domains (b). Adapted from Ref. 81.

sodium hydroxide and sodium carbonate. Higher intensities of P3 and O′3 phases in the Li-substituted phase (compared to the pristine one) suggests the contribution of lithium ions to the instability of the structure. ^{7}Li magic angle spinning nuclear magnetic resonance (MAS-NMR) showed that the lithium ions are located mainly in octahedral sites of interlayer space of each domain, contrary to P2-$Na_{0.8}[Li_{0.12}Ni_{0.22}Mn_{0.66}]O_2$[73]. Substitution of lithium into O3-$Na[Ni_{0.5}Mn_{0.5}]O_2$ was found enhancing the electrochemical performance, even within a P2/O3 intergrowth layered structure.

1.5 Scope of Thesis

This thesis presents a study of high promising P2-$Na_{0.67}[Mn_{0.5}Fe_{0.5}]O_2$ positive electrode material for sodium-ion battery; modification of the composition, by tailored substitution of transition metals, was explored to enhance its electrochemical performance, especially the cycle life. Chapter 1 presents a brief introduction to Na-ion batteries with a focus on recent important achievements on Mn and Fe-containing layered sodium transition metal oxides. Some parts of section 1.4.2 are adapted from reference 34 (D. Kundu, E. Talaie, V. Duffort, L. F. Nazar, *Angew. Chem.* **2015**, 54, 3431). The experimental methods employed in this research study are described in Chapter 2.

Chapter 3 presents a study of air-instability of P2-$Na_{0.67}[Mn_{0.5}Fe_{0.5}]O_2$ and its effect on the electrochemical performance of the material. The nature of this reactivity is described using X-ray and neutron diffraction, mass spectrometry, thermal analysis, electron microscopy, and electrochemical measurements. It is shown that this reactivity is mitigated in Ni-substituted materials, P2-$Na_{0.67}[Ni_xMn_{0.5+x}Fe_{0.5-2x}]O_2$, making them more promising candidates for the practical applications. Dr. Victor Duffort and I collaborated in performing the diffraction and thermogravimetric characterizations. Dr. Duffort performed the neutron diffraction analysis and proposed the insertion of carbonate anions into the structure in the air-exposed sample. I performed all the syntheses, electrochemical measurements, the ICP-AES and SEM characterizations. Dr. Robert Black contributed

to this study by operating the mass spectrometry experiments. This study is published in reference 55 (V. Duffort, E. Talaie, R. Black and L. F. Nazar, *Chem. Mater.* **2015**, 27, 2515).

The structural evolution of P2-$Na_{0.67}[Mn_{0.5}Fe_{0.5}]O_2$ and P2-$Na_{0.67}[Mn_{0.65}Fe_{0.20}Ni_{0.15}]O_2$ induced by extraction/insertion of sodium ions upon charge/discharge and their effect on the cycle life of the cells are discussed in Chapter 4. A combination of *operando* X-ray diffraction analysis, pair distribution function analysis, Mössbauer spectroscopy, and electrochemical measurements were employed to investigate the nature of these transitions. We demonstrate that the cyclability of the cell can be significantly improved by modifying the chemical composition (substitution of Fe ions by Mn/Ni ions in P2-$Na_{0.67}[Mn_{0.5}Fe_{0.5}]O_2$) and preventing the phase transitions by limiting the cut-off voltages. Dr. Victor Duffort and I worked together on the diffraction analyses. Dr. Duffort conducted the PDF analysis and solved the high voltage phase. A detailed description of the PDF analysis of the high voltage phase of studied materials is presented in reference 56, and the results are mentioned briefly here. The Mössbauer spectroscopy analysis was accomplished by collaboration with Dr. Hillary L. Smith and Prof. Brent Fultz in California Institute of Technology. I performed all the electrochemical characterizations. This study is reported in reference 56 (E. Talaie, V. Duffort, H. L. Smith, B. Fultz, L. F. Nazar, *Energy Environ. Sci.* **2015**, 8, 2512).

Chapter 5 presents the study of P2-$Na_{0.67}[Mn_{0.66}Fe_{0.20}Cu_{0.14}]O_2$, with a focus on its structural stability, against the atmosphere and electrochemical insertion and extraction of sodium ions, and its electrochemical performance. Because of the similarity of the compositions of P2-$Na_{0.67}[Mn_{0.66}Fe_{0.20}Cu_{0.14}]O_2$ and auspicious material P2-$Na_{0.67}[Mn_{0.65}Fe_{0.20}Ni_{0.15}]O_2$, this study provides an evaluation of the effect of incorporation of copper versus nickel into P2-$Na_{0.67}[Mn_{0.5}Fe_{0.5}]O_2$ to address the material's cyclability issue.

Chapter 6 describes the *operando* measurements of X-ray absorption spectra of $Na_x[Mn_{0.66}Fe_{0.20}Cu_{0.14}]O_2$ and $Na_x[Mn_{0.65}Fe_{0.20}Ni_{0.15}]O_2$ collected at transition metal K-edges. This study suggests the redox activity of oxide ions in the studies materials. Se Young Kim contributed to this project by assisting in the preparation of the *operando* cells and conducting the measurements at the synchrotron facility. The study was performed in collaboration with Dr. Ning Chen, the beamline scientist at the Canadian Light Source (CLS).

Chapter 7 presents the overall summary and some suggested challenges to address for future work.

Chapter 2

Characterization Methods and Techniques

2.1 Overview

The design and development of efficient batteries requires an in-depth understanding of the science underpinning these devices, including the characteristics of the electrode materials. In the research presented in this thesis, much effort was put into investigating a promising family of materials for the positive electrode in Na-ion batteries. The studies were focused mainly on the structural evolution of the materials, both caused by ambient atmosphere reactivity and induced by insertion and extraction of sodium ions during discharge/charge. Several characterization techniques were employed for this purpose.

The crystal structures of materials were determined by combined X-ray and neutron powder diffraction (XRPD, NPD). Specifically, neutron powder diffraction analysis assisted with the exploration of possible cation ordering in the synthesized materials and also the determination of the impact of atmosphere-reactivity on crystal structure. The phase transitions of the positive electrode materials induced by the insertion and extraction of sodium ions during galvanostatic discharge and charge were monitored by *operando* XRD analysis. Pair distribution function (PDF) analysis was performed to characterize the low-crystalline phase emerged over charge. The evolution of the local structure of each transition metal during the first charge/discharge cycle was probed by X-ray absorption spectroscopy (XAS).

Scanning electron microscopy (SEM) provided information about the morphology, purity, and chemical composition of the samples. Elemental concentrations of the samples were accurately determined using the inductively coupled plasma atomic emission spectroscopy (ICP-AES) technique.

Thermogravimetric analysis (TGA) was conducted to probe the thermal stability of the materials. The valence and coordination environment of iron ions were probed by Mössbauer Spectroscopy. The electrochemical performance of materials as positive electrodes vs. sodium metal was examined using galvanostatic cycling. This chapter presents a brief basic introduction to each experimental method and characterization technique employed in this research.

2.2 Diffraction Techniques

2.2.1 Powder X-Ray Diffraction

When an electron is affected by an X-ray beam, it is forced to oscillate at the same frequency as the electric field component of the incident beam, thereby re-emitting electromagnetic radiation in all directions. When a periodic distribution of electrons is irradiated by an X-ray beam, the scattered beams from every individual scattering center interfere with another to form an X-ray diffraction pattern.

Historically, X-ray diffraction by crystals was described and formulated by two approaches[82,83] in direct space: the Laue equations and Bragg's law. The Laue approach provides a rigorous mathematical description of diffraction. Bragg's law, on the other hand, is a highly simplified approach for describing the complicated process of diffraction, effectively giving the same results as the Laue treatment. In Bragg's approach, crystals are regarded as a built up of planes that behave as semi-transparent mirrors when interacting with X-rays, and that reflect some of them with the angle of reflection equal to the angle of incidence; the rest are transmitted and then reflected by adjacent planes. When two monochromatic parallel X-ray beams with a wavelength of λ encounter two subsequent crystallographic planes separated by a distance of d with an incident/reflected angle of θ (**Figure 2.1**), the reflected beams interfere constructively if the path difference they have traveled ($2dsin\theta$) is equal to integer multiples (n) of the wavelength. This relation is known as Bragg's law:

$$2dsin\theta = n\lambda \quad \textbf{(2.1)}$$

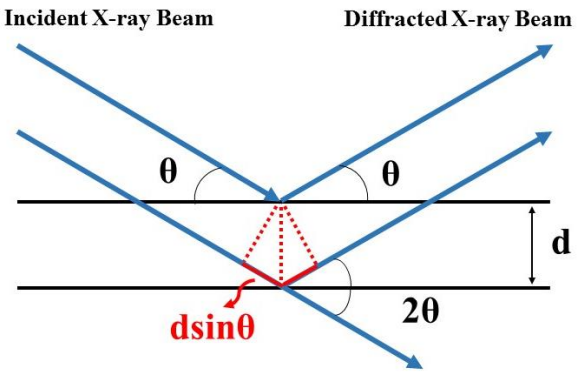

Figure 2.1 Schematic representation of Bragg's law

The θ angle at which Bragg's law is satisfied is called Bragg angle, θ_B. When the incident angle does not correspond to the crystal plane spacing and the beam wavelength to fulfill Bragg's law, the X-rays interfere destructively. In a fine powder specimen, crystallites are randomly oriented in every possible direction. Therefore, when a polycrystalline sample is irradiated by a monochromatic X-ray beam, for each set of crystallographic planes, some crystallites are oriented so that Bragg's law is satisfied and diffraction occurs. In a diffractometer, either the incident beam or the sample is rotated with respect to the other one for a certain range of angles and a moving detector collects the diffracted beam. An X-ray powder diffraction (XRPD) pattern presents the intensity of the diffracted beam at each Bragg angle and is a characteristic of the sample. An XRPD pattern could be considered as the superimposition of discrete Bragg reflections and a continuous background. Peak positions, peak intensities, and shapes of peaks are three different components, disregarding the background, that describe a typical powder diffraction pattern and present some information about the crystal structure of the material, properties of the specimen (*e.g.*, absorption, preferred orientation, grain size, *etc.*) and instrumental parameters. The positions of Bragg peaks follow the Bragg diffraction equation and depend on the radiation wavelength and distances between the crystallographic planes, or in other words, the unit cell

parameters. Atomic parameters (*e.g.*, atoms type, coordinates in the unit cell, occupancy, atomic displacement factor) are the key parameters determining the Bragg peak intensities. The shapes of the peaks are dependent mainly on instrumental parameters and also on specimen properties.

For the purpose of phase identification, XRD patterns were collected using Cu-K_α radiation with a Bruker D8-Advance powder diffractometer equipped with a Vantec-1 detector using θ-2θ Bragg-Brentano geometry. For structural refinement, air-sensitive samples were loaded in 0.3 mm capillaries in an argon-filled glovebox, and the XRD patterns were recorded on a PANalytical Empyrean instrument with a PIXcel bidimensional detector in Debye-Scherrer geometry using a parabolic X-ray mirror in the incident beam optics. *In-situ* high temperature and *operando* XRD experiments were performed using the same diffractometer with θ-θ Bragg-Brentano geometry. For the high-temperature XRD data, samples were heated in an Anton Paar HTK 1600 chamber under controlled atmosphere. Lattice parameter evolution during *in-situ* and *operando* diffraction experiments was determined by the Le Bail[84] fitting method using the FullProf [85] software suite.

2.2.2 Rietveld Refinement

Rietveld refinement is a structural refinement approach that employs the least squares method to minimize a function that represents the difference between a calculated powder pattern and an observed data. For a powder X-ray diffraction pattern, the calculated integrated intensity of a Bragg reflection with *hkl* Miller indices is described as follows[83]:

$$I_{hkl} = K \times p_{hkl} \times L_\theta \times P_\theta \times A_\theta \times T_{hkl} \times |\mathrm{F}_{hkl}|^2 \qquad \textbf{(2.2)}$$

where K is a scale factor, which normalizes the experimentally observed integrated intensity to the calculated value; p_{hkl} is the multiplicity factor, which accounts for the number of symmetrically equivalent reflections; L_θ is the Lorentz factor, which is relevant to the geometry of diffraction; P_θ is the polarization factor, which arises from partial polarization of electromagnetic wave; A_θ is the

absorption factor, which accounts for absorption of the beam by the sample, $T_{hkl}$is the preferred orientation factor, and F_{hkl} is the structure factor. The structure factor represents the overall scattering ability of all the atoms in a unit cell and is formulated as follows[83]:

$$\mathrm{F}_{hkl} = \sum_{n=1}^{N} g_n t_n(s) f_n(s) \exp[2\pi \mathrm{i}(\mathrm{h}x_n + \mathrm{k}y_n + \mathrm{l}z_n)] \quad \textbf{(2.3)}$$

where N is the total number of atoms in the unit cell, g_n is the occupation factor, t_n is the atomic displacement (temperature) factor and f_n is the atomic scattering factor, which depend on $s = sin\theta/\lambda$ for X-ray scattering, and $(x_n, \mathrm{y}_n, \mathrm{z}_n)$ represents fractional coordinates of the *n*th atom.

An initial reasonable structural model including the space group, unit cell parameters, atomic positions, peak shape parameters, *etc.* is required as the input for Rietveld refinement. The crystal structure of a known compound with a similar structure may be used as the starting model. Background, lattice parameters, sample displacement, and the profile shape function can be obtained through profile matching by use of the Le Bail method prior to running the Rietveld refinement. Following that, atom positions, atomic displacement (temperature) factor, occupancies, and microstructure parameters can be refined to obtain a precise model. The quality of a refinement is evaluated based on the agreement between the observed and calculated profiles determined by several figures of merit, including the Bragg residual:

$$R_{Bragg} = \frac{\sum_{j=1}^{m} \left| I_j^{obs} - I_j^{cal} \right|}{\sum_{j=1}^{m} I_j^{obs}} \times 100\% \quad \textbf{(2.4)}$$

and the goodness of fit:

$$\chi^2 = \frac{\sum_{i=1}^{n} \omega_i \left(Y_i^{obs} - Y_i^{cal} \right)^2}{n - p} \quad \textbf{(2.5)}$$

where m is the number of Bragg reflections, I_j^{obs} is the observed integrated intensity of the *j*th Bragg peak, I_j^{cal} is the calculated integrated intensity of the *j*th Bragg peak, n is the total number of data points used in the refinement, p is the number of refined parameters, ω_i is the weight of the *i*th data point $(= 1/Y_i^{obs})$, Y_i^{obs} is the observed intensity of the *i*th Bragg peak, and Y_i^{cal} is the calculated intensity of the *i*th Bragg peak. A refined structural model is considered satisfactory when minimum figures of merits are achieved and are sufficiently small, and also the crystal structure makes sense physically and chemically. The crystal structures presented in this thesis were refined using the Rietveld method within FullProf [85] software suite.

2.2.3 Neutron Powder Diffraction

A beam of thermal neutrons, with the energy range of 5 - 100 meV, can produce a diffraction pattern when interacting with a crystalline material. Because neutron has a zero net charge, it does not interact with electronic charge cloud of the atom and is scattered by the nuclei. The scattering of neutrons by nuclei is described by a coherent scattering length, which is equivalent to the scattering factor for X-rays. Neutron diffraction is a complementary technique to X-ray diffraction analysis for the structural characterization of crystals. This technique is especially advantageous for locating light elements such as hydrogen or lithium and can distinguish among many neighboring atoms. For example, Mn and Fe are indistinguishable by X-ray scattering because of their atomic number (Z) difference of one. However, a site occupancy distribution study is possible by neutron diffraction owing to different bound coherent scattering lengths: -3.73 fm for Mn and 9.45 fm for Fe.[86]

A neutron powder diffraction pattern can be collected by two different experimental setups based on the source of neutrons: fixed wavelength powder diffractometer and fixed angle time of flight (t.o.f) instrument. In a powder diffractometer at a reactor neutron source, the sample is irradiated by a continuous monochromatic beam of neutrons, and the intensity of diffracted neutrons is recorded as a

function of the angle of which they are scattered from the sample ($I(\theta)$ vs. 2θ). In the time of flight technique, a pulsed beam of neutrons with a wide spectrum of energies strikes the sample. The neutrons in a pulsed beam disperse on their way to the sample because of their different wavelengths. The scattered neutrons are recorded in banks of detectors located at fixed scattering angles. The wavelength of the scattered neutrons λ can be calculated from the measured total time of flight from the source to the detector and De Broglie's equation, $\lambda = h/P$, as follows:

$$t = \frac{m_n L}{h}\lambda \qquad \textbf{(2.6)}$$

where m_n is the mass of neutron, h is Planck's constant, and L is the total length of the flight path (source to sample distance + sample to detector distance).

Neutron powder diffraction data presented in this thesis was recorded by the time-of-flight (t.o.f.) diffractometer POWGEN at the Spallation Neutron Source (SNS) of the Oak Ridge National Laboratory (ORNL). The powders were loaded in 8 mm vanadium sample holders in an argon filled glovebox and sealed. Combined Rietveld refinement of neutron and X-ray powder diffraction data was performed using FullProf [85] software suite.

2.3 Pair Distribution Function (PDF) Analysis

In conventional crystallographic analyses, *e.g.*, X-ray and neutron powder diffraction, only Bragg peaks are taken into account, and the diffuse scattering is discarded in the form of the background. However, pair distribution function (PDF) analysis uses the information obtained from diffuse scattering intensity, which contains information about the local structure, in addition to Bragg peaks, which provide information about the average structure. Diffuse scattering intensity is covered between the Bragg peaks and is widely spread over Q space (Q is the magnitude of momentum transfer vector, $Q = 4\pi\sin(\theta)/\lambda$). However, at high Q regions, where the intensity of Bragg peaks is low, the diffuse scattering intensity is more prominent. The atomic pair distribution function, $g(r)$, represents the probability of finding

two atoms separated by a distance r and is related to the reduced pair distribution function, $G(r)$, as follows:[87]

$$G(r) = 4\pi r\rho_0(g(r) - 1) = \frac{2}{\pi}\int_0^\infty Q[S(Q) - 1]\sin(Qr)\,dQ \qquad \textbf{(2.7)}$$

where ρ_0 is the number density of atoms; and $S(Q)$ is total scattering structure function and is obtained from the normalization of coherent scattering function, I_{coh} *(Q)*, which is the diffracted intensity data that is corrected for Compton scattering, fluorescence, multiple scattering, and scattering from the sample environment (sample holder, air, instrument).

Although $G(r)$ is a less physically intuitive function than $g(r)$, it offers two important advantages. First, it is calculated directly from the Fourier transform of $S(Q)$, wheras calculation of $g(r)$ requires an input of the average intensity value, ρ_0. Second, random uncertainties are constant along r for $G(r)$ because it is the direct Fourier transform of the intensity data, whereas the uncertainties falls off as $1/r$ for $g(r)$. $g(r)$is normalized so that as $r \to \infty, g(r) \to 1$ and as $r \to 0, g(r) \to 0$. Consequently, as $r \to \infty, G(r)$ oscillates around zero and as $r \to 0$, $G(r)$ behaves like $(-4\pi\rho_0 r)$. For a perfect crystal, the limitation imposed by finite Q-resolution in a real experiment causes a gradual decrease in the peak-peak amplitude of the signal in $G(r)$. In a sample with higher structural disorder, the signal amplitude falls off faster indicating lower structural coherence. Another consequence of the collection of experimental data over a finite range of Q is the appearance of termination ripples (false oscillations in the data) in $G(r)$ function.

The most physically intuitive correlation function is the radial distribution function (RDF), $R(r)$:[87]

$$R(r) = 4\pi r^2\rho_0 g(r) = \sum_\nu \sum_\mu \frac{b_\nu b_\mu}{\langle b\rangle^2}\delta(r - r_{\nu\mu}) \qquad \textbf{(2.8)}$$

The sum is over all pairs of atoms ν and μ with an interatomic distance of $r_{\nu\mu}$. b_ν is the Q-independent scattering amplitude of atom ν, which is equal to the atomic number for X-rays and the coherent scattering length for neutrons; $\langle b \rangle$ is the average scattering amplitude of the sample. The coordination number for a specific coordination shell is given by

$$N_C = \int_{r1}^{r2} R(r)dr \qquad \textbf{(2.9)}$$

where r_1 and r_2 define the RDF peak corresponding to the specific coordination shell. The combination of **equations 2.7** and **2.8** gives

$$G(r) = \frac{1}{r}\sum_i \sum_j \left[\frac{b_i b_j}{\langle b \rangle^2}\delta(r - r_{ij})\right] - 4\pi r\rho_0 \qquad \textbf{(2.10)}$$

The peak positions of the PDF curve give the distances of atom-pairs; the integrated intensity of the peaks is related to the number of neighbors in that coordination shell around the origin atom, and the shape of the peaks represents the probability distribution of the atom pairs.

Experimental data for PDF analysis presented in this thesis was collected by a PANalytical Empyrean diffractometer outfitted with Ag-K_α radiation, a Rh K_β filter, and a NaI scintillation point detector. Each sample was loaded in a 1mm glass capillary in an argon filled glovebox. The collection time was increased at high Q, and the total data collection time was 48 h. The contributions of scattering intensity from the sample holder, air, and the diffractometer were taken into account by measurement of an empty capillary with the same experimental conditions and were subtracted from the data. The data transformation was performed using PDFGetX3 software[88] and the real space data was fitted by PDFgui software[89]. The instrument dependent Q damping factor was obtained by calibration of a standard silicon sample.

2.4 Mössbauer Spectroscopy

Mössbauer spectroscopy, a technique based on the Mössbauer effect and Doppler effect, probes the nuclear structure of certain isotopes in a solid matrix by emission and absorption of γ-rays. Mössbauer spectroscopy is used primarily to study the hyperfine interactions, interactions between the nucleus and the neighboring electrons, which perturbs the energies of nuclear states. The γ-rays have energies of ~ 10^4 to10^5 eV, and the energy perturbations caused by hyperfine interactions are as small as ~ 10^{-9}-10^{-7} eV.[90] These small hyperfine perturbations to the energy of the γ-ray can be measured by the Mössbauer spectroscopy technique for some nuclei. A Mössbauer spectrum may provide information about the local environment of the Mössbauer atom, such as the oxidation state and coordination. ^{57}Fe is one of the most common isotopes investigated by Mössbauer spectroscopy.

There are two main restrictions for measurement of energy perturbations of nuclear states induced by hyperfine interactions. First, these energy changes are extremely small, as mentioned above. Second, when an excited nucleus emits a γ-ray, it recoils in order to fulfill the momentum conservation law because the γ-ray has a momentum, P_γ. The recoil of the nucleus consumes energy resulting in a decrease in the energy of the γ-ray (E_γ). On the other hand, the recoil of the second nucleus requires higher energy of γ-ray upon absorption to compensate for its recoil energy. The recoil energy, E_{recoil}, is inversely proportional to the mass:

$$E_{recoil} = \frac{{P_\gamma}^2}{2m} = \frac{{E_\gamma}^2}{2mc^2} \qquad \textbf{(2.11)}$$

where c is the speed of light. The recoil energy for a single ^{57}Fe nucleus, ~ 10^{-3} eV when the mass of the nucleus is adapted, is orders of magnitude larger than the precision (ΔE ~ 10^{-9} eV) required, so that the second ^{57}Fe nucleus absorbs the γ-ray.[90] Mössbauer discovered that, under some conditions, the recoiling mass is effectively equal to the mass of crystal instead of the nucleus. Therefore, the recoil

energy would be significantly small, and the energy of the emitted γ-ray has the precise energy required to be absorbed by the second nucleus. Mössbauer spectroscopy is feasible for nuclei with high probability of recoil-free γ-ray emission and absorption. This condition is met for ^{57}Fe owing to its appropriate first nuclear transition energy, *i.e.*, the γ-ray energy, and its lifetime. In practice, the energy of the γ-ray is tuned by the Doppler effect; the sample's position is kept fixed and the radiation source moves at a velocity of v either toward or away from the sample. The shift to the γ-ray energy, ΔE, imposed by the Doppler effect is given by the following equation:

$$\Delta E = \frac{v}{c} E_\gamma \qquad \textbf{(2.12)}$$

The movement of the radiation source with a velocity of $v = 2\ mm.s^{-1}$ provides a Doppler shift of $\Delta E \sim 10^{-7} eV$ to the energy of a 14.4 KeV γ-ray of ^{57}Fe, which is large enough to cover the energy width of the Mössbauer resonance (~ 10^{-9} eV). The Mössbauer spectrum is plotted as the absorption intensity versus the radiation source velocity.

Three important features that represent three hyperfine interactions can be identified in a Mössbauer spectrum: isomer shift (IS), electric quadrupole splitting (EQS), and hyperfine magnetic field (HMF). These three characteristic features in a Mössbauer spectrum are sensitive to the local environment of the resonant nucleus and might be temperature dependent.

An isomer shift is an observable shift in the position of peaks in the Mössbauer spectrum of a specific atom in different materials. IS originates from the interaction of the nucleus and the electron density at the nucleus. The Coulombic interaction due to the overlap of the s-electron cloud with the finite nucleus perturbs the nuclear energy levels. The energy levels of the nuclear ground state and excited state are not shifted equally because of a different nucleus radius in each state, resulting a shift in the transition energy. The difference between the transition energy of the nucleus in the radiation source and the nucleus in the sample is compensated for by the Doppler effect and enforces a shift in the position of

the peaks in the Mössbauer spectrum. The isomer shift depends on the s-electron density at the nucleus and is also affected by the partial screening of the d orbital electrons. This effect is more important in ionic compounds.

The nucleus has an electric quadrupole moment that originates from the asymmetrical shape of its charge distribution. The asymmetry of the nucleus shape depends on its spin. The interaction of the electric quadrupole moment of the nucleus with an electric field gradient results in the split of the excited state energy into two levels for the I = 3/2 level in ^{57}Fe. The split of energy levels of the excited state is detectable by the appearance of a doublet in the Mössbauer spectrum (**Figure 2.2**).

The interaction of the nuclear spin with a magnetic field splits a nuclear level of spin I into (2I+1) levels. For ^{57}Fe, six transitions, which appear as a sextet in the Mössbauer spectrum are allowed based on selection rules for I=1/2 to I=3/2 transition (**Figure 2.2**).

Mössbauer spectra of the samples studied in this research were acquired with a conventional constant acceleration system with a radiation source of ^{57}Co in a Rh matrix. The velocity and isomer shift were

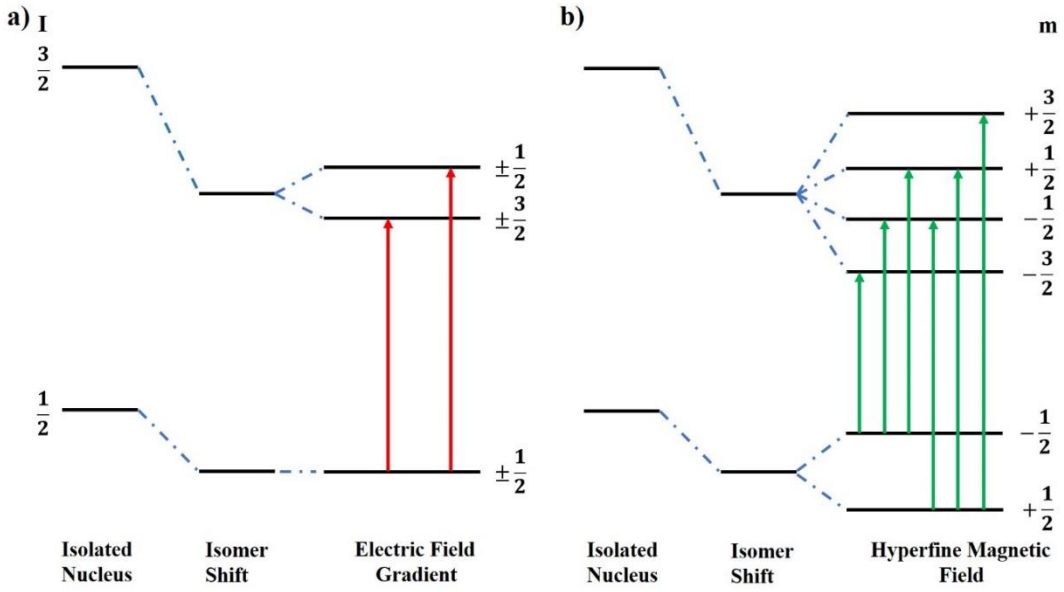

Figure 2.2 Energy diagrams of ^{57}Fe in an electric field gradient (a) and hyperfine magnetic field (b)

calibrated with reference to a room-temperature α-Fe spectrum. The spectrometer linewidth obtained from the calibration is 0.31 $mm.s^{-1}$and was used for all spectral components resulting from fitting with Lorentzian doublets.

2.5 Mass Spectrometry

Mass spectrometry is an analytical technique to measure the relative abundance of molecules in the gas phase. A mass spectrum represents the intensity of detected ions as a function of mass to charge ratio (m/z). Various designs of mass spectrometers have three basic functions in common: ionization, mass separation, and ion detection. At the first stage, the molecules are bombarded by a high energy beam of electrons emitted from a hot filament. Collision of high energy electrons with a molecule forces ejection of an electron and, therefore, ionization. The ionized molecules might fragment into smaller ions and neutral species. The ion beam is accelerated and focused by use of electrodes. The ions are generated and handled under vacuum. In the next stage, the cations in the ion beam are separated by means of magnetic or electric fields. If a uniform magnetic field is used, the ion trajectory is deflected in an arc whose radius is proportional to the mass to charge ratio (m/z), the magnitude of the magnetic field, and the accelerating voltage. By tuning the magnetic field and accelerating voltage, each ion with a particular mass to charge ratio can be separated and sent into the detector. An alternative to the use of the magnetic field is a quadrupole mass filter, which consists of four parallel rod-like electrodes to which both DC and AC electric voltages are applied. Quadrupole mass analyzer resolves the ions based on their m/z. By tuning the DC and AC (RF) voltages, all the desired ranges of m/z are scanned. The mass sensitivity (resolution) can be set electronically by changing of DC and RF voltages in a quadrupole mass analyzer, whereas in the case of a magnetic field mass separation the resolution is set mechanically by changing slits at the flight path of the ion beam.

The residual gas analysis for this research was carried out with an online electrochemical mass spectrometer (OEMS) instrument with a modified design based on a setup reported by Tsiouvaras *et al.*[91] A commercial electrochemical flow cell (EL-Cell, ECC-DEMS) was attached in-line to a gas flow controller (Bronkhurst, F-200CV) and a quadrupole mass spectrometer (Standford Research Systems, RGA 200). The evolved gasses from the cell were swept by a controlled flow of Ar (Praxair, 5.0 grade) to the quadrupole mass spectrometer through a fused silica capillary (50 μm ID). The pressure inside the chamber was 2×10^{-6} Torr during the experiment.

2.6 Inductively Coupled Plasma-Atomic Emission Spectroscopy (ICP-AES)

Inductively coupled plasma-atomic emission spectrometry (ICP-AES) is one of the most common elemental analysis techniques. Most elements can be detected and quantified by a commercial ICP-AES with a parts per billion limit of detection. In this technique, the sample is introduced into a plasma source at where the sample is dissociated into its constituent elements and then excited to higher energy levels. The excited atoms and ions return to their ground state by emission of photons with characteristic wavelengths. The elemental concentrations can be determined by comparing the intensities of emissions to the intensities of standards of known concentration.

Solid samples should be digested into a solution before analysis. The sample solution is then transformed to an aerosol by a nebulizer. The small droplets (~1-10 μm) are transferred to the plasma by an argon flow, and the large droplets are removed from the system. Desolvation, evaporation, atomization, and finally excitation or ionization of the sample takes place in an RF-induced argon plasma that sustains a high temperature (~ 4000-10000 K). When the excited atoms and ions relax to their ground states or lower excitation states, atoms emit photons of particular energies in the ultraviolet/visible range. Each element has its own characteristic emission spectrum, and the emission intensity is proportional to the element concentration in the sample.

A Prodigy high dispersion ICP (Teledyne Leeman Labs) instrument was used for elemental analysis in this research. The powder samples were digested by dilute HNO_3 and HCl.

2.7 Scanning Electron Microscopy (SEM)

A scanning electron microscope presents a highly magnified image of a sample using a focused beam of electrons instead of the light and provides information about the morphology and chemical composition of the material. In a scanning electron microscope instrument, electrons are produced by an electron gun and then accelerated to an energy level of 1 - 30 keV. The electron beam is focused, and its diameter is set by electromagnetic lenses and apertures. The microscope is held under vacuum during the experiment. The electron beam is scanned over the specimen surface along x- or y-axis by means of scanning coils. As a result of the interaction of the incident electron beam with the specimen, several signals are produced, detected, processed, and converted to images or spectra.

As the specimen surface is bombarded by an electron beam, different interactions can occur. The electron may be scattered by atomic nuclei resulting in a change in the direction of the electron with a slight reduction of energy (< 1 eV). The electron deflected back of the specimen is called a backscattered electron (BSE). The fraction of backscattered electrons is proportional to the atomic number of the scattering element. The incident electrons may interact inelastically with the specimen electrons resulting in the emission of low energy (< 50 eV) secondary electrons (SE). If the vacancy due to the emission of a secondary electron is filled by an electron at a higher level of energy, an X-ray of characteristic energy is emitted. In addition to the BSE and SE that are used to produce an image, other kinds of emissions may occur by the interaction of the electron beam and the specimen, including Auger electrons and cathodoluminescence. Detection of characteristic X-rays emitted from the surface of the specimen provides the option of identification and quantification, in the case of the calibration

of the instrument, of the constituent elements of the specimen. This technique is called energy dispersive X-ray spectroscopy (EDS). However, light elements cannot be detected by this technique.

The SEM images presented in this thesis were recorded using a Zeiss Ultra Plus scanning electron microscope (FE-SEM) at 15 kV in the secondary electron mode. The molar ratios of transition metal ions of the samples were verified by energy dispersive X-ray spectroscopy (EDS) (EDAX). The samples were coated with a thin layer of gold to increase the electron conduction.

2.8 Thermogravimetric Analysis

Thermal gravimetric analysis (TGA) measures the variation of the mass of a sample as a function of temperature under a controlled atmosphere and provides information about the thermal stability and composition of the material. The thermogravimetric analyses presented in this thesis were performed using a TA Instrument SDT Q600 under various atmospheres (air, high purity argon and oxygen, and carbon dioxide). The samples were loaded in platinum crucibles.

2.9 X-ray Absorption Spectroscopy (XAS)

X-ray absorption spectroscopy (XAS) is a widely used analytical technique that measures the energy-dependent fine structure of the X-ray absorption coefficient near the absorption edge of an element. This technique can provide information about the chemical nature and environment of atoms in a material.[92,93]

When X-rays of intensity I_0 hit a sample, the beam absorption depends on the photon energy (E) and the sample thickness; the transmitted beam intensity (I_t) is given by Beer's law

$$I_t = I_0 e^{-\mu(E)t} \qquad \textbf{(2.13)}$$

where $\mu(E)$ is the energy dependent X-ray absorption coefficient and t is the sample's thickness. Over a wide range of energy, $\mu(E)$ is inversely proportional to the photon energy ($\mu(E) \propto E^{-3}$). However,

when the photon energy exceeds the binding energy of a core-electron, a sharp increase in the absorption coefficient appears. XAS is about the measurement of the energy dependence of μ at energies near and just above the absorption edges. Each absorption edge presents a specific core-electron binding energy, *e.g.*, *K* for n = 1, *L* for n = 2, *M* for n = 3, *etc.* (n is the principal quantum number). The L and M absorption edges are in fact 3 and 5 edges, respectively, due to spin-orbit coupling.

When a core-electron absorbs a sufficiently high energy photon, it is ejected from the atom, thereby creating a vacancy. The excited state atom is relaxed typically within a few femtoseconds of the absorption event. One important relaxation mechanism is X-ray fluorescence, in which a higher energy core-level electron fills the core-vacancy, concomitant with the emission of X-rays. The emitted X-rays have characteristic energies for each atom and can be used for the identification and quantification of the concentration of the specific atom. Another important relaxation process is the Auger effect, which occurs when a higher electron level fills the vacancy followed by ejection of a shell electron (Auger electron). The X-ray absorption spectra can be measured by any of these processes mentioned above.

The X-ray absorption fine structure is commonly described in two distinct regions: X-ray absorption near-edge structure (XANES) and extended X-ray absorption fine structure (EXAFS) (**Figure 2.3**). The structure in the vicinity of the absorption edge is referred to as XANES, and the oscillations above the edge are referred to as EXAFS. There is not a distinct definition that distinguishes XANES from EXAFS. However, these terms are widely used because these two regions are analyzed differently. XANES is sensitive to the oxidation state and the geometry and is analyzed mostly qualitatively. EXAFS is sensitive to the atomic arrangement around the absorber atom and provides quantitative information about the bond length and the coordination number.

X-ray absorption spectra can be measured for all the elements (in the vacuum for the elements lighter than phosphorous). The measurements can be performed for solids, liquids, and gases, for both crystalline and amorphous materials, at high pressures, and in a wide range of temperatures. The use of XAS, on the other hand, is limited to the access to an intense and tunable X-ray source, *i.e.*, synchrotron.

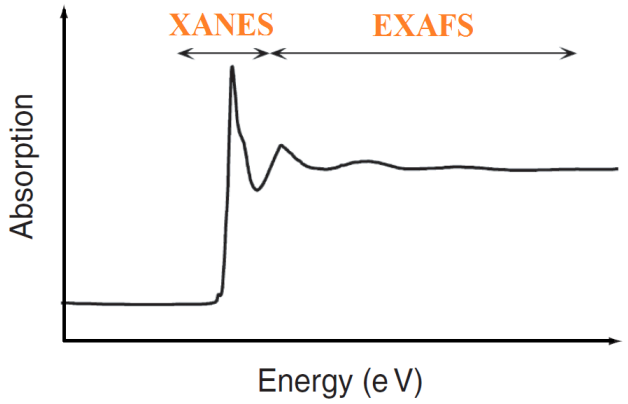

Figure 2.3 Schematic illustration of an X-ray absorption spectrum. Reproduced from Ref. 93.

The X-ray absorption coefficient can be measured either directly by measuring the intensities of the incident and transmitted beams (transmission mode) or indirectly by detecting the decay products, such as fluorescence X-ray radiation or Auger electrons. Transmission mode measurements require concentrated samples so that the difference between the incident and transmitted beam is sufficiently larger than the variation due to counting statistics. Moreover, samples must be highly homogeneous and of constant thickness. Fluorescence mode measurements are particularly effective for dilute and non-homogenous samples. For concentrated samples, the self-absorption effect should be considered and corrected. In the electron yield mode, the electrons emitted from the sample, such as photoelectrons, secondary electrons, and Auger electrons, are detected. Due to the short mean free path of the electrons, this technique is surface sensitive.

2.10 Electrochemical Measurements

Galvanostatic charge and discharge experiments are standard procedures of evaluation of the electrochemical performance of batteries. Over a galvanostatic cycling experiment, a constant current is applied to the cell, and the cell voltage is measured as a function of time. The applied current is reversed when a cut-off voltage is reached. Specific capacity, specific energy, rate capability, and cycling stability of the electrochemical cell can be determined by this analysis.

Theoretical specific capacity (C) of an electrode material, the quantity of the charge involved in the electrochemical reaction per unit mass of the active material, can be calculated from the equation below:

$$C = nF/M \qquad \textbf{(2.14)}$$

where $F = 26.901\ A.h/mol$ is the charge of one mole of electrons, *i.e.*, Faraday's constant; n is the number of electrons transferred per mole of reaction; and M is the molar mass of the active material. The specific capacity of the cell is often given in terms of $mAh.g^{-1}$. The specific energy of a cell is equal to multiplication of the voltage and specific capacity. The internal resistance of an electrochemical cell to the flow of the ionic and electronic currents deviates the operating voltage of the cell compared to its equilibrium open circuit value. This effect, called polarization, decreases the discharge voltage and increases the charge voltage from the open circuit voltage value. The voltage and specific capacity of a cell are sensitive to the current magnitude. The rate capability indicates the ability of a material to retain the capacity as the current is varied during cycling. The galvanostatic cycling rate is often expressed as C/h, where h is the number of hours at which the material becomes fully charged or discharged. In this thesis, rate $C/20$ refers to insertion or extraction of one mole of sodium ion per mole of active material every 20 hours. Cycling stability is often presented as a plot of capacity versus the cycle number. When the cell voltage changes over the cycling, specific energy retention, rather than the capacity retention, is a more appropriate parameter for the investigation of cycling

stability. Another figure of merit of an electrochemical cell is Coulombic efficiency, which is defined as the ratio of the charge capacity to the preceding discharge capacity or vice versa (discharge capacity divided to the preceding charge capacity). The former definition is used in this thesis. The deviation of the Coulombic efficiency from 100% indicates the occurrence of undesired reactions in the cell that lead to capacity loss.

The electrochemical performance of the positive electrode materials presented in this thesis was measured by a multiple channel MPG-2 galvanostat/potentiostat in galvanostatic mode. Active materials were examined as the positive electrodes in 2325 coin cells. Sodium metal (Sigma-Aldrich, ACS reagent) on a stainless steel current collector was used as the negative electrode. **Figure 2.4** is a schematic representation of the coin cell assembly. The positive and the negative electrodes were separated by two glass fiber separators (Merck Millipore). A spring was placed in the cell to ensure good contact between different components of the cell.

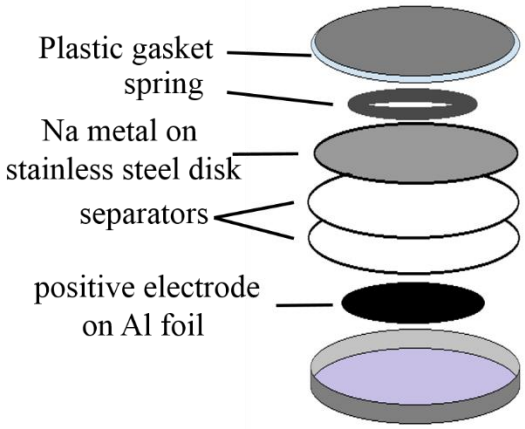

Figure 2.4 Schematic representation of a coin cell

The positive electrodes were prepared from a mixture of the active material, super P carbon (TIMCAL), to increase the conductivity of the mixture, and polyvinylidene fluoride (PVDF) (Aldrich average $M_w \sim$

534000), as a binder to increase the contact between the particles of the active material and between the active material and the current collector, with a mass ratio of 80:10:10. The mixture was suspended in N-methyl-2-pyrrolidinone (NMP) (Sigma-Aldrich, 99.5%) and cast on the aluminum foil with a typical loading of 7 - 9 $mg.cm^{-2}$. Electrodes were dried in a vacuum oven at 90 ºC. The electrolyte was 1 M $NaClO_4$ (Alfa Aesar, ≥ 98%) in propylene carbonate (BASF, 99.98%) with 2 vol% of 4-fluoro-1,3-dioxolan-2-one (FEC) (Sigma-Aldrich, 99%) as an electrolyte additive. Cell assembly was carried out in an argon filled glovebox. To prepare air-protected electrodes, all the stages of the electrode preparation were performed in an argon-filled glovebox.

Chapter 3

Air-Reactivity of P2-$Na_{0.67}[Mn_{0.5}Fe_{0.5}]O_2$

3.1 Introduction

Layered sodium transition metal oxides are the most extensively explored materials for the positive electrode in Na-ion batteries.[4,33,34] After komaba *et al.*[53] introduced the promising properties of P2-$Na_{0.67}[Mn_{0.5}Fe_{0.5}]O_2$, *i.e.*, made from earth-abundant elements and showing high specific energy and moderate capacity retention, as the positive electrode for NIBs, many efforts were devoted to investigating various P2-$Na_{0.67}[Mn_{1-x}Fe_x]O_2$ compositions[61-65]. Despite the advantages that P2-$Na_{0.67}[Mn_{0.5}Fe_{0.5}]O_2$ offers, the reactivity of this material with ambient atmosphere is an important challenge.

Many sodium transition metal oxides are known to be reactive under ambient atmosphere.[34] This is an important challenge in terms of the reproducibility of the research study results. Moreover, reactivity under ambient atmosphere is a critical concern regarding the storage and handling of these materials from a practical application perspective. About 15 years ago, Dahn *et al.*[94] reported that water molecules can intercalate into P2-$Na_{2/3}[Co_xNi_{1/3-x}Mn_{2/3}]O_2$ (x = 1/6, 1/3), but not into T2-$Li_{2/3}[Co_xNi_{1/3-x}Mn_{2/3}]O_2$ (x = 1/6, 1/3). This T2 phase is obtained from the ion exchange of Li atoms for Na atoms in the P2 structure and accommodates the Li atoms in tetrahedral sites. What differentiates these two structures are the larger interlayer distance and high concentration of large empty prismatic sites that are available in the P2 structure, making it more susceptible to the intercalation of water molecules. On the other hand, no water intercalation was observed for P2-$Na_{2/3}[Ni_{1/3}Mn_{2/3}]O_2$, as reported in the same study. The resistance of P2-$Na_{2/3}[Ni_{1/3}Mn_{2/3}]O_2$ to the intercalation of water molecules was attributed to the stronger coupling between adjacent MO_2 layers induced by superlattice ordering of Mn and Ni, and absence of Mn^{3+} ions. In a more recent study, Passerini *et al.*[95] investigated the correlation between the

intercalation of water and the sodium content in the mixed P2/P3 structure $Na_x[Ni_{0.22}Co_{0.11}Mn_{0.66}]O_2$. The cells were charged to different voltages corresponding to specific sodium contents, disassembled, and exposed to air for analysis. The analysis of X-ray diffraction (XRD) patterns collected from those electrodes suggested that water does not intercalate into this material until the sodium vacancy increases above a threshold amount. The appearance of intense (00l′) peaks in the XRD patterns of air-exposed $Na_x[Ni_{0.22}Co_{0.11}Mn_{0.66}]O_2$ electrodes with $x \leq 0.33$ illustrates a highly ordered hydrated phase with large interslab distances. In another study, Prakash *et al.*[96] reported the structural instability of O3-$Na[Ni_{1/3}Mn_{1/3}Co_{1/3}]O_2$ in the ambient atmosphere. XRD analysis revealed transition of pristine rhombohedral O3 phase to monoclinic O1 and then rhombohedral P3 phase, as aged in air. It was suggested that the reaction of the material with H_2O and CO_2 in air and formation of NaOH and Na_2CO_3 is at the origin of those phase transitions.

The study[55] of $Na_{0.67}[Mn_{0.5}Fe_{0.5}]O_2$ clearly demonstrated the reactivity of this material under ambient atmosphere. Despite the fact that the research community is aware of the air instability issues of sodium layered oxides, which is why these materials are stored in inert atmosphere,[53,61,97] the impact of air reactivity on the structural properties and electrochemical performance of substituted manganese oxides has been underestimated, leading to discrepancies in previously published reports (see below). In this study, rigorously air-protected $Na_{0.67}[Mn_{0.5}Fe_{0.5}]O_2$ was prepared and its structural and electrochemical properties was investigated compared with its air-exposed counterpart. The reactivity of $Na_{0.67}[Mn_{0.5}Fe_{0.5}]O_2$ with H_2O, CO_2, and O_2 and their combinations was examined to understand the responsible mechanism for the instability of the material in ambient atmosphere. A combination of neutron diffraction, mass spectrometry, thermogravimetric analysis, and electrochemical measurements revealed the intercalation of carbonate anions into the layered structure as a result of exposure of the material to air. Large voltage polarization and reduced specific capacity of air-exposed $Na_{0.67}[Mn_{0.5}Fe_{0.5}]O_2$ electrodes compared to rigorously air-protected electrodes exhibit the detrimental

impact of air-reactivity. The effect of composition modification on the air reactivity of the material was explored.

3.2 Synthesis

$Na_{0.67}[Mn_{0.5+y}Fe_{0.5-2y}Ni_y]O_2$ phases with y = 0, 0.1, 0.15 were synthesized by a solid-state method. Stoichiometric amounts of Na_2CO_3 (EMD Millipore, ≥ 99.5%), Mn_2O_3 (Sigma-Aldrich, 99%), NiO (Sigma-Aldrich, 99.8%), and Fe_2O_3 (Sigma-Aldrich, ≥ 99%) powders were mixed using a ball mill (250 ml agate jars, 10 mm diameter agate balls, 20 balls for 1 g of precursors mix powder, milled at 250 rpm for 1 h) and were pressed into pellets. The pellets were heated in air at 750 °C for 4 hours followed by a final annealing at 900 °C for 6 hours. Samples referred to as "air-exposed" were then cooled to room temperature in the furnace and stored under ambient conditions, whereas "air-protected" samples were obtained through heat treatment in an inert atmosphere (Ar, He or vacuum) at 600 °C for 12 hours and transferred to an argon-filled glovebox. Air-protected electrodes were prepared in an Ar-filled glovebox and dried under vacuum.

3.3 Results and Discussions

3.3.1 Air-Protected $Na_{0.67}[Mn0.5Fe_{0.5}]O_2$

The crystal structure of air-protected samples of $Na_{0.67}[Mn_{0.5}Fe_{0.5}]O_2$ was studied by combined Rietveld refinement of X-ray and neutron powder diffraction (XRPD and NPD) data (**Figure 3.1 a,b** and **Table 3.1**). $Na_{0.67}[Mn_{0.5}Fe_{0.5}]O_2$ crystallizes in undistorted P2 structure (space group *P6₃/mmc*), (**Figure 3.2 a**) and no evidence of Mn/Fe ordering at the transition metal site was obtained. The lattice parameters calculated for air-protected $Na_{0.67}[Mn_{0.5}Fe_{0.5}]O_2$ is different from those previously reported for this composition.[53, 63] This discrepancy originates from the evolution of lattice parameters even upon minor exposure to air.

hkl-dependent peak broadening is clearly noticeable in the XRPD and NPD patterns of $Na_{0.67}[Mn_{0.5}Fe_{0.5}]O_2$, as previously reported;[53] The peak profiles of (10l) reflection are much broader than (00l) and (hk0) peaks (demonstrated for two different reflections in the inset of **Figure 3.1 a** and **Figure 3.1 b**). The appearance of *hkl*-dependent broadening in the XRD pattern of $Na_{0.67}[Mn_{0.5}Fe_{0.5}]O_2$ was attributed to stacking faults.[53] The stacking faults could originate from the Jahn-Teller distortion of Mn^{3+} ions. It was shown that the high concentration of Mn^{3+} in the parent P2-$Na_{2/3}MnO_2$ results in an orthorhombic distortion of the ideal hexagonal symmetry.[39,51,98,99] Because of the impact of the

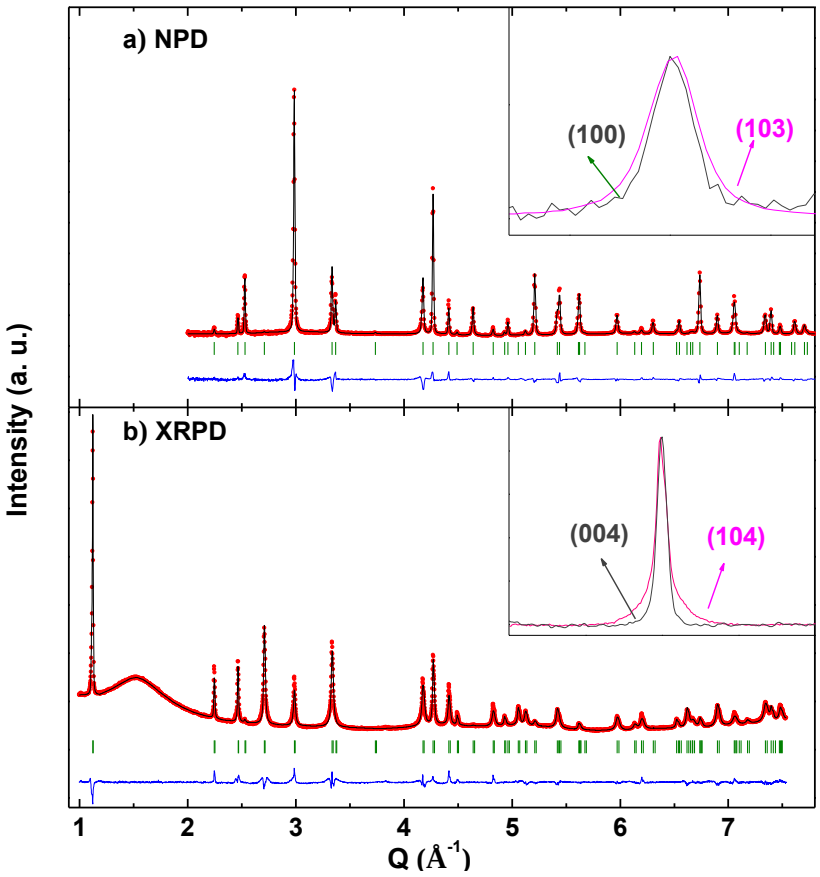

Figure 3.1 Combined Rietveld refinement of neutron (a) and X-ray powder (b) diffraction data of $Na_{0.67}[Mn_{0.5}Fe_{0.5}]O_2$. For each pattern, the observed data is shown in red, and the calculated pattern is shown in black; the difference curve is shown in blue, and the calculated Bragg reflections are shown in green. The insets show two different reflections normalized in intensity to compare the *hkl*-dependent broadening.

stacking faults, the peak shape of the patterns could not be modeled properly in the refinement, even with Stephens strain correction,[100] which is why the obtained R_{Bragg} (**equation 2.4**) (the figure of merit based on integrated peak intensity) is more satisfactory compared to χ^2 (**equation 2.5**) (the figure of merit using all the measured points) (**Table 3.1**).

Table 3.1 Atomic parameters and unit cell parameters of $Na_{2/3}[Mn_{1/2}Fe_{1/2}]O_2$ calculated from Rietveld refinement of neutron and X-ray powder diffraction data.

$P6_3/mmc$, a = 2.9429(1) Å, c = 11.1881(3) Å, Cell volume = 83.895(6) Å^3

χ^2 (XRPD/NPD) = 14.5/9.12, R_{Bragg} (XRPD/NPD) (%) = 13.8/6.27

Site	Wyck.	x	y	z	U_{eq} (Å^2)	at./f.u.
Na_e	6h	0.625(5)	0.375(5)	1/4	0.02(1)	0.45(1)
Na_f	6h	0.04(2)	0.96(2)	1/4	0.02(1)	0.22(1)
Fe/Mn	2a	0	0	0	0.015(1)	1
O	4f	1/3	2/3	0.0925(3)	0.012(1)	2

Anisotropic U_{ij} (Å^2)

Atom	$U_{11} = U_{22}$ (Å^2)	U_{33} (Å^2)	U_{12} (Å^2)
Fe/Mn	0.013(1)	0.021(2)	0.006(2)
O	0.012(2)	0.012(2)	0.006(2)

In the refinement, the fraction of sodium ions to transition metal ions was fixed to 0.67 and the ratio of Mn/Fe was fixed to 1, in agreement with the ICP-AES results. The two sodium sites available in the P2 structure (**Figure 3.2 a**), Na_e and Na_f (**Figure 3.2 b**), exhibit significant configurational disorder in $Na_{0.67}[Mn_{0.5}Fe_{0.5}]O_2$, as observed in P2-type $Na_{5/6}[Li_{1/4}Mn_{3/4}]O_2$ and $Na_{2/3}CoO_2$.[74,101] High disorder in the position of sodium ions could appear as anomalously large isotropic displacement parameters.[74,102] This disorder is modeled here by splitting the positions Na_e (2d) and Na_f (2b) into the lower symmetry 6h Wyckoff position (**Figure 3.2 c,d**), similar to the strategy used before in previous studies.[74,101] The

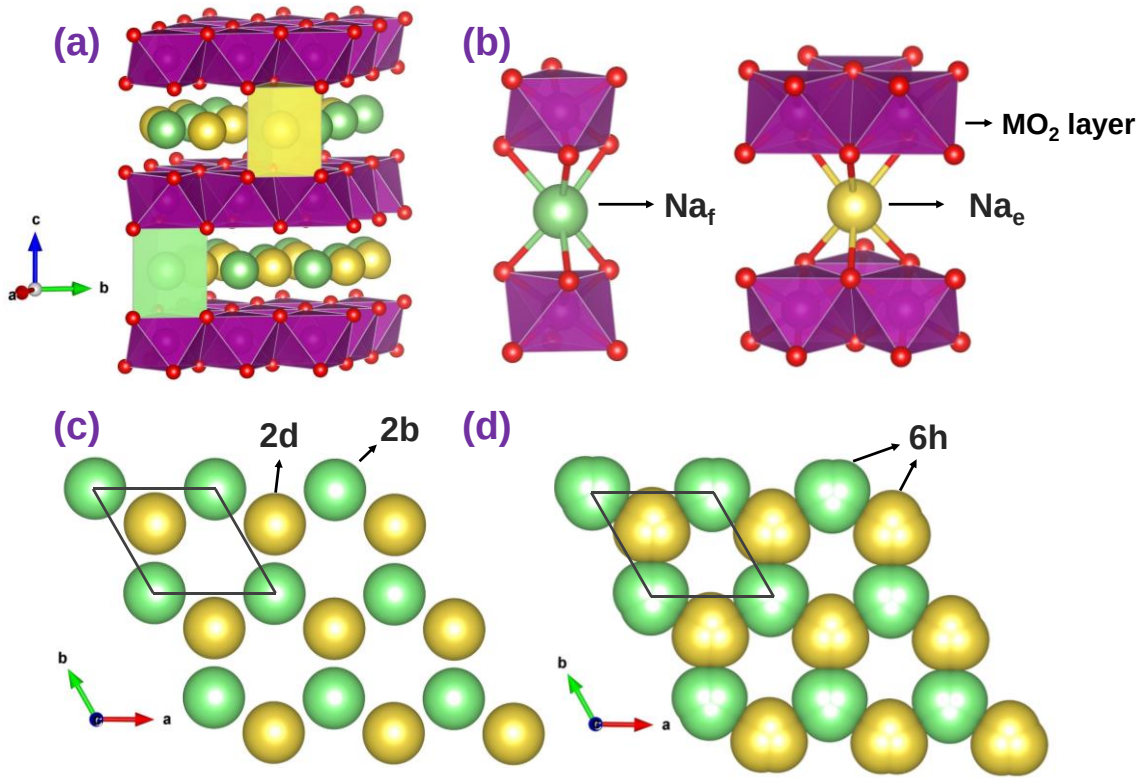

Figure 3.2 Schematic illustration of P2-$Na_{2/3}MO_2$ structure (a). Purple and red spheres represent M (transition metal) and O atoms and green and yellow spheres represent Na atoms in two different sites. Face-shared and edge-shared sodium sites (b), sodium arrangement in 2d and 2b sites (c), and in 6h sites (d).

occupancy of the Na_e site (edge-sharing with MO_6 octahedra) is twice that of the Na_f site (face-sharing with MO_6 octahedra), consistent with the larger Na-M distance of the former (*i.e.*, higher stability).

The combined refinement of the NPD and XRPD of $Na_{0.67}[Mn_{0.5}Fe_{0.5}]O_2$ showed no evidence of Mn/Fe ordering. The configurational disorder prevents long-range ordering of Na^+/vacancy, which is reflected as pronounced stepwise features in the voltage profile of some layered sodium metal oxides, such as those observed in P2-$Na_{2/3}CoO_2$,[54] P2-$Na_{2/3}VO_2$,[103] P2-$Na_{2/3}[Co_{2/3}Mn_{1/3}]O_2$,[102,104] O3-$Na[Ni_{1/2}Mn_{1/2}]O_2$,[71,105] P2-$Na_{2/3}[Mn_{2/3}Ni_{1/3}]O_2$[43]. The structural modifications associated with this ordering results in poor capacity retention and limited rate capability. $Na_{0.67}[Mn_{0.5}Fe_{0.5}]O_2$ shows a

smooth voltage profile (**Figure 3.3 a**) and delivers a large specific capacity of ≈ 200 $Wh.kg^{-1}$ over the first discharge, corresponding to the sodium intercalation over a wide range of stoichiometry ($0.15 < x < 0.9$ in $Na_x[Mn_{0.5}Fe_{0.5}]O_2$). The capacity fading of $Na_{0.67}[Mn_{0.5}Fe_{0.5}]O_2$ is moderate with 65% retention after 50 cycles (**Figure 3.3 b**), showing that, despite its reversibility, the phase transitions induced by insertion and extraction of sodium ions (discussed in Chapter 4) impacts the cycling properties of this material.

The voltage profile of $Na_{0.67}[Mn_{0.5}Fe_{0.5}]O_2$ shows small polarization in the low voltage region and much higher polarization in the high voltage range. The origin of the polarization at two different regions is described in Chapter 4. The voltage profile of an air-protected $Na_x[Mn_{0.5}Fe_{0.5}]O_2$ electrode

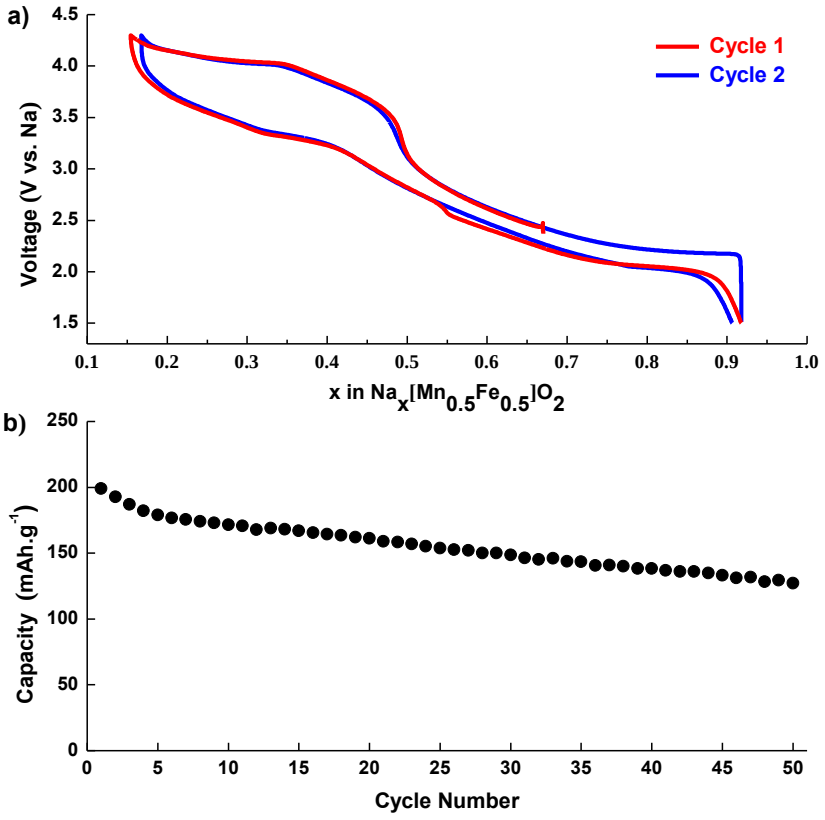

Figure 3.3 First two galvanostatic charge/discharge cycles (a) and the capacity retention (b) of air-protected P2-$Na_{0.67}[Mn_{0.5}Fe_{0.5}]O_2$ cycled at 13 $mAh.g^{-1}$ (C/20).

(**Figure 3.3 a**) exhibits a voltage jump at x = 0.5. This feature is probably related to the switch of charge compensation mechanism from Mn^{3+}/Mn^{4+} to Fe^{3+}/Fe^{4+} couple. The appearance of this feature at exactly the expected sodium stoichiometry of $Na_{0.5}[Mn_{0.5}^{4+}Fe_{0.5}^{3+}]O_2$ in an air-protected electrode, contrary to the previous report of this material,[53] confirms the excellent control of oxygen stoichiometry in the air-protected samples.

An evident difference between the results presented here and in the previous works[53,68] is the perfect overlap of the first and second charge profiles of an air-protected electrode. The similarity of the first and second charge processes implies the excellent reversibility of sodium insertion/extraction in air-protected electrodes. The feature in the voltage profile of the first discharge of $Na_x[Mn_{0.5}Fe_{0.5}]O_2$ at ≈ 2.7 V is expected to originate from the decomposition of FEC (the electrolyte additive) over the first cycle.[106] As discussed below, the exposure of the material to air, even for a short period of time, causes reaction with carbon dioxide and water, resulting in the modification of electrochemical properties.

3.3.2 Air Sensitivity of the Studied Materials

Many layered sodium transition metal oxide materials are unstable in air. Various mechanisms are proposed for the reactivity of these materials in ambient atmosphere, such as the intercalation of water molecules into the interlayer space of the layered structure,[94,95] uptake of oxygen accompanied with formation of cation vacancies,[39,40,98,107] reaction with carbon dioxide (CO_2) and moisture (H_2O) in air and formation of sodium carbonate (Na_2CO_3) at the surface of the material.[96] The reactivity of the materials depends on the precise composition of the atmosphere, temperature, and the exposure time. The changes in the appearance of the samples stored in air, such as cracks in the pellets caused by volume expansion and change of the powder color from back to brown, clearly indicate the air reactivity of P2-$Na_{0.67}[Mn_{0.5}Fe_{0.5}]O_2$.

Thermogravimetric analysis (TGA) under argon atmosphere demonstrates a two-step mass loss of more than 7% (reported with respect to the mass after heating) for a one-week-old air-exposed sample of $Na_{0.67}[Mn_{0.5}Fe_{0.5}]O_2$ (**Figure 3.4**). The nature of the released gases was investigated by Mass spectrometry (MS). The mass loss (≈ 2% wt) observed at ≈ 100 °C corresponds to the release of CO_2 and H_2O on the surface of the grains (physisorption). During the high-temperature mass loss (≈ 4.8% wt) process starting at ≈ 300 °C, CO_2 and O_2 gases are evolved, consistent with the decomposition of carbonate ions.

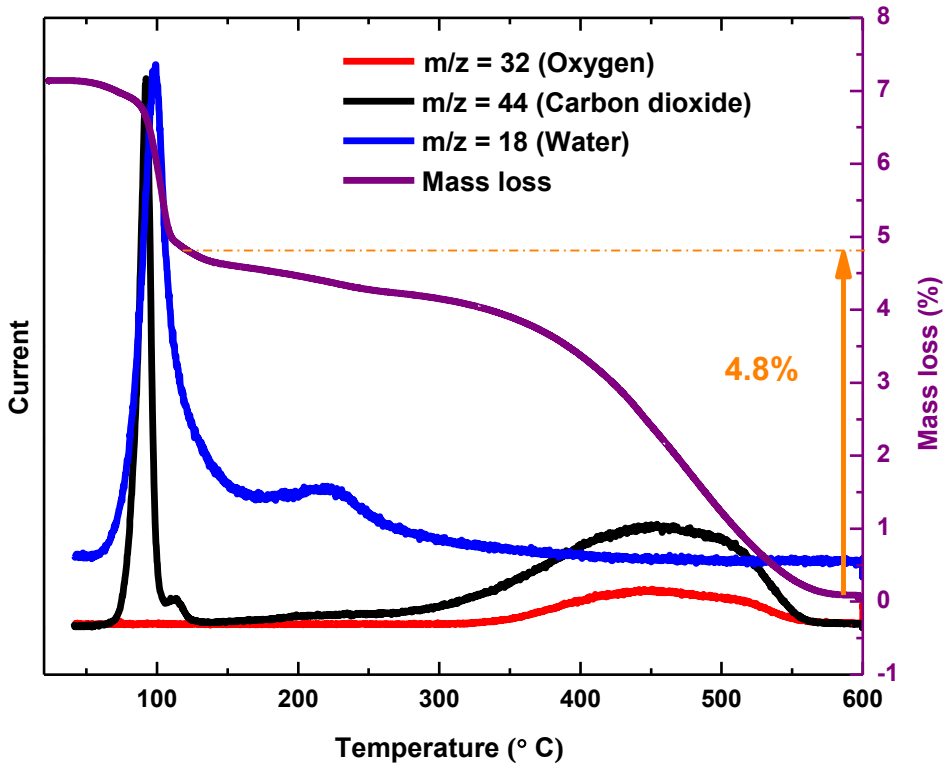

Figure 3.4 Gases evolution and mass loss of air-exposed $Na_{0.67}[Mn_{0.5}Fe_{0.5}]O_2$ during heat treatment up to 600 °C under argon, studied by TGA-MS.

Figure 3.5 shows the evolution of the lattice parameters of an air-exposed powder sample of $Na_{0.67}[Mn_{0.5}Fe_{0.5}]O_2$ with temperature, calculated from XRD data collected at certain temperatures over the heating and cooling stages of a heat treatment. In this *in-situ* XRD experiment, the sample was subjected to sequential temperature ramps (1 h temperature ramp) under helium atmosphere. At certain temperatures, 6 successive XRD patterns (10 minutes each) were collected at isothermal conditions (for 1 h). For temperatures at which the XRD patterns evolved (at the isothermal condition), the lattice parameters obtained from both the first and the last scans are presented (**Figure 3.5**). The lattice parameters are affected slightly with the mass loss mechanism occurring at ≈ 100 °C related to the decomposition of surface bound species. The more evident evolution of lattice parameters, elongation

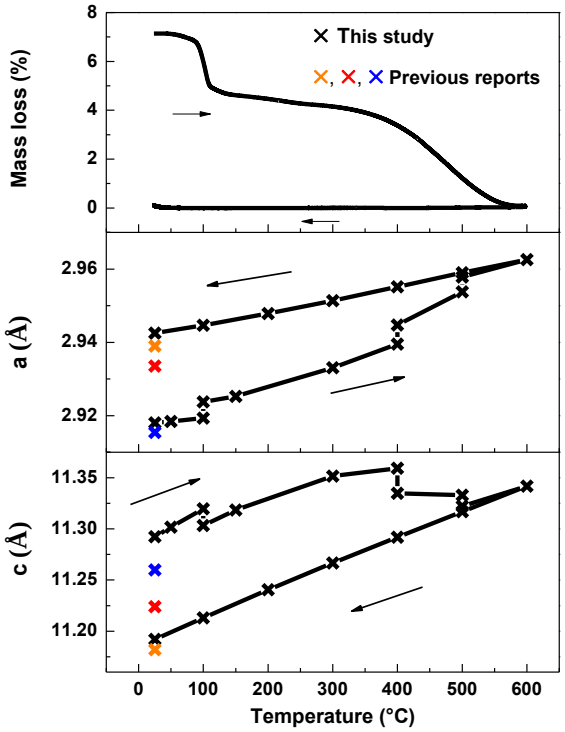

Figure 3.5 TGA curve and lattice parameters of air-exposed $Na_{0.67}[Mn_{0.5}Fe_{0.5}]O_2$ powder measured from thermo-diffraction data collected under a helium atmosphere. The arrows show the sequence in the heating and cooling processes. The red, orange, and blue markers correspond to the cell parameters reported for $Na_{0.67}[Mn_{0.5}Fe_{0.5}]O_2$ in the references 53,61,63, respectively.

of *a* lattice parameter and contraction of *c* lattice parameter, at the second mass loss implies a modification of structure at high temperature.

The formation of carbonate on the surface of layered sodium metal oxides is well-known. In the case of P2-$Na_{0.67}[Mn_{0.5}Fe_{0.5}]O_2$, no evidence of the formation of a carbonate phase was obtained from XRD pattern of aged sample, even after several months of exposure to air. This observation is very interesting considering that XRD analysis of an aged sample of O3-$Na[Mn_{0.5}Fe_{0.5}]O_2$ clearly contains peaks corresponding to thermonatrite ($Na_2CO_3 \cdot H_2O$), a hydrated sodium carbonate phase (**Figure 3.6 a**), and scanning electron microscopy (SEM) reveals the presence of an impurity phase (**Figure 3.6 b**).

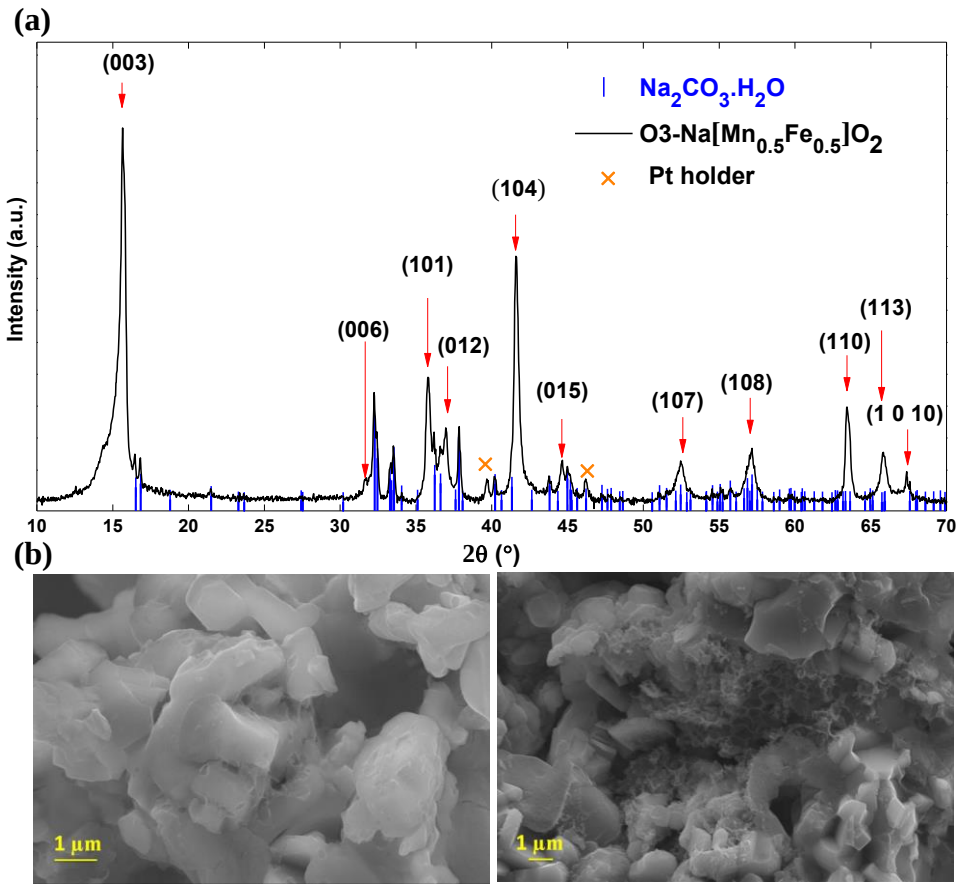

Figure 3.6 XRD pattern (a) and SEM images (b) of O3-$Na[Mn_{0.5}Fe_{0.5}]O_2$ exposed to air for months showing the presence of a crystalline sodium carbonate phase.

By employing neutron powder diffraction, carbonate anions were found within the crystal structure of an air-exposed sample of P2-$Na_{0.67}[Mn_{0.5}Fe_{0.5}]O_2$. A full description of this neutron diffraction analysis is presented in reference 55. The Rietveld refinement of the air-exposed sample shows the formation of cationic vacancies (uptake of oxygen), similar to its parent composition P2-$Na_{2/3}MnO_2$.[40,99] The difference Fourier map revealed a large residual nuclear density within the tetrahedral sites of the MO_2 layer. This residual nuclear density cannot be assigned to hydrogen or manganese ions because their negative neutron scattering lengths would result in opposite sign of nuclear density. On the other hand, this tetrahedral site is too small to accommodate the iron ion. Therefore, considering the TGA and MS data, it was concluded that the residual nuclear density in the difference Fourier map should represent carbon atoms. The structure was refined with the stoichiometry fixed to $Na_{0.60}[Fe_{0.44}Mn_{0.44}C_{0.08}]O_2$, corresponding to the complete oxidation of Mn^{3+} to Mn^{4+} balanced by the insertion of CO_3^{2-} ions formed by the reaction with CO_2, O_2 (see below), as shown in **equation 3.1**:

$$Na_{2/3}Fe^{3+}{}_{1/2}Mn^{3+}{}_{1/6}Mn^{4+}{}_{1/3}O_2 + \frac{1}{12}\left(CO_2 + \frac{1}{2}O_2\right) \rightarrow \frac{9}{8}\left(Na_{16/27}Fe^{3+}{}_{4/9}Mn^{4+}{}_{4/9}C^{4+}{}_{2/27}O_2\right) \qquad (\mathbf{3.1})$$

The equation is in close agreement with the mass loss detected by TGA (*i.e.*, the ratio of the mass of inserted carbonate ions to the mass of the original composition is equal to 0.048). The quality of the fit was significantly increased by adding the carbonate ions into the structure according to the stoichiometry in **equation 3.1**. This equation can be understood as a process by which the oxygen atoms of carbonate ions are added into the hexagonal oxygen framework of the original structure, forming cation vacancies. The carbon atom at the center of the carbonate ion is located within the tetrahedral site of the transition metal layer. It should be noted that only the average position of the atom can be resolved by a diffraction technique. It is proposed that the static picture is one where the carbon atom shifts toward the center of one of the faces of the "CO_4 tetrahedron" to adopt a 3-fold coordination

consistent with the CO_3^{2-} ion. A similar disorder has been observed for carbonate anions within the lattice of tetragonal perovskite-related $Ba_3YCu_2O_x$ phase.[108]

The following mechanism is proposed for the reactivity of P2-$Na_{0.67}[Mn_{0.5}Fe_{0.5}]O_2$ with air, resulting in the insertion of carbonate anions; the CO_2 and H_2O molecules adsorbed on the surface of the material, demonstrated by TGA-MS (**Figure 3.5**), combine and form carbonic acid (H_2CO_3) that readily dissociates to carbonate anions and protons (**equation 3.2**). The consumed water molecules are reformed as molecular oxygen is reduced at the surface of the grains with the presence of the protons (**equation 3.3**). Overall, this accounts for oxygen reduction in the presence of CO_2 (and water) to form carbonate (**equation 3.4**). This process is accompanied by the oxidation of Mn^{3+} to Mn^{4+}. P2-$Na_{0.67}[Mn_{0.5}Fe_{0.5}]O_2$ has a suitable redox potential to carry out this reaction. This is suggested by its open circuit voltage (OCV) of 2.4 V vs. Na (-0.3 vs. standard hydrogen electrode, SHE). Carbonate anion intercalated layered metal double hydroxides are well known.[109] However, the charge compensation mechanism in layered sodium metal oxides is completely different.

$$CO_{2(ads.)} + H_2O_{(ads.)} \rightarrow 2H^+_{(surf.)} + {CO_3}^{2-}_{(insert.)} \quad \textbf{(3.2)}$$

$$+2H^+_{(surf.)} + \frac{1}{2}O_{2\,(gas)} + 2e^- \rightarrow H_2O_{(ads.)} \quad \textbf{(3.3)}$$

$$CO_2 + \frac{1}{2}O_2 + 2e^- \rightarrow {CO_3}^{2-} \quad \textbf{(3.4)}$$

The role of each reactant in the air was investigated by thermogravimetric analysis under different atmospheres: air, dry oxygen, wet oxygen, wet nitrogen, dry carbon dioxide, and wet carbon dioxide. For each experiment, the sample was first heated under dry argon at 600 °C to release any air contamination and obtain a "reference material" (equivalent to an "air-protected" sample). After cooling down to room temperature under dry argon, the atmosphere was switched to the gas of interest, and the reactivity of the material was monitored at room temperature for 12 h. The temperature was

then raised to 600 °C. **Figure 3.7** shows the mass variations of the "reference material" at room temperature and upon heat treatment under different atmospheres. The mass of sample exposed to air increases at a steady rate during the entire isothermal analysis, showing that the reaction is not complete after 12 h. Further heating results in marginal mass loss up to 200 °C; the mass then increases again to reach its maximum value at ≈ 450 °C, but recovers to about its original one when heated higher up to 600 °C.

The experiment under wet CO_2 demonstrates that the reactivity with the combination of carbon dioxide and water is both fast and significant. The mass increase at room temperature is more than 5.5%

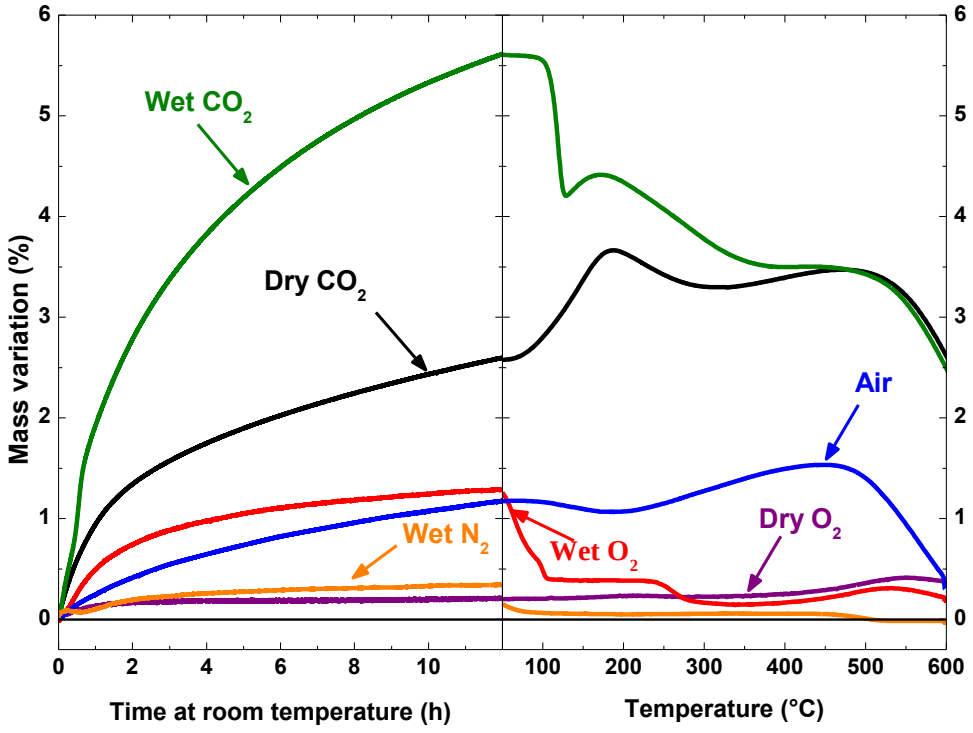

Figure 3.7 Reactivity of $Na_{0.67}[Fe_{0.5}Mn_{0.5}]O_2$ studied by TGA under different atmospheres. In each experiment, the sample was first annealed under dry Ar at 600 °C in order to obtain a reference sample free from any air contamination. After cooling down to room temperature, the atmosphere was switched to the gas of interest and the reactivity of the material with the flowing gas was inspected at 25 °C for 12 h followed by annealing to 600 °C.

after 12 h and is not saturated. An important mass loss in observed at ≈ 100 °C, related to the release of the surface species. The mass loss at temperatures higher than 400 °C should be attributed to the decomposition of the carbonate species as observed for the sample under air. The mass increase under dry CO_2 flow is lower than that of water-saturated CO_2 flow and is probably due to surface adsorption. The mass uptake under water-saturated O_2 flow starts rapidly but almost saturates after 12 hours. The mass variations upon heating under wet oxygen flow is clearly different from the experiment under air.

Figure 3.8 illustrates discernible structural evolutions of a sample of P2-$Na_{0.67}[Mn_{0.5}Fe_{0.5}]O_2$ exposed to air, revealed by scanning electron microscopy (SEM) and XRD in the study of the long-term reactivity of the material. The SEM images of a sample exposed to air for less than a week (**Figure 3.8 a**) show no evidence of an amorphous impurity phase. The SEM images of a sample exposed to air for a couple of weeks demonstrate particles with a ribbon-like morphology (**Figure 3.8 b**). Many of those particles were found in a sample exposed to air for a couple of months (**Figure 3.8 c**). These particles can be washed away with distilled water, as shown by SEM, whereas the XRD pattern remains unchanged. The nature of the ribbon-like particles could not be identified by SEM-EDS because they are damaged under the electron beam. However, the pH of the wash solution (≈ 11) and release of bubbles of gas (CO_2, presumably) suggest that the impurity particles are an amorphous carbonate phase. The ribbon-like morphology is in good agreement with a formation mechanism consisting of a progressive extrusion of the carbonate and sodium ions from within the layered structure.

The exposure of a P2-$Na_{0.67}[Mn_{0.5}Fe_{0.5}]O_2$ sample to air immediately induces small changes in the lattice parameters. New peaks appear in the XRD pattern of the sample aged in air for a long time (**Figure 3.8 d**). The XRD pattern of a sample aged in air for approximately two weeks shows a new broad peak appearing on the left side of the (002) reflection, suggesting the formation of a new poorly crystalline phase, Phase 2, with a larger interlayer spacing of ≈ 6.3 Å (compare to ≈ 5.6 Å for the pristine material). A new set of sharp reflections appears on the XRD pattern of a sample aged in air

for months, indicating a new phase, Phase 3, with a larger interlayer spacing of ≈7.1 Å. The growth of Phase 3 is concomitant with a decrease in the intensity of the peaks assigned to the P2 phase. We propose that these new phases are attributed to the intercalation of water between the MO_2 layers, because of the similarity of the positions of their XRD reflections, particularly for Phase 3, to the "hydrated phases" reported by Lu and Dahn for P2-$Na_{2/3}[Co_{1/3}Mn_{2/3}]O_2$.[94] Recently, Passerini *et al.*[95] reported that water molecules were intercalated into P2/P3-$Na_x[Ni_{0.22}Co_{0.11}Mn_{0.66}]O_2$ when the sodium content was electrochemically decreased lower than a threshold value. We conclude that the same phenomenon is true for the P2-$Na_{0.67}[Mn_{0.5}Fe_{0.5}]O_2$ composition; the formation of the sodium carbonate

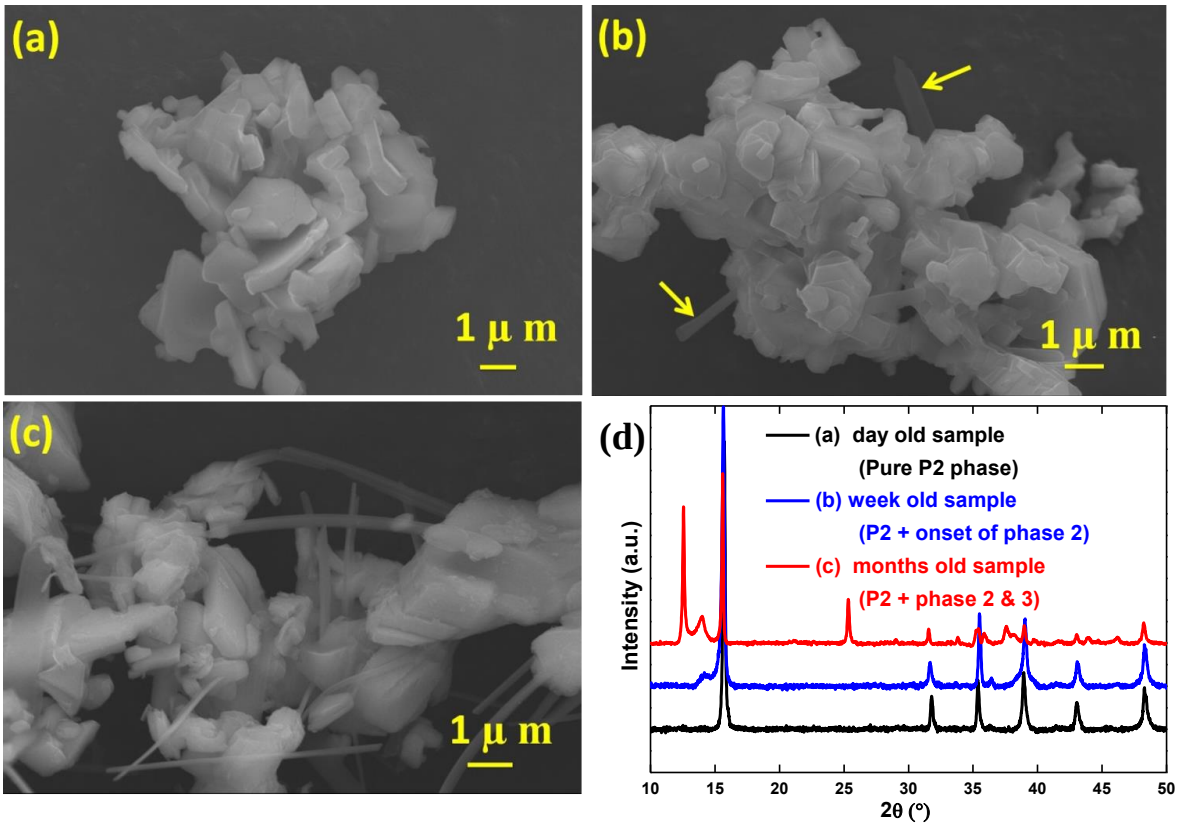

Figure 3.8 The SEM images and XRD patterns of $Na_{0.67}[Mn_{0.5}Fe_{0.5}]O_2$ exposed to air for: a day showing no evidence of impurity (a), a couple of weeks showing small amounts of ribbon-like particles (b) (see arrows), a couple of months showing numerous ribbon-like particles(c); the corresponding diffraction patterns (d).

ribbons extract the sodium from the structure, yielding a sodium-depleted P2 phase, facilitating the intercalation of water molecules. Thermo-diffraction analysis (**Figure 3.9**) shows that Phase 3 disappears below 100 °C, and Phase 2 is decomposed at 200 °C.

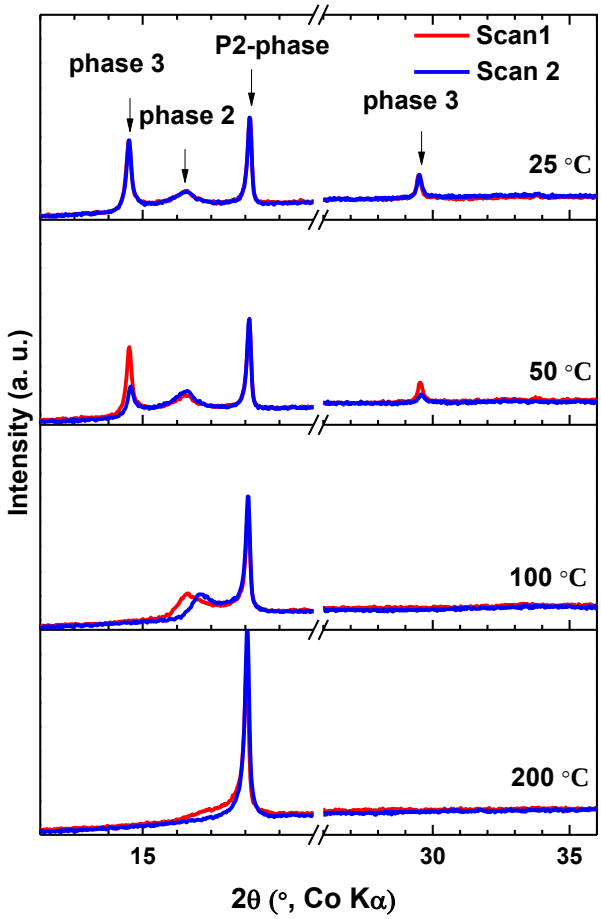

Figure 3.9 High temperature X-ray diffraction under helium of $Na_{0.67}[Fe_{0.5}Mn_{0.5}]O_2$ exposed to air for months. Scan 1 was collected as the temperature was reached and scan 2 was collected after 50 minutes at isothermal condition.

3.3.3 Influence of the Reactivity of $Na_{0.67}[Mn_{0.5}Fe_{0.5}]O_2$ with Air on Electrochemical Properties

Figure 3.10 a exhibits a comparison of the charge/discharge profile of an air-exposed P2-$Na_{0.67}[Mn_{0.5}Fe_{0.5}]O_2$ sample (red curve) with an air-protected one (gray curve). The air-exposed sample shows much lower discharge capacity (about 70% of the air-protected electrode) and larger polarization, more profound in the low voltage region. A particularly significant difference is that the first charge curve does not superimpose with the second charge curve in the air-exposed sample, contrary to the air-protected one. This fact clearly indicates a transformation after the first cycle. On the first charge profile of the air-exposed sample, the potential immediately rises. Such potential jump is observed at x = 0.5 in the air-protected sample and is attributed to the start of $Fe^{3+/4+}$ redox process.

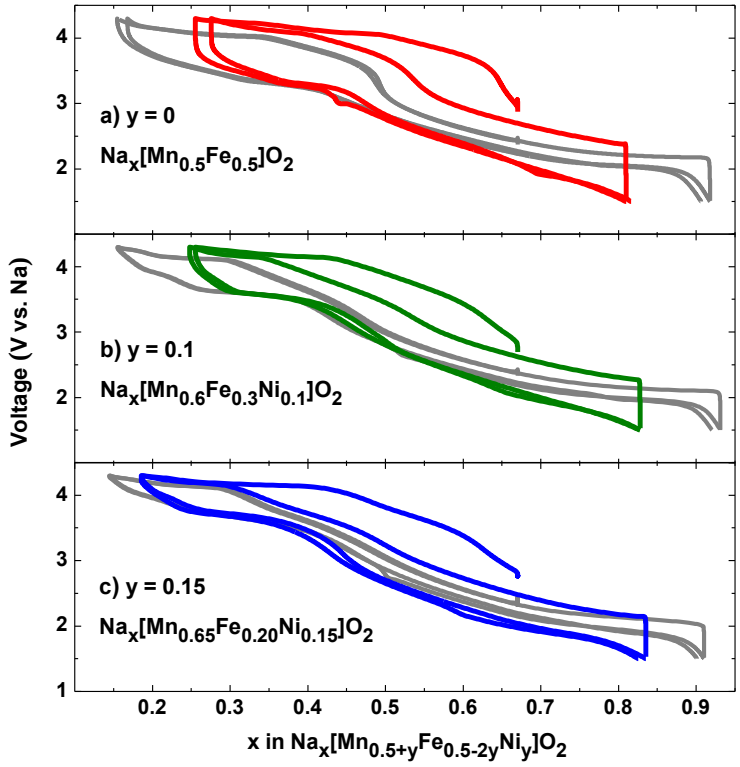

Figure 3.10 The effect of the reactivity of $Na_{0.67}[Mn_{0.5+y}Fe_{0.5-2y}Ni_y]O_2$ a) y = 0, b) y = 0.1 and c) y = 0.15 with air on charge/discharge profiles. The grey curves show the profiles for the air-protected electrodes for comparison.

This observation indicates that almost all the Mn^{3+} ions in the pristine material are oxidized to Mn^{4+} in the air-exposed sample balanced by the insertion of carbonates as described in **equation 3.1**. The substitution of Fe^{3+} by Mn^{4+}/Ni^{2+} has been shown improving the average voltage of P2-$Na_{0.67}[Mn_{0.5}Fe_{0.5}]O_2$.[68,69] We find that this substitution is also beneficial to mitigate the impact of exposure to air, as shown in **Figure 3.10 b,c** for P2-$Na_{0.67}[Mn_{0.6}Fe_{0.3}Ni_{0.1}]O_2$ and P2-$Na_{0.67}[Mn_{0.65}Fe_{0.20}Ni_{0.15}]O_2$. The higher the nickel content, the smaller is the discrepancy between the performance of the air-protected and air-exposed electrodes. This improved stability can be related to the increase of the mean oxidation state of Mn as the Ni content increases. The instability of Mn^{3+} species was previously described in P2-$Na_{2/3}MnO_2$,[40] highlighting that the insertion of carbonate in the P2 structure might be a concern of many Mn^{3+}-containing compositions.

The TGA-MS study of air-exposed P2-$Na_{0.67}[Mn_{0.5}Fe_{0.5}]O_2$ (**Figure 3.4** and **Figure 3.7**) showed that insertion of carbonates is not the only aging mechanism. The effect of the other contaminants, water and oxygen, on the electrochemical properties of the sample was also investigated. **Figure 3.11 b** shows the first and second charge/discharge profiles of a P2-$Na_{0.67}[Mn_{0.5}Fe_{0.5}]O_2$ sample annealed at 600 °C under oxygen. The sample was protected against air after the heat treatment. It shows a potential jump at x = 0.57 on the first charge voltage profile, in agreement with the oxidation of some of Mn^{3+} ions. However, the second charge voltage perfectly overlaps with the first charge voltage. The voltage step in the profile of the material exposed to wet argon and dried at 90 °C under vacuum (**Figure 3.11 c**) appears at x = 0.51, suggesting only a marginal oxidation of the sample. These experiments demonstrate that solely oxygen or water exposure cannot independently reproduce the electrochemical behavior observed for the air-exposed material. **Figure 3.11 d** illustrates the voltage profile of a sample exposed to ambient conditions for 5 months, washed with water to remove the carbonate particles, and dried at 200 °C under vacuum to remove intercalated water and produce a sodium deficient P2-$Na_{0.5}[Mn_{0.5}Fe_{0.5}]O_2$ phase. The immediate potential jump on the first charge confirms the expected

sodium stoichiometry. The superimposability of the first and second charge implies that washing the electrode material with water, as reported by others,[69] effectively removes the carbonate contamination. However, the P2-$Na_x[Mn_{0.5}Fe_{0.5}]O_2$ material annealed at 600 °C under vacuum or argon outperforms the material obtained by washing, possibly due to proton exchange in the latter case.

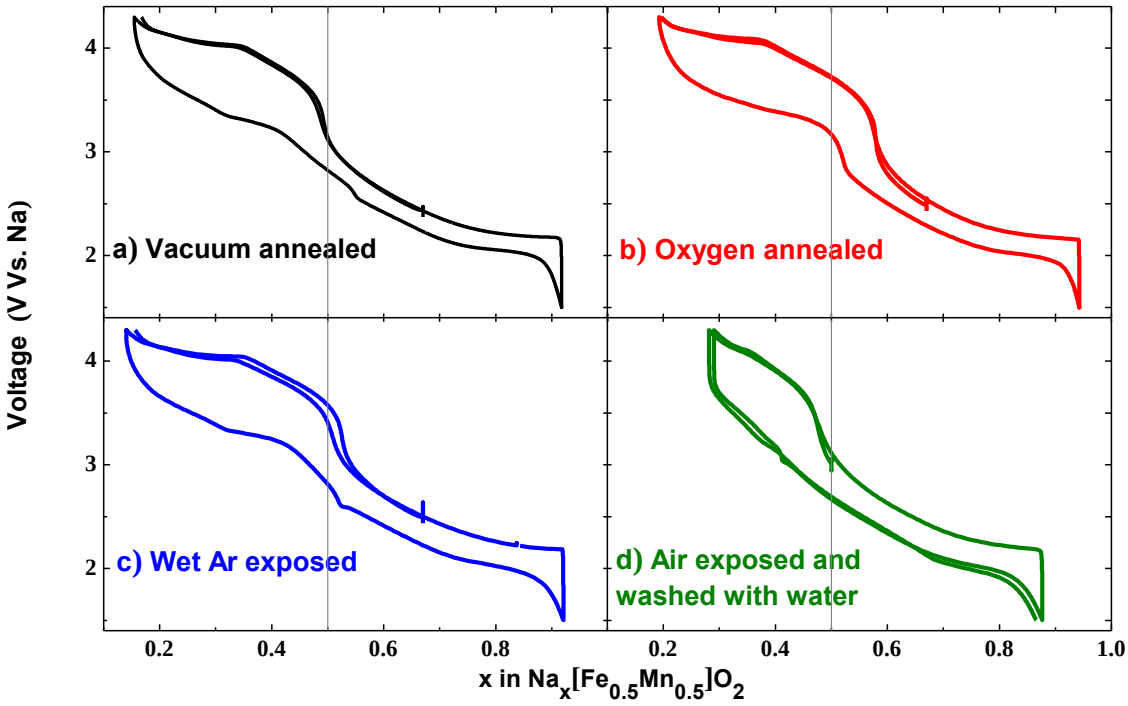

Figure 3.11 Charge/discharge profiles of $Na_{0.67}[Mn_{0.5}Fe_{0.5}]O_2$ annealed under vacuum at 600 °C (a) (for comparison), annealed under oxygen at 600 °C (b), exposed to wet argon at room temperature and dried at 90 °C under vacuum (c), and exposed to air for months, washed with distilled water, filtered, and dried at 200 ° under vacuum (d).

3.3.4 Online Electrochemical Mass Spectrometry Study of $Na_{0.67}[Mn_{0.5}Fe_{0.5}]O_2$

An online electrochemical mass spectrometry (OEMS) investigation of P2-$Na_{0.67}[Mn_{0.5}Fe_{0.5}]O_2$ was performed to monitor the gases released upon cycling (**Figure 3.12**) to obtain a better understanding of the processes responsible for the difference between air-exposed and air-protected samples. O_2, H_2O, H_2, and CO_2 gases were monitored. However, only the signal corresponding to CO_2 showed meaningful changes.

Upon the first charge. **Figure 3.12 a** shows the significant evolution of CO_2 from the air-exposed sample in the range of $0.55 < x < 0.4$, highlighted by the circle region. This feature is not observed for the air-protected sample (**Figure 3.12 b**), indicating that it is related to the evolution of carbonates inserted upon air exposure, as previously described. The carbonate ions decompose to CO_2 and oxygen species; because no oxygen evolution was detected, we assume that the oxygen reacts with the electrolyte and/or is incorporated into the lattice as oxide ions. Small amounts of CO_2 is released from the air-exposed sample at $x = 0.67$ and from the air-protected sample at $x = 0.5$, *i.e.*, at the potential jump of each sample. CO_2 evolution at the onset of Fe^{4+} formation suggests that Fe^{4+} ions decompose the electrolyte. The small range in which these peaks are observed is probably due to the passivation of the surface by the decomposition products.

Upon the first discharge. A large amount of CO_2 is released from the air-exposed sample and the air-protected sample, starting at $x \approx 0.7$ and $x \approx 0.5$, respectively. The CO_2 evolution upon discharge starts at the same sodium stoichiometry at which the second charge gas evolution initiated, *i.e.*, where the redox couple switches between $Mn^{3+/4+}$ and $Fe^{3+/4+}$. This fact suggests that the gas evolution upon discharge is related to the formation of Mn^{3+} ions. This probably originates from surface disproportionation of Mn^{3+} and dissolution of Mn^{2+}, which induces the decomposition of the electrolyte. A similar mechanism was proposed for lithium manganese spinel electrode materials.[110,111]

Upon the second charge. Larger amounts of CO_2 are released from the both samples, at the stoichiometry which the Fe^{4+} formation starts, upon the second charge compared to the first one. This is consistent with the higher concentration of iron ions at the surface of the grains after the dissolution of some manganese ions upon discharge. The shift in the sodium stoichiometry at which the $Fe^{3+/4+}$ redox couple is activated upon the first and second charge of the air-exposed sample suggest that some oxygen species produced from the decomposition of carbonate ions in the first charge are incorporated into the structure as oxide ions.

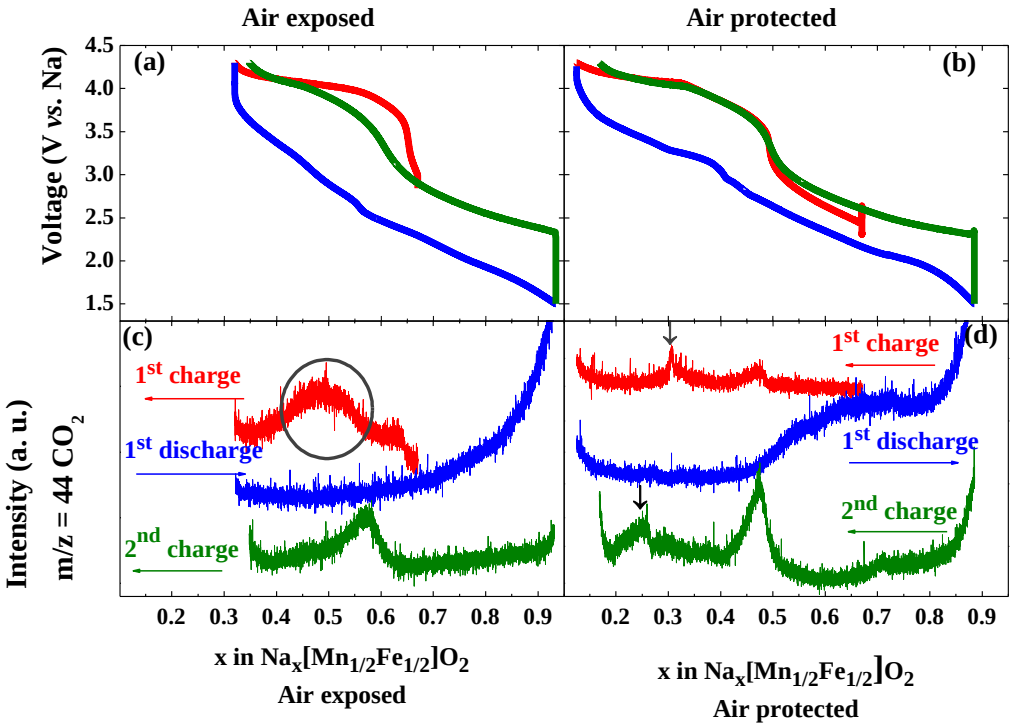

Figure 3.12 Cycling data of air-exposed (a) and air-protected $Na_{0.67}[Mn_{0.5}Fe_{0.5}]O_2$ electrode, and the corresponding CO_2 evolution signal measured by OEMS (c and d). The peaks marked by ↓ are due to sudden pressure change in the system and do not correspond to the sample.

3.4 Conclusions

The layered P2-$Na_{0.67}[Mn_{0.5}Fe_{0.5}]O_2$ is a promising electrode material for sodium-ion battery, owing to its high specific energy and the earth-abundant and non-toxic nature of its constituent elements. It shows a smooth voltage profile resulting from the disorder on the transition metal site, revealed by the neutron diffraction characterization. However, similar to many other layered sodium transition metal oxides, P2-$Na_{0.67}[Mn_{0.5}Fe_{0.5}]O_2$ is unstable in ambient conditions. This study reveals the nature of the reactivity of this material with air and demonstrates its important impact on the electrochemical properties. Rigorous protection of P2-$Na_{0.67}[Mn_{0.5}Fe_{0.5}]O_2$ is necessary to obtain good electrochemical

performance. Using neutron and X-ray diffraction coupled with mass spectrometry and thermogravimetric analysis, we have demonstrated the insertion of carbonate ions into the structure of P2-$Na_{0.67}[Mn_{0.5}Fe_{0.5}]O_2$ on exposure to CO_2, H_2O, and O_2 in air at room temperature, concomitant with oxidation of Mn^{3+} to Mn^{4+}. Online electrochemical mass spectrometry demonstrates the decomposition of the carbonate ions over the first charge. Electrochemical characterization of samples subjected to different air contaminants confirmed that the non-superimposability of the first two charge curves and the large polarization observed in the voltage profile of an air-exposed electrode originates from the presence of carbonate ions. Substituted materials P2-$Na_{0.67}[Mn_{0.6}Fe_{0.3}Ni_{0.1}]O_2$ and P2-$Na_{0.67}[Mn_{0.65}Fe_{0.20}Ni_{0.15}]O_2$ exhibit lower reactivity to ambient conditions, making them more promising compared to the parent composition P2-$Na_{0.67}[Mn_{0.5}Fe_{0.5}]O_2$ for practical applications. The complex reactivity described in this work is probably not limited to the compositions studied here and should be considered when studying sodium layered oxides.

Chapter 4

Structural Investigation and Electrochemical Evaluation of $P2\text{-}Na_{0.67}[Mn_{0.5+x}Fe_{0.5-2x}Ni_x]O_2$ (x = 0, 0.15) as the Positive Electrode for Na-ion Batteries

4.1 Introduction

Layered oxides of various transition metals (Ti, V, Cr, Mn, Fe, Co, Ni, Cu and their combinations) have been synthesized and evaluated as host materials for the intercalation of sodium ions for Na-ion batteries (NIBs) application.[4,33,35] Layered Na_xMO_2 ($x \leq 1$, M = transition metal) are built up of edge-sharing MO_6 layers with different oxygen stacking order along the *c*-axis resulting in several polytypes. The most common polytypes are P2, with trigonal prismatic sodium environment and ABBA oxygen stacking, and O3, with octahedral sodium environment and ABCABC oxygen stacking, according to the notation of Delmas *et al.*[38]. Each unit cell contains 2 and 3 MO_2 layers in the P2 and O3 structures, respectively.

Not only sodium layered oxides deliver comparable energy densities to their Li counterparts, but also they show important advantages. Some redox couples unavailable in lithium host materials are active in their sodium analogues *(i.e.,* $Fe^{3+/4+}$ and $Cr^{3+/4+}$).[12,13] Also, large ionic radius difference between the sodium ion and transition metal ions impedes cation mixing that is observed in Li-ion host materials. On the other hand, many sodium layered oxides are known to be reactive to ambient atmosphere (Chapter 3). Structural evolution induced by insertion/extraction of sodium ions during discharge/charge are also critical challenges intrinsic in these systems, resulting from strong Na^+/vacancy interactions, and cause poor capacity retention and rate capability.[42,43,54,57,112] For example, $NaCoO_2$, which is isostructural to $LiCoO_2$, goes through a sequence of phase transitions, O3-O′3-P′3-P3-P′3, as sodium ions are extracted from the structure during the charge. Modifying the chemical

composition and limiting the cutoff voltage are two important approaches to limit the phase transitions and their detrimental effects. For instance, the capacity retention in a $Na_x[Mn_{2/3}Ni_{1/3}]O_2$/Na cell increases from 65% after 10 cycles to 95% after 50 cycles when the P2-O2 phase transition was avoided by limiting the high voltage range from 4.5 V to 4.1 V.[47] P2-$Na_{0.80}[Li_{0.12}Ni_{0.22}Mn_{0.66}]O_2$ [73] preserves its structure up to 4.4 V and demonstrates superior capacity retention, more than 91% after 50 cycles, to P2-$Na_{2/3}[Mn_{2/3}Ni_{1/3}]O_2$.

$Na_{0.67}[Mn_{0.5}Fe_{0.5}]O_2$ exhibits promising electrochemical performance based on $Fe^{3+/4+}$ redox couple as a positive electrode material and was introduced by Komaba *et al.*[53]. Following that, much effort was devoted to exploring manganese and iron based oxides.[61-63,65,113,114] $Na_{0.67}[Mn_xFe_{1-x}]O_2$ is composed of non-toxic and low-cost elements and delivers high specific energy. However, this family of material is air-sensitive[55] (Chapter 3) and shows poor capacity retention due to phase transitions occurring upon cycling.[53,57] Substitution of nickel is shown to improve the structural stability in ambient atmosphere[55] (Chapter 3) and enhances the capacity retention and average voltage.[68]

In the study[56] presented in this chapter, the structural evolution of P2-$Na_{0.67}[Mn_{0.5}Fe_{0.5}]O_2$ and P2-$Na_{0.67}[Mn_{0.65}Fe_{0.20}Ni_{0.15}]O_2$ upon cycling and its impact on the electrochemical performance of these materials are investigated. The phase transitions during the first charge and discharge were monitored by *operando* X-ray diffraction (XRD) analysis. The high voltage phase was investigated by PDF analysis and Mössbauer spectroscopy. The effect of each phase transition on the electrochemical performance are described.

4.2 Experimental

Synthesis. P2-$Na_{0.67}[Mn_{0.5+x}Fe_{0.5-2x}Ni_x]O_2$ (x = 0, 0.1, 0.15) were synthesized by a solid-state method. For each composition, a mixture of stoichiometric amounts of Na_2CO_3 (EMD Millipore, ≥99.5%), Mn_2O_3 (Sigma-Aldrich, 99, %), Fe_2O_3 (Sigma-Aldrich, ≥99%) and NiO (Sigma-Aldrich, 99.8%) was ball-milled at 250 rpm for 1 hour and then pelletized. The pellets were heated at 700 ºC for 4 hours and

then 900 ºC for 6 hours in air. To prepare materials free from any air contamination, the pellets were heated at 600 ºC under an argon flow and then transferred into an Ar-filled glovebox in a sealed tube. *Operando X-ray Diffraction (XRD). Operando* XRD experiments were performed in a home-made cell. During the acquisition, the cells were cycled at a rate of C/20 with a pattern collection time of ≈ 20 min ($\Delta x \approx 0.02$ in Na_xMO_2). The lattice parameters evolution during charge/discharge were determined using the Le Bail method.[84] The electrode preparation and cell assembly for *operando* XRD experiments were similar to those described in Chapter 2, but the electrodes were deposited on a thin glassy carbon (SIGRADUR, HTW) substrate to allow the penetration of X-rays.

4.3 Results and Discussions

4.3.1 Structural and Electrochemical Overview

The X-ray and neutron time of flight diffraction analyses were carried out on air-protected powder samples of $Na_{0.67}[Mn_{0.6}Fe_{0.3}Ni_{0.1}]O_2$ and $Na_{0.67}[Mn_{0.65}Fe_{0.20}Ni_{0.15}]O_2$. The crystal structures of both compositions were solved by combined Rietveld refinement of X-ray and neutron time of flight diffraction data (**Figure 4.1**, **Table 4.1**), which demonstrate an undistorted P2 structure (*$P6_3/mmc$)* for both compositions, similar to $Na_{0.67}[Mn_{0.5}Fe_{0.5}]O_2$. The data shows that the substitution of Fe^{3+} in $Na_{0.67}[Mn_{0.5}Fe_{0.5}]O_2$ by Mn^{4+}/Ni^{2+} ions affects only the cell parameters, which correlate with the cation diameter, *i.e.*, the cell parameters of $Na_{0.67}[Mn_{0.5}Fe_{0.5}]O_2$, a = 2.9429(1) Å, c = 11.1881(3) Å, decrease to a = 2.9276(1) and c = 11.1690(2) in $Na_{0.67}[Mn_{0.6}Fe_{0.3}Ni_{0.1}]O_2$ and a = 2.9207(1) and c = 11.1598(8) in $Na_{0.67}[Mn_{0.65}Fe_{0.20}Ni_{0.15}]O_2$ as Fe^{3+} ions (radius 0.65 Å) are partially replaced by Mn^{4+}/Ni^{2+} ions (radii of 0.53 Å, and 0.69 Å, respectively).[115]

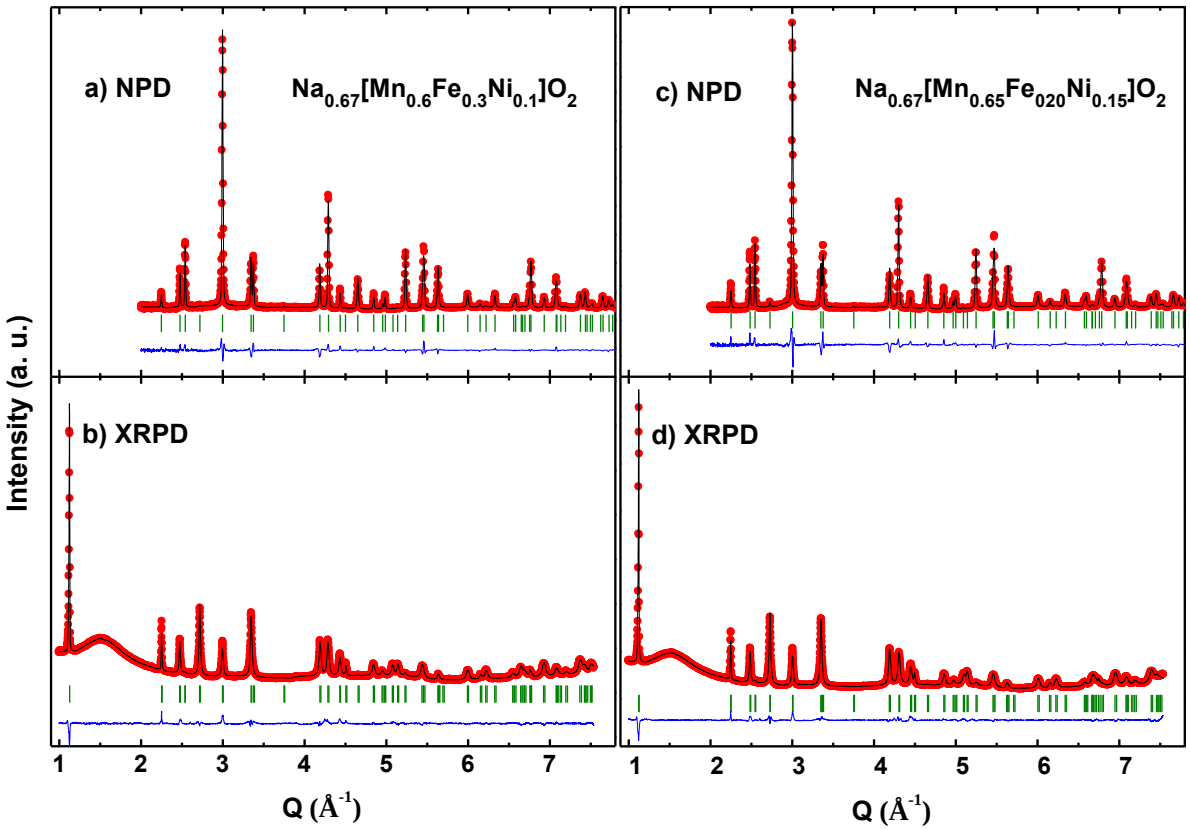

Figure 4.1 Combined Rietveld refinement of neutron (a,c) and X-ray (b,d) powder diffraction data of $Na_{0.67}[Mn_{0.6}Fe_{0.3}Ni_{0.1}]O_2$ (a,b) and $Na_{0.67}[Mn_{0.65}Fe_{0.20}Ni_{0.15}]O_2$ (c,d). For each pattern, the observed data is shown in red, and the calculated pattern is shown in black, the difference curve is shown in blue, and the calculated Bragg reflections are shown in green.

Two trigonal prismatic sites are available in the P2 structure to accommodate sodium ions: Na_e and Na_f, which share edges and faces, respectively, with the MO_6 octahedra. In many P2 structures, the electron density is not localized at those two prismatic sites and is found distributed over the layer.[74,101] Configurational disorder in the sodium or lithium sites is considered the origin of the good mobility of those ions in the host structures.[74,116] The high distribution of electron density in the sodium layer is reflected as anomalously large isotropic displacement parameters for sodium atoms in some layered structures.[74,102] Similar to the strategy employed before to model this disorder,[74,101] off-centered (split) positions were considered for sodium ions, *i.e.*, lower symmetry 6h Wyckoff position rather than 2d

and 2b sites. The refinements showed that occupancy of the Na_e site is about twice that of Na_f in both compositions, implying the higher stability of Na_e site over Na_f due to longer Na-M distances.

Table 4.1 Atomic parameters and unit cell parameters of $Na_{0.67}[Mn_{0.6}Fe_{0.3}Ni_{0.1}]O_2$ and $Na_{0.67}[Mn_{0.65}Fe_{0.20}Ni_{0.15}]O_2$ calculated from Rietveld refinement of neutron and X-ray powder diffraction data.

		$Na_{0.67}[Mn_{0.6}Fe_{0.3}Ni_{0.1}]O_2$	$Na_{0.67}[Mn_{0.65}Fe_{0.20}Ni_{0.15}]O_2$
	Space Group	*P*6$_3$/*mmc*	*P*6$_3$/*mmc*
	χ^2 (XRPD/NPD)	10.1/6.04	12.6/14.4
	R_{bragg} (XRPD/NPD) (%)	4.71/4.72	3.58/4.87
	a (Å)	2.9276(1)	2.9207(1)
	c (Å)	11.1690(2)	11.1598(8)
	Cell Volume (Å^3)	82.904(6)	82.444(6)
Mn/Fe/Ni (2a) (0, 0, 0)	- $U_{11} = U_{22}$ (Å^2)	0.014(2)	0.016(2)
	- U_{33} (Å^2)	0.023(2)	0.021(2)
	- U_{12} (Å^2)	0.007(2)	0.008(2)
Na_e (6h) (x, 2x, 1/4)	- x	0.623(4)	0.621(5)
	- occ.	0.154(4)	0.150(5)
	- U_{iso} (Å^2)	0.02(1)	0.02(1)
Na_f (6h) (x, 2x, 1/4)	- x	0.04(2)	0.03(2)
	- occ.	0.069(4)	0.074(5)
	- U_{iso} (Å^2)	0.02(2)	0.02(1)
O (4f) (1/3, 2/3, z)	- z	0.0925(2)	0.0926(3)
	- $U_{11} = U_{22}$ (Å^2)	0.013(2)	0.015(2)
	- U_{33} (Å^2)	0.011(2)	0.013(2)
	- U_{12} (Å^2)	0.007(2)	0.007(2)

The combined refinement of the neutron and X-ray data showed no evidence of ordering of cations (Ni, Fe, and Mn) over the transition metal site. The long range ordering of Na^+/vacancies in many layered sodium metal oxides, such as P2-$Na_{2/3}VO_2$,[103] P2-$Na_{2/3}CoO_2$,[54] and P2-$Na_{2/3}[Mn_{2/3}Ni_{2/3}]O_2$,[43] cause structural transitions, which are reflected as step-wise features on the charge/discharge voltage profiles. Those structural transitions impede the capacity retention and rate capability. Disorder on transition metal site seems to prevent the long-range Na^+/vacancy ordering.[41] Smooth voltage profiles

of $Na_{0.67}[Mn_{0.5+y}Fe_{0.5-2y}Ni_y]O_2$ (y = 0, 0.10, 0.15) imply the facile (de)intercalation of sodium ions, and perfectly superimposable first and second charges exhibit the reversibility of the process (**Figure 4.2**). All three compositions deliver a specific capacity close to 200 $mAh.g^{-1}$ at the first discharge and exhibit similar capacity retention. The capacity fading is more prominent over the first five cycles. The voltage profiles of $Na_{0.67}[Mn_{0.5+y}Fe_{0.5-2y}Ni_y]O_2$ (y = 0, 0.10, 0.15) show large polarization at high voltage region. The cell polarization at high voltage clearly shrinks as the nickel content increases in the composition.

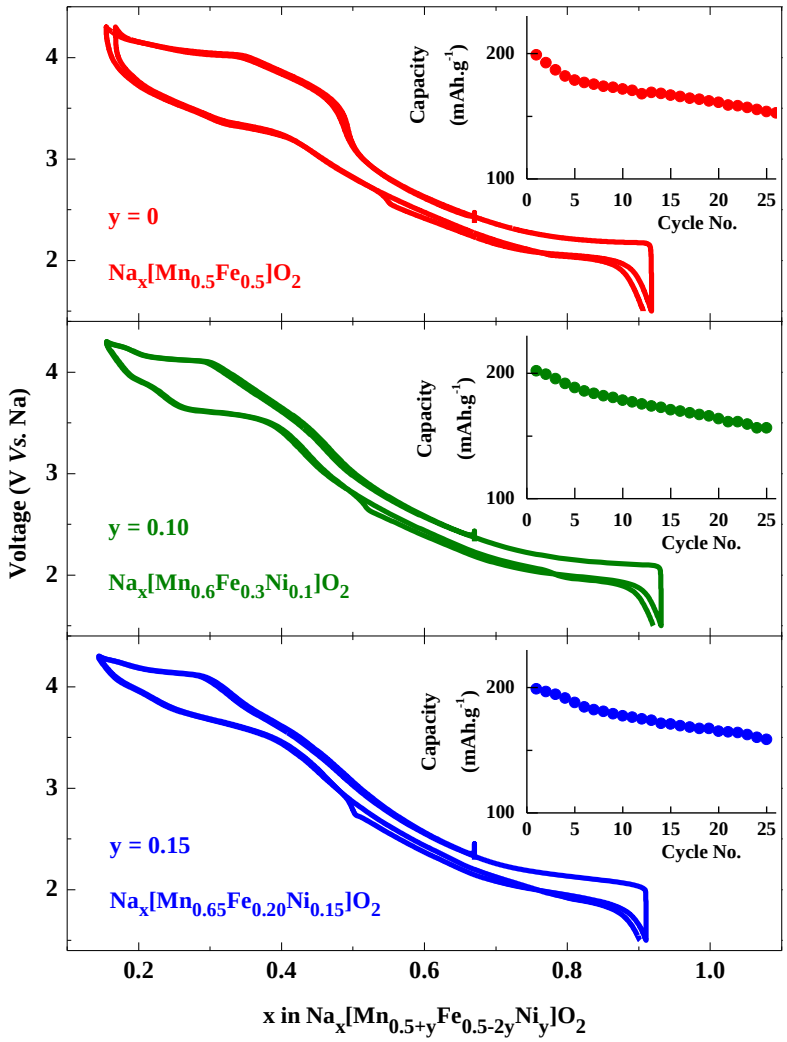

Figure 4.2 First two galvanostatic charge/discharge cycles and specific capacity of P2-$Na_{0.67}[Mn_{0.5+y}Fe_{0.5-2y}Ni_{2y}]O_2$ (y = 0, 0.1, 0.15) over 25 cycles at 13 $mAh.g^{-1}$ (C/20).

The specific energy of $Na_{0.67}[Mn_{0.65}Fe_{0.20}Ni_{0.15}]O_2$, 561 $Wh.kg^{-1}$, is slightly higher than that of the nickel-free composition (545 $Wh.kg^{-1}$).

The combined refinement of X-ray and neutron diffraction data showed that the substitution of nickel into P2-$Na_{0.67}[Mn_{0.5}Fe_{0.5}]O_2$ does not significantly impact the average crystal structure. Therefore, the improved electrochemical performance of Ni-substituted compositions seems to originate from the change in charge compensation mechanism from the $Fe^{3+/4+}$ couple to $Ni^{2+/4+}$. A comparative study on the structural evolution upon cycling of $Na_x[Mn_{0.5}Fe_{0.5}]O_2$ and $Na_x[Mn_{0.65}Fe_{0.2}Ni_{0.15}]O_2$ was performed to investigate the effect of composition modification on structural evolution induced by insertion and extraction of sodium ions and its effect on the electrochemical performance.

4.3.2 *Operando* XRD Study of $Na_x[Fe_{0.5}Mn_{0.5}]O_2$ and $Na_x[Mn_{0.65}Fe_{0.20}Ni_{0.15}]O_2$ Upon Cycling

The structural changes upon cycling of P2-$Na_{0.67}[Mn_{0.5}Fe_{0.5}]O_2$ and P2-$Na_{0.67}[Mn_{0.65}Fe_{0.20}Ni_{0.15}]O_2$ were investigated by *Operando* X-ray diffraction (XRD) analysis. The evolution of the diffraction patterns of $Na_x[Mn_{0.5}Fe_{0.5}]O_2$ and $Na_x[Mn_{0.65}Fe_{0.20}Ni_{0.15}]O_2$ along with the voltage profile of the cells over the first cycle are demonstrated in **Figure 4.3** and **Figure 4.4**, respectively, and the comparison of the phase diagram for the two compositions are shown in **Figure 4.5**. $Na_x[Mn_{0.5}Fe_{0.5}]O_2$ and $Na_x[Mn_{0.65}Fe_{0.20}Ni_{0.15}]O_2$ show the same three phases over cycling; in agreement with reports previously published on P2-$Na_{0.67}[Mn_{0.5}Fe_{0.5}]O_2$,[53,57] the initial P2 converts to a distorted P'2 phase at low voltage and to an low-crystalline phase, referred here to as the "Z" phase, at high voltage.

P2 phase. The initial P2 phase is preserved over a wide range of x in $Na_x[Mn_{0.5+y}Fe_{0.5-2y}Ni_{2y}]O_2$ (y = 0, 0.15). **Figure 4.6** (blue markers) shows the evolution of lattice parameters as a function of sodium content during the first discharge. As the sodium ions are inserted into the structure during the discharge, the in-plane cell parameters ($a_{hex} = b_{hex}$) increases in both compositions, in agreement with the reduction of transition metal ions. The interlayer distance ($c_{hex}/2$) shows the opposite trend,

however; the increase of the sodium content screens more effectively the electrostatic repulsion between the adjacent oxygen layers in the structure resulting in a decrease of interlayer distance. **Figure 4.5** shows that the voltage window at which the material upholds the P2 structure is extended to 2.0 - 4.1 V in $Na_x[Mn_{0.65}Fe_{0.20}Ni_{0.15}]O_2$ compared to 2.1 - 4.0 V in $Na_x[Mn_{0.5}Fe_{0.5}]O_2$.

P2-P'2 transition. As the sodium content exceeds $x \approx 0.8$ in $Na_x[Mn_{0.5+y}Fe_{0.5-2y}Ni_{2y}]O_2$ ($y = 0, 0.15$) upon discharge, a transition occurs from hexagonal P2 ($P6_3/mmc$) phase to orthorhombic P'2 ($Cmcm$) phase. The P'2 phase is triggered by cooperative distortion of Mn^{3+} ions and was previously described in Na_xMnO_2 [51] and $Na[Mn_{0.5}Fe_{0.5}]O_2$ [57]. The P'2 is reported in the Ni-substituted composition for the first time in this study. The P'2 phase converts back to the P2 phase during the second charge as the concentration of Mn^{3+} ions decreases.

The hexagonal cell can be described in an orthorhombic space group using the following relationship, $a_{ortho} = a_{hex}$, $b_{ortho} = a_{hex} + 2b_{hex}$ and $c_{ortho} = c_{hex}$. Therefore, $a_{ortho} = b_{ortho}/\sqrt{3}$ in an undistorted cell. The P2-P'2 phase transition occurs at the same sodium content in both compositions during the first discharge due to the similar concentration of Mn^{3+} ions. The *operando* XRD analysis shows the presence of both P2 and P'2 phases in $Na_x[Mn_{0.5}Fe_{0.5}]O_2$ at low voltage (< 2.1 V), whereas $Na_x[Mn_{0.65}Fe_{0.20}Ni_{0.15}]O_2$ completely converts to P'2 phase at ≈ 2.0 V upon discharge. **Figure 4.6** (green markers) shows that the orthorhombic distortion increases (*i.e.*, the b_{ortho}/a_{ortho} ratio deviates progressively from $\sqrt{3}$) as more sodium ions are intercalated into the structure and concentration of Mn^{3+} ions increases. However, the lattice parameters of $Na_x[Mn_{0.5}Fe_{0.5}]O_2$ do not show any significant evolution in the P'2 domain, as expected for a two-phase mechanism.

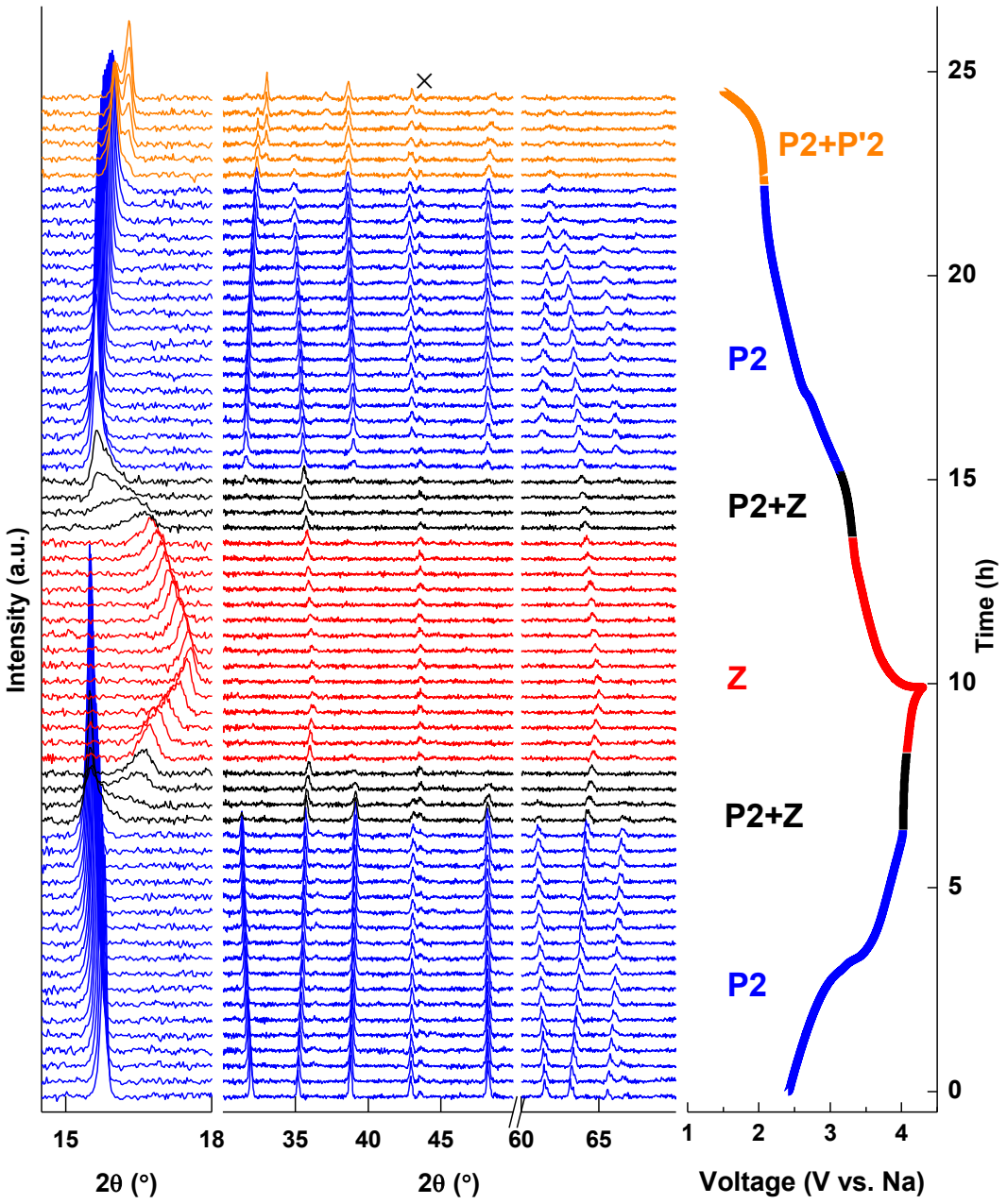

Figure 4.3 *Operando* XRD data recorded during galvanostatic cycling of $Na_{0.67}[Mn_{0.5}Fe_{0.5}]O_2$ at a rate of C/20 (left) along with illustration of the voltage profile of the cell (right) for the first cycle. The XRD patterns are color-coded with respect to the electrochemical profile on the right to reflect the structural composition of the positive electrode material. The sign × marks the diffraction peak from iron in the cell.

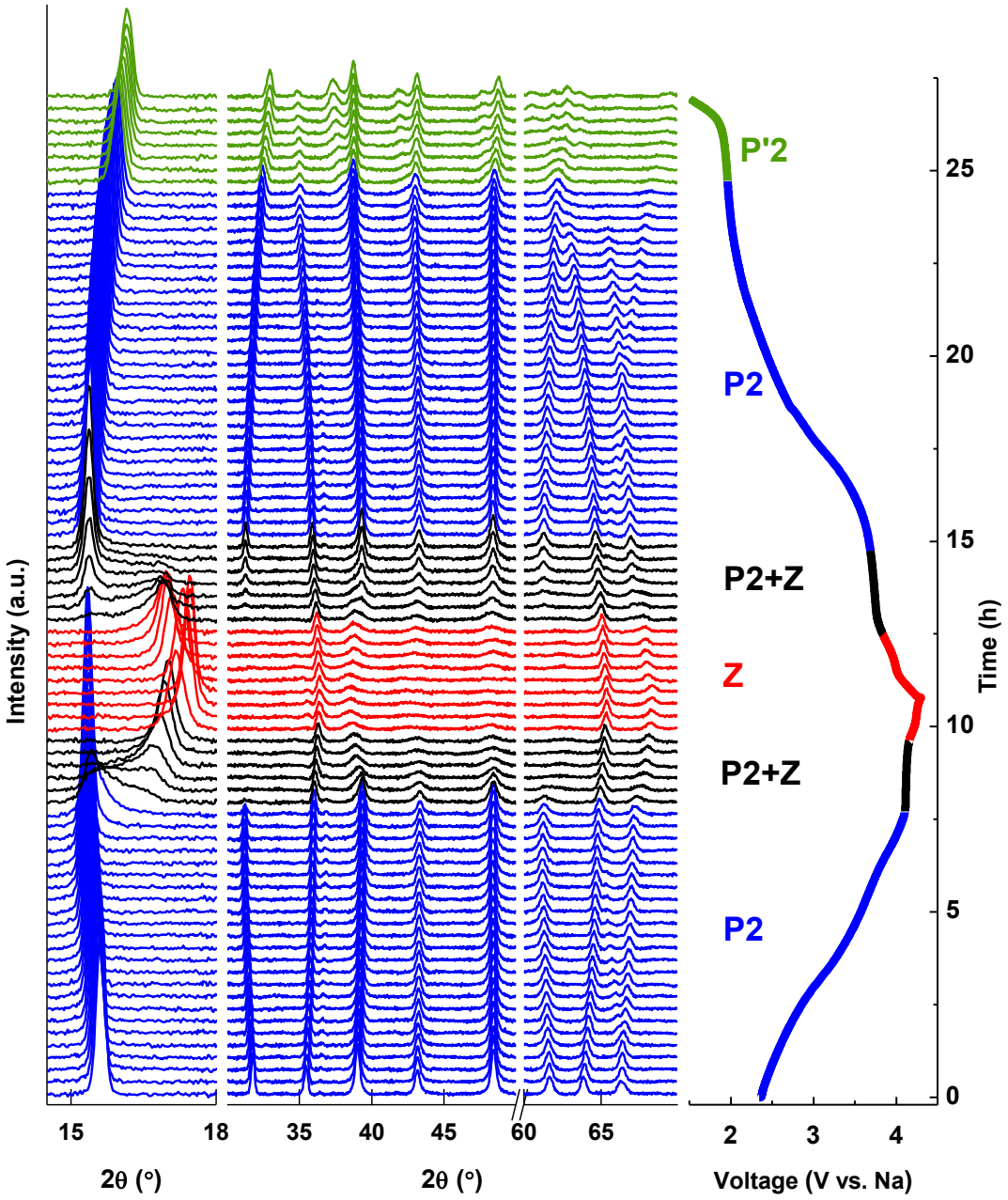

Figure 4.4 *Operando* XRD data recorded during galvanostatic cycling of $Na_{0.67}[Mn_{0.65}Fe_{0.20}Ni_{0.15}]O_2$ at a rate of C/20 (left) along with illustration of the voltage profile of the cell (right) for the first cycle. The XRD patterns are color-coded with respect to the electrochemical profile on the right to reflect the structural composition of the positive electrode material.

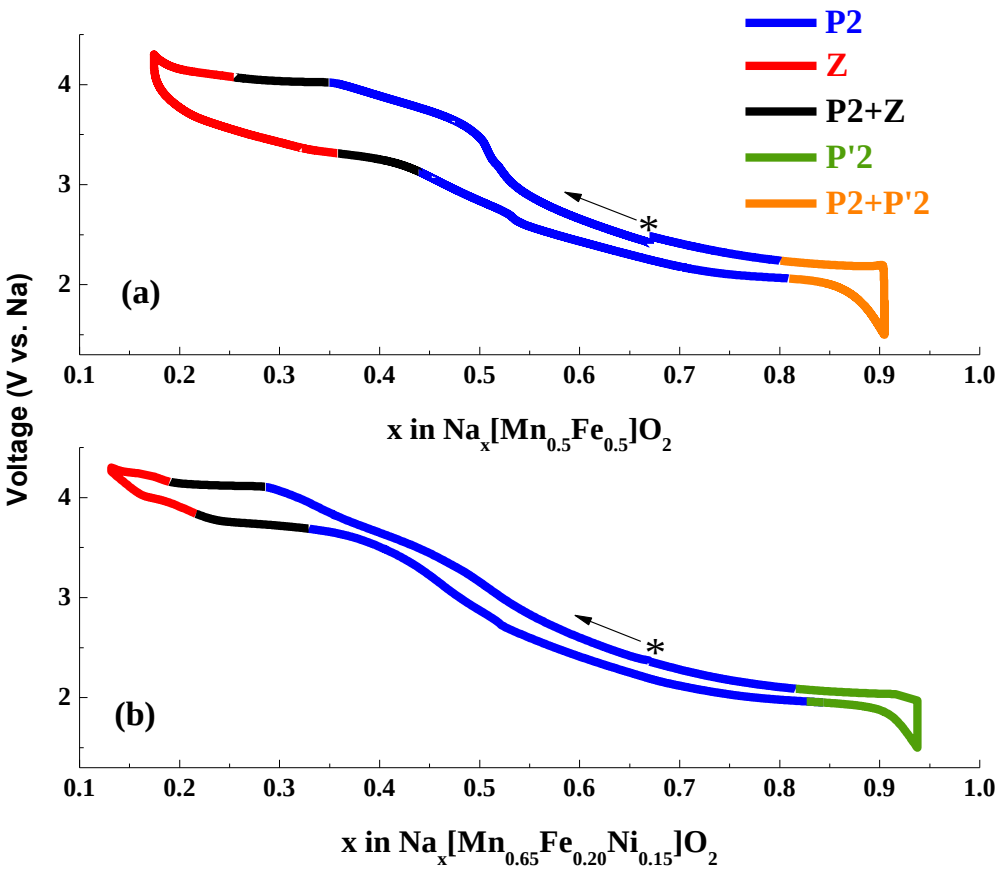

Figure 4.5 Phase evolution within $Na_{0.67}[Mn_{0.5}Fe_{0.5}]O_2$ (a) and $Na_{0.67}[Mn_{0.65}Fe_{0.20}Ni_{0.15}]O_2$ (b) as a function of the sodium content during the first cycle. The sign * shows the starting point of cycling.

P2-Z transition. When $Na_x[Mn_{0.5+y}Fe_{0.5-2y}Ni_y]O_2$ (y = 0, 0.15) is charged vs. Na in an electrochemical cell, a new phase is formed at high voltage (at 4.0 V for y = 0, at 4.1 V for y = 0.15) that shows weak and broad diffraction peaks. The structure of this phase cannot be solved by conventional diffraction techniques due to the low crystallinity of the phase. The *operando* experiment clearly demonstrate that the (100) and (110) reflections (located at $2\theta \approx 36^\circ$ and 65°, respectively, in **Figure 4.3** and **Figure 4.4**) are preserved as the P2 structure converts to the high voltage phase (Z phase), whereas (hkl) reflections

with $l \neq 0$ (any other peaks in **Figure 4.3** and **Figure 4.4**) broaden evidently. These evolutions of XRD patterns revealed by *operando* experiment implies the destruction of long range order along the *c*-axis at high voltage, but very little change within the MO_2 layer. Komaba *et al.*[53] proposed an indexation in $P\bar{6}m2$ space group for charged $Na_x[Mn_{0.5}Fe_{0.5}]O_2$ structure, compatible with the OP4 structure comprised of alternate stacking of O and P-type layers. However, the pair distribution function (PDF) analysis of the high voltage phase does not support an OP4 structure (see below). Delmas *et al.*[57] referred to the high voltage phase of charged $Na_x[Mn_{0.5}Fe_{0.5}]O_2$ as "Z phase" because of the uncharacterized nature of its structure. We follow Delmas's nomenclature in this study.

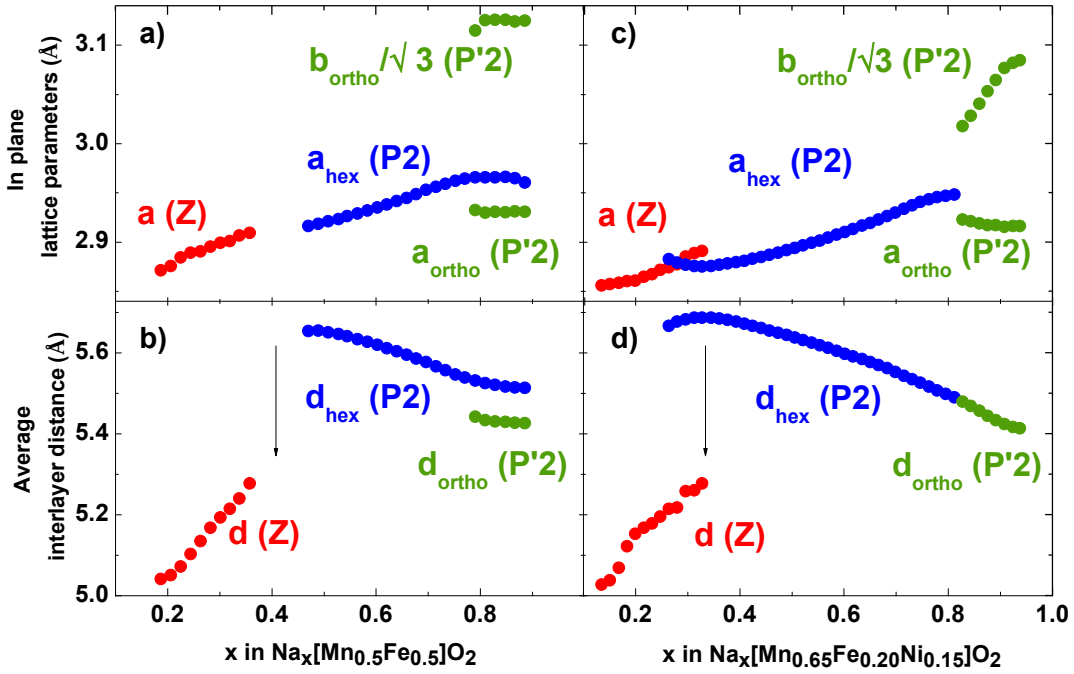

Figure 4.6 Evolution of lattice parameters, in-plane (a),(c) and out of plane (b),(d) of $Na_{0.67}[Mn_{0.5}Fe_{0.5}]O_2$ (a),(b) and $Na_{0.67}[Mn_{0.65}Fe_{0.20}Ni_{0.15}]O_2$ (c),(d) as a function of sodium content during the first discharge.

The shift in the position of (002) peak from 2θ ≈ 15° to ≈ 17° shows an important contraction of the interlayer distance in the transition from the P2 to Z phase. **Figure 4.6** (red markers) demonstrates the evolution of lattice parameters of the Z phase calculated using a hexagonal cell ($P\bar{6}m2$ space group). The abrupt decease in the interlayer spacing in transition from the P2 to Z phase can be explained by a transition from a P-type to an O-type structure, because in a P stacking type structure the oxygen atom of neighboring MO_2 layers are aligned with each other along the *c*-axis, whereas they are not in an O stacking type structure. However, the progressive contraction of the interlayer spacing of the Z phase with deintercalation of sodium ions is opposite to the expected trend in the layered structures. This observed trend indicates that at high voltage, a mechanism is involved that increases the interlayer interaction. The P2-Z phase transition occurs at different sodium content during the first charge of two studied compositions, *i.e.*, $Na_{0.35}[Mn_{0.5}Fe_{0.5}]O_2$ and $Na_{0.29}[Mn_{0.65}Fe_{0.20}Ni_{0.15}]O_2$, implying that the mechanism involved in high voltage modifications depend on the chemical composition of the oxide.

4.3.3 Study of High Voltage Z-Phase

4.3.3.1 Pair Distribution Function (PDF) Analysis

The conventional diffraction techniques cannot provide much information about the structure of the Z phase due to its poor crystallinity. However, pair distribution function (PDF) analysis is a powerful technique for characterization of the local structure of non-crystalline and crystalline materials. PDF presents the probability of finding any pair of atoms at a specific interatomic distance, regardless of crystallinity of the structure. The PDF technique has been successfully employed for the characterization of complex battery materials. [117-119]

Because of the sensitivity of the PDF technique to amorphous phases, chemically oxidized samples were prepared for this study to prevent any interference that would arise from the additive carbon and binder in composite electrode materials. Pristine $Na_{0.67}[Mn_{0.5}Fe_{0.5}]O_2$ and $Na_{0.67}[Mn_{0.65}Fe_{0.20}Ni_{0.15}]O_2$

materials were mixed with an excess amount of NO_2BF_4 in acetonitrile and fully washed (by acetonitrile) and dried after 2 days inside a glovebox. The extraction of sodium in the oxidized samples were confirmed by inductively coupled plasma (ICP) spectroscopy.

A full description of the PDF analysis of Z-$Na_{0.14}[Mn_{0.5}Fe_{0.5}]O_2$ and Z- $Na_{0.1}[Mn_{0.65}Fe_{0.20}Ni_{0.15}]O_2$ are presented in reference 56, and only the conclusions are mentioned here. The comparison of the PDF curves of P2-$Na_{0.67}[Mn_{0.5}Fe_{0.5}]O_2$ and Z-$Na_{0.14}[Mn_{0.5}Fe_{0.5}]O_2$ revealed three important facts: (i) The peak assigned to the first neighbor M-O distance is neither split nor broadened in the PDF curve of the Z-phase. (ii) The intense peaks assigned to the interlayer M-M distances in the pristine phase disappear in the PDF curve of the oxidized sample. (iii) The peak representing the first neighbor in-plane M-M distance in the pristine phase split in the PDF curve of the Z phase, whereas the M-O distances remain in the Z phase. The observation (i) indicates that the PDF analysis does not show any evidence of cooperative distortion of Jahn-Teller active Fe^{4+} ions in the Z phase and therefore rules out Jahn-Teller stabilization of Fe^{4+} as a driving force of the structural transition at high voltage, in contrary to the low voltage phase transition that is triggered by Jahn-Teller stabilization of Mn^{3+} ions. The observation (ii) illustrates the complete destruction of long-range correlation along the *c*-axis. The observation (iii) implies the modification of the hexagonal packing of transition metal layers and can be explained by displacement of transition metal atoms along *c*-axis.

The best fit for the experimental PDF data of Z-$Na_{0.14}[Mn_{0.5}Fe_{0.5}]O_2$ and Z-$Na_{0.1}[Mn_{0.65}Fe_{0.20}Ni_{0.15}]O_2$ were achieved for a supercell made up of MO_2 bilayers. This model is referred to as “bi-layer model”. The position of bilayers in the supercell was randomized in the *ab*-plane. Each bilayer upholds the O2 oxygen stacking scheme, and some transition metals are accommodated in the tetrahedral sites available between two adjacent MO_2 layers (**Figure 4.7**). The best agreement with the experimental PDF data was obtained for 1/8 and 1/32 transition metals accommodated in the tetrahedral sites in Z-$Na_{0.14}[Mn_{0.5}Fe_{0.5}]O_2$ and Z- $Na_{0.1}[Mn_{0.65}Fe_{0.20}Ni_{0.15}]O_2$, respectively.

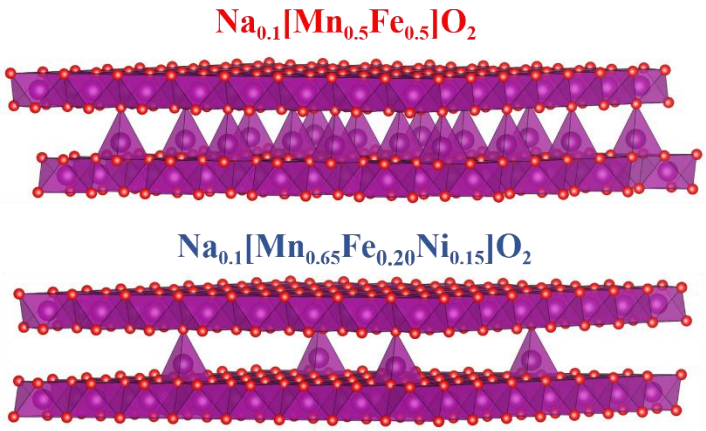

Figure 4.7 Representation of the bilayer models used to fit the PDF curves of $Na_{0.1}[Mn_{0.5}Fe_{0.5}]O_2$ and $Na_{0.1}[Mn_{0.65}Fe_{0.20}Ni_{0.15}]O_2$. The fitting of the PDF data showed mitigated migration of transition metals into the tetrahedral sites of the interlayer space in the Ni-substituted sample.

4.3.3.2 Mössbauer Spectroscopy

The pristine and deintercalated $Na_x[Mn_{0.5+y}Fe_{0.5-2y}Ni_y]O_2$ (y = 0, 0.10, 0.15) materials were studied by ^{57}Fe Mössbauer spectroscopy for further investigation of the high voltage phase transition. The deintercalated samples were recovered from the composite electrodes in the electrochemical cells that were charged to 4.3 V and then disassembled in an Ar-filled glovebox. The spectra of the pristine materials (x = 0.67, **Figure 4.8 a-c**) and the fully charged materials (x ≈ 0.15, **Figure 4.8 d-f**) were recorded at room temperature.

The pristine samples show similar spectra composed of a single sharp doublet with an isomer shift (IS) of ≈ 0.24 $mm.s^{-1}$ and a quadrupole splitting (QS) of ≈ 0.73 $mm.s^{-1}$ (**Table 4.2**), consistent with Fe^{3+} in an octahedral environment. The spectra of charged samples demonstrate asymmetry in the doublets, with more spectral weight shifted to negative velocity. This effect is more evident in the spectrum of $Na_{0.15}[Mn_{0.5}Fe_{0.5}]O_2$ than that of $Na_{0.15}[Mn_{0.65}Fe_{0.20}Ni_{0.15}]O_2$. The spectra of the charged materials (x ≈ 0.15, **Figure 4.8 d-f**) were fitted using three components (**Table 4.2**). The main component is assigned

to $Fe^{3+}O_6$ in an octahedral environment and has a similar isomer shift and quadrupole splitting values compared to its pristine counterpart. The second component with an isomer shift of 0.17 $mm.s^{-1}$ and a large quadrupolar splitting of ≈ 1.5 $mm.s^{-1}$ is assigned to $Fe^{3+}O_4$ (tetrahedral coordination) owing to the non-centrosymmetry of its ligand environment. The third component with an isomer shift close to zero and a quadrupole splitting of ≈ 0.7 $mm.s^{-1}$ is consistent with $Fe^{4+}O_6$ in sodium layered oxides.[11,49,62,120]

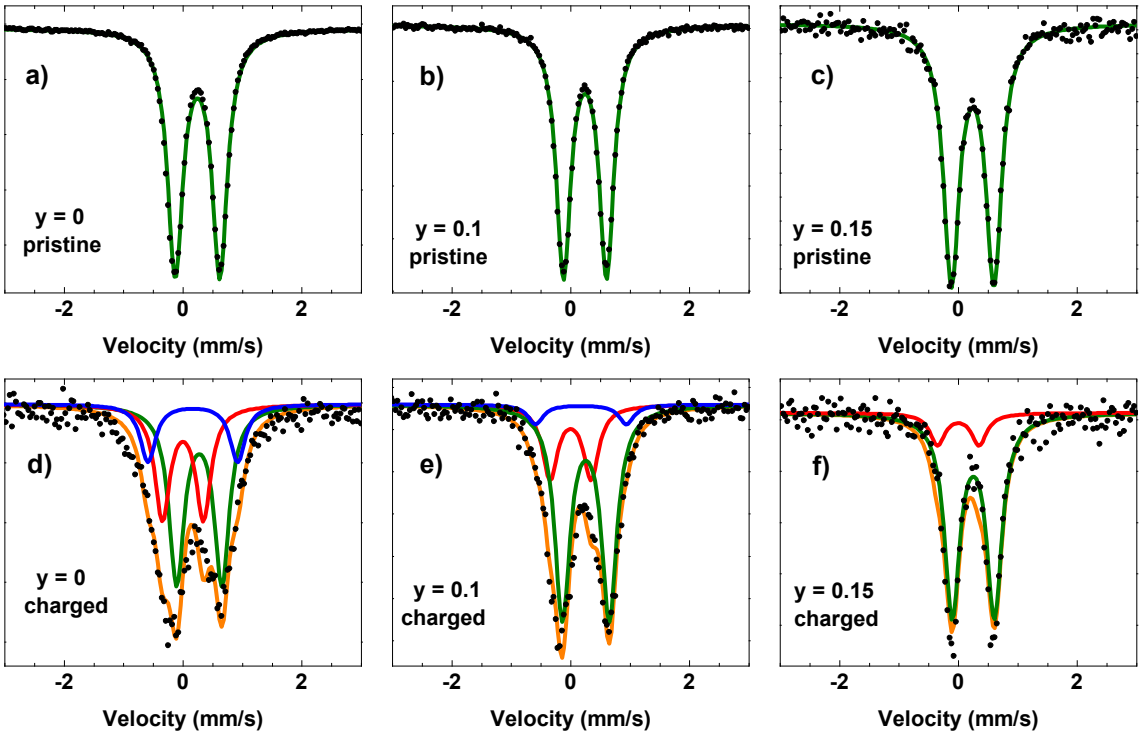

Figure 4.8 ^{57}Fe Mössbauer spectra of $Na_x[Mn_{0.5+y}Fe_{0.5-2y}Ni_y]O_2$ pristine (a-c) and charged to 4.3 V (d-f) for y = 0 (a and d), y = 0.1 (b and e), and y = 0.15 (c and f). Raw data is shown in black. Individual spectral components of $Fe^{3+}O_6$, $Fe^{3+}O_4$ and $Fe^{4+}O_6$ from fitting are shown in green, blue, and red. The sum of all spectral components results in the orange curves.

Table 4.2 Parameters resulting from fitting of ^{57}Fe Mössbauer spectra of $Na_x[Mn_{0.5+y}Fe_{0.5-2y}Ni_y]O_2$ (y = 0, 0.1, 0.15); pristine and charged to 4.3 V.

y in $Na_x[Mn_{0.5+y}Fe_{0.5-2y}Ni_y]O_2$		**Component**	**IS (mm/s)**	**QS (mm/s)**	**% Area**
y = 0.00	pristine	$Fe^{3+}O_6$	0.25	0.75	100.0
	charged	$Fe^{3+}O_6$	0.28	0.76	50.9
		$Fe^{3+}O_4$	0.17	1.51	16.6
		$Fe^{4+}O_6$	0.00	0.69	32.5
y = 0.10	pristine	$Fe^{3+}O_6$	0.24	0.73	100.0
	charged	$Fe^{3+}O_6$	0.26	0.79	69.5
		$Fe^{3+}O_4$	0.17	1.53	6.5
		$Fe^{4+}O_6$	0.00	0.69	24.0
y = 0.15	pristine	$Fe^{3+}O_6$	0.24	0.72	100.0
	charged	$Fe^{3+}O_6$	0.25	0.71	84.2
		$Fe^{4+}O_6$	0.00	0.70	15.8

The data shows that the refined ratio of $Fe^{4+}O_6$ (**Table 4.2**) is systematically lower than what is expected for $Na_{0.15}[Mn_{0.5+y}Fe_{0.5-2y}Ni_y]O_2$ according to a simple, purely ionic model, *i.e.*, 70%, 50% and 25% respectively for y = 0, 0.1, 0.15, assuming that all the manganese and nickel ions are oxidized to tetravalent, *i.e.*, $Na_{0.15}[Mn^{4+}_{0.5}Fe^{4+}_{0.35}Fe^{3+}_{0.15}]O_2$, $Na_{0.15}[Mn^{4+}_{0.60}Fe^{4+}_{0.15}Fe^{3+}_{0.15}Ni^{4+}_{0.10}]O_2$, and $Na_{0.15}[Mn^{4+}_{0.65}Fe^{4+}_{0.05}Fe^{3+}_{0.15}Ni^{4+}_{0.15}]O_2$. This important discrepancy indicates that the charge compensation mechanism at high voltage is more complex than the straightforward oxidation of Fe^{3+} to Fe^{4+}. Moreover, the X-ray absorption spectroscopy (XAS) of P2-$Na_x[Mn_{0.5}Fe_{0.5}]O_2$ reported by Komaba *et al.*[53] illustrated evident shift in the position of the spectrum at the Mn K-edge from the pristine material to the charge one, but no shift was observed in the position of the spectrum at the Fe K-edge and only the absorption maxima were affected.

Yamada *et al.* [49] have proposed the important role of ligand-to-metal charge transfer (LMCT) in the electrochemical properties of layered sodium metal oxides. Moreover, electron transfer from oxygen p orbitals to iron d orbitals is demonstrated in Fe^{4+} containing perovskite structures such as $CaFeO_3$ and $SrFeO_3$.[121-123] The Fe^{4+} oxidation state can be stabilized by transferring electrons from oxide ions. A similar mechanism is proposed to be involved in the case of $Na_{0.15}[Mn_{0.5+y}Fe_{0.5-2y}Ni_y]O_2$ materials. The electron transfer from oxygen anions to iron atoms weakens the chemical bonding of the surrounding metal atoms, facilitating their migration out of MO_2 plane that was identified by PDF analysis.

The fitting of Mössbauer spectra revealed that the concentration of iron atoms in tetrahedral coordination decreases from 16.6% in $Na_{0.15}[Mn_{0.5}Fe_{0.5}]O_2$ to 6.5 % in $Na_{0.15}[Mn_{0.6}Fe_{0.3}Ni_{0.1}]O_2$ (**Table 4.2**). The signal corresponding to the tetrahedrally coordinated iron atoms was probably too small to be refined for $Na_{0.15}[Mn_{0.65}Fe_{0.20}Ni_{0.15}]O_2$, in agreement with the lower concentration of tetrahedral species illustrated by PDF analysis. On the other hand, detecting no $Fe^{3+}O_4$ in $Na_{0.15}[Mn_{0.65}Fe_{0.20}Ni_{0.15}]O_2$ might be due to the preferred migration of Mn^{4+} ions rather than Fe^{3+} ions. Fe^{4+} and Ni^{4+} are usually not found in tetrahedral coordination, but cannot be completely ruled out.

4.3.3.3 Discussion of the Mechanism

Based on the combination of *operando* XRD experiment, PDF analysis, and Mössbauer spectroscopy, The following mechanism for the deintercalation of P2-$Na_x[Mn_{0.5+y}Fe_{0.5-2y}Ni_y]O_2$ electrode materials is proposed; the formation of Fe^{4+} species is stabilized by transfer of electrons from the oxygen orbitals. The hybridization of iron with oxygen orbitals weaken the bonding of neighboring atoms and results in the migration of transition metals, mostly Fe^{3+} ions, out of the MO_2 planes. High concentrations of sodium vacancies and the interaction of the migrated atom with adjacent MO_2 layers induce gliding of the layers and the formation of an O2-type oxygen stacking scheme in the bi-layer model with available tetrahedral sites. The increased number of migrated atoms into the interlayer tetrahedral sites driven by

extraction of sodium ions explains the contraction of interlayer space over the Z phase domain during charge.

As the Fe ions in $Na_x[Mn_{0.5}Fe_{0.5}]O_2$ are substituted by Mn/Ni, fewer atoms are affected by this mechanism, owing to the lower concentration of Fe^{4+} ions. A lower concentration of migrated atoms out of the MO_2 plane is consistent with the delay of P2-Z transition in $Na_x[Mn_{0.65}Fe_{0.20}Ni_{0.15}]O_2$ compared to $Na_x[Mn_{0.5}Fe_{0.5}]O_2$ and the lower polarization in the voltage profiles of nickel substituted samples, meaning that lower energy is required for reversibility of the transition (**Figure 4.2**).

It is worth noting that for O3-$NaFeO_2$, a degradation mechanism triggered by the migration of some Fe^{3+} ions into tetrahedral sites at high voltage is proposed based on *ex-situ* XRD and XAS studies.[4] The important difference in the high voltage degradation mechanism of O3-$NaFeO_2$ and P2-$Na_{0.67}[Mn_{0.5+y}Ni_yFe_{0.5-2y}]O_2$ is the reversibility of the transition; the charge capacity of O3-$NaFeO_2$ increases by the increase of the cut-off voltage, whereas the reversible capacity highly diminishes by the expansion of cut-off voltage higher than 3.5 V, indicating the irreversibility of its high voltage structural modifications. However, the high voltage and low voltage phase transitions in the P2-$Na_{0.67}[Mn_{0.5+y}Ni_yFe_{0.5-2y}]O_2$ are reversible proven by the perfect overlap of the lattice parameters as a function of the sodium content during the first and second charge (shown for $Na_x[Mn_{0.65}Fe_{0.20}Ni_{0.15}]O_2$ in **Figure 4.9**).

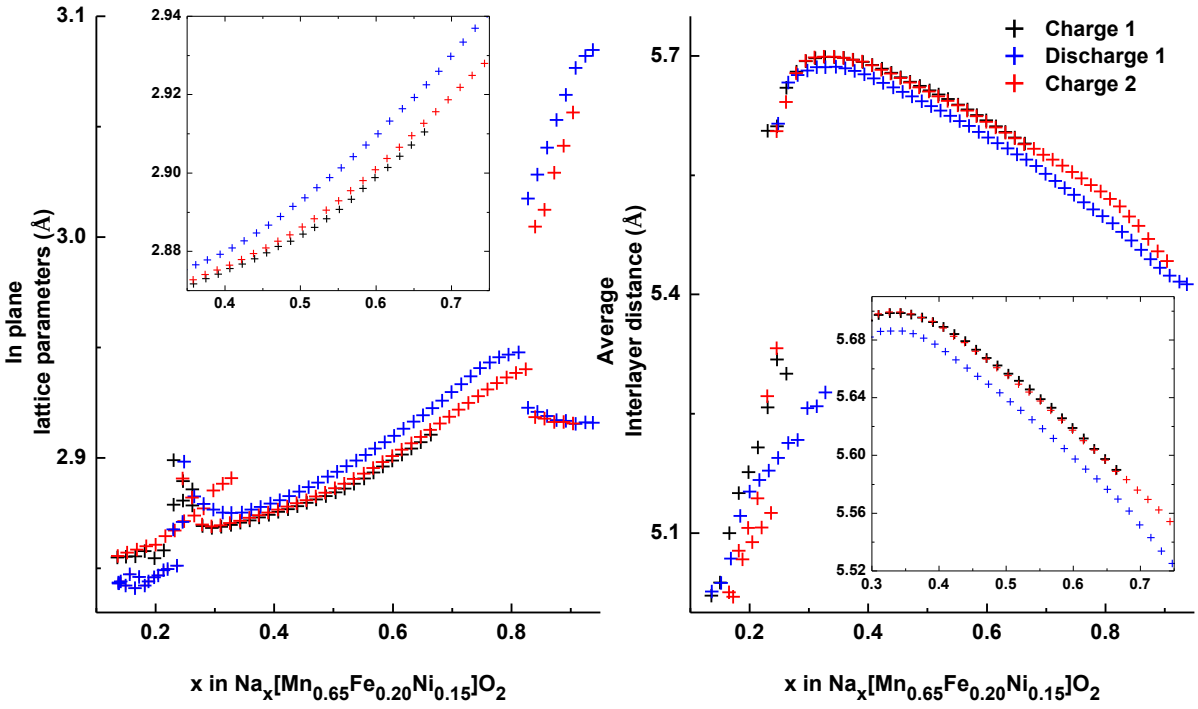

Figure 4.9 Evolution of in-plane lattice parameters (left) and average interlayer distance (right) of $Na_x[Mn_{0.65}Fe_{0.20}Ni_{0.15}]O_2$ as a function of the sodium content for the first cycle and the second charge. Parameters and phase domains are not labeled for clarity and can be found in Figure 4.6. The insets show expanded views of the stability domain of the P2 phase, highlighting the perfect overlap of the lattice parameters over the first and second charge.

4.3.4 Electrochemistry: Effect of Structural Transitions on Cycling

4.3.4.1 Effect of Voltage Window on Capacity

Structural transitions induced by insertion/extraction of sodium ions during discharge/charge cause changes in crystallographic cell volume, imposing mechanical stress on the material. These structural modifications results in the energy fading of electrode materials when charged and discharged in a wide range of voltage. Phase transitions occurs in many layered sodium metal oxides when cycled, which is why electrode degradation is an important drawback with these materials. P2-$Na_{0.67}[Mn_{0.5}Fe_{0.5}]O_2$ is a promising positive electrode material owing to its relatively wide range of P2 stability domain.

Moreover, *Operando* XRD analysis showed that the substitution of nickel increases the stability domain of the P2 phase.

The effect of phase transitions on the electrochemical performance of $Na_x[Mn_{0.5}Fe_{0.5}]O_2$ and $Na_x[Mn_{0.65}Fe_{0.2}Ni_{0.15}]O_2$ was investigated by cycling each material in four different voltage ranges, at which both the P2-Z and P2-P′2 phase transitions occur (**Figure 4.10**, dark cyan), only the P2-Z phase transition is allowed (**Figure 4.10**, red), only the P2-P′2 phase transition happens (**Figure 4.10**, blue), and no phase transition occurs (**Figure 4.10**, green). *Operando* XRD experiments show that the P2 phase is preserved in the $Na_x[Mn_{0.5}Fe_{0.5}]O_2$ and $Na_x[Mn_{0.65}Fe_{0.2}Ni_{0.15}]O_2$ materials when the cutoff voltage is limited to 2.1- 4.0 V and 2.0 - 4.1V, respectively (**Figure 4.5**).

Figure 4.10 illustrates that preventing the formation of the orthorhombic P'2 phase does not impact significantly the low voltage polarization. Therefore, the low voltage polarization can be related to intrinsic properties of the P2 phase such as the sodium mobility. On the other hand, when the cutoff voltage is limited so that the formation of the Z phase is avoided, the high-voltage polarization substantially decreases, indicating that the high voltage polarization is related to the energy required to convert the Z phase back to the P2 phase. When cycled at the stability domain of the P2-phase, the voltage profile of $Na_x[Mn_{0.5}Fe_{0.5}]O_2$ shows slightly larger polarization at x = 0.50 compared to $Na_x[Mn_{0.65}Fe_{0.2}Ni_{0.15}]O_2$. The polarization around the potential jump at the voltage profile of the $Na_x[Mn_{0.5}Fe_{0.5}]O_2$ was attributed to the decrease in electronic conductivity due to the absence of transition metals with a mixed valence state.[57] The absence of that polarization in the voltage profile of $Na_x[Mn_{0.65}Fe_{0.2}Ni_{0.15}]O_2$ cycled over the P2 Phase stability domain indicates that the material remains electronically conductive over the whole cycling range.

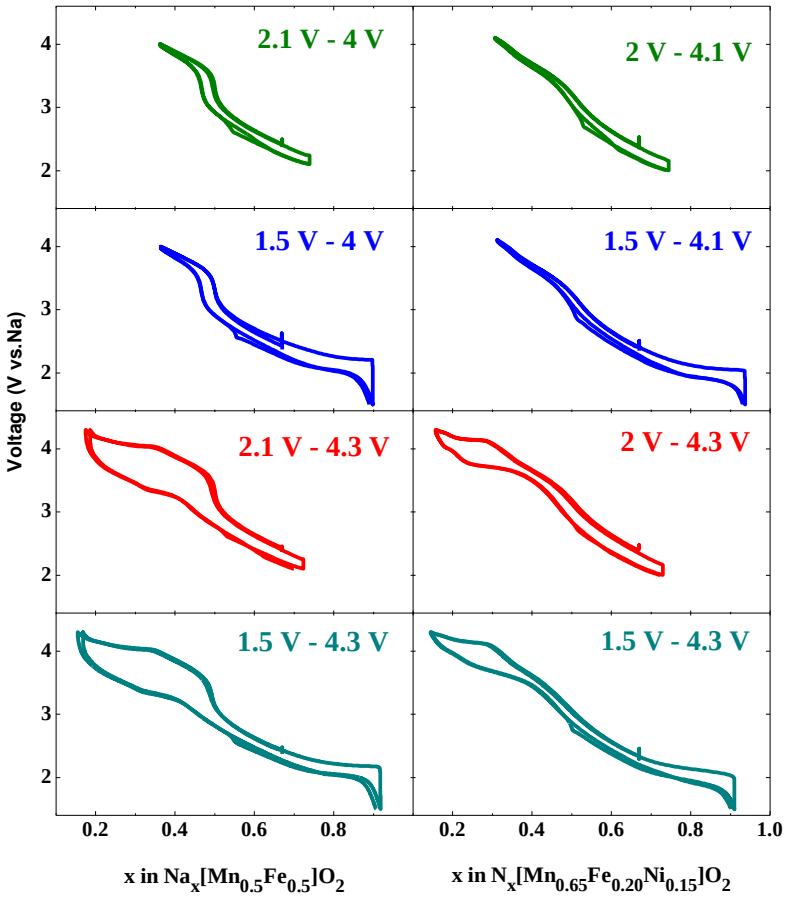

Figure 4.10 The galvanostatic charge/discharge profile of $Na_{0.67}[Mn_{0.5}Fe_{0.5}]O_2$ and $Na_{0.67}[Mn_{0.65}Fe_{0.20}Ni_{0.15}]O_2$ cycled at C/20 in different voltage windows.

4.3.4.2 Improving the Specific Energy

Figure 4.11 shows the specific capacity (a,b) and specific energy (c,d) delivered by $Na_{0.67}[Mn_{0.5}Fe_{0.5}]O_2$ (a,c) and $Na_{0.67}[Mn_{0.65}Fe_{0.20}Ni_{0.15}]O_2$ (b,d) cycled within four different voltage ranges at the rate of C/20 over 30 cycles. Because the structural modifications affect the polarization in addition to the capacity, energy retention is a more relevant parameter to study the cycling performance of the materials rather than capacity retention. **Figure 4.12** shows the evolution of columbic efficiency of the cells cycled

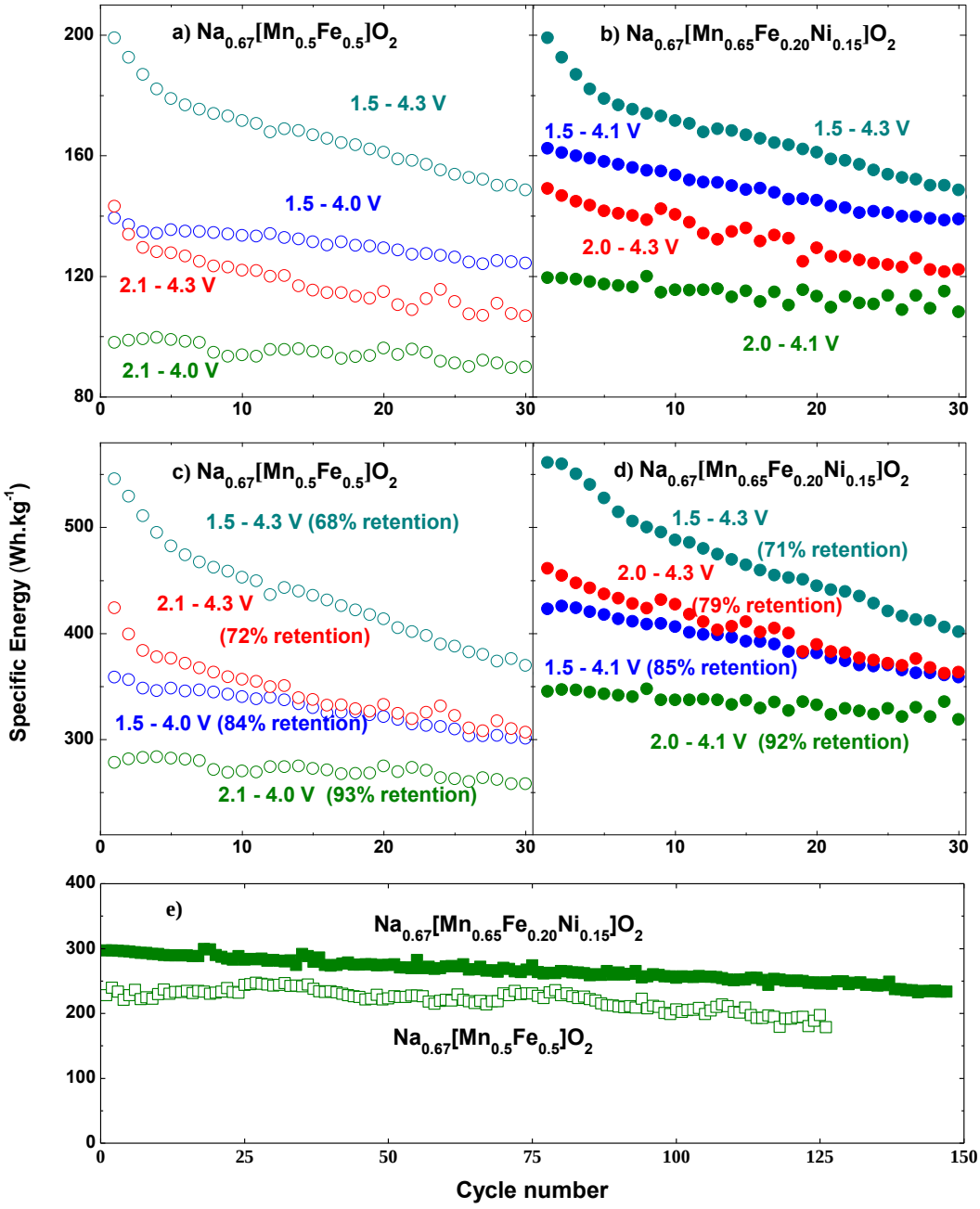

Figure 4.11 Specific capacity (a,b) and specific energy (c,d) of $Na_{0.67}[Mn_{0.5}Fe_{0.5}]O_2$ (a,c) and $Na_{0.67}[Mn_{0.65}Fe_{0.20}Ni_{0.15}]O_2$ (b,d) as a function of cycle number, cycled at C/20 within different voltage windows. Specific energy of $Na_{0.67}[Mn_{0.5}Fe_{0.5}]O_2$ and $Na_{0.67}[Mn_{0.65}Fe_{0.20}Ni_{0.15}]O_2$ cycled at C/10 in the 2.1 - 4.0 V and 2.0 - 4.1 V window, respectively; energy fade rate for the latter is 0.13% per cycle (c).

within the extended (1.5 - 4.3 V) and the limited (P2 phase stability domain) voltage ranges. Coulombic efficiency is defined here as the ratio of charge capacity to the preceding discharge capacity. The cells cycled within 1.5 - 4.3 V voltage window show poor coulombic efficiencies over the first five cycles, which is reflected in their pronounced fading (**Figure 4.11 a-d**). However, Coulombic efficiencies are within 1 ± 0.5% range from cycle 6 to 30. The accuracy of the measured charge values in this study is ~ 0.5%. More accurate measurement of charge values by high precision instruments is necessary for attributing Coulombic efficiency of the cells to their electrochemical performance.

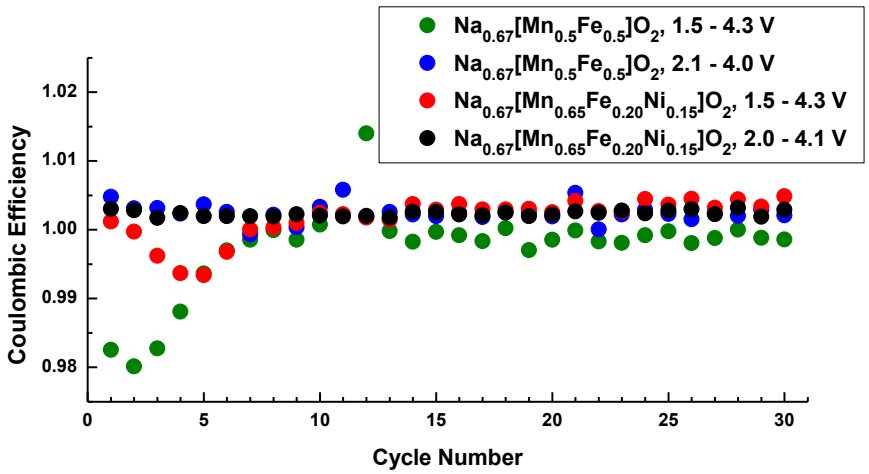

Figure 4.12 Coulombic efficiency of $Na_{0.67}[Mn_{0.5}Fe_{0.5}]O_2$ and $Na_{0.67}[Mn_{0.65}Fe_{0.20}Ni_{0.15}]O_2$ cycled over P2- phase region and the full voltage range of 1.5 - 4.3 V at the rate of C/20.

$Na_{0.67}[Mn_{0.5}Fe_{0.5}]O_2$ and $Na_{0.67}[Mn_{0.65}Fe_{0.20}Ni_{0.15}]O_2$ show about 70 % specific energy retention after 30 cycles when cycled within 1.5 - 4.3 V. Avoiding the formation of orthorhombic P'2 phase slightly enhances the specific energy retention. However, when the high voltage P2-Z phase transition is prevented, the energy retention is increased by about 15 %. Beyond 90% of specific energy is retained after 30 cycles when the phase transitions are avoided by limiting the cutoff voltage. Within the same voltage range and with twice current rate (C/10 or 26 $mA.g^{-1}$), the $Na_{0.67}[Mn_{0.65}Fe_{0.20}Ni_{0.15}]O_2$ cell exhibited ≈ 80 % energy retention over 150 cycles (**Figure 4.11**). It should be noted that the electrodes

were not optimized and were cycled vs. sodium metal; considering that, $Na_{0.67}[Mn_{0.65}Fe_{0.20}Ni_{0.15}]O_2$ exhibits promising performance for further development of positive electrode material for NIBs.

These results show that limiting the cut-off voltage is a greatly effective approach to increase the cycle life of P2-$Na_{0.67}[Mn_{0.5+y}Fe_{0.5-2y}Ni_y]O_2$, at the expense of energy loss, however. P2-$Na_{0.67}[Mn_{0.65}Fe_{0.20}Ni_{0.15}]O_2$ delivers only ≈ 3% higher specific energy compared to P2-$Na_{0.67}[Mn_{0.5}Fe_{0.5}]O_2$ when cycled in 1.5 - 4.3 V window (561 $Wh.kg^{-1}$ vs. 545 $Wh.kg^{-1}$ on the first discharge). However, when cycled within the P2-stability domain, the specific energy obtained from P2-$Na_{0.67}[Mn_{0.65}Fe_{0.20}Ni_{0.15}]O_2$ is 25% higher than that of P2-$Na_{0.67}[Mn_{0.5}Fe_{0.5}]O_2$ (345 Wh kg^{-1} vs. 278 $Wh.kg^{-1}$), owing to the extended range of the P2 region in the nickel substituted composition.

4.4 Conclusions

Here, a comparative study of structural evolution induced in P2-$Na_{0.67}[Mn_{0.5}Fe_{0.5}]O_2$ and P2-$Na_{0.67}[Mn_{0.65}Fe_{0.20}Ni_{0.15}]O_2$ upon (de)intercalation of sodium ions is presented. *Operando* X-ray diffraction experiments showed that both compositions maintain the P2 phase over a wide range of stoichiometry, transform to a P'2 orthorhombic phase induced by cooperative Jahn-Teller distortion of Mn^{3+} cations at low voltage, and convert to a poor crystalline disordered phase, Z phase, at high voltage. Pair distribution function analysis showed the destruction of long-range order along *c*-axis and the migration of transition metal ions out of MO_2 planes. In contrast to O3-$NaFeO_2$ [4] and $NaCrO_2$[124], for which a similar degradation mechanism at high voltage was proposed, the migration of transition metals are reversible in $Na_x[Mn_{0.5+y}Ni_yFe_{0.5-2y}]O_2$, although results in significant voltage polarization.

The impact of both P2-P'2 and P2-Z phase transitions on the electrochemical performance of P2-$Na_{0.67}[Mn_{0.5}Fe_{0.5}]O_2$ and P2-$Na_{0.67}[Mn_{0.65}Fe_{0.20}Ni_{0.15}]O_2$ were investigated by adjusting the cycling voltage window. The high voltage phase transition cause a more significant destructive effect on the cycling performance of the cells. If both phase transitions are avoided by limiting the cutoff voltage,

92% specific energy is retained by P2-$Na_x[Mn_{0.65}Fe_{0.20}Ni_{0.15}]O_2$ after 30 cycles, showing a significant improvement to $\approx$ 71 % in 1.5 - 4.3 V range at C/20. This material maintains 80% of original specific energy after 150 cycles when cycled within 2.0 - 4.1 V at C/10. The detrimental P2-Z phase transition is delayed to slightly higher voltage when 60% of Fe^{3+} ions in $Na_{0.67}[Mn_{0.5}Fe_{0.5}]O_2$ are substituted by Mn^{4+}/Ni^{2+}, resulting in 25% energy boost when the cell is cycled within the P2 stability domain.

The concentrations of oxidized iron ions (Fe^{4+}) in charged $Na_x[Mn_{0.5+y}Fe_{0.5-2y}Ni_y]O_2$ samples detected by Mössbauer spectroscopy were lower than the values required to compensate the charge measured from electrochemical cells based on only cationic redox reactions. Electron transfer from oxygen to transition metal orbitals is proposed to be the driving force for the high voltage transition. Further studies are needed to fully understand the role of LMCT in these oxides.

Chapter 5

Structural Investigation and Electrochemical Evaluation of P2-$Na_{0.67}[Mn_{0.66}Fe_{0.20}Cu_{0.14}]O_2$ as the Positive Electrode for Na-ion Batteries

5.1 Introduction

Sodium ion battery (NIB) technology is considered as a promising alternative for lithium ion battery (LIB) for large-scale application, such as grid storage, where cost is a more important criterion than the volumetric and gravimetric energy density, due to the cost and resource availability concerns about lithium, whereas sodium has high abundance. Therefore, low cost and environmental impact are among important criteria of material design for NIBs. Various oxide compositions are investigated to accomplish high-performance electrode materials which offer a balance among different criteria: energy density, cyclability, rate capability, cost, and safety.[47,56,67,73,77] Layered oxide sodium host materials composed of low-cost and non-toxic transition metals, such as Mn and Fe, have been the focus of many studies and show auspicious performance.[53,57,63,62,65,112] Copper-based sodium metal oxides are promising owing to their cost and safety advantages and have been explored over only the last couple of years as potential positive electrode materials for Na battery based on $Cu^{2+/3+}$ redox activity. O3-$NaCuO_2$ was first reported by Takahashi *et al.*[125] to deliver a specific capacity of more than 140 $mAh.g^{-1}$ in the voltage range of 0.75 - 3.0 V, but with poor capacity retention (≈ 30 $mAh.g^{-1}$ at 15^{th} cycle). P2-$Na_{0.68}[Cu_{0.34}Mn_{0.66}]O_2$ and P2-$Na_{0.68}[Cu_{0.34}Mn_{0.50}Ti_{0.16}]O_2$ were investigated as positive electrode materials in Na half-cells and both showed specific capacities less than 70 $mAh.g^{-1}$ in the first cycle at the current rate of C/10.[126] In another study[127], O3-$Na_{0.9}[Cu_{1/4}Fe_{1/4}Mn_{1/4}Ti_{1/4}]O_2$ was reported

to deliver a specific capacity of 78 mAh.g^{-1} with a capacity retention of 60% after 90 cycles when cycled within 2.5 - 4 V at a rate of 1C. It was reported that P2-$Na_{2/3}[Cu_{1/3}Mn_{2/3}]O_2$[128] delivered a specific capacity of 67 mAh.g^{-1} at the first discharge in a Na half-cell cycled in the voltage range of 3.0 - 4.2 V at the rate of C/4 and survived after 1000 cycles with 61% of capacity retained. X-ray absorption spectroscopy revealed a charge compensation mechanism based on the $Cu^{2+/3+}$ redox couple, whereas manganese ions remained electrochemically inactive. In a different study, $Cu^{2+/3+}$ and $Fe^{3+/4+}$ ions were proved responsible for the redox activity of O3-$Na_{0.9}[Cu_{0.22}Fe_{0.30}Mn_{0.48}]O_2$.[129] In another recent research by Hu *et al*.,[70] P2-$Na_{7/9}[Cu_{2/9}Fe_{1/9}Mn_{2/3}]O_2$ was synthesized and studied. Excellent capacity retention (87% of initial 69 mAh.g^{-1} capacity was maintained after 150 cycles at the cycling rate of 1C), stability of the P2 structure over the potential window of 2.5 - 4.2 V, and air stability was reported for this material.

The studies mentioned above provide evidence of the promise and advantages that substitution of copper into layered sodium metal oxides may offer regarding cost reduction, safety, and the improvement of stability. However, further in-depth structural characterizations are required to understand the effect of substitution of copper in different sodium metal oxide systems on their phase transitions during charge/discharge, the reactivity to the ambient atmosphere, and charge compensation mechanisms. Clear insight into these issues is necessary to optimize the composition for obtaining suitable stability with minimum compromise on the energy density. The study on the positive effect of substitution of Mn^{4+}/Ni^{2+} for Fe^{3+} on the structural stability and electrochemical performance of P2-$Na_{2/3}[Mn_{1/2}Fe_{1/2}]O_2$ are presented in Chapter 4. In the study presented in this chapter, P2-$Na_{0.67}[Mn_{0.66}Fe_{0.20}Cu_{0.14}]O_2$, a composition close to $Na_{0.67}[Mn_{0.65}Ni_{0.15}Fe_{0.20}]O_2$, was synthesized to systematically investigate the effect of substitution of copper for nickel. Air stability, electrochemical performance, and the structural evolution during charge/discharge are described.

5.2 Experimental

Synthesis. P2-$Na_{0.67}[Mn_{0.66}Fe_{0.20}Cu_{0.14}]O_2$ was synthesized by a solid state method. A mixture of stoichiometric amounts of Na_2CO_3 (EMD Millipore, ≥99.5%), Mn_2O_3 (Sigma-Aldrich, 99, %), Fe_2O_3 (Sigma-Aldrich, ≥99%), and CuO (J. T. Baker, 99.5%) was ball-milled at 250 rpm for 1 hour and then pelletized. The pellets were heated at 700 ºC for 4 hours and then 900 ºC for 6 hours in air. To prepare a material free from any air contamination, the pellets were heated at 600 ºC under an argon flow and then transferred into an Ar-filled glovebox in a sealed tube.

Operando X-ray Diffraction (XRD). Operando XRD experiment was performed in a home-made cell. During the acquisition, the cell was cycled at a rate of C/20 with a pattern collection time of ≈ 20 min ($\Delta x \approx 0.02$ in Na_xMO_2). The lattice parameters evolution during charge/discharge were determined using the Le Bail method.[84] The electrode preparation and cell assembly procedures for the *operando* XRD experiment were similar to those described in Chapter 2, but the electrode was deposited on a thin glassy carbon (SIGRADUR, HTW) substrate to allow the penetration of X-rays.

5.3 Results and Discussion

5.3.1 Structure and Air Stability

The target composition, $Na_{0.67}[Mn_{0.65}Fe_{0.20}Cu_{0.15}]O_2$, was synthesized by a solid state method. The XRD pattern of the sample (**Figure 5.1**, blue) confirms an undistorted P2 structure (space group $P6_3/mmc$) for the material. The P2 structure (**Figure 5.1 b**) can be described as a stack of edge-sharing MO_6 layers accommodating two different prismatic sodium sites in between, Na_e and Na_f, which share edges and faces, respectively, with the MO_6 octahedra. The XRD pattern of the material reveals the presence of a minor impurity phase (marked by ↓). The small peak at ≈ 38.7º matches with the main characteristic peak of CuO XRD pattern. The second main peak of CuO at ≈ 35.5º has overlap by (100) reflection of the P2 phase. The appearance of CuO or another unidentified impurity was reported before for the synthesis of copper-substituted P2 compositions.[126,128] These observations suggest that only limited

amount of copper could be incorporated in the P2 layered structure, probably due to the larger ionic radius of Cu^{2+} (0.73 Å) compared to the other transition metal cations; Mn^{4+} (0.53 Å), Mn^{3+} (high spin, 0.65 Å), Fe^{3+} (high spin, 0.65 Å), and Ni^{2+} (0.69 Å).[115] A single phase material was achieved when 10 wt% less copper oxide was used in the precursors, resulting in the $Na_{0.67}[Mn_{0.66}Fe_{0.20}Cu_{0.14}]O_2$ composition (**Figure 5.1 a**, red).

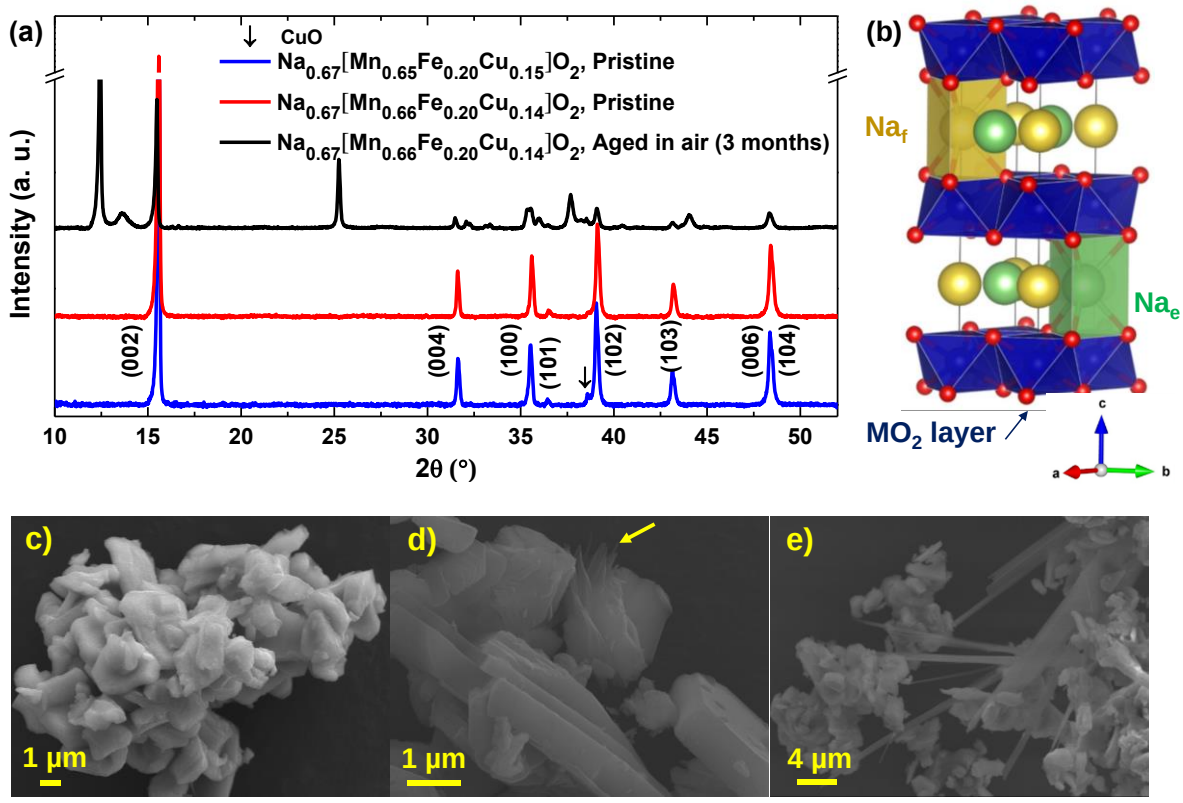

Figure 5.1 XRD pattern of pristine $Na_{0.67}[Mn_{0.65}Fe_{0.2}Cu_{0.15}]O_2$ (blue), pristine $Na_{0.67}[Mn_{0.66}Fe_{0.2}Cu_{0.14}]O_2$ (red), and aged $Na_{0.67}[Mn_{0.66}Fe_{0.2}Cu_{0.14}]O_2$ in air for 3 months (black) (a). Symbol (↓) marks the CuO impurity peak. Schematic presentation of P2-Na_xMO_2 (b). SEM images of pristine $Na_{0.67}[Mn_{0.66}Fe_{0.2}Cu_{0.14}]O_2$ (c) and the sample aged in air for 3 weeks (d) and 3 months (e).

Figure 5.2 shows the result of Rietveld refinement of the X-ray powder diffraction data of $Na_{0.67}[Mn_{0.66}Fe_{0.20}Cu_{0.14}]O_2$. The analysis was performed on a sample loaded into a glass capillary in an argon filled glovebox and sealed from exposure to air. The lattice parameters, a = 2.9280 Å and c = 11.1800 Å, are slightly larger than those of $Na_{0.67}[Mn_{0.65}Ni_{0.15}Fe_{0.20}]O_2$, a = 2.9207 Å and c = 11.1598 Å (Chapter 4), in agreement with the larger size of Cu^{2+} than Ni^{2+}. *hkl*-dependent peak broadening was observed in the XRD pattern of $Na_{0.67}[Mn_{0.66}Fe_{0.20}Cu_{0.14}]O_2$, similar to previously reported Na_xMO_2 materials[53,55]; (10l) Bragg peaks are broader than (00l) reflections. Application of a micro-strain correction[100] improved much the modeling of peak profiles. The atomic displacement parameters of sodium sites were fixed and off-centered site positions were taken to model the high disorder in electron density distribution in the sodium layer, similar to the approach reported before[74]. The total occupancy of sodium ions to the transition metal ions was fixed to 0.67.

Figure 5.1 c shows the SEM image of an as-prepared sample of $Na_{0.67}[Mn_{0.66}Fe_{0.20}Cu_{0.14}]O_2$. The particles have mostly plate-like morphology, with hundreds of nanometer thickness and several micron diameters. No impurity phase based on morphology is distinguished by SEM images. However, the SEM image of a sample exposed to air for three weeks (**Figure 5.1 d**) shows the initiation of growth of a new phase (marked by a yellow arrow). The SEM image of a sample aged in air for three months (**Figure 5.1 e**) clearly demonstrates the new phase with ribbon-like morphology. EDS detected carbon, oxygen, and sodium as the constituent elements of the emerged impurity. The XRD pattern of an aged sample for about 3 months (**Figure 5.1 a**, black) shows the appearance of new peaks. The growth of ribbon-like sodium carbonate particles and similar evolution of XRD pattern were previously observed for an aged sample of its parent composition, P2-$Na_{2/3}[Mn_{1/2}Fe_{1/2}]O_2$, reported in a previous study[55] (Chapter 3). A comprehensive study of air reactivity of P2-$Na_{2/3}[Mn_{1/2}Fe_{1/2}]O_2$ showed that carbonate anions are inserted into the structure as a consequence of exposure of the material to the moisture and CO_2 in the atmosphere. Carbonate anions and sodium cations progressively form amorphous sodium

carbonate ribbons resulting in depletion of sodium ions. Water molecules are finally intercalated into the sodium deficient P2 phase and form hydrated phases detected by XRD. The hydrated phases with similar XRD patterns were previously reported for air-exposed P2 phases.[43,95] Substitution of Mn^{4+}/Ni^{2+} for Fe^{3+} was shown to decrease the reactivity of P2-$Na_{2/3}[Mn_{1/2}Fe_{1/2}]O_2$ to the atmosphere (Chapter 3). Recently, it was reported that no air reactivity was observed for P2-$Na_{7/9}[Cu_{2/9}Fe_{1/9}Mn_{2/3}]O_2$ up to two months.[70] These results imply that incorporation of copper into P2-$Na_{2/3}[Mn_{1/2}Fe_{1/2}]O_2$ could mitigate its reactivity, but does not suppress it, and the stability of P2-$Na_{7/9}[Cu_{2/9}Fe_{1/9}Mn_{2/3}]O_2$ should have another origin. Further investigations of $Na_{0.67}[Mn_{0.66}Fe_{0.20}Cu_{0.14}]O_2$ discussed in this work were performed on air-protected samples.

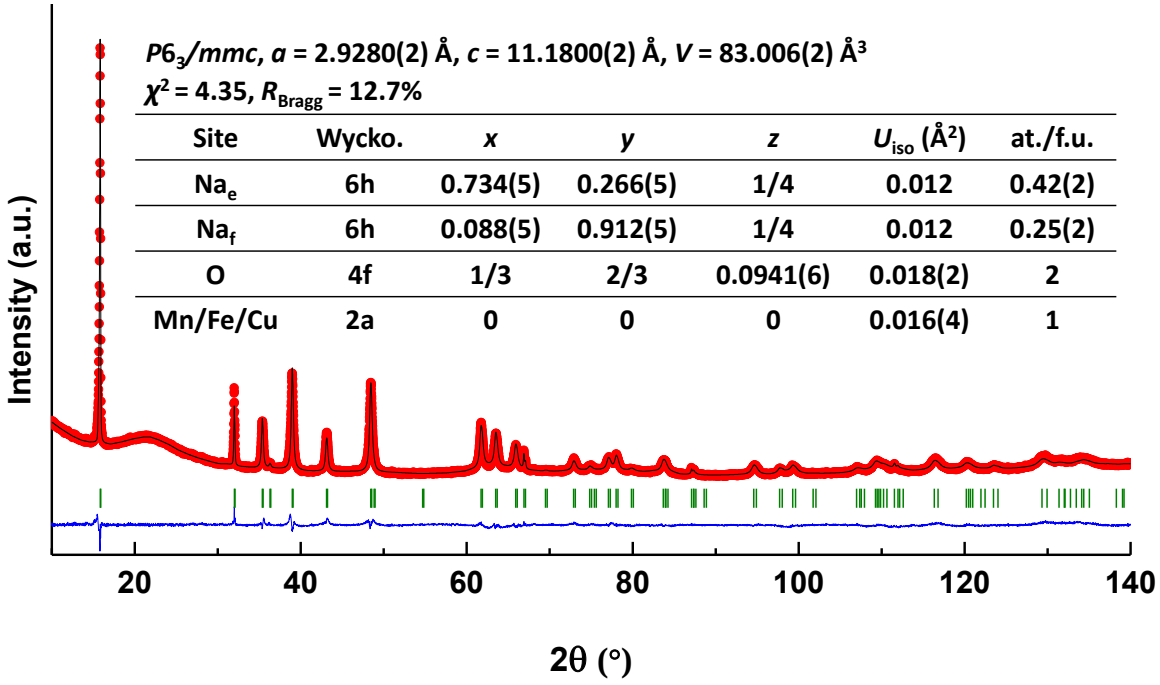

Figure 5.2 Rietveld refinement of X-ray powder diffraction data of P2-$Na_{2/3}[Mn_{1/2}Fe_{1/2}]O_2$. The observed data is shown in red markers, the calculated pattern is shown in black, the difference curve is shown in blue, and the Bragg reflection are shown in green. The unit cell parameters and atomic parameters are presented in the inset of the figure.

5.3.2 *Operando* X-ray Diffraction Analysis (XRD)

Phase transitions of $Na_x[Mn_{0.66}Fe_{0.20}Cu_{0.14}]O_2$ during galvanostatic charge and discharge were examined by *operando* XRD analysis. **Figure 5.3 a** presents a color map illustration of the evolution of $Na_x[Mn_{0.66}Fe_{0.20}Cu_{0.14}]O_2$ diffraction peaks over the first discharge between 4.3V to 1.5 V at a cycling rate of C/20. It is worth noting that recent studies[130,131] showed the dependency of phase transitions in layered Na_xMO_2 to the cycling rate. *Operando* XRD analysis showed that the phase transitions induced by insertion and extraction of sodium ions into/from $Na_x[Mn_{0.66}Fe_{0.20}Cu_{0.14}]O_2$ occurs similarly as in $Na_x[Mn_{0.5}Fe_{0.5}]O_2$[57], and $Na_x[Mn_{0.65}Fe_{0.20}Ni_{0.15}]O_2$[56]. Initial P2 structure is preserved over a wide range of composition range, converts to a low-crystalline phase, referred to as "Z" phase,[57,56] at high voltage, and a P2-P′2 phase transition occurs at low voltage.

The P2 stability voltage window in $Na_x[Mn_{0.66}Fe_{0.20}Cu_{0.14}]O_2$, 2.1 – 4.1 V (**Figure 5.4 a**), is slightly broadened compared to its parent composition $Na_x[Mn_{0.5}Fe_{0.5}]O_2$, 2.1 - 4.0 V. In-plane lattice parameter of the P2 structure (a_{hex}), *i.e.*, the first neighbor M-M distance (M = transition metal), increases by insertion of sodium ions (**Figure 5.4 c**, blue, blue) in agreement with reduction of transition metal ions. On the other hand, the interlayer distance contracts (**Figure 5.4 b**, blue) due to increasing of the screening effect of sodium ions resulting in weaker electrostatic repulsion between adjacent oxygen layers.

The low voltage P′2 phase (space group: *Cmcm*) can be described as the orthorhombic distortion of hexagonal P2 phase (space group: $P6_3/mmc$) which is induced by the cooperative effect of Jahn-Teller active ions.[57,132] It is clearly visible (**Figure 5.3 a**) that (10l) reflections of P2 phase split into two peaks over P′2 domain, whereas (00l) peaks are preserved. The P2-P′2 phase transition in $Na_x[Mn_{0.66}Fe_{0.20}Cu_{0.14}]O_2$ commences at $x \approx 0.72$ and 2.1 V (**Figure 5.4 a**), which is at lower sodium content compared to the transition onset in $Na_x[Mn_{0.5}Fe_{0.5}]O_2$ and $Na_x[Mn_{0.65}Fe_{0.20}Ni_{0.15}]O_2$ ($x \approx 0.8$) (Chapter 4). All of these three compositions have a similar concentration of Jahn-Teller active Mn^{3+}

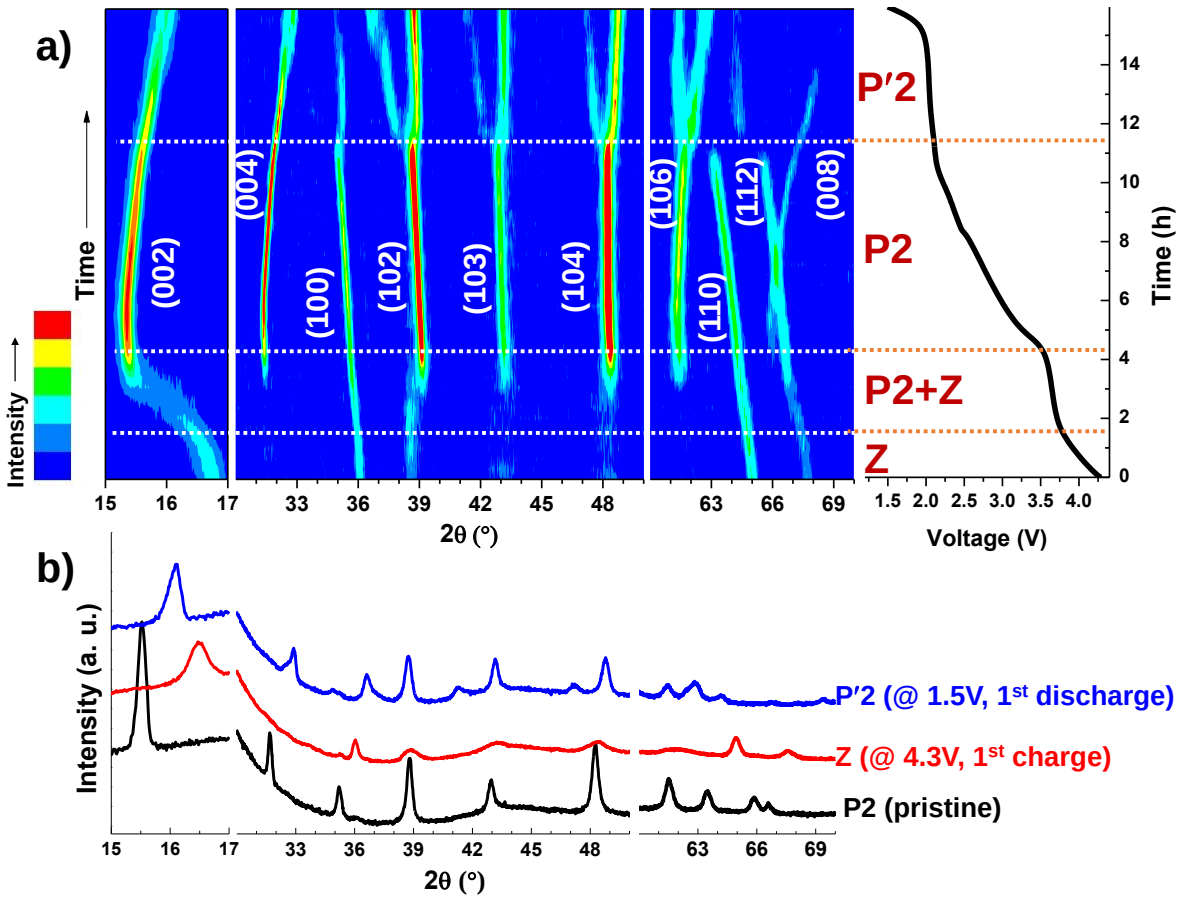

Figure 5.3 Color map illustration of evolution of XRD pattern of $Na_x[Mn_{0.66}Fe_{0.2}Cu_{0.14}]O_2$ recorded over the first discharge during galvanostatic cycling at a rate of C/20, along with voltage profile of the cell vs. time (a). The hkl reflections corresponding to the P2 phase are marked on the map. XRD pattern of pristine $Na_x[Mn_{0.66}Fe_{0.2}Cu_{0.14}]O_2$ is shown in black, at "Z" phase collected over full charge at 4.3 V is presented in red, and at P′2 phase collected over full discharge at 1.5 V is shown in blue (b).

ions at a particular x (in Na_xMO_2). The advanced occurrence of the P2-P′2 transition in the copper-substituted composition should be attributed to the role of Jahn-Teller active Cu^{2+} ions (d^9 electronic state)[133]. It was reported that no distortion of the hexagonal cell was observed when P2-$Na_{2/3}[Mn_{1/2}Fe_{1/4}Co_{1/4}]O_2$ was discharged to 1.5 V.[70] That extended domain of stability was attributed to the reduction of Co^{3+} to Co^{2+} during discharge, instead of the reduction of Mn^{4+} to the Jahn-Teller active Mn^{3+} ions. A direct P2-P′2 transition occurs in $Na_x[Mn_{0.66}Fe_{0.20}Cu_{0.14}]O_2$ at low voltage, whereas a

biphasic region is observed for the parent composition $Na_x[Mn_{0.5}Fe_{0.5}]O_2$. An undistorted hexagonal phase can be described in an orthorhombic cell with the following relationship between lattice parameters; $a_{ortho} = a_{hex}$, $b_{ortho} = a_{hex} + 2b_{hex}$ (*i.e.*, $a_{ortho} = b_{ortho}/\sqrt{3}$) and $c_{ortho} = c_{hex}$. Therefore, the divergence of b_{ortho}/a_{ortho} from $\sqrt{3}$ implies higher distortion from the hexagonal cell. Increased orthorhombic distortion is observed in P′2-$Na_x[Mn_{1/2}Fe_{1/4}Co_{1/4}]O_2$ by insertion of more sodium ions into the structure (**Figure 5.4 c**, green).

The transition to the "Z" phase at high voltage initiates at 4.1 V, $x \approx 0.30$ in $Na_x[Mn_{0.66}Fe_{0.2}Cu_{0.14}]O_2$ at the first charge and proceeds through a two-phase mechanism until 4.2V and $x \approx 0.21$, at which it thoroughly converts to the "Z" phase. **Figure 5.3** shows that $(100)_{P2}$ and $(110)_{P2}$ reflections are maintained in the XRD pattern of the charged material, $Na_{0.1}[Mn_{0.66}Fe_{0.2}Cu_{0.14}]O_2$, which proves uphold of coherence within MO_2 layers. Nevertheless, the substantial broadening of $(00l)_{P2}$ and $(10l)_{P2}$ peaks indicates the loss of the long-range order along the *c*-axis. The transition from the P2 structure to this low crystalline phase is reported for iron-containing layered oxide compositions $Na_x[Mn_{1/2}Fe_{1/2}]O_2$,[53,57,58] $Na_x[Mn_{0.65}Fe_{0.20}Ni_{0.15}]O_2$,[56] $Na_x[Mn_{1/2}Fe_{1/4}Co_{1/4}]O_2$[67]. Formation of an OP4 structure ($P\bar{6}m2$ space group) with stacking faults was first proposed for the high voltage phase of $Na_x[Mn_{1/2}Fe_{1/2}]O_2$.[53,58] The OP4-type structure is composed of alternative stacking of P-type and O-type layers. Structural evolution resulting in the formation of octahedral environment for sodium ions (ABAC oxygen stacking) is expected for high concentration of sodium vacancies, in order to avoid the high columbic repulsion due to the alignment of oxygen ions of adjacent layers along the *c*-axis in the P2 stacking (ABBA oxygen array). For example, appearance of the O2 stacking faults was reported for charged $Na_x[Mn_{2/3}Ni_{1/3}]O_2$.[43] In the previous study presented in Chapter 4,[56] a model was proposed to describe the "Z" phase, using x-ray pair distribution function (PDF) analysis. According to this model, migration of transition metals (mainly iron) into the interlayer space causes a short range order between two adjacent layers with an O2 stacking scheme, referred to as a "bi-layer". The interlayer space within

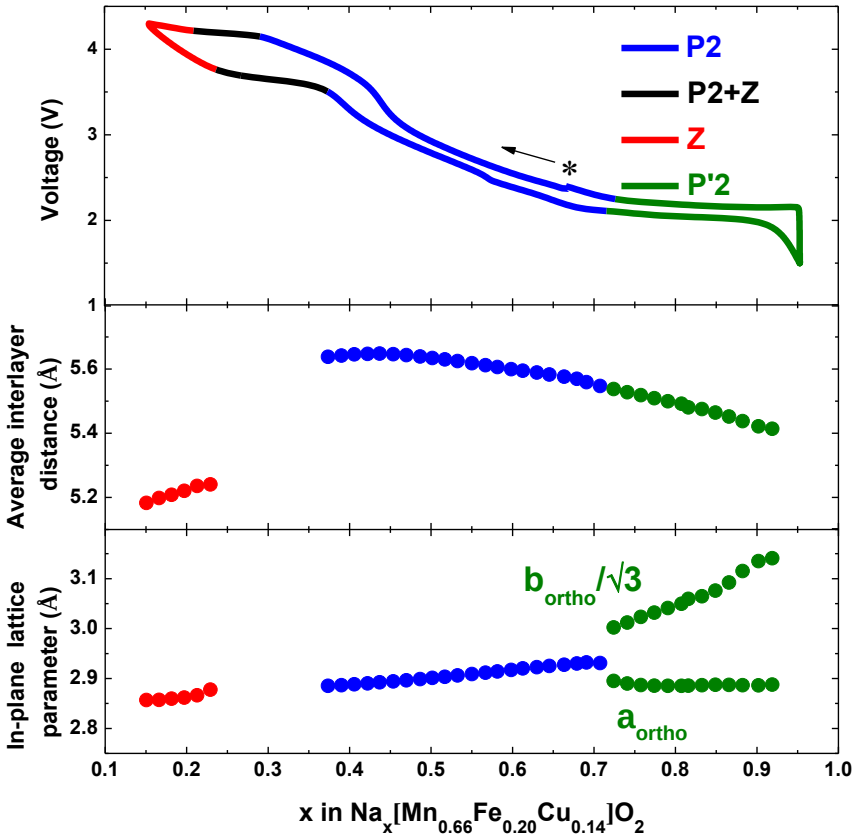

Figure 5.4 Phase evolution of $Na_x[Mn_{0.66}Fe_{0.2}Cu_{0.14}]O_2$ vs. sodium content over the first cycle (a). ∗ sign shows the starting point of the cycling. Evolution of the average interlayer distance (b) and in-plane lattice parameter of $Na_x[Mn_{0.66}Fe_{0.2}Cu_{0.14}]O_2$ (c) as a function of sodium content during the first discharge. The abrupt decrease of average interlayer distance due to transition from P2 to "Z" phase is highlighted with the arrow.

a bi-layer is shrank significantly, explaining the trend observed in the lattice parameter evolution (**Figure 5.4 b**, red). Irreversible migration of transition metals into interlayer tetrahedral sites upon charge was proposed in O3-Na_xFeO_2 [4] and O3-Na_xCrO_2[124]. The growth of the pre-edge peak at the X-ray absorption near-edge structure (XANES) spectra of charged samples was attributed to occupation of tetrahedral sites upon charge. This structural rearrangement, which is irreversible in O3 oxides, results in significant capacity fading. However, the high voltage phase transition in P2 oxides is

reversible, as proven by the electrochemical performance and also the perfect correspondence of the evolution of lattice parameters with the sodium content in the first and second cycle (Chapter 4).

5.3.3 Pair Distribution Function (PDF) Analysis of the "Z" Phase

Pair distribution function (PDF) analysis using laboratory X-ray data was employed to investigate the low-crystalline Z-$Na_x[Mn_{0.66}Fe_{0.20}Cu_{0.14}]O_2$ observed at high voltage. PDF presents the probability of finding any pair of atoms at a specific interatomic distance, regardless of the crystallinity of the structure. PDF analysis is a complementary technique to Rietveld refinement for the characterization of crystalline structures and provides information about the short-range order. However, it becomes much more beneficial when the structural study of a low-crystallinity material is concerned.

Because of the sensitivity of the PDF technique to amorphous phases, a chemically oxidized sample was prepared for this study to avoid any complexity that would arise from additive carbon and binder in an electrochemically oxidized electrode sample. $Na_{0.67}[Mn_{0.66}Fe_{0.20}Cu_{0.14}]O_2$ was mixed with an over-stoichiometric amount of NO_2BF_4 in acetonitrile. The average interlayer distance of the oxidized sample was measured ≈ 5.1 Å by XRD, based on which the composition stoichiometry is estimated as $Na_{0.1}[Mn_{0.66}Fe_{0.20}Cu_{0.14}]O_2$ by interpolating from the data in **Figure 5.4 b**. The chemical oxidation resulted in the depletion of a higher amount of sodium compared to an electrochemical charge.

Figure 5.5 a shows a comparison of the experimental PDF data of Z-$Na_{0.1}[Mn_{0.66}Fe_{0.20}Cu_{0.14}]O_2$, with Z-$Na_{0.1}[Mn_{0.65}Fe_{0.20}Ni_{0.15}]O_2$, Z-$Na_{0.1}[Mn_{0.5}Fe_{0.5}]O_2$, and pristine P2-$Na_{0.67}[Mn_{0.5}Fe_{0.5}]O_2$, in the interatomic distance range of 1 - 6 Å. For all four graphs, "Peak 1" and "Peak 4", highlighted by gray shading, correspond to the 1st M-O (d_1) and 3rd M-O (d_4) correlation length (**Figure 5.5 b**), respectively. The 2nd M-O correlation length gives rise to a small peak at ≈ 3.6 Å for P2- $Na_{0.67}[Mn_{0.5}Fe_{0.5}]O_2$ (**Figure 5.5 a**, magenta markers) which has low intensity because it has half the coordination number of the 3rd M-O neighbor. This peak is screened by Peak 3 in the oxidized samples. "Peak 2" and "Peak 5" are ascribed to the 1st M-M (d_2) and 2nd M-M (d_5) correlation lengths, respectively. A peak attributed to M-

M correlation is stronger than M-O at the same distance and with the same coordination number because of a higher X-ray scattering factor of transition metals than oxygen. Contraction of M-O and M-M distances in $Na_x[Mn_{0.5}Fe_{0.5}]O_2$ after chemical oxidation is clearly observable. In the oxidized samples, a new peak, "Peak 3", emerges, whereas the intensity of "Peak 2" decreases. The split of 1st M-M peak

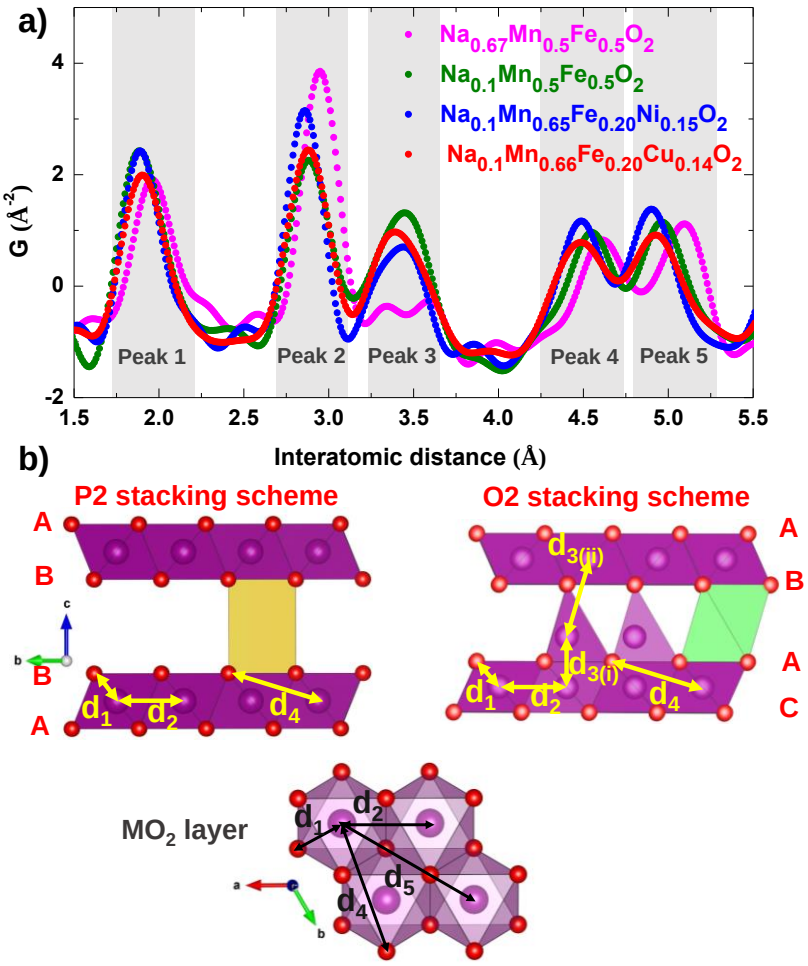

Figure 5.5 Comparison of experimental PDF data of chemically oxidized $Na_x[Mn_{0.66}Fe_{0.20}Cu_{0.14}]O_2$ with pristine P2 and chemically oxidized Z phase $Na_x[Mn_{0.5}Fe_{0.5}]O_2$ and chemically oxidized Z phase $Na_x[Mn_{0.65}Fe_{0.20}Ni_{0.15}]O_2$ (a). The purple and red spheres represent the transition metals and oxygen atoms, and yellow and green polyhedral represent two different NaO_6 polyhedra. Representation of interatomic distances d_1, d_2, d_3, d_4, and d_5, corresponding to peak 1, peak 2, peak 3, peak 4, peak 5 in PDF data (grey shading in part a) on pristine P2 structure and O2 stacking scheme of oxidized Z phase (b).

in Z-$Na_{0.1}[Mn_{0.5}Fe_{0.5}]O_2$ and Z-$Na_{0.1}[Mn_{0.65}Fe_{0.20}Ni_{0.15}]O_2$ phases along with the disappearance of interlayer M-M correlation peaks were explained by the migration of transition metals into the interlayer space and destruction of P2 stacking.[56] It was proposed that the transfer of electrons from oxygen orbitals to Fe^{4+} cations weakens the bonding of neighboring atoms. This mechanism induces migration of most possibly Fe^{3+} and Mn^{4+} ions out of octahedral sites of MO_2 layer. The interaction of removed transition metals with the adjacent oxygen layers causes contraction of the interlayer distance, in agreement with the trend observed by *operando* XRD. The presence of migrated transition metal cations within the interlayer space and high concentration of sodium vacancies result in glide of adjacent MO_2 layer and formation of a bilayer with O2 stacking scheme that accommodates the migrated M cations in the interlayer tetrahedral sites, and sodium ions in the octahedral sites.

The PDF curve of Z-$Na_{0.1}[Mn_{0.66}Fe_{0.20}Cu_{0.14}]O_2$ was fit by use of a modification of the bilayer model (**Figure 5.6 a**) previously proposed for Z-$Na_{0.1}[Mn_{0.5}Fe_{0.5}]O_2$ and Z-$Na_{0.1}[Mn_{0.65}Fe_{0.20}Ni_{0.15}]O_2$,[56] in which a 2×2×10 and 4×4×10 supercell of the pristine hexagonal cell was adopted, respectively. Each supercell was built up of 10 bilayers with random translation in *ab*-plane to model the disorder along the *c*-direction. Each bilayer, which holds an O2 oxygen stacking scheme, accommodates sodium ions in octahedral sites and the migrated transition metal cations in interlayer tetrahedral sites. Sodium ions can be neglected in the model for simplicity, owing to their low concentration in the Z-phase and their low scattering factor. The interlayer distance of each bilayer in Z-$Na_{0.1}[Mn_{0.66}Fe_{0.20}Cu_{0.14}]O_2$ was set so that both M_{Oh}-O and M_{Td}-O distances are equal to the value, d_1 = 1.91 Å, determined by peak 1 (**Figure 5.5**). The distance between centers of bilayers (10.2 Å) was determined from the position of the first peak in the XRD pattern assuming that it represents (00l) reflection. The in-plane distances were set based on the positions of M-M peaks in the PDF data. In an ideal hexagonal packing, the ratio of the second M-M distance to the first one (d_5/d_2 in **Figure 5.5 b**) is equal to √3. In Z-$Na_{0.1}[Mn_{0.66}Fe_{0.20}Cu_{0.14}]O_2$, there is a small deviation of d_5/d_2 = (4.91 Å)/(2.89 Å) = 1.70 from the ideal

value (1.73) of an undistorted hexagonal array of cations, contrary to Z-$Na_{0.1}[Mn_{0.5}Fe_{0.5}]O_2$ (d_5/d_2 = (4.97 Å)/(2.88 Å) = 1.73). Although it is a small deviation (compare it to the significant distortion of b_{ortho}/a_{ortho}=1.88 in the electrochemically discharge sample, $Na_{0.9}[Mn_{0.66}Fe_{0.20}Cu_{0.14}]O_2$ in **Figure 5.5 c**), choice of an orthorhombic cell and the refinement of *a* and *b* lattice parameters improved fitting of the PDF data, specially at higher atomic distances. Therefore, an orthorhombic 4×2×10 supercell, which contains 320 transition metal atoms and 640 oxygen atoms, was used to model the structure of Z-$Na_{0.1}[Mn_{0.65}Fe_{0.20}Ni_{0.15}]O_2$.

Superposition of the peaks corresponding to two M_{Td}-M_{Oh} distances, $d_{3(i)}$ = 3.28 Å and $d_{3(ii)}$ = 3.42 Å (**Figure 5.5 b**), give rise to peak 3 (**Figure 5.5 a**) in the PDF data of Z-$Na_{0.1}[Mn_{0.66}Fe_{0.20}Cu_{0.14}]O_2$. An important feature observed in **Figure 5.5 a** is that ratio of the Peak 3 intensity to Peak 2 intensity, related to the concentration of migrated M cations, in PDF data of Z-$Na_{0.1}[Mn_{0.66}Fe_{0.20}Cu_{0.14}]O_2$ is lower than Z-$Na_{0.1}[Mn_{0.5}Fe_{0.5}]O_2$, but higher than Z-$Na_{0.1}[Mn_{0.65}Fe_{0.20}Ni_{0.15}]O_2$. It was reported[56] that the best fits were obtained for Z-$Na_{0.1}[Mn_{0.5}Fe_{0.5}]O_2$ and Z-$Na_{0.1}[Mn_{0.65}Fe_{0.20}Ni_{0.15}]O_2$ phases accounting for migration of 1/8 and 1/32, respectively, of transition metal cations from each bilayer. In this study, we examined bilayer models with the migration of 2/32 and 3/32 of transition metal cations to fit the PDF data of Z-$Na_{0.1}[Mn_{0.66}Fe_{0.20}Cu_{0.14}]O_2$. The concentration of migrated transition metal cations affects mainly the ratio of the Peak 3 intensity to the Peak 2 intensity (**Figure 5.5 a**). The best fit was obtained when migration of 3/32 of cations into interlayer tetrahedral sites was considered (**Figure 5.6 a**).

Figure 5.6 b shows the experimental (red markers) and calculated (black graph) PDF of Z-$Na_{0.1}[Mn_{0.66}Fe_{0.20}Cu_{0.14}]O_2$ fit by use of a bilayer model with 3/32 of M cations migrated. Overestimation of the intensity of peak located at ≈ 4.9 Å in calculated PDF (**Figure 5.6 b**) originates from superimposition of 2nd in-plane M-M and 1st interlayer M-M correlation lengths. Similarly, the peak located at ≈ 5.7 Å represents both 3rd in-plane M-M and 2nd interlayer M-M distances. In the pristine crystalline P2-$Na_{0.67}[Mn_{0.66}Fe_{0.20}Cu_{0.14}]O_2$, 1st interlayer M-M distance is located at ≈ 5.6 Å, but

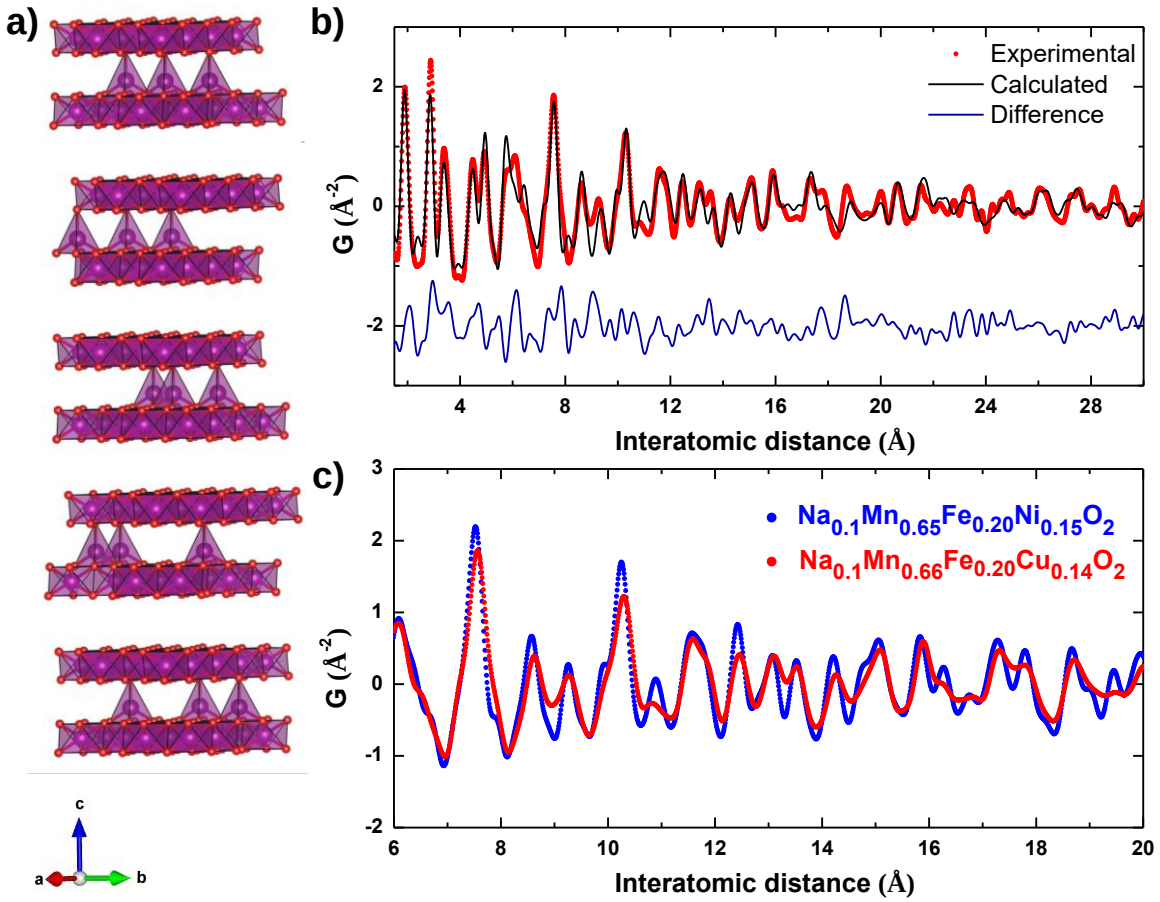

Figure 5.6 Schematic representation of bilayers in Z-$Na_{0.1}[Mn_{0.66}Fe_{0.2}Cu_{0.14}]O_2$ (a). Fit of PDF curve of Z-$Na_{0.1}[Mn_{0.66}Fe_{0.2}Cu_{0.14}]O_2$ in a orthorhombic 4×2×10 supercell (b). Comparison of experimental PDF curves of Z-$Na_{0.1}[Mn_{0.66}Fe_{0.2}Cu_{0.14}]O_2$ and Z-$Na_{0.1}[Mn_{0.65}Fe_{0.20}Ni_{0.15}]O_2$ within the inter-atomic distance range of 6 - 20 Å.

has low coordination number, and the 2nd interlayer M-M shows up at ≈ 6.3 Å. Overestimation of calculated PDF peaks at interlayer M-M correlation lengths implies the absence of order along c-axis even at this short range, and there is probably a distribution of bilayer distances. In addition, comparison of the experimental PDF data of Z-$Na_{0.1}[Mn_{0.66}Fe_{0.20}Cu_{0.14}]O_2$ and Z-$Na_{0.1}[Mn_{0.65}Fe_{0.20}Ni_{0.15}]O_2$ at the interatomic distance of 6 - 20 Å (**Figure 5.6 c**) shows intensity decrease and/or broadening for many peaks of the copper-substituted sample, suggesting lower structural coherence and increased disorder

in this sample. Further improvement of the structural modeling of this phase requires more powerful approaches for solving complicated disordered structures, such as Reverse Monte Carlo (RMC) calculations which are shown significantly beneficial in the modeling of complicated features in electrode materials.[117,118,119]

The average interlayer distance in $Na_{0.1}[Mn_{0.66}Fe_{0.20}Cu_{0.14}]O_2$, ≈ 5.1 Å, is larger than the value in Z-$Na_{0.1}[Mn_{0.65}Fe_{0.20}Ni_{0.15}]O_2$, 4.95 Å, although a higher concentration of migration has occurred in the copper substituted sample. This observation shows that the higher concentration of migrated cations does not yield lower interlayer distance and the average interlayer distance in Z-phase is probably related to the nature of the cations. It was proposed that the majority of the migrated transition metal cations are Fe^{3+}, and the oxidation of iron is the driving force of the P2-Z transition, using structural characterizations and Mössbauer spectroscopy (Chapter 4). Hence, the higher concentration of migration in the Z-phase copper-substituted material might be related to the higher concentration of Fe^{4+} compared to that in the charged nickel-substituted sample. On the other hand, *operando* XRD shows that the P2-Z phase transition commences at a similar voltage and sodium content, which suggests a similar concentration of oxidized iron cations. This observed contradiction might originate from the different reaction rates of chemical oxidation and slow galvanostatic oxidation, which possibly influence each composition in different ways. On the other hand, the intensified high voltage migration in the Cu-substituted material, compared to the Ni-substituted composition, might originate from increased ligand to metal charge transfer (LMCT) effect. It was proposed that stabilization of Fe^{4+} in $Na_x[Mn_{0.5+x}Ni_xFe_{0.5-x}]O_2$ (x = 0, 10, 0.15) by transfer of electrons from oxygen orbital weakens the bonding of the surrounding atoms and facilitates the migration of transition metal out of the MO_2 plane (Chapter 4). The ligand to metal (O-to-Cu) charge transfer energy for Cu^{3+} containing oxides was found to be negative.[134-136] Charge transfer from oxygen p-orbital to Cu^{3+} d-orbital is proposed to facilitate the

migration of transition metals out of the MO_2 layers at high voltage. Further experimental and calculation studies are required to validate the role of these mechanisms.

5.3.4 Electrochemical Performance

$Na_{0.67}[Mn_{0.66}Fe_{0.20}Cu_{0.14}]O_2$ delivers a high specific capacity of ≈ 176 mAh.g^{-1} when cycled within the voltage range of 1.5 - 4.3 V with a rate of C/20 (13 mA.g^{-1}). The smooth galvanostatic charge/discharge profile (**Figure 5.7 a**) indicates facile (de)intercalation of sodium ions. The perfect superimposition of the first and second electrochemical charge profiles shows the reversibility of the mechanism. The large voltage polarization observed at high voltage, similarly observed for the voltage profiles of $Na_{0.67}[Mn_{0.5+y}Fe_{0.5-2y}Ni_y]O_2$, (y = 0, 0.15) (Chapter4), disappears when the P2-Z phase transition is avoided by limiting the cutoff voltage (**Figure 5.7 b**), indicating the high energy required for the reversible structural evolution at this region. Preventing the P2-P′2 phase transition, however, does not impede low voltage polarization, indicating that it is related to the P2 phase properties. The stress imposed to the structure due to the phase transitions drastically affect the voltage profile over cycling (**Figure 5.7 c**), resulting in fading of the average voltage and thus delivered energy. Voltage fading is also a critical challenge with the high energy density Li_2MnO_3-based electrode materials and is proposed to be caused by irreversible structural changes.[137] When $Na_{0.67}[Mn_{0.66}Fe_{0.20}Cu_{0.14}]O_2$ is cycled within its P2-stability window, 2.1 - 4.1 V (determined from *operando* XRD analysis), only ≈ 94 mAh.g^{-1} reversible capacity is obtained. However, the voltage profile shows excellent stability over 100 cycles (**Figure 5.7 d**).

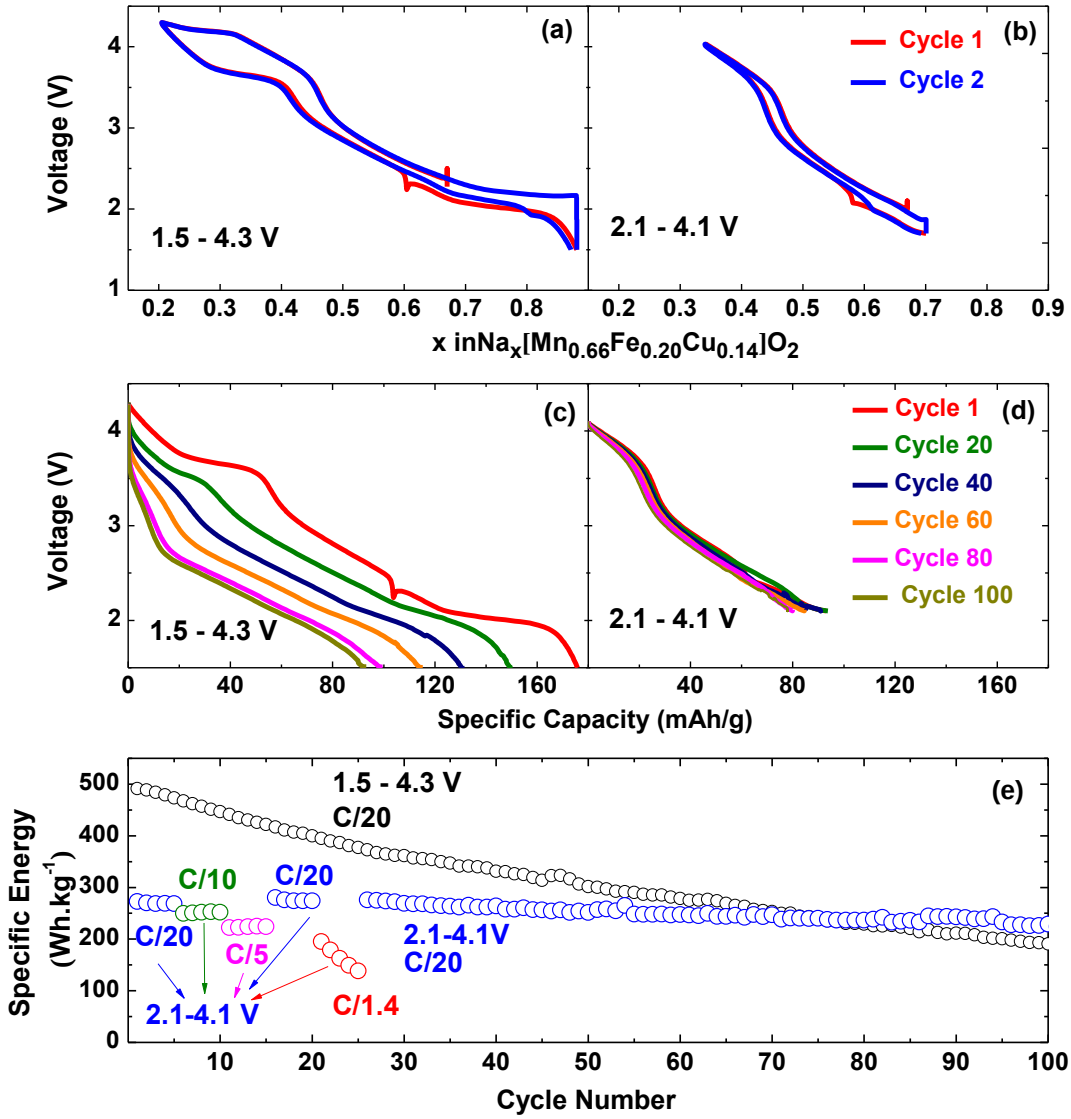

Figure 5.7 The galvanostatic charge/discharge profiles at the cycling a rate of C/20 (a,b) and voltage curves vs. discharge specific capacity (c,d) of $Na_{0.67}[Mn_{0.66}Fe_{0.2}Cu_{0.14}]O_2$ cycled within the voltage range of 1.5 - 4.3 V (a,c) and 2.1 - 4.1 V (b,d). Specific energy vs. the cycle number of $Na_{0.67}[Mn_{0.66}Fe_{0.2}Cu_{0.14}]O_2$ cycled within the voltage window of 1.5 - 4.3 V at a rate of C/20 (filled circles) (e) and cycled within the voltage range of 2.1 - 4.1 V at different rates (hollow circles).

$Na_{0.67}[Mn_{0.66}Fe_{0.20}Cu_{0.14}]O_2$ delivers an initial specific energy of ≈ 491 $Wh.kg^{-1}$ when cycled between 1.5 - 4.3 V at a rate of C/20 and retains only 39% after 100 cycles. The cell exhibits much lower initial specific capacity of ≈ 272 $Wh.kg^{-1}$ when cycled between 2.1 - 4.1 V. However, it shows an improved specific energy retention of 84% after 100 cycles. $Na_{0.67}[Mn_{0.66}Fe_{0.20}Cu_{0.14}]O_2$ exhibits relatively good rate capability when cycled within the P2 stability window; it retains 93% of specific energy when the rate is increased from C/20 (13$mA.g^{-1}$) to C/10 (26 $mA.g^{-1}$) and from C/10 to C/5. However, when a large specific current of 190 $mA.g^{-1}$(C/1.4) is applied to the cell, it shows poor specific energy retention.

Figure 5.8 shows a comparison of specific energy retention for $Na_{0.67}[Mn_{0.66}Fe_{0.2}Cu_{0.14}]O_2$ (red markers), $Na_{0.67}[Mn_{0.65}Fe_{0.20}Ni_{0.15}]O_2$ (blue markers), $Na_{0.67}[Mn_{0.5}Fe_{0.5}]O_2$ (green markers) cycled at a rate of C/20 within 1.5 - 4.3 voltage window (filled circles) and at a rate of C/10 over P2 stability

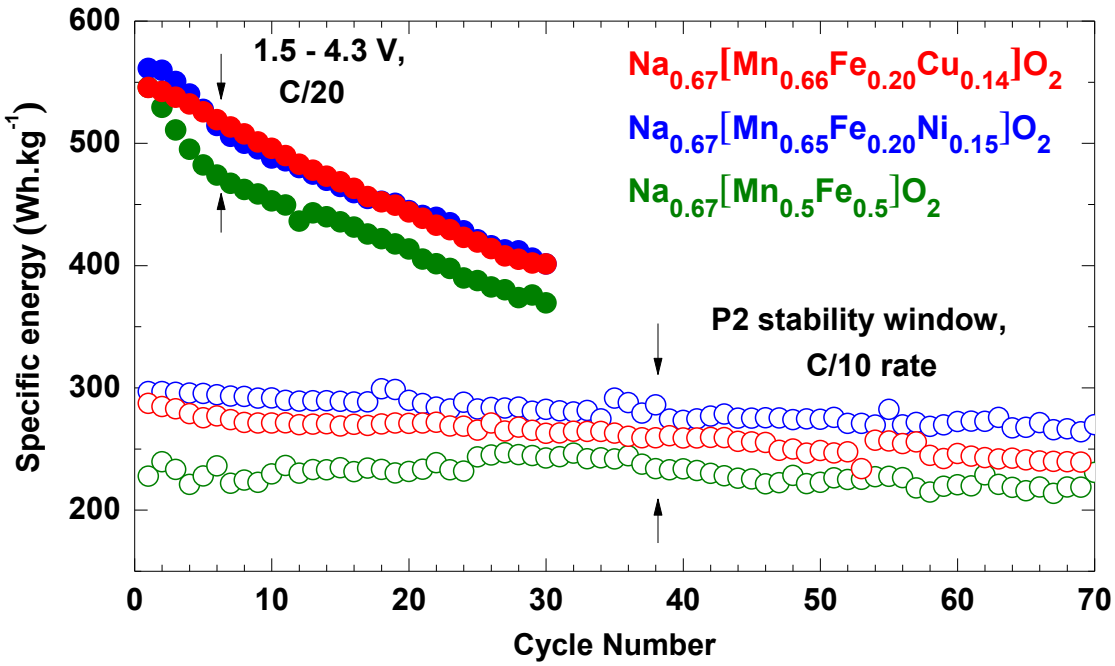

Figure 5.8 Specific energy of $Na_{0.67}[Mn_{0.66}Fe_{0.2}Cu_{0.14}]O_2$ (blue), $Na_{0.67}[Mn_{0.65}Fe_{0.20}Ni_{0.15}]O_2$ (red), $Na_{0.67}[Mn_{0.5}Fe_{0.5}]O_2$ (green) cycled within 1.5-4.3 V at a C/20 rate (filled circles) and over P2-stability window at a C/10 rate (hollow circles).

domain of each composition (hollow circles), 2.1 - 4.1V, 2.0 - 4.1 V, 2.0 - 4.0 V, respectively. At the full voltage range, $Na_{0.67}[Mn_{0.5}Fe_{0.5}]O_2$ shows more severe fading over initial five cycles. However, all three compositions exhibit similar fading over the next 25 cycles. $Na_{0.67}[Mn_{0.66}Fe_{0.20}Cu_{0.14}]O_2$ and $Na_{0.67}[Mn_{0.50}Fe_{0.5}]O_2$ deliver comparable specific energy in the both P2 and the extended voltage window. $Na_{0.67}[Mn_{0.65}Fe_{0.20}Ni_{0.15}]O_2$ shows superior specific energy to those of the parent composition, $Na_{0.67}[Mn_{0.50}Fe_{0.5}]O_2$, and the Cu-substituted material, owing to the contribution of $Ni^{2+/4+}$ to redox processes.

5.4 Conclusions

Here, a comprehensive study of structural stability and electrochemical performance of P2-$Na_{0.67}[Mn_{0.66}Fe_{0.20}Cu_{0.14}]O_2$ is presented and the effect of incorporation of copper, in comparison with nickel (Chapter 4), into a high-performance positive electrode material, P2-$Na_{0.67}[Mn_{0.5}Fe_{0.5}]O_2$, is investigated.

All the characterization procedures were performed on air-protected samples due to the reactivity of P2-$Na_{0.67}[Mn_{0.66}Fe_{0.20}Cu_{0.14}]O_2$ to the atmosphere, similar to most of other layered sodium transition metal oxides. $Na_x[Mn_{0.66}Fe_{0.20}Cu_{0.14}]O_2$ shows a P2-Z phase transition at x = 0.30 and V = 4.1 V over galvanostatic charge, and a P2-P2′ phase transition at x = 0.72 and V = 2.1 V over discharge at a rate of C/20, exhibited by *Operando* XRD. The stability domain of P2-structure for $Na_x[Mn_{0.66}Fe_{0.20}Cu_{0.14}]O_2$ is slightly limited compared to $Na_x[Mn_{0.65}Fe_{0.20}Ni_{0.15}]O_2$ (2 - 4.1 V), most probably because of cooperative effect of Jahn-Teller active Cu^{2+} in addition to Mn^{3+} ions. The disordered Z phase formed at high voltage, driven by migration of transition metal ions into interlayer tetrahedral sites, commences at the similar voltage and sodium content as in $Na_x[Mn_{0.65}Fe_{0.20}Ni_{0.15}]O_2$, but is delayed compared to $Na_x[Mn_{0.5}Fe_{0.5}]O_2$. PDF analysis of a chemically oxidized sample revealed that the migration of transition metals into the interlayer space is mitigated in Z-$Na_{0.1}[Mn_{0.66}Fe_{0.20}Cu_{0.14}]O_2$ compared to Z-$Na_{0.1}[Mn_{0.5}Fe_{0.5}]O_2$. However, an increased fraction of

transition metals, more than twice, was found to have migrated in Z-$Na_{0.1}[Mn_{0.66}Fe_{0.20}Cu_{0.14}]O_2$ in comparison to Z-$Na_{0.1}[Mn_{0.65}Fe_{0.20}Ni_{0.15}]O_2$. Electron transfer from the oxygen p-orbital to the copper d-orbital is proposed to be at the origin of the intensified transition metal migration in the high voltage phase.

$Na_{0.67}[Mn_{0.66}Fe_{0.20}Cu_{0.14}]O_2$ was evaluated as a positive electrode material versus sodium metal. The cell delivers a high specific energy of 491 $Wh.kg^{-1}$ at the first discharge when cycled between 1.5 - 4.3 V with a rate of C/20. Phase transitions cause poor cycling and voltage fading, similar to $Na_{0.67}[Mn_{0.5}Fe_{0.5}]O_2$ and $Na_{0.67}[Mn_{0.65}Fe_{0.20}Ni_{0.15}]O_2$. When cycled within the voltage window corresponding to the P2-structure domain, $Na_{0.67}[Mn_{0.66}Fe_{0.20}Cu_{0.14}]O_2$ shows excellent stability in its voltage profile over 100 cycles. $Na_{0.67}[Mn_{0.66}Fe_{0.20}Cu_{0.14}]O_2$ and $Na_{0.67}[Mn_{0.5}Fe_{0.5}]O_2$ show comparable values of delivered specific energy in the P2-stability window, but ≈ 15% lower than that value obtained from $Na_{0.67}[Mn_{0.65}Fe_{0.20}Ni_{0.15}]O_2$.

Chapter 6

Operando X-Ray Absorption Spectroscopy Investigation of P2-$Na_{0.67}[Mn_yFe_zM_{1-y-z}]O_2$ (M: Ni, Cu) Electrodes in Sodium Batteries

6.1 Introduction

Layered sodium transition metal oxides have been extensively explored in the recent years as promising candidates for the positive electrode material in Na-ion batteries. Many efforts have been devoted to investigating the effect of the composition modifications (*i.e.*, cation substitution) on the structural stability of the oxide materials upon cycling.[4,33,34] *Operando* X-ray diffraction technique has been employed by many research groups to characterize the structural evolution of materials upon cycling and understand their correlation to the electrochemical performance.[41,57,66] However, not much attention seems to be paid on an in-depth understanding of redox reactions in these systems. The comprehensive understanding of the charge compensation mechanism in these materials is necessary for the future design and development of high-performance electrode materials for Na-ion batteries that are capable of competing with the state-of-the-art Li-ion battery technology.

X-ray absorption spectroscopy (XAS) techniques are recognized as powerful means of probing redox processes in the energy storage research. *Operando* measurements of X-ray absorption spectra have been widely employed to investigate the contribution of various redox reactions to the charge compensation mechanism in layered lithium metal oxides.[138-140] The ambient atmosphere structural stability, phase transitions upon cycling, and electrochemical performance of P2-type $Na_{0.67}[Mn_yFe_zM_{1-y-z}]O_2$, M: Ni, Cu are studied (Chapters 4 and 5). This chapter presents an *operando* XAS study of the samples to shed light on the charge compensation mechanisms involved in the charge and discharge processes. The X-ray absorption spectra of the materials were measured at the Mn, Fe, and Cu K-edges for P2-$Na_{0.67}[Mn_{0.66}Fe_{0.20}Cu_{0.14}]O_2$, and at the Ni K-edge for $Na_{0.67}[Mn_{0.65}Fe_{0.20}Ni_{0.15}]O_2$ at different

states of charge and discharge of the first cycle to probe the evolution in the atomic and electronic local structures of each transition metal during cycling.

6.2 Experimental

6.2.1 Synthesis

P2-$Na_{0.67}[Mn_{0.66}Fe_{0.20}Cu_{0.14}]O_2$ and P2-$Na_{0.67}[Mn_{0.65}Fe_{0.20}Ni_{0.15}]O_2$ were synthesized by a solid-state method, as described in Chapters 4 and 5. A mixture of stoichiometric amounts of oxide precursors was ball-milled and pelletized. The pellets were heated at 700 ºC for 4 hours and then 900 ºC for 6 hours in air. To prepare samples free from any air contamination, the pellets were heated at 600 ºC under an argon flow and then transferred into an Ar-filled glovebox in a sealed tube.

6.2.2 Electrochemistry

Each active material was mixed with 10 wt% carbon black (TIMCAL) and 10 wt% polyvinylidene fluoride (PVDF) (Aldrich average Mw ~ 534 000) suspended in N-methyl-2-pyrrolidinone (NMP) (Sigma-Aldrich, 99.5%) and cast on porous carbon paper (AvCarb P50, Ballard Material Products) with a loading of ≈ 3-5 $mg.cm^{-2}$. 1M $NaClO_4$ (Alfa Aesar, ≥ 98%) in propylene carbonate (BASF, 99.98%) with 2 vol% fluoroethylene carbonate (FEC) (Sigma-Aldrich, 99%) was used as the electrolyte, and sodium metal (Sigma-Aldrich, ACS reagent) was used as the counter electrode. Modified coin cells were used for *operando* X-ray absorption spectroscopy experiments. An 8μm aluminized Kapton™ (Sheldahl) window was placed on the positive case of a 2325 coin cell for the penetration of the X-ray beam (**Figure 6.1**). Each electrode was located in a coin cell so that the active material faces the Kapton window. The electrodes were separated by two sheets of glass fiber separators (Merck Millipore). All the steps of electrode preparation and cell assembly were carried out in an Ar-filled glovebox to protect the air-sensitive samples from exposure to air. The cells were continuously charged up to 4.3 V vs.

Na/Na^+ at a rate of C/20 and discharged to 1.5 V vs. Na/Na^+ at a rate of C/10 in the galvanostatic mode. Each cell was relaxed at open circuit voltage (OCV) for an hour at the end of charge.

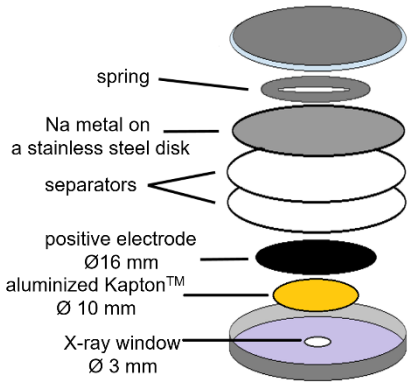

Figure 6.1 Schematic representation of the coin cell used for *operando* XAS study.

6.2.3 X-Ray Absorption Spectroscopy

Mn, Fe, Cu, Ni K-edge XANES spectra of the samples were collected at the Hard X-ray Micro-Analysis (HXMA) beamline (06ID-1) at the Canadian Light Source (CLS). The CLS storage ring operated at 2.9 GeV and 200-250 mA in the injection mode during the experiment. The beamline was equipped with Si (111) and Si (220) double crystal monochromators and Rh and Pt-coated focusing mirrors. Reduction of higher-order harmonics was achieved by detuning the 2nd monochromator crystal to 50% of the peak intensity. Data collection was performed in the fluorescence mode using a 32 element Ge detector. The scan step-sizes were 10 eV/step, 0.25 eV/step, and 0.1 $Å^{-1}$/step for pre-edge, XANES, and EXAFS regions, respectively. The data acquisition time was set to 1 s/step for the pre-edge and XANES regions and was progressively increased to 5 sec/step for the EXAFS region. The total collection time for each pattern was 40 minutes, equivalent to $\Delta x \approx 0.03$ and 0.07 in Na_xMO_2 during charge and discharge, respectively. The energy calibration for each spectrum was performed using the first inflection point of the reference channel spectrum, which was simultaneously collected from the metal foil. The reference spectra were aligned for comparison of the ensemble of data. The raw XAS data were corrected for pre-

edge and post-edge background and normalized to unit step height. The X-ray absorption near edge structure (XANES) data were analyzed using Athena software package.[141]

6.3 Results and Discussions

6.3.1 The Electrochemical Cell for *Operando* XAS Measurements

Figure 6.2 shows a comparison of the first and second galvanostatic charge/discharge profile of P2-$Na_{0.67}[Mn_{0.66}Fe_{0.20}Cu_{0.14}]O_2$ cycled vs. Na metal obtained from a conventional coin cell and a cell designed for *operando* XAS measurements, at a current rate of C/20. The data collected from the cell developed for *operando* XAS experiment shows good similarity to the data obtained from the standard coin cell; the former has a slightly higher voltage polarization, however, which is expected due to the modified coin cell design used for the *operando* measuerements. Lack of uniform stack pressure and conductivity in the modified coin cell designs for *operando* experiments are shown to affect the electrode reactivity.[142] The overlap of the charge voltage profiles of the first and the second cycles of the sample in this cell confirms that the electrode is well protected against the air contamination during preparation and also within the modified coin cell. This data shows that this simple design of the coin cells can be effectively used for an *operando* experiment during charge and discharge. The XANES spectra of $Na_x[Mn_{0.66}Fe_{0.20}Cu_{0.14}]O_2$ at Mn, Fe, and Cu K-edges and the XANES spectra of $Na_x[Mn_{0.65}Fe_{0.20}Ni_{0.15}]O_2$ at the Ni K-edge were collected during the first charge and discharge in order to gain insight into the charge compensation mechanisms and local structure perturbations induced by insertion and extraction of sodium ions.

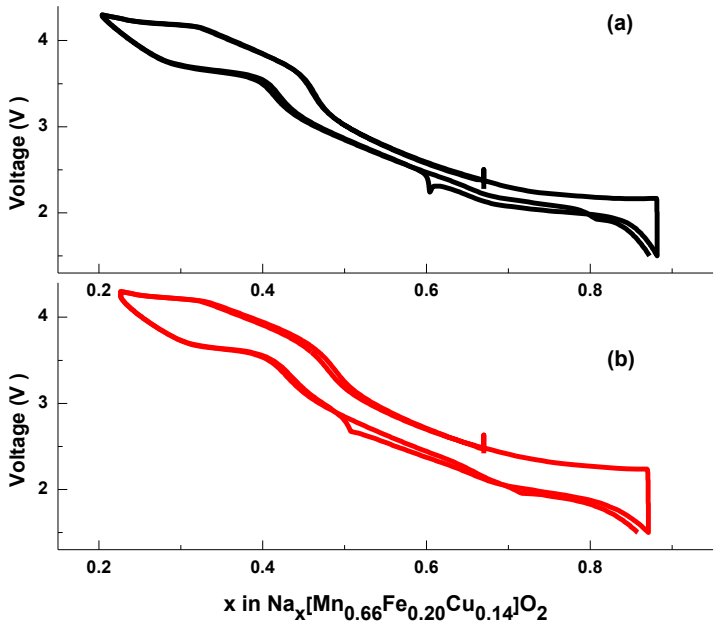

Figure 6.2 First two galvanostatic charge/discharge cycles of $Na_x[Mn_{0.66}Fe_{0.20}Cu_{0.14}]O_2$ vs. Na metal collected from an standard coin cell (a) and a coin cell modified for *operando* XAS study (b).

6.3.2 X-Ray Absorption Spectra of $Na_x[Mn_{0.66}Fe_{0.20}Cu_{0.14}]O_2$ at the Mn K-Edge

Figure 6.3 a and **Figure 6.4 a** show the first cycle charge/discharge profile of a $Na_x[Mn_{0.66}Fe_{0.20}Cu_{0.14}]O_2$ electrode (vs. Na metal), from which the XANES spectra of the sample at the Mn K-edge were measured at various compositions (sodium contents). The marks on those graphs demonstrate the points at which each scan was started. Those marks are color coded with their corresponding normalized XANES spectra presented in **Figure 6.3 b-f**, and the first derivative of normalized XANES spectra presented in **Figure 6.4 b-f**. The XANES spectra of $Na_x[Mn_{0.66}Fe_{0.20}Cu_{0.14}]O_2$ at the Mn K-edge progressively shifted to higher energy form scan M1 to M5 over the first charge (**Figure 6.3 b**), indicating the oxidation of Mn ions within this voltage range. The capacity obtained up to the point that the scan M5 was started (V = 3.4 V and t = 3.94 h, equivalent to $\Delta x \approx 0.20$ in Na_xMO_2) is in excellent agreement with the oxidation of all the trivalent manganese ions

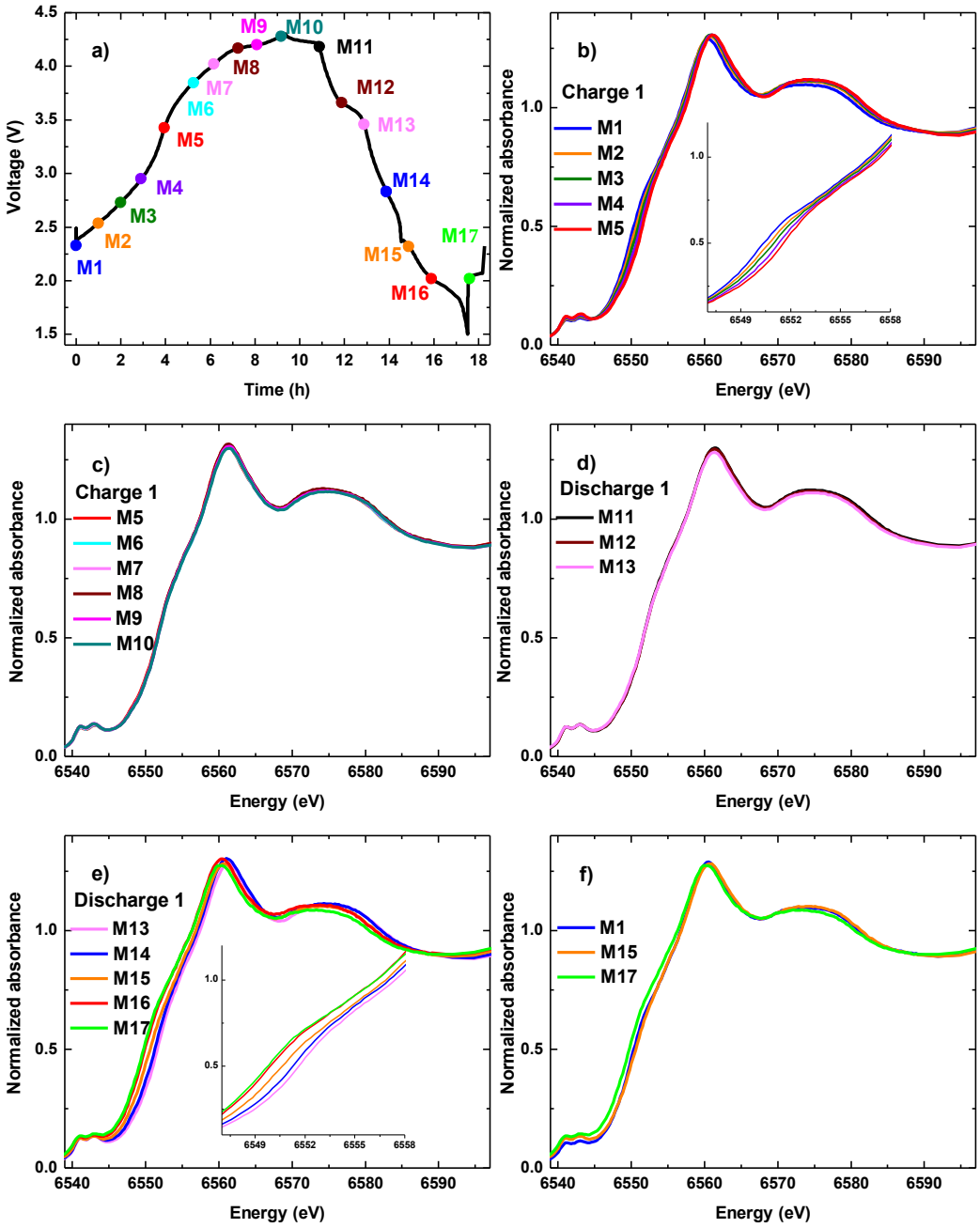

Figure 6.3 The voltage profile of a $Na_x[Mn_{0.66}Fe_{0.20}Cu_{0.14}]O_2$ electrode (vs. Na metal) from which the X-ray absorption spectra at the **Mn** K-edge were collected (a). The marks on the graph show the points at which data collection was started. Normalized XANES spectra of $Na_x[Mn_{0.66}Fe_{0.20}Cu_{0.14}]O_2$ at the **Mn** K-edge during the first charge (b,c), first discharge (d,e), and the comparison of the initial state and the end of discharge (f).

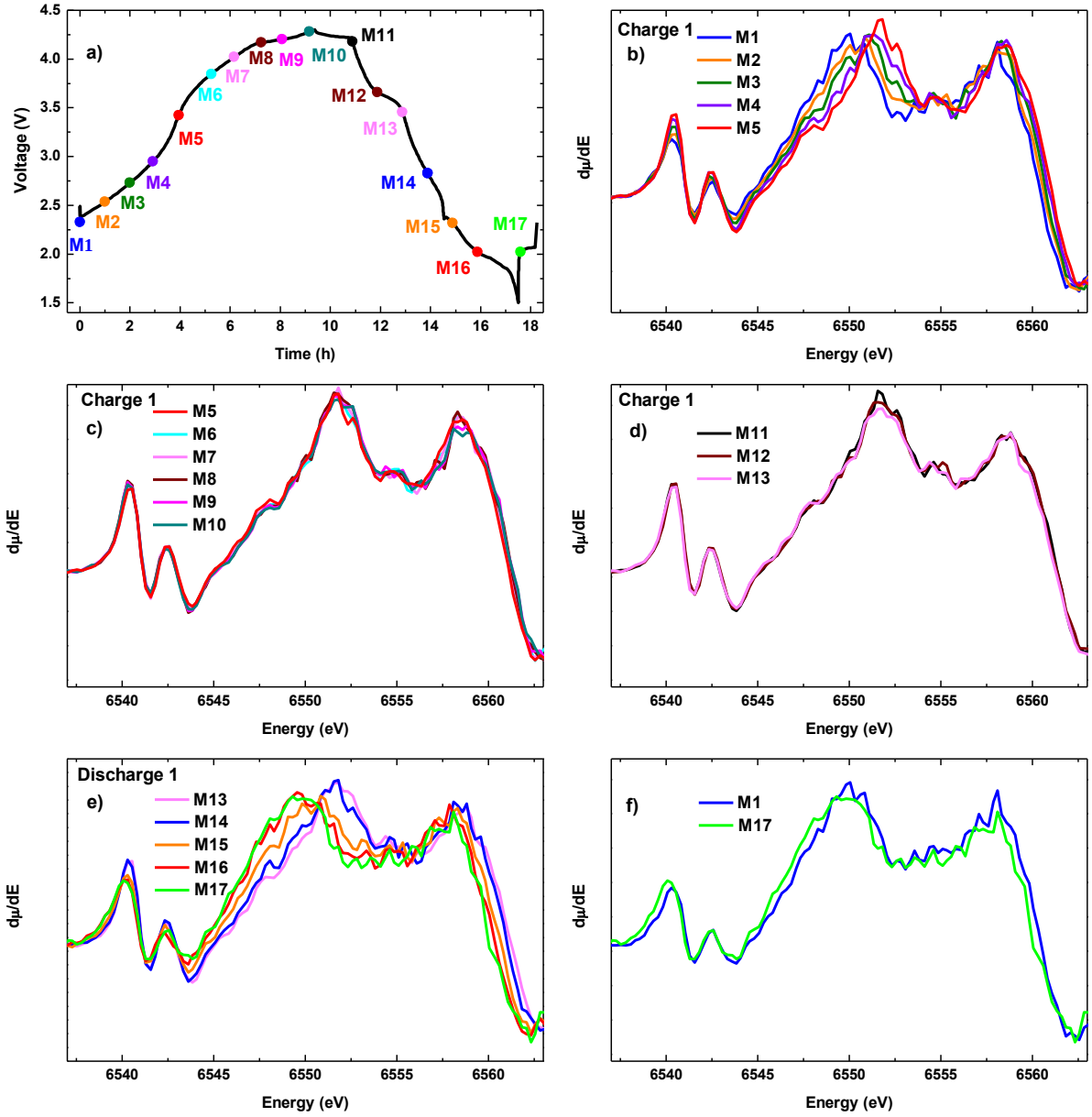

Figure 6.4 The voltage profile of a $Na_x[Mn_{0.66}Fe_{0.20}Cu_{0.14}]O_2$ electrode (vs. Na metal) from which the X-ray absorption spectra at the **Mn** K-edge were collected (a). The marks on the graph show the points at which data collection was started. Normalized first derivative of XANES spectra of $Na_x[Mn_{0.66}Fe_{0.20}Cu_{0.14}]O_2$ at the **Mn** K-edge during the first charge (b,c), first discharge (d,e), and the comparison of the initial state and the end of discharge (f).

in $Na_{0.67}[Mn^{3+}_{0.19}Mn^{4+}_{0.47}Fe^{3+}_{0.20}Cu^{2+}_{0.14}]O_2$ to the tetravalent state, assuming that Cu and Fe ions are not electrochemically active in this voltage range (see below), and no parasitic reaction occurs. The Mn K-edge XANES spectra did not change significantly from scan M5 to M10, implying that Mn ions do not participate in the redox process at voltages higher than 3.4 V. Over discharge, the Mn K-edge spectra remained unchanged from scan M10 to M13, but shifted to lower energy from scan M13 to M17, indicating the reduction of Mn ions (**Figure 6.3 d,e**). The edge position in the XANES spectrum of scan M17 is at lower energy compared to that of M1, which corresponds to the pristine composition (**Figure 6.3 f**). This shift indicates that the concentration of trivalent manganese ions in the discharged material exceeds the value in the pristine composition. Higher concentration of Mn^{3+} ions explains the orthorhombic distortion of $Na_x[Mn_{0.66}Fe_{0.20}Cu_{0.14}]O_2$ at low voltage, revealed by *operando* XRD analysis (Chapter 5). The changes in the first derivative curves are in perfect agreement with the modifications observed in the normalized XANES spectra.

The Mn K-edge XANES spectrum of $Na_{0.67}[Mn_{0.66}Fe_{0.20}Cu_{0.14}]O_2$ shows a well-resolved doublet pre-edge peak (**Figure 6.5 a**). The pre-edge peak in a K-edge XANES spectrum appears mainly due to two mechanisms.[143] First, the electric dipole transition from the 1s orbital to the p component of p-d hybridized orbitals. Second, a 1s-3d transition, which is forbidden in the electric dipole transition mechanism, but can occur due to the electric quadrupole transition. The probability of an electric quadrupole transition is much lower than that of an electric dipole transition, meaning much lower intensity of the pre-edge peak resulting from an electric quadrupole transition. An electric quadrupole transition can occur for any symmetries, whereas the p-d hybridization, therefore electric dipole transition from 1s to the p-d hybridized orbitals, does not happen for an ideal octahedral symmetry. However, the distortion of octahedral symmetry causes mixing of 3d and 4p orbitals resulting in an increase in the intensity of the pre-edge peak. The pre-edge peaks in K-edge XANES spectra of

transition metals are sensitive to, and therefore provide information about, the coordination number, symmetry, and the number of electrons of the absorbing atom.

A doublet pre-edge peak in the K-edge XANES spectrum of a 3d transition metal with the octahedral environment is assigned to quadrupole electric transitions to t_{2g} and e_g orbitals.[138,139,143] The intensity of Mn pre-edge peaks increased from scan M1 to scan M8 and remained unchanged from scan M8 to M10, the region at which the material adopts the Z-phase (Chapter 5) (**Figure 6.5 a**). The positions of the pre-edge peaks of Mn K-edge spectra do not demonstrate any discernible shift upon charge although the continuous shift of the edge from scan M1 to M5 indicates the change of oxidation state of Mn ions. The pre-edge peak intensity is inversely related to the number of 3d electrons.[143,144] However, the pre-edge peak intensity of the initial composition was not recovered at the end of discharge (**Figure 6.5 b**). The pre-edge peak intensity depends significantly on the coordination number; the pre-edge peak intensities of four-coordinated transition metal compounds are much higher than those of six-coordinated compounds.[143] Migration of transition metals into the interlayer tetrahedral site is known to occur in some Li_xMO_2[137,145] and Na_xMO_2[4,56] (M: 3d metal) at high voltage. However, the increase in the intensity of pre-edge peak of this material at voltages lower than 4.1 V cannot be assigned to the migration of a fraction of manganese ions into a tetrahedral site because no tetrahedral site exists within the interlayer space of a P2 structure and the tetrahedral site in the transition metal layer is too small to accommodate any manganese ions (a distance of $\approx$ 1.7 Å between X and O in XO_4 tetrahedron). Formation of O-type stacking faults with available tetrahedral sites does not seem to happen because the *operando* X-ray diffraction analysis of the material did not show any notable peak broadening. The increase in the intensity of the pre-edge peaks of XANES spectra at the Mn K-edge during the charge was also observed in $Li_{1.2}[Ni_xMn_yCo_z]O_2$.[138-140] It was reported that the initial oxidation state of manganese ions is 4+ in those compositions and remains unchanged during cycling. However, the

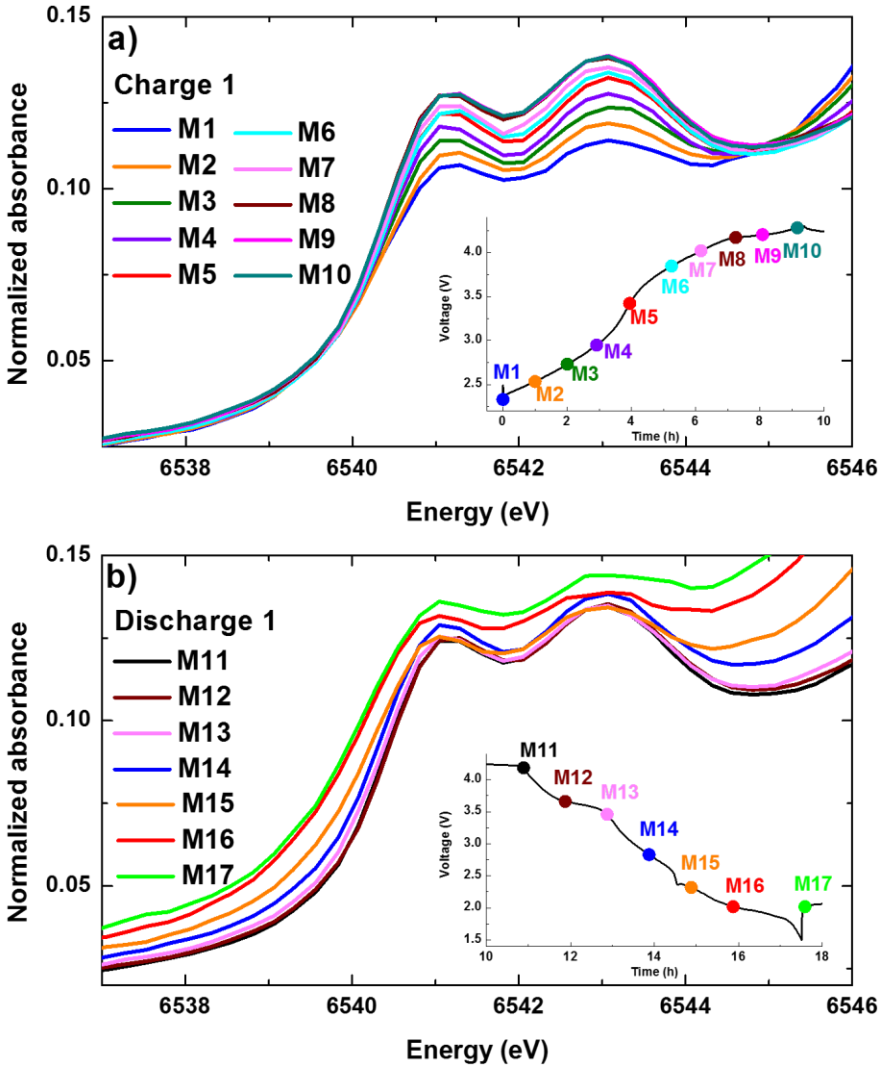

Figure 6.5 Pre-edge normalized XANES spectra of $Na_x[Mn_{0.66}Fe_{0.20}Cu_{0.14}]O_2$ electrode during the first charge (a) and the first discharge (b) collected at the Mn K-edge. The insets show the voltage profile and the points at which each scan was started.

progressive increase and decrease in the distortion of octahedral symmetry of manganese ions in $Li_{1.2}[Ni_xMn_yCo_z]O_2$ during the charge and discharge are proposed to cause increase and decrease in the intensity of pre-edge peaks during the charge and discharge. The higher intensity of Mn pre-edge peaks compared to those of Fe, Cu, and Ni pre-edge peaks in the XANES spectra of the materials in this study can be attributed to the lower number of 3d electrons in Mn^{3+} and Mn^{4+}. The significant increase of the pre-edge intensity at the Mn K-edge spectra should originate from the Mn ions octahedral symmetry distortion that we do not have an exact description of, similar to the case of some Li-rich transition metal oxides.[138-140]

6.3.3 X-Ray Absorption Spectra of $Na_x[Mn_{0.66}Fe_{0.20}Cu_{0.14}]O_2$ at the Cu K-Edge

Sodium metal oxide positive electrode materials working based on oxidation/reduction of copper ions were introduced not long ago.[125] *Ex-situ* XAS measurement at K-edge revealed the reversible oxidation of Cu ions in $Na_{2/3}[Cu_{1/3}Mn_{2/3}]O_2$ from divalent state in the pristine material to the trivalent state in the sample charged to 4.2 V (vs. Na/Na^+), whereas no significant redox activity was detected for Mn ions.[128] In another study, oxidation of Cu^{2+} and Fe^{3+} ions were shown responsible processes during the charge of O3-$Na_{0.9}[Cu_{0.22}Fe_{0.30}Mn_{0.48}]O_2$.[129] **Figure 6.6** and **Figure 6.7** show the normalized XANES spectra of $Na_x[Mn_{0.66}Fe_{0.20}Cu_{0.14}]O_2$ and their first derivative curves measured at Cu K-edge during the first charge and discharge, along with the charge profile of the cell. The spectra do not show any significant changes from scan C1 to scan C5. A small shift to higher energy is observed in the position of XANES spectra from scan C5 to scan C7. Following that, no important change in the position and the shape of the spectra is observed, indicating that the oxidation of copper ions are suppressed. During the discharge, the K-edge peak position shifts to lower energy from scan C11 to C12, in agreement with reduction of Cu ions. The overlap of absorption edges in scan C15 with scan C1 (**Figure 6.6 f**) indicates that all the copper ions oxidized during the charge are reduced to the divalent state at the end of the first

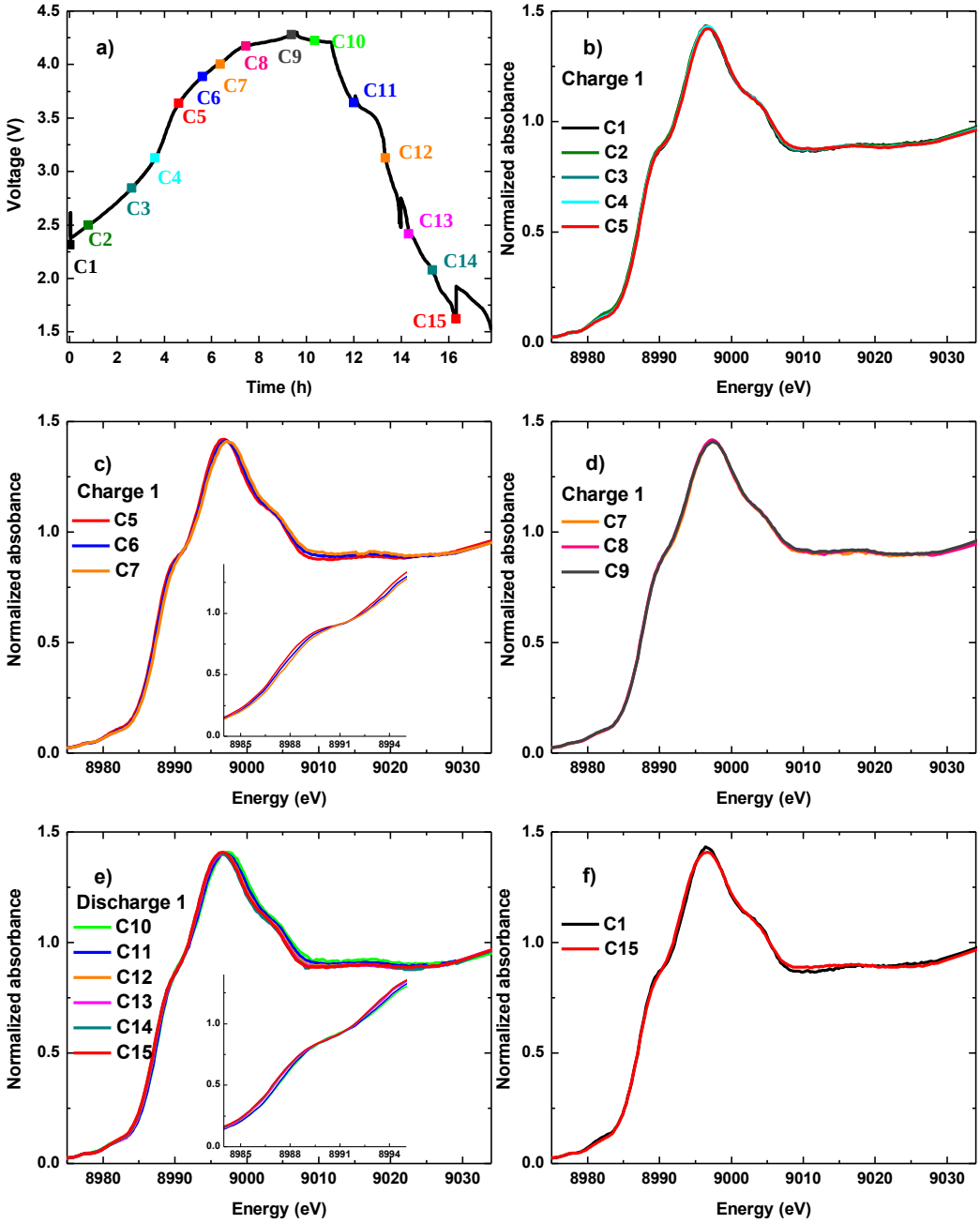

Figure 6.6 The voltage profile of a $Na_x[Mn_{0.66}Fe_{0.20}Cu_{0.14}]O_2$ electrode (vs. Na metal) from which the X-ray absorption spectra at the **Cu** K-edge were collected (a). The marks on the graph show the points at which data collection was started. Normalized XANES spectra of $Na_x[Mn_{0.66}Fe_{0.20}Cu_{0.14}]O_2$ at the **Cu** K-edge during the first charge (b-d), first discharge (e), and the comparison of the initial state and the end of discharge (f).

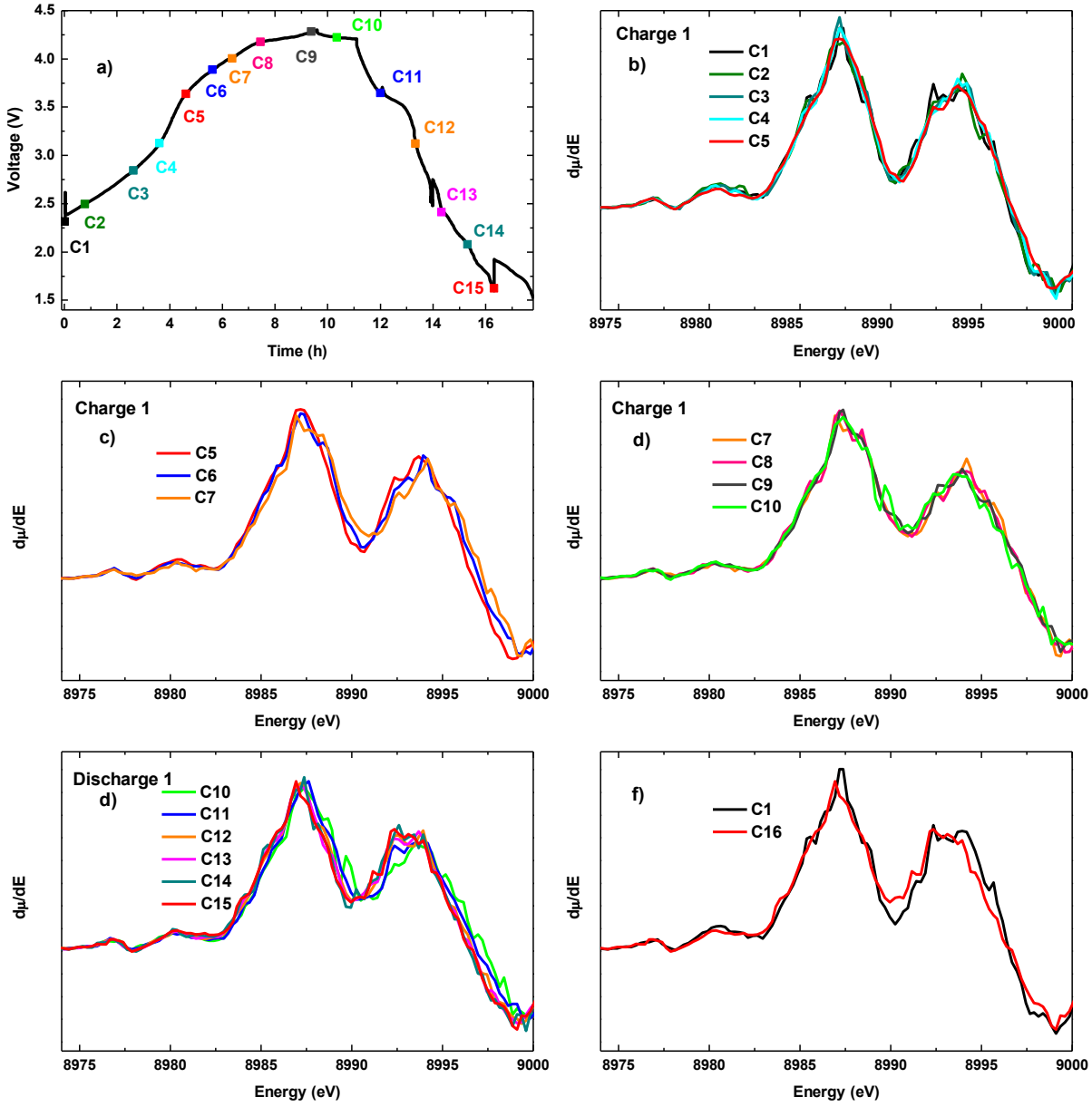

Figure 6.7 The voltage profile of a $Na_x[Mn_{0.66}Fe_{0.20}Cu_{0.14}]O_2$ electrode (vs. Na metal) from which the X-ray absorption spectra at the **Cu** K-edge were collected (a). The marks on the graph show the points at which data collection was started. Normalized first derivative of XANES spectra of $Na_x[Mn_{0.66}Fe_{0.20}Cu_{0.14}]O_2$ at the **Cu** K-edge during the first charge (b-d), first discharge (e), and the comparison of the initial state and the end of discharge (f).

discharge. It is worth noting that the shift in the position of the absorption edge and the modification of the peak features due to the charging process are more prominent in the spectrum collected from $Na_x[Cu_{1/3}Mn_{2/3}]O_2$ reported before[128] compared with the material studied in this work. This observation suggests that most probably not all the copper ions are oxidized in $Na_x[Mn_{0.66}Fe_{0.20}Cu_{0.14}]O_2$ during charge. Another mechanism that might be involved in the alteration of the local structure of Cu ions is electron transfer from oxide ions to copper ions. Negative ligand to metal charge transfer energy is reported for high valence transition metals such as Cu^{3+} and Fe^{4+} in oxide framework.[135,146,147]

The Cu K-edge spectrum of $Na_{0.67}[Mn_{0.66}Fe_{0.20}Cu_{0.14}]O_2$ shows a very weak single pre-edge peak (**Figure 6.8**). A single pre-edge peak is expected for Cu^{2+} (d^9) absorbing atoms because the t_{2g} orbital is fully occupied and only an electric quadrupole transition to the e_g orbital can occur. The X-ray absorption spectra of the latter elements of the first-row transition metals, particularly Cu, show much weaker intensity in the pre-edge peak compared to those of early transition metals; however, their pre-edge peak intensities increase significantly by changing from a six-fold coordination to a four-fold coordination environment.[143] The intensity of the pre-edge peak in the Cu K-edge spectrum of $Na_{0.67}[Mn_{0.66}Fe_{0.20}Cu_{0.14}]O_2$ is much lower than that of the Mn K-edge spectrum. Moreover, the pre-edge peak does not show any significant changes during the first charge and discharge, suggesting that the octahedral environment of copper ions is well preserved during cycling.

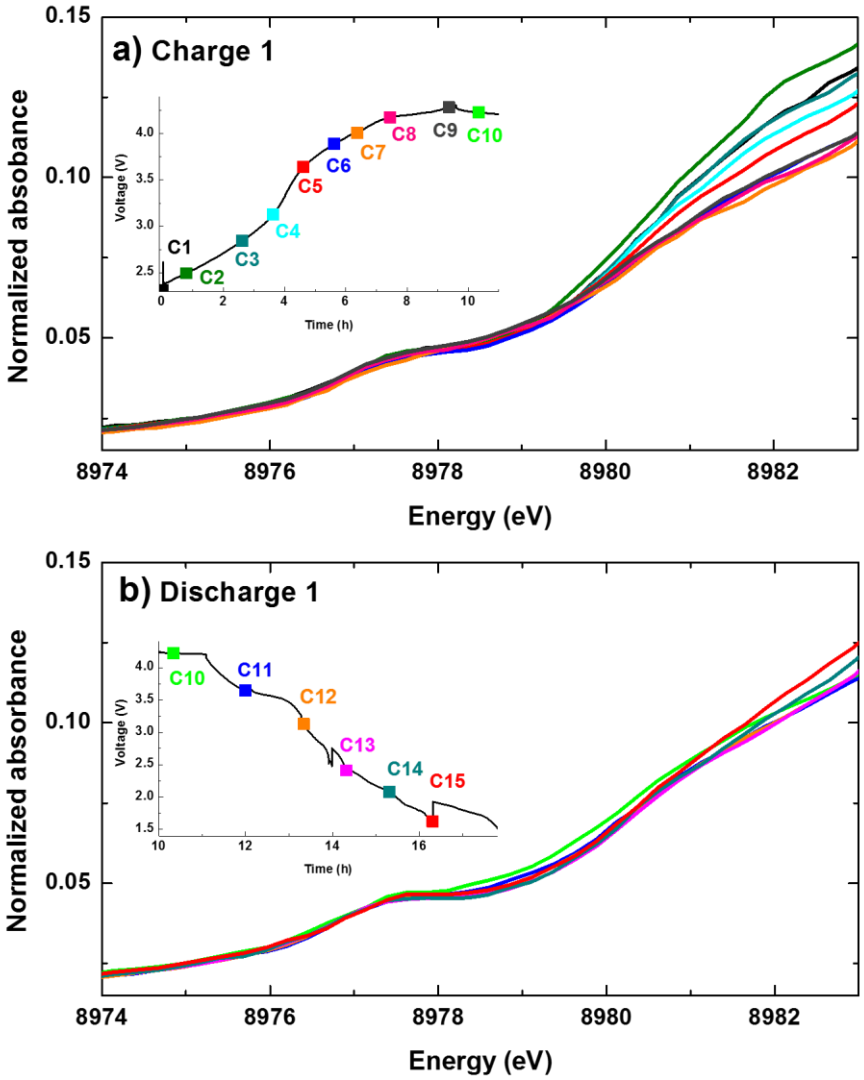

Figure 6.8 Pre-edge of the normalized XANES spectra of $Na_x[Mn_{0.66}Fe_{0.20}Cu_{0.14}]O_2$ electrode during the first charge (a) and the first discharge (b) collected at the **Cu** K-edge. The insets show the voltage profile and the points at which each scan was started.

6.3.4 X-Ray Absorption Spectra of $Na_x[Mn_{0.66}Fe_{0.20}Cu_{0.14}]O_2$ at the Fe K-Edge

The X-ray absorption spectra of Fe ions in $Na_x[Mn_{0.66}Fe_{0.20}Cu_{0.14}]O_2$ demonstrate no discernable change in the rising edge of absorption spectra from scan F1 to F6 during charge, but small modifications are observed in the absorption maxima (**Figure 6.9 b**). The most noticeable evolution in the Fe K-edge spectra during charge appears at scan F7 (the scan started at the voltage of 4.06 V); the peak maximum intensity obviously decreased (**Figure 6.9 c**). Similar behavior was observed for the Fe K-edge XANES spectrum of P2-$Na_{2/3}[Mn_{1/2}Fe_{1/2}]O_2$ when charged from 3.8 V to 4.2 V.[53] The *operando* XAS measurements show that scan F8 and scan F9 overlap perfectly over both the rising edge and the peak maximum, and change slightly at the absorption maximum compared to scan F7 (**Figure 6.9 d**). However, scan F10, collected at open circuit voltage after charging to 4.3 V, shows a slight change of the absorption edge and maximum compared with scans F8 and F9. During discharge, the Fe K-edge XANES spectra do not change much from scan F10 to scan F12, but an evident modification is noticed from scan F12 to scan F13 (**Figure 6.9 e**). A comparison of scan F1 and F13 demonstrates an irreversible modification in the shape of the spectrum, at the absorption maximum and higher energy region, caused by charge and discharge processes (**Figure 6.9 f**). Importantly, no shift is observed in the position of the Fe K-edge in the first derivative curves of the normalized XANES spectra of $Na_x[Mn_{0.66}Fe_{0.20}Cu_{0.14}]O_2$ at various compositions during the charge and discharge although the intensity changes at high voltage (**Figure 6.10**). This behavior is contrary to those of observed for other transition metals measured in this study that the evolution in the normalized XANES spectra is reflected in the position of peaks in the derivative curves. The changes in the shape and the intensity of absorption maxima in Fe K-edge XANES spectra seem to originate from Fe ions local structure modifications, although no change in the position of dμ/dE curve occurs; similar behavior is reported for $Na_x[Mn_{1/2}Fe_{1/2}]O_2$ [53] and Na_xFeO_2 [4], in which the oxidation of Fe^{3+} to Fe^{4+} is proved by Mössbauer spectroscopy.

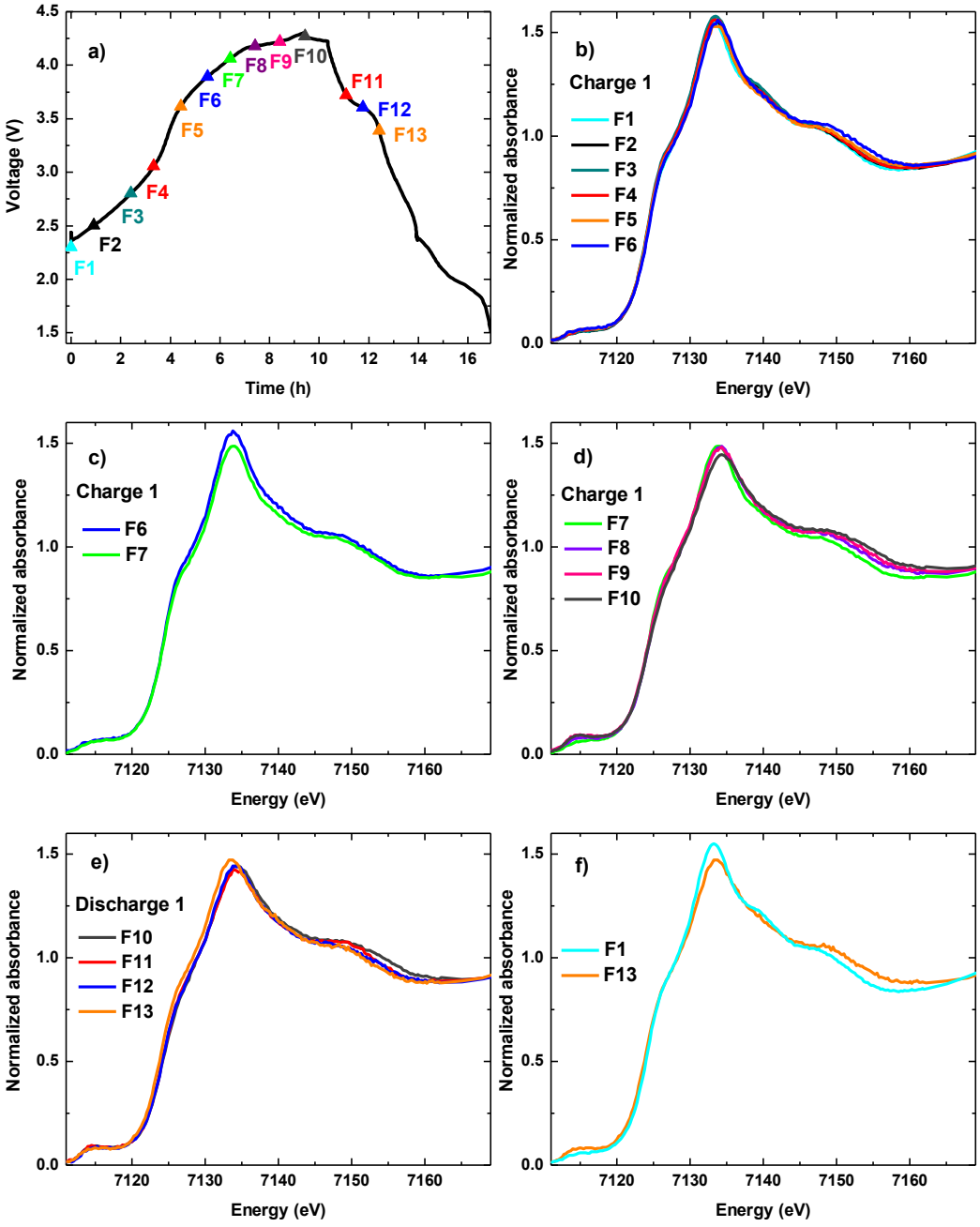

Figure 6.9 The voltage profile of a $Na_x[Mn_{0.66}Fe_{0.20}Cu_{0.14}]O_2$ electrode (vs. Na metal) from which the X-ray absorption spectra at the **Fe** K-edge were collected (a). The marks on the graph show the points at which data collection was started. Normalized XANES spectra of $Na_x[Mn_{0.66}Fe_{0.20}Cu_{0.14}]O_2$ at the **Fe** K-edge during the first charge (b-d), first discharge (e), and the comparison of the initial state and the end of discharge (f).

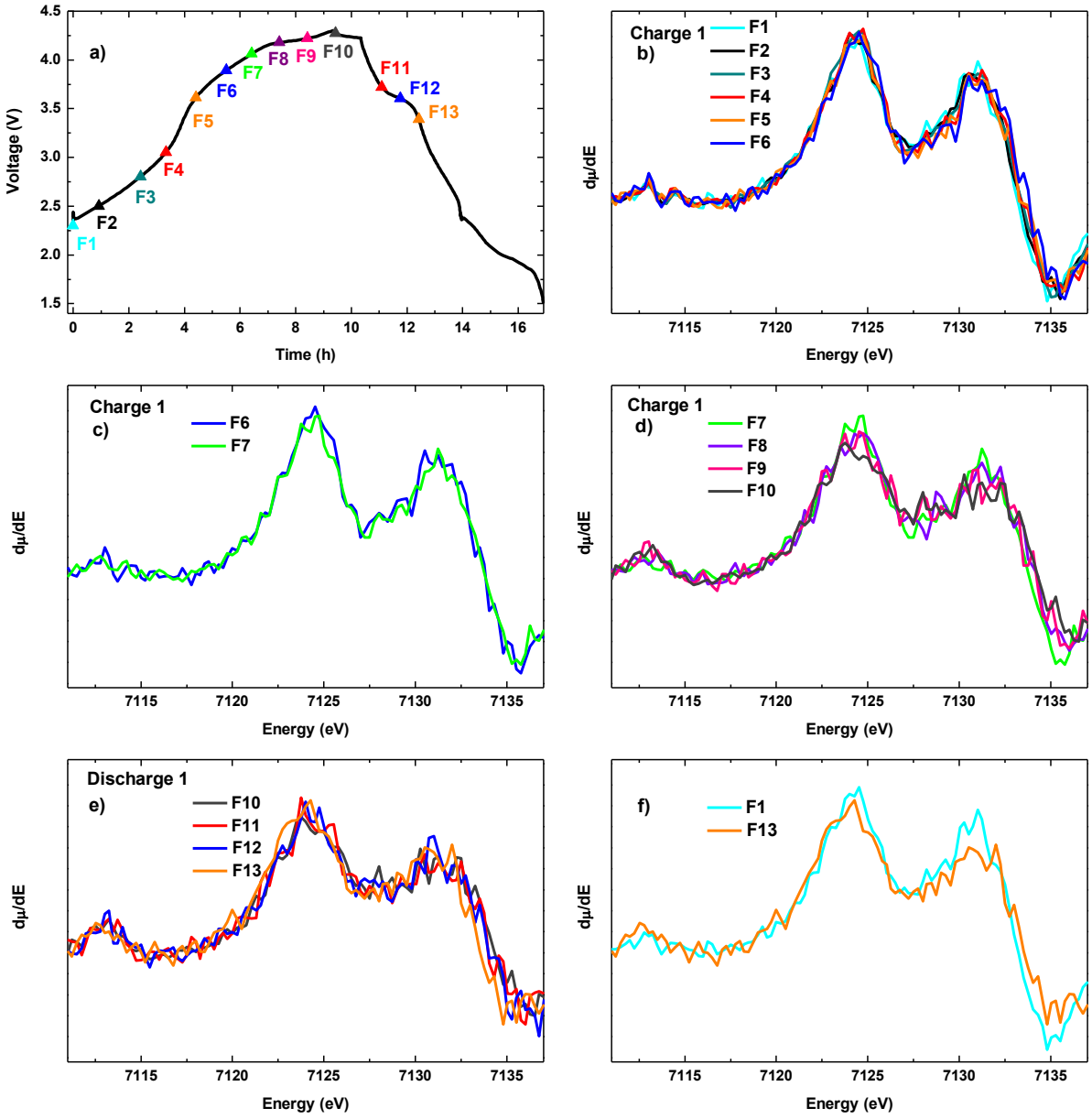

Figure 6.10 The voltage profile of a $Na_x[Mn_{0.66}Fe_{0.20}Cu_{0.14}]O_2$ electrode (vs. Na metal) from which the X-ray absorption spectra at the **Fe** K-edge were collected (a). The marks on the graph show the points at which data collection was started. Normalized first derivative of XANES spectra of $Na_x[Mn_{0.66}Fe_{0.20}Cu_{0.14}]O_2$ at the **Fe** K-edge during the first charge (b-d), first discharge (e), and the comparison of the initial state and the end of discharge (f).

If the modifications in the shape and intensity of the normalized XANES spectra of Fe K-edge is attributed to the oxidation of iron ions, only a small fraction of Fe ions get oxidized during the charge of the $Na_x[Mn_{0.66}Fe_{0.20}Cu_{0.14}]O_2$/Na cell, *i.e.*, less than 25% of Fe ions assuming that $Fe^{3+/4+}$ redox process is the only responsible mechanism within the narrow voltage window of 3.9 to 4.1 V (corresponding to scan F6 to F7). In the study[56] presented in Chapter 4, it was reported that the concentrations of Fe^{4+} ions in the oxidized states of $Na_x[Mn_{0.5+y}Ni_yFe_{0.5-2y}]O_2$ ($x \approx 0.15$, $y = 0, 0.1, 0.15$) measured by Mössbauer spectroscopy were systematically lower than the values expected from electrochemical measurements. The redox activity of oxide ions was suggested based on a combination of structural characterizations, Mössbauer spectroscopy, and electrochemical measurements. In another study, [148] it was shown that about 20% of Fe^{4+} ions formed by charging O3-$NaFeO_2$ to 3.6 V were reduced back to Fe^{3+} during the storage of the charged cell at open circuit voltage. It was suggested that although conventional organic electrolytes are expected to be stable over this voltage range, the catalytic effect of Fe^{4+} ions facilitates the oxidation of the electrolyte. However, the chemical instability of Fe^{4+} ions is not expected to affect the spectra in this study because of the real-time nature of this characterization.

The shape of the pre-edge peak in the Fe K-edge spectrum of $Na_{0.67}[Mn_{0.66}Fe_{0.20}Cu_{0.14}]O_2$ is unclear due to the level of noise induced by the interference from the Mn ions X-ray absorption. However, it is clearly observable that the pre-edge peak intensity increases from scan F7 to F9 (**Figure 6.11 a**), at the voltage region which the Z-phase is formed. Similarly, the intensity of pre-edge peak was increased in the Fe K-edge XANES spectra of O3-$Na_{1-x}FeO_2$ when it was charged up to 4 V vs. Na.[4] Moreover; the EXAFS data showed decreases in the length of the first coordination shell (Fe-O) and the intensity of the second coordination shell (Fe-Fe). Significant improvement is found in the capacity retention and the voltage polarization of O3-$NaFeO_2$ when the cutoff voltage is limited to 3.4 V. Electrochemical measurements, and ex-situ XRD analysis indicated an irreversible phase transition in $Na_{1-x}FeO_2$

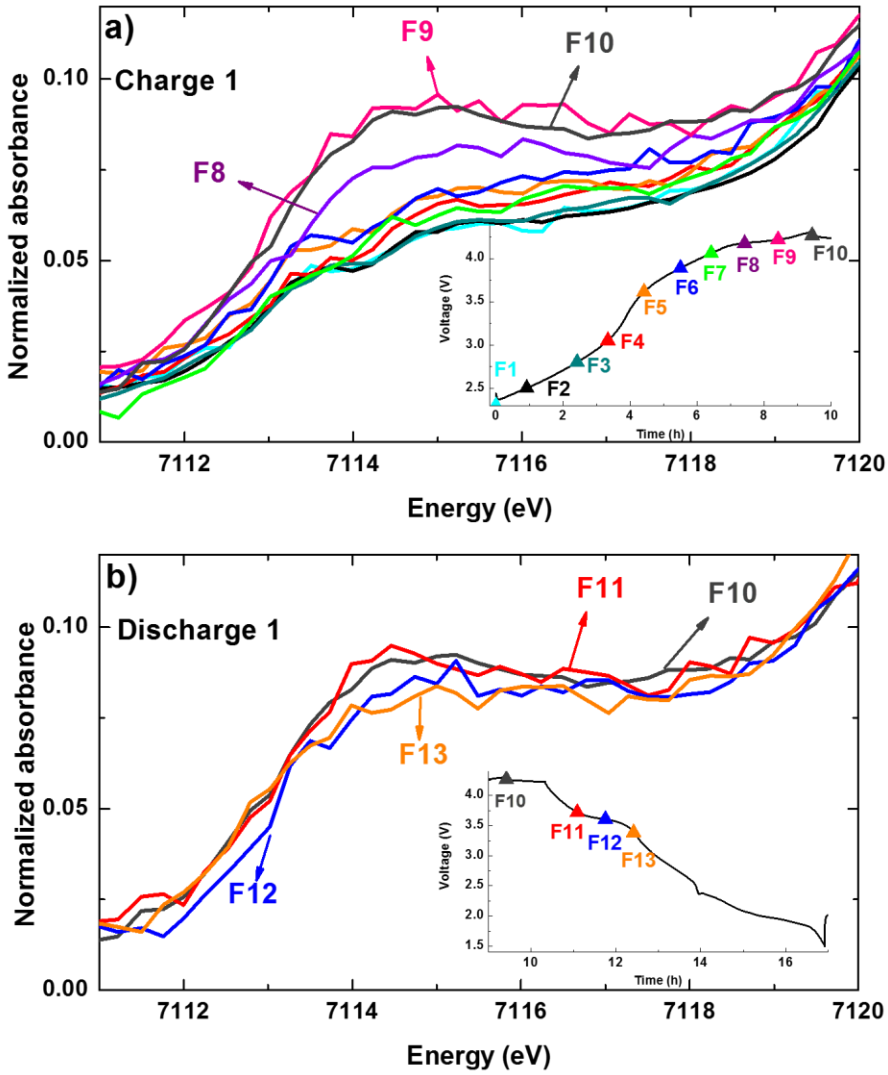

Figure 6.11 Pre-edge of normalized XANES spectra of $Na_x[Mn_{0.66}Fe_{0.20}Cu_{0.14}]O_2$ electrode during the first charge (a) and the first discharge (b) collected at the **Fe** K-edge. The insets show the voltage profile and the points at which each scan was started.

induced by extraction of sodium ions upon charge.[4] Based on the evolution of Fe K-edge XANES data, irreversible migration of some of Fe^{3+} ions into tetrahedral sites available in the interlayer space at high voltage was suggested as the origin of the degradation of O3-$NaFeO_2$.[4] The increase in the intensity of pre-edge peak in the Fe K-edge XANES spectra supports the migration of a small fraction of Fe ions into interlayer tetrahedral sites at high voltage (> 4 V) suggested by the PDF analysis of this material and other Fe-containing P2-type sodium metal oxides.[56] The intensity of the pre-edge peak did not recover to its initial value during discharge to 3.4 V, at which scan F13 was collected (**Figure 6.11 b**). However, the reversibility of the high voltage phase in the P2-type Fe-containing oxides is importantly different from O3-type ones as evidenced by the electrochemical performance; a P2-$Na_{0.67}[Mn_{0.66}Fe_{0.20}Cu_{0.14}]O_2$/Na cell delivers ≈ 96% of its initial capacity in the fifth discharge when cycled within 1.5 - 4.3 V range (Chapter 5), whereas an O3-$NaFeO_2$/Na cell shows less than 20% of its initial capacity after 5 cycles when cycled within the 2.5 - 4.0 V range. Moreover, the first discharge capacity of O3-$NaFeO_2$ is decreased by increasing the upper limit of the cycling voltage from 3.5 to 4.5 V.

6.3.5 X-Ray Absorption Spectra of $Na_x[Mn_{0.65}Fe_{0.20}Ni_{0.15}]O_2$ at the Ni K-Edge

The X-ray absorption spectra of $Na_x[Mn_{0.65}Fe_{0.20}Ni_{0.15}]O_2$ at the Ni K-edge do not show any notable change from scan N1 to N3 (**Figure 6.12 b**, **Figure 6.13 b**). The spectra shifted progressively to higher energy from scan N3 to scan N7 (**Figure 6.12 c**, **Figure 6.13 c**), demonstrating the oxidation of Ni ions upon charge within this range. The XANES spectra remain unchanged upon charge from scan N7 to scan N10 (**Figure 6.12 d**, **Figure 6.13 d**). During discharge, the absorption spectra shifted to lower energy from scan N11 to scan N15, indicating the reduction of nickel ions (**Figure 6.12 d**, **Figure 6.13 e**). Excellent overlap of scan N17 and scan N1 demonstrates the reversibility of the nickel redox reaction in $Na_x[Mn_{0.65}Fe_{0.20}Ni_{0.15}]O_2$ in this voltage range (**Figure 6.12 f**).

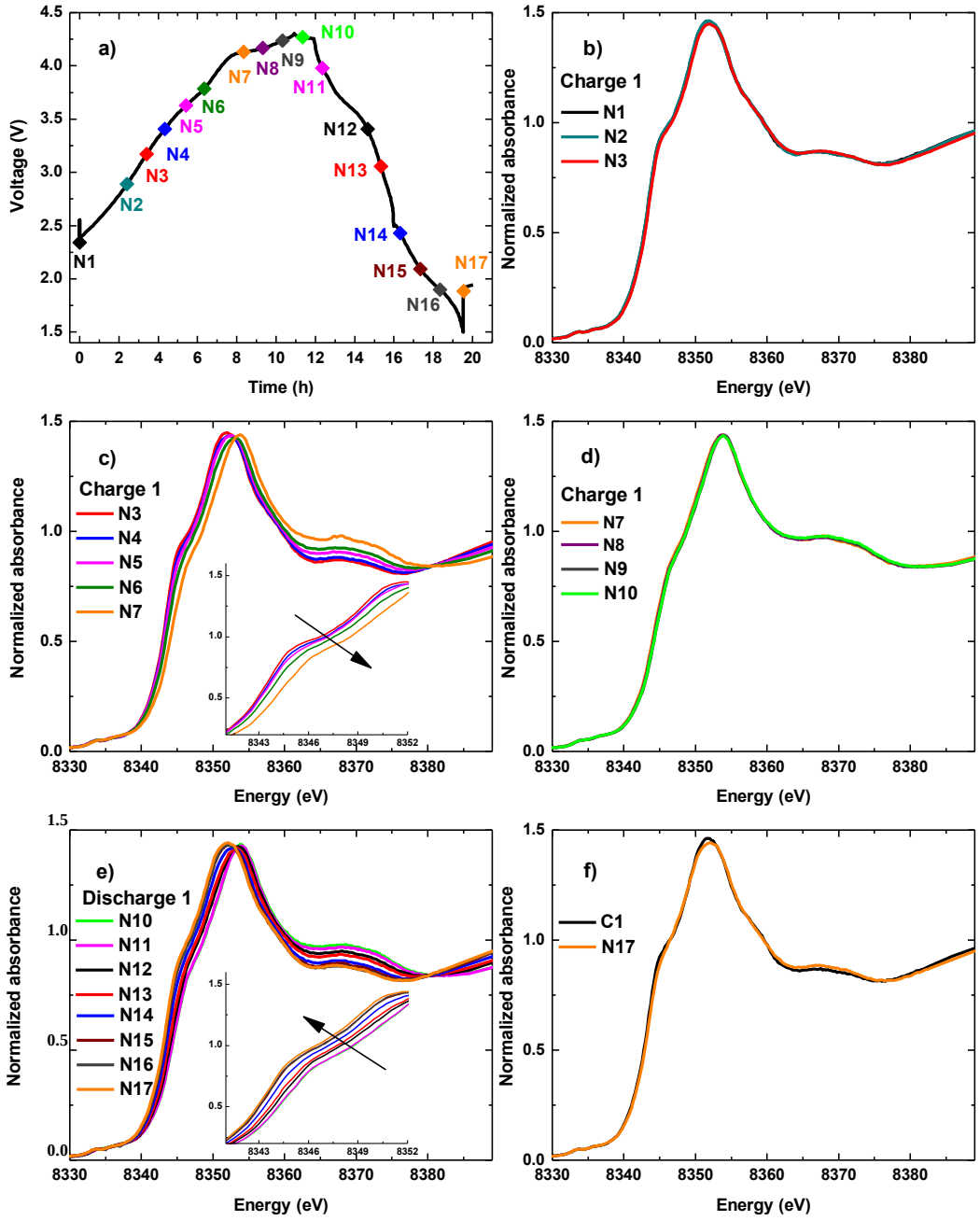

Figure 6.12 The voltage profile of a $Na_x[Mn_{0.65}Fe_{0.20}Ni_{0.15}]O_2$ electrode (vs. Na metal) from which the X-ray absorption spectra at the **Ni** K-edge were collected (a). The marks on the graph show the points at which data collection was started. Normalized XANES spectra of $Na_x[Mn_{0.65}Fe_{0.20}Ni_{0.15}]O_2$ at the **Ni** K-edge during the first charge (b-d), first discharge (e), and the comparison of the initial state and the end of discharge (f).

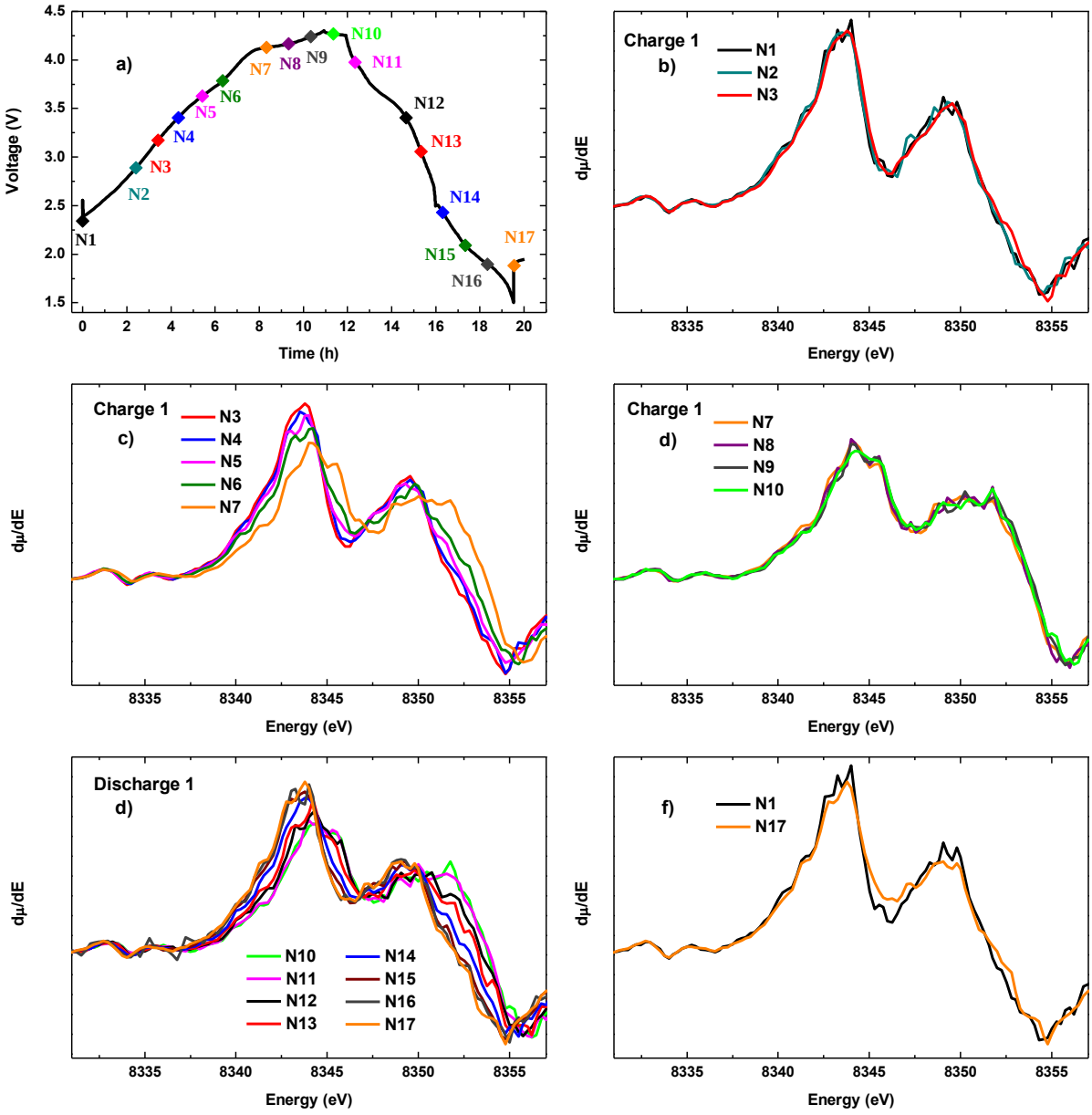

Figure 6.13 The voltage profile of a $Na_x[Mn_{0.65}Fe_{0.20}Ni_{0.15}]O_2$ electrode (vs. Na metal) from which the X-ray absorption spectra at the **Ni** K-edge were collected (a). The marks on the graph show the points at which data collection was started. Normalized first derivative of XANES spectra of $Na_x[Mn_{0.65}Fe_{0.20}Ni_{0.15}]O_2$ at the **Ni** K-edge during the first charge (b-d), first discharge (e), and the comparison of the initial state and the end of discharge (f).

The shift in the position of the absorption peak at the Ni K-edge in $Na_x[Mn_{0.65}Fe_{0.20}Ni_{0.15}]O_2$ from the pristine composition to the charged one is about two times higher than that value for the Mn K-edge in $Na_x[Mn_{0.66}Fe_{0.20}Cu_{0.14}]O_2$. This fact suggests the oxidation of Ni^{2+} to Ni^{4+} upon charge. Reversible oxidation of Ni^{2+} ions to Ni^{4+} or $Ni^{3/4+}$ is commonly observed during the charge/discharge of lithium metal oxides[139,140,149] and sodium metal oxides.[49,150] The maximum capacity that can be achieved from charging a $Na_x[Mn_{0.65}Fe_{0.20}Ni_{0.15}]O_2$/Na cell from scan N3 to N7 is equivalent to the extraction of ≈ 0.26 mole Na^+ from one mole of active material (**Figure 6.12 a**), implying partial oxidation of nickel ions to tetra-valence.

A low-intensity doublet pre-edge peak in the Ni K-edge XANES spectrum of $Na_{0.67}[Mn_{0.65}Fe_{0.20}Ni_{0.15}]O_2$ is evident (**Figure 6.14**). The presence of two pre-edge peaks in the XANES spectra of Ni^{2+} (d^8) ions was reported in $Li[Li_{0.2}Ni_{0.16}Mn_{0.56}Co_{0.08}]O_2$.[139] The first and the second peaks in the pre-edge peak of Ni^{2+} ions were assigned to the dipole transition and quadrupole transition, respectively, in rock-salt type NiO.[151] The intensity of the pre-edge peak in this study did not change during the first charge and discharge. However, the peak positions shifted to higher/lower energy during oxidation/reduction.

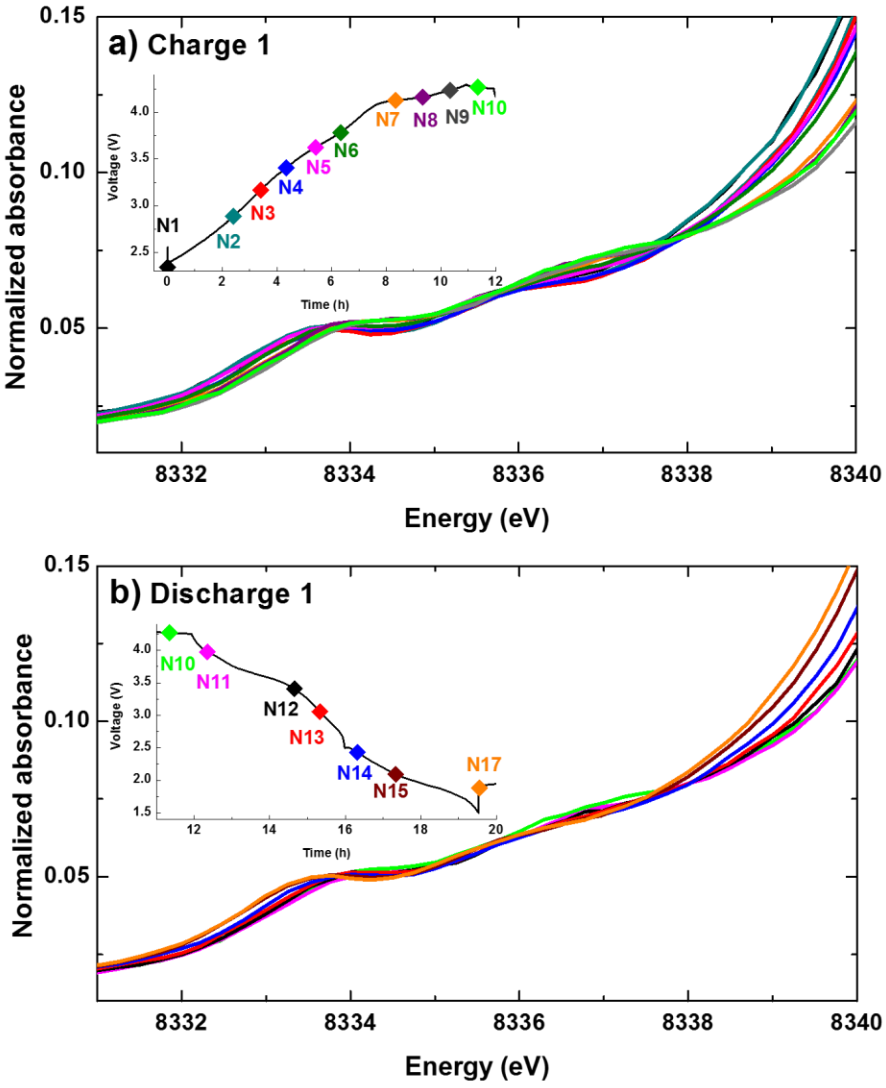

Figure 6.14 Pre-edge of **Ni** K-edge normalized XANES spectra of $Na_x[Mn_{0.65}Fe_{0.20}Ni_{0.15}]O_2$ electrode during the first charge (a) and the first discharge (b). The inset shows the voltage profile and the points at which each scan was started.

6.3.6 Discussion

A $Na_{0.67}[Mn_{0.66}Fe_{0.20}Cu_{0.14}]O_2$/Na cell was cycled at a constant current rate of 13 $mA.g^{-1}$ (C/20) in the 4.3 - 1.5 V window. Electrochemical measurements showed the extraction of ≈ 0.45 mol Na^+ per one mole of active material in the first charge. The *operando* X-ray absorption spectra of $Na_x[Mn_{0.66}Fe_{0.20}Cu_{0.14}]O_2$ collected at Mn, Fe and Cu K-edges during the first charge showed modifications at certain voltage ranges, indicating the contribution of each transition metal ion to the oxidation reaction. An important observation is that the XANES spectra of the transition metals show no discernable evolution at voltages higher than 4.1 V, at which the high voltage phase transition occurs as demonstrated by *operando* XRD. In other words, the oxidation of Mn^{3+}, Fe^{3+} and Cu^{2+} to Mn^{4+}, $Fe^{3+,4+}$, $Cu^{2+,3+}$, respectively, compensate the charge for the extraction of ≈ 0.35 mol Na^+, demonstrated by the shift in the position of the absorption edges. This observation suggests the contribution of the oxide anions to the redox reaction. Moreover, the XANES spectra of $Na_x[Mn_{0.66}Fe_{0.20}Cu_{0.14}]O_2$ collected at Mn, Cu, and Fe K-edges do not show any discernible evolution when discharged from high voltage to 3.6 V. This fact implies the reversibility of the oxygen redox reaction.

The role of ligand to metal charge transfer was previously proposed in P2-$Na_{0.67}[Mn_{0.5}Fe_{0.5}]O_2$, based on a combination of Mössbauer spectroscopy, structural analyses, and electrochemical measurements.[56] The redox chemistry of oxide anions in Li_2MO_3-based oxides (M: transition metal), such as $Li_{1+x}[Ni_yCo_zMn_{1-x-y-z}]O_2$ and $Li_2[Ru_{1-y}M_y]O_3$, is known and has gained much attention for investigation.[145,152,153,154] Lithium-excess manganese-rich transitional metal oxides deliver high capacities (beyond the values expected from cationic redox reactions) along with a characteristic voltage plateau during the first charge. Oxygen evolution from the structure has been considered an important mechanism involved in the first charge oxidation process of Li_2MnO_3-based oxides.[155,156] It was reported that the oxygen participation into the first charge process of $Li_{1.20}[Mn_{0.54}Co_{0.13}Ni_{0.13}]O_2$[153] is in the form of irreversible O_2 gas evolution at the surface, whereas oxide ions are partially oxidized

without leaving the structure within the bulk and are reduced back at the following discharge. A combination of X-ray photoelectron spectroscopy, transmission electron microscopy, and density functional theory (DFT) calculations studies of $Li_2[Ru_{1-y}M_y]O_3$ revealed the reversible oxidation of oxide ions to peroxo-like O_2^{2-} species, concomitantly with the migration of transition metals within the metal and lithium layers.[145] In a recent study,[157] a significant contribution of oxygen orbitals to the redox reaction of O3-$NaFe_{0.5}Ni_{0.5}O_2$ was disclosed by a combination of X-ray spectroscopy, Mössbauer spectroscopy, and density functional theory calculations.

This *operando* XANES study of P2-$Na_{0.67}[Mn_{0.66}Fe_{0.20}Cu_{0.14}]O_2$ suggests the reversible participation of oxide anions in the redox process. Electrolyte decomposition cannot be the main responsible mechanism that accounts for the charge obtained at voltages higher than 4.1 V because the phase transition occurring at that voltage implies an evolution of the structure. The evolution of oxygen gas from the structure is not the principal oxidation mechanism in this system as demonstrated by the good reversibility of the redox reaction. The reversible contribution of oxide anions is concomitant with the migration of transition metals, as suggested by pair distribution function analysis (Chapter 5). Further study of anionic redox chemistry in this material, such as O K-edge and 3d metal L-edge XANES measurement, is in the process in our research team to achieve an in-depth understanding of the involved redox reactions, which is necessary for the design of high-performance electrode materials for Na-ion batteries.

6.4 Conclusions

In this study, the redox reactions involved in the charge and discharge processes of P2-$Na_{0.67}[Mn_xFe_yM_{1-x-y}]O_2$ (M: Cu, Ni) were investigated by *operando* X-ray absorption spectroscopy. The X-ray absorption spectra were measured at the Mn, Fe, and Cu K-edges in $Na_x[Mn_{0.66}Fe_{0.20}Cu_{0.14}]O_2$, and at the Ni K-edge in the $Na_x[Mn_{0.65}Fe_{0.20}Ni_{0.15}]O_2$ during the first charge and discharge. The modifications of the local structure of each transition metal were probed by monitoring the evolution

of the XANES data. The first charging process in $Na_x[Mn_{0.66}Fe_{0.20}Cu_{0.14}]O_2$ starts with the oxidation of Mn^{3+} ions to Mn^{4+}, and is followed by the partial oxidation of Cu^{2+} to Cu^{3+} and Fe^{3+} to Fe^{4+}. Ni^{2+} ions in $Na_{0.67}[Mn_{0.65}Fe_{0.20}Ni_{0.15}]O_2$ are oxidized to $Ni^{3+/4+}$ during the first charge. Fe, Cu, and Ni ions are reduced back to their initial valence states in the pristine compositions during the first discharge, whereas the concentration of Mn^{3+} increases as the electrode is discharged to 1.5 V vs. Na. The XANES spectra collected at Mn, Cu, Fe, and Ni K-edges remained unchanged during the first charge at voltages higher than 4.1 V and during the first discharge at voltages higher than 4.0 V. This observation suggests a reversible contribution of oxide ions to the redox process. The redox chemistry of oxide anions is recognized in lithium-rich transition metal oxides.[145,152,154]

The intensity of the pre-edge peaks in the XANES spectra increased from the start of the charge up to 4.1 V at the Mn and K-edge, and from 4.1 V to the end of charge at the Fe K-edge, indicating the irreversible evolution of their local structures at different voltage ranges. The increase of the pre-edge peaks at the Fe K-edge at voltages higher than 4.1 V, at which the high voltage phase transition occurs, supports the degradation mechanism caused by the migration of Fe^{4+} cations into the interlayer tetrahedral sites, proposed by PDF analysis.

Chapter 7

Summary and Future Outlook

This thesis presents a study of manganese and iron containing layered P2-type oxides as auspicious materials for positive electrodes in Na-ion batteries. P2-$Na_{0.67}[Mn_{0.5}Fe_{0.5}]O_2$ is a promising candidate for this application owing to its high specific energy (> 500 $Wh.Kg^{-1}$), sustainability, and safety. Nevertheless, this material suffers from air-instability, similar to many other layered sodium metal oxides. The instability of this material in ambient conditions was known by the research community. However, the nature of this reactivity was not understood, and its important impact on electrochemical performance was underestimated. The TGA-MS characterizations, diffraction analyses, and SEM investigations, coupled with electrochemical measurements revealed the complex reactivity of P2-$Na_{0.67}[Mn_{0.5}Fe_{0.5}]O_2$ with air, including the room temperature insertion of carbonate anions into the lattice, concomitant with oxidation of Mn^{3+} ions into Mn^{4+} (Chapter 3). The rigorous protection of electrodes against air is necessary for good electrochemical performance; an air-exposed electrode of P2-$Na_{0.67}[Mn_{0.5}Fe_{0.5}]O_2$ demonstrates larger polarization and lower capacity compared to an air-protected electrode. Moreover, in contrary to the case of an air-protected electrode, the second charge profile of an air-exposed electrode does not superimpose with the first charge, due to the decomposition of carbonate anions upon the first charge, as revealed by online electrochemical mass spectrometry. We demonstrated that the substitution of Fe in P2-$Na_{0.67}[Mn_{0.5}Fe_{0.5}]O_2$ by Mn/Ni ions diminishes the air-reactivity of the material, as evidenced by electrochemical characterization. This fact indicates the importance of composition modifications to address the instability issue of layered oxides for further development of Na-ion batteries.

Chapter 4 presents a study of the structural evolution of P2-$Na_{0.67}[Mn_{0.5}Fe_{0.5}]O_2$ and P2-$Na_{0.67}[Mn_{0.65}Fe_{0.20}Ni_{0.15}]O_2$ when subjected to electrochemical extraction and insertion of sodium ions,

and its correlation with the electrochemical performance of those materials. As demonstrated by *operando* X-ray diffraction analysis, $Na_x[Mn_{0.5}Fe_{0.5}]O_2$ and $Na_x[Mn_{0.65}Fe_{0.20}Ni_{0.15}]O_2$ uphold their initial P2 structure over a wide range of stoichiometry, but show two phase transitions when cycled between 4.3 - 1.5 V vs. Na/Na^+; first, a transition to a poor crystalline phase, referred to as Z-phase, at high voltage, and second, a transition to the orthorhombic P′2 phase at low voltage, induced by cooperative distortion of Jahn-Teller active Mn^{3+} ions. The high voltage Z phase, which is observed only in Fe-containing layered oxides, was characterized by PDF analysis. It was proposed that the Z-phase formation is induced by migration of transition metals from MO_2 layers into the interlayer space at high sodium vacancy concentrations. The impact of the phase transitions on the electrochemical performance of the P2-$Na_{0.67}[Mn_{0.5}Fe_{0.5}]O_2$ and P2-$Na_{0.67}[Mn_{0.65}Fe_{0.20}Ni_{0.15}]O_2$ electrodes was investigated by adjusting the cut-off voltage. The delivered specific energy of the cells as a function of cycle number deteriorates due to the impact of phase transitions, especially the high voltage one. When the cutoff voltage is set so that the phase transitions are avoided, a P2-$Na_{0.67}[Mn_{0.65}Fe_{0.20}Ni_{0.15}]O_2$/Na cell retains ≈ 80% of the initial specific energy after 150 cycles (C/10 rate). This remarkably enhanced cycle life is achieved at the expense of energy. The P2 phase stability domain in the nickel-substituted composition, P2-$Na_{0.67}[Mn_{0.65}Fe_{0.20}Ni_{0.15}]O_2$, is slightly larger than that of the parent P2-$Na_{0.67}[Mn_{0.5}Fe_{0.5}]O_2$, resulting in a 25% energy boost when cycled within a range that the phase transitions are hindered.

The most likely future application of Na-ion batteries would be for large-scale energy storage, such as grid storage, where cost-effectiveness and sustainability are more critical concerns compared to gravimetric and volumetric energy density. This is because of the estimated increasing price of high-performance Li-ion batteries, whereas Na-ion batteries are more cost-effective and sustainable, but deliver lower energy. Therefore, resource availability and low cost are important criteria for Na-ion battery materials design. P2-$Na_{0.67}[Mn_{0.66}Fe_{0.20}Cu_{0.14}]O_2$, a material composed of low-cost transition

metals, was synthesized and investigated (Chapter5). This study presents a systematic comparison of the impact of substitution of copper and nickel ions into the parent sodium manganese iron oxide material. *Operando* X-ray diffraction analysis upon charge/discharged revealed slightly limited P2 stability domain of $Na_x[Mn_{0.66}Fe_{0.20}Cu_{0.14}]O_2$ compared to the nickel-substituted composition, due to Jahn-Teller effect of Cu^{2+} ions and increased migration of transition metals at high voltage, as revealed by PDF analysis. Besides that, the total capacity delivered by $Na_x[Mn_{0.66}Fe_{0.20}Cu_{0.14}]O_2$ is lower than that of $Na_x[Mn_{0.65}Fe_{0.20}Ni_{0.15}]O_2$, due to lower contribution of the Cu^{2+}/Cu^{3+} couple to the redox process, compared with $Ni^{2+/}Ni^{3+,4+}$.

The redox reactions involved in the charge and discharge processes of the substituted materials reported in previous chapters were investigated by *operando* X-ray absorption spectroscopy (Chapter 6). The evolution of the local structure of each transition metal in $Na_x[Mn_{0.66}Fe_{0.20}Cu_{0.14}]O_2$ upon cycling was probed by monitoring the XANES spectra collected at the Mn, Fe, and Cu K-edges. The data indicated the complete oxidation of Mn^{3+} ions to Mn^{4+} upon charge, followed by partial oxidation of Cu^{2+} to Cu^{3+} and Fe^{3+} to Fe^{4+}. The *operando* measurement of the XANES spectra of $Na_x[Mn_{0.65}Fe_{0.20}Ni_{0.15}]O_2$ at the Ni K-edge showed the oxidation of Ni^{2+} to $Ni^{3+/4+}$ upon the first charge. A particularly important observation was that the XANES spectra of $Na_x[Mn_{0.66}Fe_{0.20}Cu_{0.14}]O_2$ at the Mn, Fe, and Cu K-edges did not show any discernible evolution at high voltage region (> 4.1 V vs. Na/Na^+ upon charge), suggesting the contribution of oxide ions into the redox processes, similar to the case of Li-rich transition metal oxide positive electrode materials for Li-ion batteries.

The specific energy delivered by $Na_x[Mn_{0.65}Fe_{0.20}Ni_{0.15}]O_2$ is comparable to that of $LiFePO_4$, which is employed as a positive electrode material in some commercial Li-ion batteries. Moreover, this amount of energy is obtained from a material synthesized by the simple and scalable conventional solid state method and without any carbon coating, whereas carbon coating and small particle size are necessary to obtain the good electrochemical performance of $LiFePO_4$. The future development of

layered Mn, Fe-containing oxides for Na-ion batteries should address the instability and inadequate cyclability of these materials. The necessity of storage and handling of these materials with avoiding the exposure to moisture and CO_2 in air increases the cost of their practical application. The air reactivity issue described in this study is probably not limited to this family of materials and could be a concern with any P2-type Mn^{3+}-containing oxide. The systematic investigation of air instability in a larger group of layered oxides and the exploration of tailored substitutions to suppress this issue should be an avenue of the future work. Positive electrode materials based on the $Fe^{3+/4+}$ redox couple are attractive regarding providing a high voltage, and therefore high energy. However, transition metal migration induced by the formation of Fe^{4+} needs to be prevented. In this study, the damaging impact of phase transitions induced upon cycling, especially the high voltage transition, on energy retention was demonstrated. The reversibility and the onset of transition metal migration at high voltage are related to the type of structure (it differs in the P2 and O3 structures), the concentration of Fe ions, the nature of the other transition metals in the lattice, and the concentration of sodium vacancies. The strong hybridization of Fe^{4+} 3d orbitals with oxygen 2p orbitals is probably the origin of the high voltage phase transition. The contribution of oxide ions into the redox processes was also concluded from an *operando* XAS study. Further investigation of this process by a combination of XAS experiments and computational studies would provide in-depth understanding and insightful information for the future of this research path.

We demonstrated that when the electrode is protected against exposure to air and the cut-off voltage is adjusted so that the phase transitions are avoided, a $Na_{0.67}[Mn_{0.65}Fe_{0.20}Ni_{0.15}]O_2$/Na cell with an organic electrolyte cycled at C/10 rate loses 20% of its initial capacity after 150 cycles. The interactions of the positive and the negative electrodes with the electrolyte solution should contribute to the capacity fading. For example, dissolution of transition metals from the surface of lithium metal oxide positive electrodes is a well-known aging mechanism in Li-ion batteries.[154] Surface coating and using electrolyte

additives are two approaches to address this issue.[158-161] The surface chemistry of oxide materials in contact with electrolytes is not much explored for Na-ion batteries and deserves further investigation. Certainly, finding suitable negative electrodes is inevitable for the development of Na-ion batteries.

Bibliography

1 U.S. Energy Information Administration, International Energy Outlook **2013**.

2 Renewable Energy Policy Network for the 21st Century (REN21), Global Status Report **2015**.

3 U.S. Department of Energy, Grid Energy Storage **2013**.

4 N. Yabuuchi, S. Komaba, *Sci. Technol. Adv. Mater.* **2014**, 15, 043501.

5 Y.-F. Y. Yao, J. T. Kummer, *J. Inorg. Nucl. Chem.* **1967**, 29, 2453.

6 T. Oshima, M. Kajita, A. Okuno, *Int. J. Appl. Ceram. Technol.* **2004**, 1, 269.

7 Ceramatec, Inc. WO2012061823A2, patent application, 2012.

8 A. Hayashi, K. Noi, A. Sakuda, M. Tatsumisago, *Nat. Commun.* **2012**, 3, 856.

9 M. S. Whittingham, *Prog. Solid State Chem.* **1978**, 12, 4.

10 A. S. Nagelberg, W. L. Worrell, *J. Solid State Chem.* **1979**, 29, 345.

11 Y. Takeda, K. Nakahara, M. Nishijima, N. Imanishi, O.Yamamoto, M. Takano, R. Kanno, *Mater. Res. Bull.* **1994**, 29, 659.

12 S. Okada, Y. Takahashi, T. Kiyabu, T. Doi, J. Yamaki, T. Nishida, *210th ESC Meeting Abstracts* **2006,** MA2006-02, 201.

13 S. Komaba, C. Takei, T. Nakayama, A. Ogata, N. Yabuuchi, *Electrochem. Commun.* **2010**, 12, 355.

14 K. Mizushima, P. C. Jones, P. J. Wiseman, J. B. Goodenough, *Mat. Res. Bull.* **1980**, 15, 783.

15 Y. Takayuki, H. Kato, M. Anzai, US Patent 5053297, **1991**.

16 D. Andre, S.-J. Kim, P. Lamp, S. F. Lux, F. Maglia, O. Paschos, B. Stiaszny, *J. Mater. Chem. A* **2015**, 3, 6709.

17 C. M. Julien, A. Mauger, K. Zaghib, H. Groult, *Inorganics* **2014**, 2, 132.

18 R. J. Brodd, Batteries for Sustainability, Springer Science+Business Media, New York **2013**.

19 B. L. Ellis, K. T. Lee, L. F. Nazar, *Chem. Mater.* **2010**, 22, 691.

20 C. Masquelier, L. Croguennec, *Chem. Rev.* **2013**, 113, 6552.

21 J. Vetter, P. Novak, M.R. Wagner, C. Veit, K.-C. Möller, J.O. Besenhard, M. Winter, M. Wohlfahrt-Mehrens, C. Vogler, A. Hammouche, *J. Power Sources* **2005**, 147, 269.

22 S. Komaba, Y. Matsuura, T. Ishikawa, N. Yabuuchi,W. Murata, S. Kuze, *Electrochem. Commun*. **2012**, 21, 65.

23 M. Dahbi, N. Yabuuchi, K. Kubota, K. Tokiwac, S. Komaba, *Phys. Chem. Chem. Phys.* **2014**, 16, 15007.

24 M. Dahbi, T. Nakano, N. Yabuuchi, T. Ishikawa, K. Kubota, M. Fukunishi, Sota Shibahara, J.-Y. Son, Y.-T. Cui, H. Oji, S. Komaba, *Electrochem. Commun.* **2014**, 44, 66.

25 H. Kang, Y. Liu, K. Cao, Y. Zhao, L. Jiao, Y. Wang, H. Yuan, *Mater. Chem. A* **2015**, 3, 17899.

26 S. Komaba, W. Murata, T. Ishikawa, N. Yabuuchi, T. Ozeki, T. Nakayama, A. Ogata, K. Gotoh, K. Fujiwara, *Adv. Funct. Mater*. **2011**, 21, 3859.

27 D. A. Stevensa, J. R. Dahn, *J. Electrochem. Soc.* 2001, 148, A803.

28 M. S. Whittingham, *Science* **1976**, 192, 1126.

29 G. H. Newman, L. P. Klemann, *J. Electrochem. Soc.* **1980**, 127, 2097.

30 C. Delmas, J.-J. Braconnier, C. Fouassier, P. Hagenmuller, *Solid State Ion.* **198**1, 3, 165.

31 P. Moreau, D. Guyomard, J. Gaubicher, F. Boucher, *Chem. Mater.* **2010**, 22, 4126.

32 K. T. Lee, T. N. Ramesh, F. Nan, G. Botton, L. F. Nazar, *Chem. Mater.* **2011**, 23, 3593.

33 M. H. Han, E. Gonzalo, G. Singha, T. Rojo, *Energy Environ. Sci.* **2015**, 8, 81.

34 D. Kundu, E. Talaie, V. Duffort, L. F. Nazar, *Angew. Chem*. **2015**, 54, 3431.

35 N. Yabuuchi, K. Kubota, M. Dahbi, S. Komaba, *Chem. Rev.* **2014**, 114, 11636.

36 K. Kuratani, N. Uemura, H. Senoh, H. T. Takeshita, T. Kiyobayashi, *J. Power Sources* **2013**, 223, 175.

37 S. P. Ong, V. L. Chevrier, G. Hautier, A. Jain, C. Moore, S. Kim, X. Ma, G. Ceder, *Energy Environ. Sci.* **2011**, 4, 3680.

38 C. Delmas, C. Fouassier, P. Hagenmuller, *Physica B+C* **1980**, 99, 81.

39 A. Mendiboure, C. Delmas, P. Hagenmuller, *J. Solid State Chem.* **1985**, 57, 323.

40 R. Stoyanova R, D. Carlier, M. Sendova-Vassileva, M. Yoncheva, E. Zhecheva, D. Nihtianova, C. Delmas, *J. Solid State Chem.* **2010**, 183, 1372.

41 X. Li, D. Wu, Y.-N. Zhou, L. Liu, X.-Q. Yang, G. Ceder, *Electrochem. Commun.* **2014**, 49, 51.

42 Y. Lei, X. Li, L. Liu, G. Ceder, *Chem. Mater.* **2014**, 26, 5288.

43 Z. Lu, J. R. Dahn, *J. Electrochem. Soc.* **2001**, 148, A1225.

44 J. M. Paulsen,J. R. Dahn, *J. Electrochem. Soc.* **2000**, 147, 2478.

45 R. Fielden, M. N. Obrovac, *J. Electrochem. Soc.* **2015**, 162, A453.

46 C. Delmas, A. Maazaz, C. Fouassier, J.-M. Réau, P. Hagenmuller, *Mater. Res. Bull*. **1979**, 14, 329.

47 D. H. Lee, J. Xu, Y. S. Meng, *Phys. Chem. Chem. Phys.* **2013**, 15, 3304.

48 H.Tomita, K. Kubota, R. Kanno, *J. Power Sources* **2011**,196, 6809.

49 X. Wang, G. Liu, T. Iwao, M. Okubo, A. Yamada, *J. Phys. Chem. C* **2014**, 118, 2970.

50 X. Ma, H. Chen, G. Ceder, *J. Electrochem. Soc.* **2011**, 158, A1307.

51 R. Stoyanova, D. Carlier, M. Sendova-Vassileva, M. Yoncheva, E. Zhecheva, D. Nihtianova, C. Delmas, *J. Solid State Chem.* **2010**,183, 1372.

52 A. Caballero, L. Hernan, J. Morales, L. Sanchez, J. Santos Pena, M. A. G. Aranda, *J. Mater. Chem.* **2002**, 12, 1142.

53 N. Yabuuchi, M. Kajiyama, J. Iwatate, H. Nishikawa, S. Hitomi, R. Okuyama, R. Usui, Y. Yamada, S. Komaba, *Nature Mater.* **2012**, 11, 512.

54 R. Berthelot, D. Carlier, C. Delmas, *Nature Mater.* **2011**, 10, 74.

55 V. Duffort, E. Talaie, R. Black, L. F. Nazar, *Chem. Mater.* **2015**, 27, 2515.

56 E. Talaie, V. Duffort, H. L. Smith, B. Fultz, L. F. Nazar, *Energy Environ. Sci*. **2015**, 8, 2512.

57 B. Mortemard de Boisse, D. Carlier, M. Guignard, L. Bourgeois, C. Delmas, *Inorg. Chem*. **2014**, 53, 11197.

58 G. Singh, J. L. del Amo, M. Galceran, S. Perez-Villar, T. Rojo, *J. Mater. Chem. A* **2015**, 3, 6954.

59 K. Park, B. C. Yu, J. B. Goodenough, *Chem. Mater.* **2015**, 27, 6682.

60 G. Singh, B. Acebedo, M. C. Cabanas, D. Shanmukaraj, M. Armand, T. Rojo, *Electrochem. Commun*. **2013**, 37, 61.

61 B. Mortemard de Boisse, D. Carlier, M. Guignard, C. Delmas, *J. Electrochem. Soc*. **2013**, 160, A569.

62 J. S. Thorne, R. A. Dunlap, M. N. Obrovac, *J. Electrochem. Soc.* **2013**, 160, A361.

63 J. Xu, S. L. Chou, J. L. Wang, H. K. Liu, S. X. Dou, *ChemElectroChem* **2014**, 1, 371.

64 S. Kalluri, K. Hau Seng, W. Kong Pang, Z. Guo, Z. Chen, H.-K. Liu, S. X. Dou, *ACS Appl. Mater. Interfaces* **2014**, 6, 8953.

65 N. Sharma, E. Gonzalo, J. C. Pramudita, M. H. Han, H. E. A. Brand, J. N. Hart, W. K. Pang , Z. Guo, T. Rojo, *Adv. Funct. Mater.* **2015**, 25, 4994.

66 M. H. Han, E. Gonzalo, N. Sharma, J. M. L. del Amo, M. Armand, M. Avdeev, J. J. S. Garitaonandia, T. Rojo, *Chem. Mater.* **2016**, 28, 106.

67 L. Liu, X. Li, S.-H. Bo, Y. Wang , H. Chen, N. Twu, D. Wu, G. Ceder, *Adv. Energy Mater.* **2015**, 1500944.

68 D. Yuan, X. Hu, J. Qian, F. Pei, F. Wu, R. Mao, X. Ai, H. Yang, Y. Cao, *Electrochim. Acta* **2014**, 116, 300.

69 I. Hasa, D. Buchholz, S. Passerini, B. Scrosati, J. Hassoun, *Adv. Energy Mater.* **2014**, 4, 1400083.

70 Y. Li, Z. Yang, S. Xu, L. Mu, L. Gu, Y.-S. Hu, H. Li, L. Chen, *Adv. Sci.* **2015**, 2, 1500031.

71 S. Komaba, N. Yabuuchi, T. Nakayama, A. Ogata, T. Ishikawa, I. Nakai, *Inorg. Chem.* **2012**, 51, 6211.

72 H. Yoshida, N. Yabuuchi, S. Komaba, *Electrochem. Commun.* **2014**, 49, 51.

73 J. Xu, D. H. Lee, R. J. Clément, X. Yu, M. Leskes, A. J. Pell, G. Pintacuda, X.-Q. Yang, C. P. Grey, Y. S. Meng, *Chem. Mater*. **2014**, 26, 1260.

74 N. Yabuuchi, R. Hara, M. Kajiyama, K. Kubota, T. Ishigaki, A. Hoshikawa, S. Komaba, *Adv. Energy Mater.* **2014**, 4, 1301453.

75 D. Wang, I. Belharouak, G. Zhou, K. Amine, *Adv. Funct. Mater*. **2013**, 23, 1070.

76 D. Mohanty, A. Huq, E. Andrew Payzant, A. S. Sefat, J. Li, D. P. Abraham, D. L. Wood, C. Daniel, *Chem. Mater*. **2013**, 25, 4064.

77 J. Billaud, G. Singh, A. R. Armstrong, E. Gonzalo, V. Roddatis, M. Armand, T. Rojo, P. G. Bruce, *Energy Environ. Sci.* **2014**, 7, 1387.

78 N. Yabuuchi, R. Hara, K. Kubota, J. Paulsen, S. Kumakura, S. Komaba, *J. Mater. Chem. A* **2014**, 2, 16851.

79 S. LeVine, The Powerhouse: Inside the Invention of a Battery to Save the World, Publisher: Viking Adult, **2015**.

80 D. Kim, E. Lee, M. Slater, W. Lu, S. Rood, C. S. Johnson, *Electrochem. Commun.* **2012**, 18, 66.

81 E. Lee, J. Lu, Y. Ren, X. Luo, X. Zhang, J. Wen, D. Miller, A. DeWahl, S. Hackney, B. Key, D. Kim, M. D. Slater, C. S. Johnson, *Adv. Energy Mater*. **2014**, 4, 1400458.

82 A. R. West, Basic Solid State Chemistry, Second Edition, John Wiley & Sons LTD. **1999**.

83 V. K. Pecharsky, P. Y. Zavalij, Fundamentals of Powder Diffraction and Structural Characterization of Materials, Springer Science+Business Media, LLC **2009**.

84 A. Le Bail, *Powder Diffr.* **2005**, 20, 316.

85 J. Rodriguez-Carvajal, *Phys. B* **1993**, 192, 55.

86 V. F. Sear, *Neutron News* **1992**, 3, 29.

87 T. Egami, S. J. L. Billinge, Underneath the Bragg Peaks Structural Analysis of Complex Materials, R. Cahn, Ed.; Oxford/Pergamon Press, New York **2004**.

88 P. Juhas, T. Davis, C. L. Farrow, S. J. Billinge, *J. Appl. Crystallogr.* **2013**, 46, 560.

89 C. L. Farrow, P. Juhas, J. W. Liu, D. Bryndin, E. Božin, J. Bloch, T. Proffen, S. J. L. Billinge, *Phys.: Condens. Matter* **2007**, 19, 335219.

90 B. Fultz, Mössbauer Spectrometry in Characterization of Materials, E. Kaufmann, Ed.; John Wiley, New York, **2011**.

91 N. Tsiouvaras, S. Meini, I. Buchberger, H. A. Gasteiger, *J. Electrochem. Soc.* **2013**, 160, A471.

92 C. S. Schnohr, M. C. Ridgway, X-Ray Absorption Spectroscopy of Semiconductors, Springer Series in Optical Sciences **2015**.

93 J. E. Penner-Hahn, Introduction to XAFS, Cambridge University Press **2010**.

94 Z. Lu, J. R. Dahn, *Chem. Mater.* **2001**, 13, 1252.

95 D. Buchholz, L. G. Chagas, C. Vaalma, L. Wu, S. Passerini, *J. Mater. Chem. A* **2014**, 2, 13415.

96 M. Sathiya, K. Hemalatha, K. Ramesha, J. M. Tarascon, A. S. Prakash, *Chem. Mater*. **2012**, 24, 1846.

97 H. Liu, J. Xu, C. Maa, Y. S. Meng, *Chem. Commun.* **2015**, 51, 4693.

98 M. J. Paulsen, J. R. Dahn, *Solid State Ionics* **1999**, 126, 3.

99 L. Bordet-Le Guenne, P. Deniard, P. Biensan, C. Siret, R. Brec, *J. Mater. Chem.* **2000**, 10, 2201.

100 P. W. Stephens, *J. Appl. Crystallogr.* **1999**, 32, 281.

101 Y. Ono, N. Kato, Y. Ishii, Y. Miyazaki, T. Kajitani, *J. Jpn. Soc. Powder Powder Metall.* **2003**, 50, 469.

102 D. Carlier, J. H. Cheng, R. Berthelot, M. Guignard, M. Yoncheva, R. Stoyanova, B. J. Hwang, C. Delmas, *Dalton Trans.* **2011**, 40, 9306.

103 M. Guignard, C. Didier, J. Darriet, P. Bordet, E. Elkaïm, C. Delmas, *Nature Mater.* **2013**, 12, 74.

104 X. Wang, M. Tamaru, M. Okubo, A. Yamada, *J. Phys. Chem. C* **2013**, 117, 15545.

105 N. Yabuuchi, M. Yano, H. Yoshida, S. Kuze, S. Komaba, *J. Electrochem. Soc.* **2013**, 160, A3131.

106 S. Komaba,T. Ishikawa, N. Yabuuchi, W. Murata, A. Ito, Y. Ohsawa, *ACS Appl. Mater. Interfaces* **2011**, 3, 4165.

107 Y. U. Jeong, A. Manthiram, *J. Solid State Chem.* **2001**, 156, 331.

108 C. Greaves, P. Slater, *Physica C.* **1991**, 178, 175.

109 V. R. L. Constantino, T. J. Pinnavaia, *Inorg. Chem.* 1995, 34, 883.

110 J. C. Hunter, *J. Solid State Chem.* **1981,** 39, 142.

111 R. J. Gummow, A. de Kock, M. M. Thackeray, *Solid State Ionics* **1994,** 69, 59.

112 B. Mortemard de Boisse, J.-H. Cheng, D. Carlier, M. Guignard, C. -J. Pan, S. Bordere, D. Filimonov, C. Drathen, E. Suard, B.-J. Hwang, A. Wattiaux, C. Delmas, *J. Mater. Chem. A* **2015**, 3, 10976.

113 J. S. Thorne, R. A. Dunlap, M. N. Obrovac, J. Electrochem. Soc. **2014**, 161, A2232.

114 J. S. Thorne, S. Chowdhury, R. A. Dunlap, M. N. Obrovac, *J. Electrochem. Soc.* **2014**, 161, A1801.

115 R. D. Shannon, *Acta Cryst.* **1976**, 32, 751.

116 C. A. Geiger, E. Alekseev, B. Lazic, M. Fisch, T. Armbruster, R. Langner, M. Fechtelkord, N. Kim, T. Pettke, W. Weppner, *Inorg. Chem.* **2010**, 50, 1089.

117 D. Zeng, J. Cabana, J. Bréger, W.-S. Yoon, C. P. Grey, *Chem. Mater.* **2007**, 19, 6277.

118 J. Bréger, N. Dupre´, P. J. Chupas, P. L. Lee, T. Proffen, J. B. Parise, C. P. Grey, *J. Am. Chem. Soc*. **2005**, 127, 7529.

119 J. Bréger, K. Kang, J. Cabana, G. Ceder, C. P. Grey, *J. Mater. Chem*. **2007**, 17, 3167.

120 J. Zhao, L. Zhao, N. Dimov, S. Okada, T. Nishida, *J. Electrochem. Soc.* **2013**, 160, A3077.

121 A. E. Bocquet, T. Mizokawa, T. Saitoh, H. Namatame, A. Fujimori, *Phys. Rev. B* **1992**, 46, 3771.

122 M. Takano, N. Nakanishi, Y. Takeda, S. Naka, T. Takada, *Mater. Res. Bull.* **1977**, 12**,** 923.

123 A. E. Bocquet, A. Fujimori, T. Mizokawa, T. Saitoh, H. Namatame, S. Suga, N. Kimizuka, Y. Takeda, M. Takano, *Phys. Rev. B* **1992**, 45, 1561.

124 K. Kubota, I. Ikeuchi, T. Nakayama, C. Takei, N. Yabuuchi, H. Shiiba, M. Nakayama, S. Komaba, *J. Phys. Chem. C* **2015**, 119, 166.

125 Y. Ono, Y. Yui, M. Hayashi, K. Asakura, H. Kitabayashi, K. I. Takahashia, *ECS Transactions* **2014**, 58, 33.

126 S. Y. Xu, X. Y. Wu, Y. M. Li, Y.-S. Hu, L. Q. Chen, *Chin. Phys. B* **2014**, 23, 118202.

127 L. Q. Mu, Y.-S. Hu, L. Q. Chen, *Chin. Phys. B* **2015**, 24, 038202. *Chin. Phys. B* **2015**, 24, 038202.

128 C. W. Mason, F. Lange, K. Saravanan, F. Lin, D. Nordlund, *ECS Electrochem. Lett.* **2015**, 4, A41.

129 L. Mu, S. Xu, Y. Li, Y.-S. Hu, H. Li, L. Chen, X. Huang, *Adv. Mater.* **2015**, 27, 6928.

130 N. Sharma, N. Tapia-Ruiz, G. Singh, A. R. Armstrong, J. C. Pramudita, H. E. A. Brand, J. Billaud, P. G. Bruce, T. Rojo, *Chem. Mater.* **2015**, 27, 6976.

131 N. Sharma, M. H. Han, J. C. Pramudita, E. Gonzalo, H. E. A. Brand, T. Rojo. *J. Mater. Chem. A* **2015**, 3, 21023.

132 J.-P. Parant, R. Olazcuaga, M. Devalette, C. Fouassier, P. Hagenmuller, *Solid State Chem.* **1971**, 3, 1.

133 P. Burns, F. C. Hawthorne, *Can. Mineral.* **1996**, 34, 1089.

134 D. Choudhury, P. Rivero, D. Meyers, X. Liu, Y. Cao, S. Middey, M. J. Whitaker, S. Barraza-Lopez, J. W. Freeland, M. Greenblatt, J. Chakhalian, *Phys. Rev. B* **2015**, 92, 201108.

135 S. Nimkar, D. D. Sarma, H. R. Krishnamurthy, *Phys. Rev. B* **1993**, 47, 10927.

136 J. B. Goodenough, J.-S. Zhou, K. Allan, *J. Mater. Chem.* **1991**, 1, 715.

137 D. Mohanty, J. Li, D. P. Abraham, A. Huq, E. A. Payzant, D. L. Wood, C. Daniel, *Chem. Mater.* **2014**, 26, 6272.

138 M. Oishi, T. Fujimoto, Y. Takanashi, Y. Orikasa, A. Kawamura, T. Ina, H. Yamashige, D. Takamatsu, K. Sato, H. Murayama, H. Tanida, H. Arai, H. Ishii, C. Yogi, I. Watanabe, T. Ohta, A. Mineshige, Y. Uchimoto, Z. Ogumi, *J. Power Sources* **2013**, 222, 45.

139 D. Buchholz, J. Li, S. Passerini, G. Aquilanti, D. Wang, M. Giorgetti, *ChemElectroChem* **2015**, 2, 85.

140 H. Koga, L. Croguennec, M. Ménétrier, P. Mannessiez, F. Weill, C. Delmas, S. Belin, *J. Phys. Chem. C* **2014**, 118, 5700.

141 B. Ravel, M. Newville, *J. Synchrotron Radiat.* **2005**, 12, 537.

142 O. J. Borkiewicz, K. M. Wiaderek, P. J. Chupas, K. W. Chapman, *J. Phys. Chem. Lett.* **2015**, 6, 2081.

143 T. Yamamoto, *X-Ray Spectrom.* **2008**, 37, 572.

144 Y. Iwasawa (ed.), X-ray Absorption Fine Structure for Catalysts and Surfaces, World Scientific Publishing Co. Pte. Ltd. **1996**.

145 M. Sathiya, A. M. Abakumov, D. Foix, G. Rousse, K. Ramesha, M. Saubanère, M. L. Doublet, H. Vezin, C. P. Laisa, A. S. Prakash, D. Gonbeau, G. VanTendeloo, J-M. Tarascon, *Nature Mater.* **2015**, 14, 230.

146 D. Choudhury, P. Rivero, D. Meyers, X. Liu, Y. Cao, S. Middey, M. J. Whitaker, S. Barraza-Lopez, J. W. Freeland, M. Greenblatt, J. Chakhalian, *J. Phys. Rev. B* **2015**, 92, 201108.

147 T. Tsuyama, T. Matsuda, S. Chakraverty, J. Okamoto, E. Ikenaga, A. Tanaka, T. Mizokawa, H. Y. Hwang, Y. Tokura, H. Wadati, *Phys. Rev. B* **2015**, 91, 115101.

148 E. Lee, D. E. Brown, E. E. Alp, Y. Ren, J. Lu, J.-J. Woo, C. S. Johnson, *Chem. Mater.* **2015**, 27, 6755.

149 A. Deb, U. Bergmann, S. P. Cramer, E. J. Cairns, *J. Appl. Phys.* **2005**, 97, 113523.

150 N. K. Karan, M. D. Slater, F. Dogan, D. Kim, C. S. Johnson, M. Balasubramanian, *J. Electrochem. Soc.* **2014**, 161, A1107.

151 Z. Y. Wu, D. C. Xian, T. D. Hu, Y. N. Xie, Y. Tao, C. R. Natoli, E. Paris, A. Marcelli, *Phys. Rev. B* **2004**, 70, 033104.

152 M. Sathiya, G. Rousse, K. Ramesha, C. P. Laisa, H. Vezin, M. T. Sougrati, M.-L. Doublet, D. Foix, D. Gonbeau, W.Walker, A. S. Prakash, M. Ben Hassine, L. Dupont, J.-M. Tarascon, *Nature Mater.* **2013**, 12, 827.

153 H. Koga, L. Croguennec, M. Menetrier, K. Douhil, S. Belin, L. Bourgeois, E. Suard, F. Weill, C. Delmas, *J. Electrochem. Soc.* **2013**, 160, A786.

154 D. Foix, M. Sathiya, E. McCalla, J.-M. Tarascon, D. Gonbeau, *J. Phys. Chem. C* **2016**, 120, 862.

155 F. La Mantia, F. Rosciano, N. Tran, P. Novák, *J. Electrochem. Soc.* **2009**, 156, A823.

156 J. Rana , M. Stan , R. Kloepsch , J. Li , G. Schumacher,E. Welter , I. Zizak , J. Banhart, M. Winter, *Adv. Energy Mater*. **2014**, 4, 1300998.

157 Y. Nanba, T. Iwao, B. Mortemard de Boisse, W. Zhao, E. Hosono, D. Asakura, H. Niwa, H. Kiuchi, J. Miyawaki, Y. Harada, M. Okubo, A. Yamada, *Chem. Mater.* **2016**, 28, 1058.

158 M.-S. Park, J-W. Lee, W. Choi, D. Im, S.-G. Doo, K.-S. Park, J. *Mater. Chem.* **2010**, 20, 7208.

159 H. M. Wu, I. Belharouak, A. Abouimrane, Y.-K. Sun, K. Amine, *J. Power Sources* **2010**, 195, 2909.

160 D. Takamatsu, S. Mori, Y. Orikasa, T. Nakatsutsumi, Y. Koyama, H. Tanida, H. Arai, Y. Uchimoto, Z. Ogumi, *J. Electrochem. Soc.* **2013**, 160, A3054.

161 K. Amine, Z. Chen, Z. Zhang, J. Liu, W. Lu, Y. Qin, J. Lu, L. Curtis, Y.-K. Sun, *J. Mater. Chem.* **2011**, 21, 17754.